UNIVERSITE BRETAGNE SCIENCES LOIRE POUR L'INGENIEUR

UNIVERSITÉ DE NANTES

THESE DE DOCTORAT DE

L'UNIVERSITE DE NANTES
COMUE UNIVERSITE BRETAGNE LOIRE

ECOLE DOCTORALE N° 602
Sciences pour l'Ingénieur
Spécialité : Génie Civil

Par
« Habib TAHA »

« Mechanical behavior of eroded soils: numerical study based on the DEM »

Thèse présentée et soutenue à « Saint Nazaire », le « 13 Septembre 2019 »
Unité de recherche : GeM - Institut de recherche en génie civil et mécanique - UMR CNRS 6183

Composition du Jury :

Président :	Eric VINCENS	Professeur, Ecole Centrale de Lyon
Rapporteurs :	Pierre PHILIPPE Luc SIBILLE	Directeur de Recherche, IRSTEA, Aix-en-Provence Maître de conférences, HDR, Université Grenoble Alpes
Examinateurs :	Nadia BENAHMED	Chargé de recherche, IRSTEA, Aix en Provence
Directeur de thèse :	Didier MAROT	Professeur, Université de Nantes
Co-directeur de thèse :	Abbas HIJAZI	Professeur, Université Libanaise
Co-encadrants de thèse:	Ngoc-Son NGUYEN Khalil ABOU-SALEH	Maître de conférences, Université de Nantes Maître de conférences, Université Libanaise

Acknowledgements

" The future depends on what we do in the present " (Mahatma GANDHI). This present is lit by the support of beloved people. Such people deserve appreciation in every single moment. For that, i would like to grasp the opportunity to express my gratitude to all those people who have been a reason in the successful completion of this research.

My deepest gratitude is to my supervisors: Prof. Didier MAROT, Prof. Abbas HIJAZI, Dr. Ngoc-Son NGUYEN and Dr. Khalil ABOU-SALEH. I have been amazingly fortunate to work with supervisors who gave me the freedom to explore on my own, and at the same time the guidance to recover when my steps faltered. they taught me how to question my thoughts and express ideas. Their patience, support, comments, remarks and engagement are the reasons which helped me overcome all the obstacles faced during this work.

I would like to sincerely thank Prof. Eric VINCENS, Dr. Luc SIBILLE, Dr. Pierre PHILIPPE, Dr. Nadia BENAHMED for being members of the jury and for their insightful comments on my study.

A big appreciation to all members of the IEG team in Saint Nazaire who helped me very well, especially the former leader Prof. Abdelhafid KHELIDJ, Prof. Nordine LEKLOU, Dr. Rachel GELET, Dr. Fateh BENDAHMANE for encouraging me all the time as well for their scientific advice. Special thanks are devoted to our secretary Mrs. Maryse RADIN for her good sense of humor and support, and for Mrs. Laurence GUIHENEUF and Mr. Philippe LEROUY for their positive vibes.

Furthermore, i would like to thank all my friends: Abdallah, Abdo, Abed, Bahaa, Arnaout, Carla, Quentin, Nadgib, Achour, Ishak, Camilo, Haydar, Hammoud, Jawad, Anna, Doja, Nadine, Francois, Jean, Khodor, Philippe, Wassim, Christelle, Mira, Tarhine, Hisham, Johney, Nehme, Karim, Antoinette, for their support and encouragement which drive me to give my best. A special appreciation is devote to Mrs. Jacqueline DUCLOU for her unconditional support and love.

Finally, i would to thank my parents, my brother and my sister for their encouragement and their kindness. The greatest appreciation is kept for my soul mate, my wife Alaa KODIEH. I extremely grateful for having her by my side and for her belief in me and in my goals. I would like to thank her for helping me achieving one of my dreams.

Contents

List of Figures

List of Tables

List of symbols

C_{v}	Coefficient of variation
C, F	Coarse and fine fractions
$C-C$	Coarse-coarse contacts
$C-F$	Coarse-fine contacts
$F-F$	Fine-fine contacts
C_u	Coefficient of uniformity
D_{min}, D_{max}	Minimum and maximum diameters of coarse particles
d_{min}, d_{max}	Minimum and maximum diameters of fine particles
$D_r = (e_{max}\text{-}e)/(e_{max}\text{-}e_{min})$	Relative density
e_{min}	Minimum void ratio
e_{max}	Maximum void ratio
e	Global void ratio
e_c	Intergranular void ratio
e_f	Interfine void ratio
E_{m}	Young's modulus of the particle material
E_{flow}	Water seepage
f_c	Fine content
f_n, f_t	Normal and tangential contact forces
$\boldsymbol{f}^k$	Force at a given contact k
f_d	Dry density
f_c^{th}	Threshold value of fine content
f_c^*	Critical fine content
f_p	External force exerted on a unit volume of the fluid
f^{eq}	Distribution function at thermodynamic equilibrium
f_{unb}^p	Unbalanced force on a particle p
f	Cost function
G_{r}	Gap ratio
H_{ij}	Fabric tensor
H_d	Anisotropy index
i_c	Hydraulic gradient
I_α	Erosion resistance index
I	Inertia number
K_n, K_t	Normal and tangential contact stiffnesses
k_n, k_t	Normal and tangential particle stiffnesses
L	Sample size
$\boldsymbol{l}^k$	Branch vector joining two particle centers at a given contact k

$\boldsymbol{M}^p$	Internal moment tensor of a given particle p
m^p	Mean internal moment
m^f	Mass of fine particles
m^c	Mass of coarse particles
m	Mass of all particles
m_{fry}	Dry mass
n	Global porosity
N_c	Number of coarse particle
N_f	Number of fine particles
$\mathcal{N}$	Coordination number
$\mathcal{N}_C^{C-C}$	Average number of $C-C$ contacts per coarse particle
$\mathcal{N}_C^{C-F}$	Average number of $C-F$ contacts per coarse particle
$\mathcal{N}_F^{F-F}$	Average number of $F-F$ contacts per fine particle
p	Mean stress
α_p^F	Mean stress ratio for the fine fraction
p^F, q^F	Mean and deviatoric stresses carried by the fine fraction
q	Deviatoric stress
α_q^F	Deviatoric stress ratio for the fine fraction
$(q/p)_{max}$	Peak shear strength
q_{ij}	Pressure difference between two pores i and j
REV	Representative volumetric Element
R^2	Coefficient of correlation
$U_{i,j}$	Partial differentiation of the displacement vector U with respect to the plane vector x
u_i	Relative displacement of contact points
V	Total volume of a sample
ρ	Mass density
ζ	Damping coefficient
φ	Contact friction angle
$\boldsymbol{\sigma}$	Stress tensor
σ	Standard deviation
σ_1	Major principal stress
σ_2, σ_3	Lateral stresses
$\boldsymbol{\varepsilon}$	Strain tensor
ε_{11}	Axial strain
ε_{v}	Volumetric strain
V_{v}, V_{s}	Void and solid volumes
$\boldsymbol{l}^k$	Branch vector joining two particle centers at a given contact k
$\boldsymbol{\sigma}^{C-C}$	Contribution of the $C-C$ contacts to the macro-stress
$\boldsymbol{\sigma}^{C-F}$	Contribution of the $C-F$ contacts to the macro-stress
$\boldsymbol{\sigma}^{F-F}$	Contribution of the $F-F$ contacts to the macro-stress
ϕ^α	Volume fraction of a given phase α
$\boldsymbol{\sigma}^\alpha$	Intrinsic averaged stress of a given phase α
$\widehat{\boldsymbol{\sigma}}^\alpha$	Partial stress of a given phase α
α	Stress reduction factor

$\widehat{p}^F$	Contribution of the fine fraction to the macroscopic mean stress
$\widehat{q}^F$	Contribution of the fine fraction to the macroscopic deviatoric stress
∇	Gradient
∇^2	Square gradient
μ	Mean value
δ	Overlap between two adjacent inscribed spheres
γ	Relative overlap between two adjacent inscribed spheres
$\gamma_{\max}$	Maximal relative overlap
γ^{th}	user-specified value of γ
ξ	Relative intersection between inscribed void spheres and solid particles
$\xi_{\max}$	Maximal relative intersection between inscribed void spheres and solid particles
μ_e	Percentage of extracted fine particles
Δ_{μ_e}	Extraction rate
η	Stress ratio
τ_m	Shear stress applied on the sample
σ_m	Isotropic stress applied on the sample
$\|\| \ \|\|$	Norm of vector
$\| \ \|$	Absolute value

Abstract

Suffusion can induce a loss of fine particles to granular soils and consequently a modification of their mechanical behavior. In this PhD thesis, we aim to study the effect of the loss of fine particles caused by suffusion on mechanical properties of soils at the macroscopic and microscopic scales by using the Discrete Element Method (DEM). Granular samples composed of spherical particles with a gap-graded particle size distribution (PSD) are simulated by the DEM. Due to a very high computational cost, the fluid flow through the void space between solid particles is not simulated. Instead, we propose a representation of the internal state of soils after suffusion at three different levels with increasing complexity. For the level 1, a sample considered as eroded is generated at a target density and with a fine content lower than that of the original sample. The level 2 consists in removing a fraction of fine particles from the original sample at a given stress state. We proposed thus a method to identify the loose fraction composed of particles which do not carry significantly stresses. The level 3 aims to take into account the transport of fine particles in the pore network of the solid skeleton and the blockage of fine particles by constrictions. The key point in this model is how to describe the pore network. This study showed that fine particles can have a negligible effect, positive or negative effect on the shear strength depending on fine content. A removal of fine particles causes a significant reduction in shear strength to gap-graded soils. It was also showed that a random removal of fine particles leads to a greater reduction in shear strength than a removal of only fine particles in the loose fraction. For the description of the pore network of the solid skeleton, we propose a new method for merging neighboring tetrahedra issued from the Delaunay triangulation. This pore network will be incorporated into a model to take into account the transport and blockage of fine particles within the pore network of the solid skeleton.

Résumé

La suffusion peut induire une perte de particules fines au sein de sols granulaires et par conséquent une modification leur comportement mécanique. Cette thèse a pour objectif d'étudier la conséquence de cette perte de particules fines sur les propriétés mécaniques des sols aux échelles macroscopique et microscopique en utilisant la méthode des éléments discrets (MED). Des échantillons granulaires composés de particules sphériques dont la taille suit une distribution granulométrique lacunaire sont modélisés par la MED. A cause d'un coût de calcul élevé, l'écoulement du fluide à travers l'espace poral entre particules solides n'est pas modélisé. Nous proposons plutôt une représentation de l'état interne du sol après la suffusion suivant trois niveaux de complexité croissante. Pour le niveau 1, des échantillons considérés comme érodés sont générés à une densité donnée et avec un pourcentage des fines plus petit que celui de l'échantillon original. Le niveau 2 consiste à retirer une fraction des particules fines de l'échantillon original à un état de contrainte donné. Pour cela, nous proposons une méthode permettant d'identifier une fraction lâche composée des particules qui ne participent pas significativement à supporter la sollicitation. Le niveau 3 a pour objectif de prendre en compte le transport et le blocage des particules fines par des constrictions dans l'espace poral formé par le squelette solide. Le point essentiel à ce niveau réside dans la description du réseau des pores. Cette étude a montré que les particules fines peuvent avoir un effet négligeable, positif ou négatif sur la résistance mécanique selon le pourcentage de fines. Une extraction des particules fines conduit à une diminution de la résistance mécanique des sols érodés. Nous avons montré que la réduction de la résistance mécanique est plus forte si des particules fines sont retirées de façon aléatoire que si seules des particules fines de la fraction lâche sont retirées. Pour la description du réseau des pores, une nouvelle méthode a été proposée pour associer des tétraèdres voisins résultant de la triangulation de Delaunay. Ce réseau des pores sera incorporé dans un modèle pour prendre en compte le transport et le blocage des particules fines au sein de l'espace poral formé par le squelette solide.

Résumé étendu

1. Contexte général et objectifs

Des milliers d'ouvrages hydrauliques en terre tels que des barrages et des digues ont été construits dans le monde entier afin d'assurer la protection contre les inondations et la submersion, pour permettre la production d'hydroélectricité et pour constituer des réserves d'eau. Plusieurs études ont montré que les deux principales causes d'instabilités que peuvent subir ces ouvrages hydrauliques en terre sont la surverse et les différents processus d'érosion interne. La suffusion est un de ces processus et elle mobilise la fraction fine des sols pulvérulents qui ont une distribution continue convexe ou une distribution lacunaire. Lorsqu'un sol est sujet au processus de suffusion, une partie de sa fraction fine peut migrer sous l'effet de l'écoulement interne. Or la fraction fine joue un rôle important dans le comportement mécanique des sols granulaires. La suffusion peut donc induire d'importantes modifications des propriétés mécaniques des sols ce qui pourrait à terme, affecter la stabilité des ouvrages hydrauliques en terre. Plusieurs études expérimentales ont montré que la suffusion peut produire une réduction de la résistance au cisaillement des sols suffusifs et une modification de leur comportement, de dilatant à contractant (Chen et al., 2016; Chang and Zhang, 2011). Toutefois, une interrogation persiste sur le moyen de modéliser le comportement mécanique d'un sol érodé.

Dans la littérature, plusieurs approches ont d'ores et déjà été proposées pour modéliser le comportement mécanique d'un sol érodé. Hicher (2012, 2013) a développé une technique d'homogénéisation afin de prendre en compte les modifications de la microstructure du sol induites par la suffusion. Rousseau et al. (2018) ont utilisé la théorie poro-élasto-plastique pour modéliser le comportement mécanique en supposant une variation irréversible au cours du cisaillement du sol à cause de la porosité induite par la suffusion. Ces deux modèles prédisent que la suffusion va s'accompagner d'une diminution de la résistance au cisaillement. Toutefois, il convient de noter que la suffusion provoque un accroissement de l'hétérogénéité de l'échantillon qui n'est pas prise en compte dans ces deux modèles. Vis-à-vis de cette problématique, la Méthodes des Eléments Discrets (DEM) apparaît être un outil adapté pour modéliser le comportement mécanique de sols granulaires à l'échelle des grains. Cette méthode permet de reproduire les principales caractéristiques du comportement mécanique des sols granulaires: telles que la non linéarité, l'adoucissement, la dilatance et l'anisotropie (Belheine et al., 2009). L'un des principaux avantages de cette méthode réside dans la possibilité d'accéder aux informations locales à l'échelle des particules permettant ainsi de caractériser le milieu poreux d'un point de vue micromécanique. Par ailleurs, la DEM peut être couplée à un modèle de fluide pour décrire son écoulement dans le milieu et prendre ainsi en considération l'interaction fluide – particules solides. Plusieurs couplages DEM-modèle de fluide ont ainsi été développées comme DEM-CFD (Zhao et Shan, 2013; Benmezroua, 2011), DEM-LDM (Lominé et al., 2013; Tran et al., 2017) et DEM-SPH (Sjah, 2013; Robinson et al., 2013). Toutefois ces méthodes couplées DEM-fluide nécessitent d'importants moyens de calculs et engendrent d'énormes temps de calcul car à l'intérieur du réseau poral, le fluide est modélisé très précisément à l'échelle des particules. Dans ce contexte, des méthodes simplifiées ont été proposées comme la méthode DEM-PFV (Chareyre et al., 2012; Catalano et al., 2014) et la méthode simplifiée DEM-CFD (Zhao et Shan, 2013; Hu et al., 2019; Shafipour et Soroush, 2008; Kawano et al., 2018; Pirnia et al., 2019). Au lieu de modéliser finement le fluide, ces méthodes simplifiées décrivent en moyenne le fluide à l'intérieur de l'espace poral réduisant ainsi le temps

de calcul. Néanmoins le temps de calcul reste trop important pour simuler le processus de suffusion dans un sol à distribution lacunaire ou continue convexe et seule l'initiation du processus peut être simulée (Hu et al., 2019; Kawano et al., 2018; Pirnia et al., 2019; Aboul Hosn, 2017). Une alternative qui consiste à enlever une fraction des particules solides de l'échantillon initial a été développée par différents auteurs sans utiliser de modèle de fluide (Wood and Maeda, 2008; Muir Wood et al., 2010; Scholtès et al., 2010; Aboul Hosn, 2017). Ces développements ont permis de reproduire la réduction de la résistance au cisaillement sus-évoquée. Il convient toutefois de noter que ce type d'approche nécessite d'identifier les particules fines qui sont enlevées et qu'il convient de prendre aussi en compte le transport et le blocage éventuel des particules fines.

Dans ce contexte, cette thèse a pour objectif d'étudier les conséquences de la suffusion sur le comportement mécanique des sols érodés en utilisant la DEM. Pour simuler l'ensemble du processus de suffusion, au lieu d'utiliser une méthode qui couple la DEM et un modèle de fluide qui est très couteuse en temps de calcul, seule la fraction solide est modélisée mais trois niveaux de complexité sont développés pour représenter l'état du sol érodé. Le premier niveau est inspiré de l'étude expérimentale de Sterpi (2003) dans laquelle aucun essai de suffusion n'est réalisé. Par contre l'auteur a préparé des échantillons avec une proportion de particules fines plus faible que le sol initial et les a compacté en visant une densité donnée. Ces échantillons sont supposés représenter le sol érodé mais à ce niveau, aucun mécanisme de suffusion n'est réellement pris en compte. Le deuxième niveau est inspiré de l'étude expérimentale réalisée par Chen et al. (2016) qui ont remplacé une partie des particules fines par du sel qui se dissout lorsque de l'eau est injectée. Cette approche expérimentale est comparable à l'enlèvement de particules fines par la méthode DEM. Deux processus d'enlèvement de particules fines sont utilisés: l'enlèvement aléatoire et l'enlèvement de particules fines faiblement chargées mécaniquement. L'identification de ces particules faiblement chargées est réalisée par la détermination des chaines de forces faibles et fortes. Donc à ce niveau, seul le détachement des particules est pris en compte.

Le troisième niveau a pour objectif de considérer aussi le transport des particules détachées et leur éventuel blocage géométrique au sein du milieu poreux. Le milieu poreux est représenté par un squelette constitué des particules qui ne sont pas détachables. Le réseau poral qui entoure ce squelette est décomposé en pores et constrictions qui peuvent être traversés par les particules détachables. Toutefois une particule détachable sera bloquée dans une constriction si elle est plus grosse que la taille de la constriction. Les travaux réalisés dans le cadre de cette thèse sont présentés en cinq chapitres et sont suivis par les conclusions et perspectives qui peuvent être élaborées à partir des travaux menés.

2. Chapitre 1

L'étude bibliographique fait l'objet de ce premier chapitre et dresse un bilan du rôle des particules fines dans le comportement mécanique des sols granulaires ainsi que les conséquences de la suffusion sur les propriétés mécaniques des sols érodés. Plusieurs conclusions peuvent être établies: La présence de particules fines influence fortement la densité du sol et l'indice des vides est minimal pour un pourcentage particulier de particules fines. Les particules fines jouent un rôle important dans le comportement mécanique des sols granulaires avec une variation de la résistance mécanique et de la dilatance en fonction du pourcentage de fines. Jusqu'à ce jour les conséquences de la suffusion sur le comportement mécanique sont méconnues mais des études préliminaires indiquent que la suffusion semble induire une diminution de la résistance mécanique et une dilatance des sols érodés. Les méthodes numériques et plus particulièrement la DEM qui ont été développées pour modéliser la suffusion et le comportement mécanique des sols érodés sont également présentées. Ces méthodes consistent à enlever les particules les plus petites et les moins chargées mécaniquement. Les conclusions de ces travaux correspondent aux conclusions des études expérimentales préliminaires. Toutefois les méthodes numériques reposent sur l'hypothèse de l'accroissement de porosité induite par la suffusion sans réarrangement des grains; or la validité de cette hypothèse constitue toujours

une interrogation.

3. Chapitre 2

Dans le chapitre 2 sont présentées la méthode des éléments discrets (DEM) ainsi que la procédure pour simuler des essais triaxiaux. Des échantillons constitués de mélanges de billes de verre à distribution lacunaire sont modélisés avec un gap ratio (rapport du diamètre maximum et du diamètre minimal de l'étendu lacunaire) de 3 et un pourcentage de fines compris entre 0 et 100%. Une analyse du volume élémentaire représentatif est réalisée afin de limiter le temps de calcul tout en garantissant la représentativité des simulations. Pour un pourcentage de fines $f_c \leq 60\%$, le volume élémentaire représentatif peut être défini par le rapport $L/D_{\max} > 7{,}0$ avec L: longueur de l'échantillon et $D_{\max}$: diamètre maximum des grains. Pour un pourcentage de fines $f_c > 60\%$, le rapport $L/D_{\max}$ est réduit afin d'avoir des temps de calcul raisonnables. Par ailleurs, le comportement mécanique du mélange étant majoritairement piloté par la fraction fine, le mélange modélisé avec $f_c > 60\%$ est considéré comme le volume élémentaire représentatif. Des échantillons à granulométrie lacunaire et avec plusieurs pourcentages de fines sont compactés pour obtenir les états les plus denses et les plus lâches. L'étude montre que l'indice des vides est minimal pour un pourcentage de fines $f_c = 32\%$. Des essais triaxiaux sont effectués sur les échantillons lâches et denses. L'effet des particules fines sur le comportement contrainte-déformation du mélange a pu être mis en évidence pour un pourcentage de fines $f_c \geq 20\%$. La dilatance et la résistance au cisaillement sont plus élevées pour $f_c = 32\%$ qui correspond aussi au minimum de l'indice des vides. A partir de 60% de fines, le comportement contrainte-déformation semble indépendant du pourcentage de fines.

4. Chapitre 3

Ce chapitre est dédié à l'étude micromécanique des effets de la fraction fine sur le comportement mécanique des échantillons à distribution lacunaire et avec un pourcentage de fines compris entre 0 et 100%. Cette étude est menée en identifiant la contribution à la résistance au cisaillement macroscopique, des contacts entre les différentes particules, c'est-à-dire entre les particules grossières (contact grossier-grossier), entre les particules grossières et les particules fines (contact grossier-fine) et entre les particules fines (contact fine-fine). Pour un pourcentage de fines $f_c < 20\%$, les particules fines flottent dans le réseau poral et ne participent pas de manière significative à la résistance au cisaillement. A partir de 20%, les fines ont deux effets opposés sur la microstructure: elles viennent au contact des particules grossières et contribuent à renforcer la microstructure, mais elles peuvent aussi séparer les particules grossières et fragiliser la microstructure. Au fur et à mesure de l'accroissement du pourcentage de fines, l'effort de cisaillement est supporté de plus en plus par les contacts grossier-fine et de moins en moins par les contacts grossier-grossier. Pour un pourcentage de fines inférieur à 30%, la résistance au cisaillement est principalement supportée par les contacts grossier-grossier. La diminution de la contribution des contacts grossier-grossier est compensée par un fort accroissement par la contribution des contacts grossier-fine. Il en résulte un accroissement de la résistance au cisaillement du mélange, mais au-delà de 30% de fines, la résistance au cisaillement diminue. Les contacts fine-fine n'ont une contribution significative à la résistance mécanique qu'à partir d'un pourcentage de fines supérieur à 40%. A partir de 60% de fines, ce sont les contacts fine-fine qui contribuent majoritairement à la résistance au cisaillement. Il a été également observé que les chaines de forces fortes pour les mélanges étudiés incluent presque toutes les particules grossières, mais jamais plus de 50% des particules fines. Ainsi une majorité des contacts fine-fine est située dans les chaines de forces faible. Pour un pourcentage de fines $f_c < 20\%$ les particules grossières constituent le squelette solide. Entre 20 et 60% de fines, les fines participent activement à la résistance au cisaillement en renforçant le squelette solide. Au-delà de 60% de fines, les particules grossières se comportent comme des inclusions dans la matrice formée par les fines. A partir de cette étude, quatre catégories de microstructure sont proposées en fonction du pourcentage de fines et en prenant en compte le rôle des trois types de contacts.

5. Chapitre 4

L'objet de ce chapitre concerne les conséquences de la perte de particules fines sur le comportement mécanique des échantillons. L'état initial de l'échantillon est représenté suivant le niveau 2. Différentes méthodes d'enlèvement des particules sont présentées. L'enlèvement inspiré des travaux expérimentaux de Chen et al. (2016) est réalisé de manière aléatoire. Pour un pourcentage initial de fines supérieur à 20%; la résistance au cisaillement diminue avec l'accroissement de l'enlèvement de particules fines. Toutefois certaines particules ainsi enlevées peuvent être fortement chargées mécaniquement et donc probablement non mobilisables par la suffusion. Il convient donc d'identifier les particules fines faiblement chargées qui pourraient être enlevées. Scholtès et al. (2010) identifient les particules fines les moins chargées en utilisant le tenseur des moments défini pour chaque particule. Toutefois une petite particule tend à avoir une faible valeur de ce tenseur et finalement ce critère aboutit sensiblement aux mêmes résultats que l'enlèvement aléatoire. Nous proposons une nouvelle méthode d'identification des particules fines à enlever sur la base du réseau des chaines de forces. Seules les particules fines comprises dans la chaine de forces faible peuvent être enlevées. Suivant cette méthode, l'enlèvement des particules perturbe moins le squelette solide et l'impact sur la résistance au cisaillement s'en trouve réduit. Donc pour un même l'état initial, différentes méthodes d'enlèvement des particules peuvent conduire à différents comportements contrainte-déformation.

6. Chapitre 5

Dans ce chapitre, un modèle de réseau poral est introduit afin de représenter le sol érodé suivant le niveau 3. Les particules sont tout d'abord différenciées en deux catégories: non-détachables si elles appartiennent au squelette solide et détachable si elles appartiennent aux chaines de forces faibles. Les particules détachables peuvent se déplacer dans le réseau poral qui entoure le squelette solide constitué par les particules non détachables. Si la taille d'une particule détachable excède la taille d'une constriction, elle est bloquée, sinon elle traverse la constriction et atteint donc le pore voisin. Cette méthode suppose toutefois une description fine du réseau poral avec identification des pores et des constrictions qui les séparent. Suivant cet objectif, les différentes techniques décrites dans la littérature pour représenter ce réseau poral sont analysées. Ensuite à partir de la triangulation de Delaunay, une nouvelle méthode de définition du réseau poral est élaborée. La fusion de pores voisins fait aussi l'objet de développements en comparant les distributions de tailles de pores et de tailles de constrictions obtenues à l'aide des différentes méthodes susmentionnées.

7. Conclusion et perspectives

Les travaux de cette thèse traitent des conséquences de la suffusion sur le comportement mécanique des sols granulaires en utilisant la méthode des éléments discrets (DEM). Tout modèle couplé DEM-fluide nécessite d'importants moyens de calculs et génèrent de très importants temps de calcul. Pour contourner cette difficulté, seule la fraction solide est modélisée et l'état initial du sol érodé est représenté suivant trois niveaux de complexité. Au niveau 1, l'échantillon est préparé suivant la même distribution et la même densité que le sol érodé mais sans considérer les mécanismes de la suffusion. Le niveau 2 consiste à mimer la perte de fines en enlevant des particules fines suivant différentes méthodes. Pour le niveau 3, le réseau poral est décrit afin de prendre en compte le transport et l'éventuel blocage géométrique des particules détachées. Les échantillons étudiés ont une distribution lacunaire avec un gap ratio de 3 et un pourcentage de fines fc compris entre 0 et 100%. Après l'identification du volume élémentaire représentatif, une étude micromécanique est réalisée sur les effets de la faction fine sur le comportement mécanique des échantillons. L'influence des fines est significative à partir d'un pourcentage $fc > 20\%$. Pour un pourcentage $fc < 30\%$, la contribution des contacts grossier-fine permet un accroissement de la

résistance au cisaillement mais pour un pourcentage fc supérieur, la résistance au cisaillement diminue. Au-delà d'un pourcentage $f_c > 60\%$, les particules grossières se comportent comme des inclusions au sein de la matrice de fines. Lorsque l'enlèvement des particules fines est réalisé de manière aléatoire, la résistance au cisaillement diminue en fonction de l'enlèvement. La nouvelle méthode d'enlèvement proposée est basée sur le réseau des chaines de forces et dans ce cas, l'enlèvement des particules a moins d'impact sur la résistance au cisaillement. Enfin pour réaliser l'enlèvement des particules suivant le niveau 3, le réseau poral est défini à partir de la triangulation de Delaunay et une nouvelle méthode de fusionnement des pores. Ces travaux permettent d'obtenir une meilleure compréhension du rôle complexe des particules fines dans le comportement mécanique des sols granulaires. Ils permettent également d'ouvrir de nombreuses perspectives de recherche concernant les conséquences de la suffusion sur le comportement mécanique des sols érodés et à terme, sur son implication dans les instabilités des ouvrages hydrauliques en terre.

General introduction

Nowadays thousands of earth structures, such as dams and dikes exist all over the world to prevent flooding and submersion, but also to produce hydropower, to store freshwater water for drinking or irrigation. Overtopping and internal erosion are two main causes of failure of such earth structures. Suffusion is a particular form of internal erosion, which might occur inside granular soils having gap-graded or widely graded particle size distributions. When a granular soil subjected to suffusion, due to the seepage force of the fluid flow, a fraction of fine particles migrate throughout the void space between coarser particles, causing a loss of fine particles to the suffusive soil. Fine particles play an important role in mechanical behavior of granular soils; as a consequence, suffusion can lead to a change in mechanical properties of suffusive soils, which might affect the stability of earth structures. Several experimental studies have shown that suffusion causes a reduction in shear strength and dilatancy to suffusive soils (Chen et al., 2016; Chang and Zhang, 2011). On open question is how to model the mechanical behavior of an eroded soil.

Several approaches have been proposed to model the mechanical behavior of an eroded soil. Hicher (2012, 2013) developed a homogenization technique to take into account the structural changes resulting from the loss of fine particles caused by suffusion. Rousseau et al. (2018) used the poro-elastoplastic theory to develop a model of the mechanical behavior of eroded soils by assuming that part of irreversible volume changes during the shear loading due to a variation in porosity caused by suffusion. Both models predicted a reduction in the shear strength of the soil subjected to suffusion. It should be noted that suffusion causes the increase of the heterogeneity in the sample which is not taken into account in these two models.

Discrete Element Method (DEM) appears to be a tool very suited to modeling of granular materials at the particle scale. This method is able to reproduce the main features of the mechanical behavior of granular materials such as the non-linearity, the softening phase, the dilatancy and the induced anisotropy Belheine et al. (2009). One of its main advantages is that any local information at the particle scale can be accessed, which makes the DEM very suitable for investigating granular media from a micro-mechanical point of view. The DEM can be coupled to a fluid model to describe the fluid flow throughout the void space and to take into consideration interaction between fluid and solid particles. Several coupled DEM-fluid models have been developed such as DEM-CFD (Zhao and Shan, 2013; Benmezroua, 2011), DEM-LBM (Lominé et al., 2013; Tran et al., 2017) and DEM-SPH (Sjah, 2013; Robinson et al., 2013). However, these coupled DEM-fluid models require a powerful computational resources and a huge computational time since they model finely the fluid flow within the void space. Some simplified DEM-fluid models have been proposed such as DEM-PFV (Chareyre et al., 2012; Catalano et al., 2014) and simplified DEM-CFD models (Zhao and Shan, 2013; Hu et al., 2019; Shafipour and Soroush, 2008; Kawano et al., 2018; Pirnia et al., 2019). Instead of modeling finely the fluid flow, these simplified models describe the fluid flow throughout the void space in an average sense to reduce the computational cost. Despite this simplification, these models are still very expensive to simulate the suffusion process within a gap-graded or widely graded granular material and only the early stage of the suffusion process can be simulated (Hu et al., 2019; Kawano et al., 2018; Pirnia et al., 2019; Aboul-Hosn, 2017). Alternative methods which consist in removing a fraction of fine particles from the original samples have been used by several authors

to represent the internal state of a soil subjected to suffusion without resort to a coupled DEM-fluid model (Wood and Maeda, 2008; Wood et al., 2010; Scholtès et al., 2010; Aboul-Hosn, 2017). These methods were found to be capable of reproducing a reduction in shear strength of the eroded soil. It is of great importance in this kind of approaches to identify accurately fine particles to be removed and to take into account the transport and blockage of fine particles within the void space.

This PhD thesis aims to study the consequences of suffusion on the mechanical behavior of eroded soils by using the DEM. Instead of using a coupled DEM-fluid model to simulate the whole suffusion process, the internal state of an eroded soil is represented at three different levels with increasing complexity:

- The level 1 is inspired from the experimental study of Sterpi (2003) in which no suffusion test is performed. The author prepared samples with fine content lower than the original fine content and compacted them to obtain a target relative density. These samples are considered as being *eroded*. This procedure is adopted in our study to represent the internal state of eroded samples. At this level, no main mechanism of suffusion is taken into consideration.

- The level 2 is inspired from the experimental study of Chen et al. (2016) in which a fraction of fine particles were first replaced by salts which were subsequently dissolved by an injection of water. This experimental procedure is similar to a removal of fine particles from the original sample, which can be performed by the DEM. Two methods will be used for removing fine particles. For the first method, fine particles are randomly removed, while only loose fine particles, which do not carry significantly stresses, are removed for the second method. These loose fine particles are identified by investigating the strong and weak force chains. This level takes into consideration only the detachment of fine particles.

- The level 3 is aimed at taking into account the transport and blockage of fine particles within the void space by using a pore network model. The pore network composed of pores and constrictions is formed by the undetachable particles. A detachable particle is moved from one pore to another according to a certain rule until either it is blocked by a constriction smaller than its size or it moves out the sample.

This PhD thesis report is divided into five chapters:

- Chapter 1 presents a literature review about the role of fine particles in the mechanical behavior of granular soils, suffusion and its consequences on the mechanical properties of eroded soils. We present also some numerical methods, particularly the DEM and coupled DEM-fluid models, which have been developed to model the suffusion process and the mechanical behavior of eroded soils.

- Chapter 2 gives a brief description of the DEM and of the procedure to simulate triaxial tests on numerical samples. Gap-graded samples composed of spherical particles with different fine contents are simulated. An analysis of the representative volume element for the simulated samples will be then presented. Finally, the effect of fine content on the void ratios and on the stress-strain behavior of the simulated samples will be presented and discussed.

- Chapter 3 is dedicated to a micro-mechanical investigation of the effect of fine content on the mechanical behavior of the simulated gap-graded samples. This micro-mechanical investigation focuses on how fine content affects the micro-structure and the transmission of the shear stress through the contact network. The participation of the fine particles in carrying the shear stress will be also analyzed. Based on this micro-mechanical investigation, we will propose a new classification

of gap-graded soils according to fine content.

- Chapter 4 presents a study of the consequences of a loss of fine particles on the mechanical behavior of eroded samples. The internal state of eroded samples is represented at the level 2. Different methods for removing fine particles will be used. A new method will be proposed to identify the loose fine particles which do not carry significantly stresses by considering the weak and strong force chains. A comparison between different methods will be presented.

- In Chapter 5, a pore network model will be introduced to represent the internal state of eroded samples at the level 3. The primary importance in such a model lies in the description of the pore network formed by the solid skeleton. This chapter focuses then on different methods in the literature to describe the pore network based on the Delaunay triangulation. Their drawbacks will be put in evidence and a new method will be proposed to overcome these drawbacks. Although the proposed pore network model is not complete yet, the capability of the new method proposed in this chapter to extract the pore network will be demonstrated by comparing it to other methods.

Chapter 1

Literature review

1.1 Introduction

This chapter presents a literature review of the role of the fine particles in widely graded soils and consequences of a loss of fine particles caused by internal erosion on their mechanical behavior. We start this literature review by a brief presentation of granular materials in earth-filled structures: classification of these materials and some generalities of their mechanical behavior in Section 1.2. The variation of the void ratios and the mechanical behavior of widely graded soils with fine content will be discussed in Section 1.3. An earth-filled structure might be subjected to suffusion, a particular form of internal erosion, during which fine particles are washed out from the soil solid skeleton by seepage flow. Sections 1.4 and 1.5 will be dedicated to suffusion and its impact on the mechanical behavior of the eroded soils. Last but not least, Section 1.6 presents some approaches for modeling suffusion and the mechanical behavior of eroded soils. Then we end this literature by setting up some conclusions.

1.2 Granular materials in earth-filled structures

1.2.1 Classification of granular materials

In soil mechanics, a material is said to be granular when it consists of grains or solid elements that interact at contact zones. Figure 1.1 presents a classification of granular materials in order to promote the understanding of the various terms used (Salot, 2007). Three families of granular materials can be distinguished: synthetic materials (created from scratch by humans), model materials, much used in research (steel beads, glass beads, ..) and geomaterials such as soils and rocks. Among the geomaterials, we can distinguish natural materials from geocomposites such as sand-gravel mixtures, sand-tire mixture or concrete,whose mechanical and geometrical are modified by humans.

Natural soils are classified into two families: cohesive soils and cohesionless soils. The latter ones can also be referred to as frictional soils. These two families of natural soils can be differentiated by the type of predominant interactions between grains. For cohesionless soils, interactions between two particles are dominated by friction forces. On the other hand, the interactions between grains of cohesive soils are dominated by surface forces, such as Van Der Walls forces or electric forces that create cohesion. Another type of contact forces such as capillary forces are exerted by the liquid bridges within the granular medium. The magnitude of capillary forces depends on the quality of the existing liquid and also on the particle shape, orientation and surface properties, such as contact angle and roughness. Cohesive particles can be linked also by solid joints which can be developed by cementing of carbonates, silicas, aluminas, iron oxides and organic compounds.

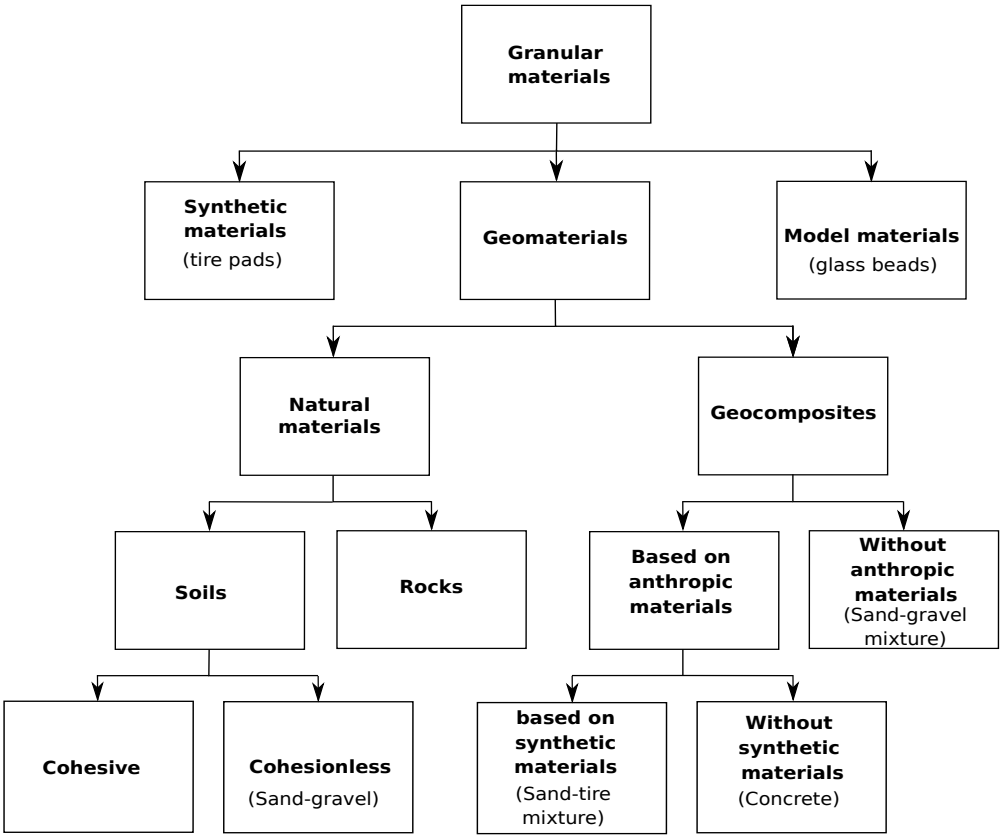

Figure 1.1: Non-exhaustive flow chart of granular materials in soil mechanics (Salot, 2007).

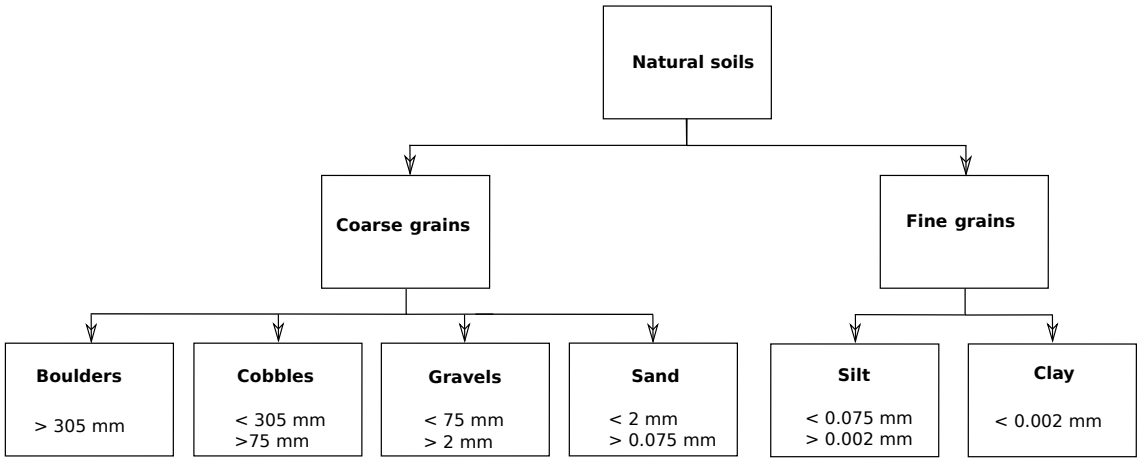

Figure 1.2: Classification of natural soils (NYSDOT, 2013).

Natural soils are often used for construction of hydraulic earth-filled structures such as dikes, levees, embankment dams, etc. Embankment dams are of two types: the earth-filled dam made of compacted soil and the rock-filled dam, which are mainly built with rocks and/or gravels. Natural soils used in the earth-filled dams are divided into two categories: the coarse-grained soils and the fine-grained soils. Based on the classification proposed in the design manual of the New York State Department of Transportation (NYSDOT, 2013), these two categories can be defined as follow:

- **Coarse-grained soils** that contain less than 50% of soil particles passing through 0.075 mm opening.

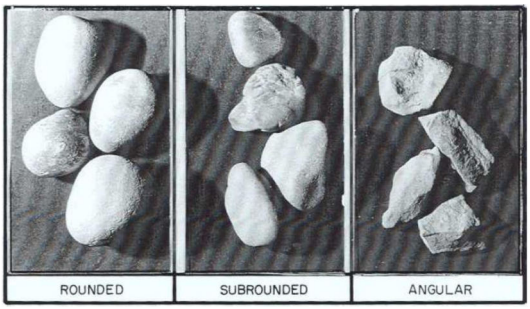

Figure 1.3: Three main types of the shape of particles (NYSDOT, 2013).

- **Fine-grained soils** that contain more than 50% of soil particles passing through 0.075 mm opening.

Figure 1.2 presents this classification of the natural soils. It can be seen that the coarse-grained soils consist predominately of cobbles, gravels or sands which are cohesionless soils. The fine-grained soils consist of silt or clay.

According to NYSDOT (2013), particle shape of granular soils can be classified into three mains types: rounded, subrounded and angular as shown Figure 1.3. Angular grains have sharp edges and relatively plane sides with unpolished surfaces. Subrounded grains have nearly plane sides but have well rounded corners and edges, while rounded grains have smoothly curved sides and no edges.

Granular soils can be also classified according to their grain size distribution. There are two main types: well-graded and gap-graded size distributions. A well-graded soil is defined by a broad gradation and has a good representation of all sizes (curves A and B in Figure 1.4). Sherard and Dunnigan (1989) proposed to classify well-graded soils into three different categories according to their fine content, which is defined as the ratio of the mass of the fine particles to the total mass. In the first category for the fine content smaller than 5%, the fine particles only fill part of the pores formed by the coarse and medium-sized particles (Figure 1.5(a)). In the second category where the fine content is between 5% and 20%, some of the coarse and medium-sized particles are enclosed by fine particles (Figure 1.5(b)). In the third category where the fine content is more than 20%, the pores formed by the coarse particles are fully filled by the medium-sized particles and the pores between the medium-sized particles are fully filled by the fine particles (Figure 1.5(c)).

For a gap-graded soil, a portion of grain sizes is significantly under-represented (curve C in Figure 1.4) or completely absent (curve D in Figure 1.4). Referring to the classification proposed by Sherard and Dunnigan (1989), gap-graded soils are classified into three different categories according to their fine content. In the first category, the fine content is less than 10% and fine grains only fill part of the pores formed by the coarse (Figure 1.6(a)). In the second category, the fine content is between 10% and 35% and the coarse particles are enclosed by the fine particles (Figure 1.6(b)). In the third category, the fine content is more than 35% and the coarse particles float in the fine particles (Figure 1.6(c)).

1.2.2 Mechanical behavior of granular soils

In an earth-filled structure, soils are usually subjected to shear loading and they reach rupture when the shear stress goes beyond their shear resistance. The shear resistance of a granular soil is characterized by the friction angle and the cohesion. These two parameters can be determined by performing tests on soil samples in the laboratory with the triaxial device or with the shear box. The triaxial test consists in consolidating first the tested sample until the fluid pressure achieves a target pressure, and then increasing

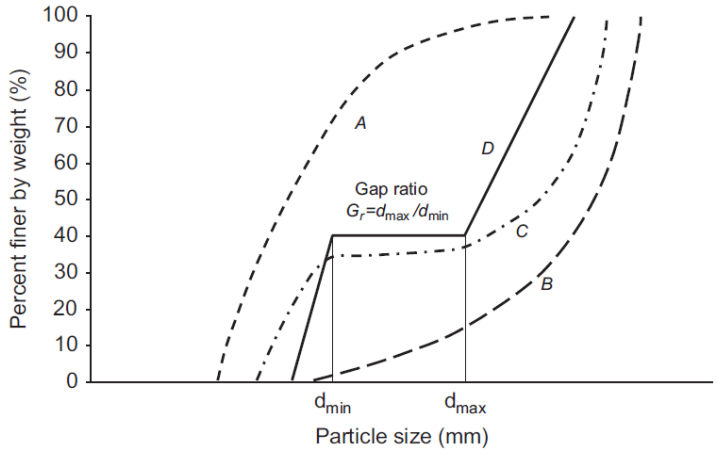

Figure 1.4: Illustration of grain size distribution curves for well-graded and gap-graded soils. (Chang and Zhang, 2013).

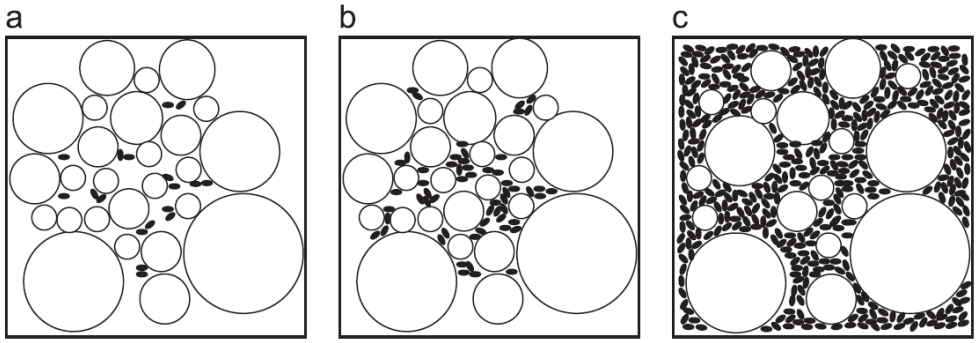

Figure 1.5: Classification of well-graded soils: (a) with fine content less than 5%; (b) with fine content between 5% and 20%; (c) with fine content more than 20% (Sherard and Dunnigan, 1989).

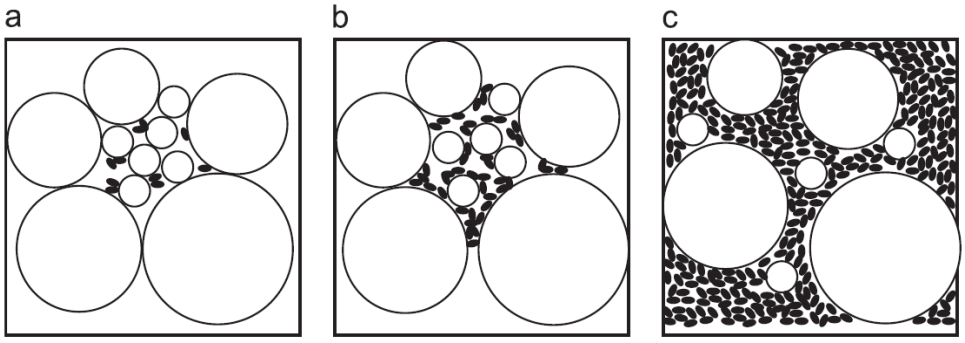

Figure 1.6: Classification of gap-graded soils: (a) with fine content less than 10%; (b) with fine content between 10% and 35% ; (c) with fine content more than 35%. (Sherard and Dunnigan, 1989).

the stress σ_1 in the longitudinal axis (the major principal stress), while keeping the lateral stresses, σ_2 and σ_3 constant and equal to the confining pressure. The difference between the axial stress and the lateral stresses causes shear stress to develop in the sample. The triaxial test can be conducted in drained or undrained conditions.

The behavior of dense and loose soils under a triaxial test are illustrated in Figure 1.7. In this figure, q is the deviatoric stress ($q = \sigma_1 - \sigma_3$) and ε_v is the volumetric strain. The mechanical behavior differs from

the loose soil to the dense one. For the dense soil, the shear stress increases and then reaches a maximum value (the peak state). After the peak, the shear stress decreases and finally reaches a constant value (the critical state). In the case of a loose soil, the shear stress increases steadily during the test and tends to a constant value at the critical state. During the test, the dense soil shows first a small contractant phase followed by a strong dilatant phase, while the loose soil shows only a contractant phase. It is interesting to note that no volumetric variation is observed at the critical state and the residual shear strength is the same for both soils.

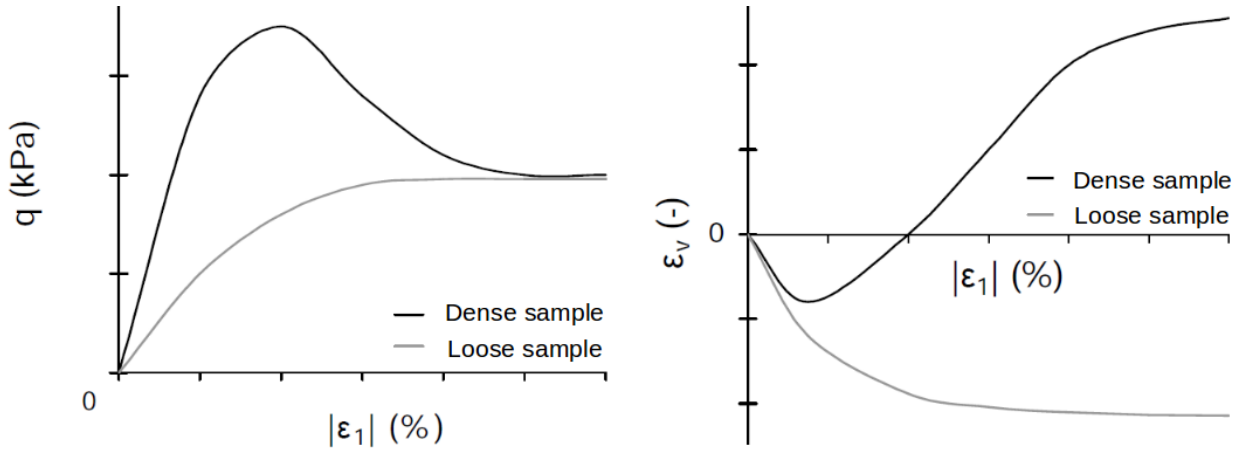

Figure 1.7: Deviatoric stress q versus axial strain ε_1 (left); volumetric strain ε_v versus axial strain ε_1 (right).

1.3 Effect of fine particles on the mechanical properties of granular soils

In Section 1.2.1, different types of natural soils were presented, which can be classified as coarse-grained soils, fine-grained soils or mixtures of both fine and coarse particles. Based on the grain size distribution, granular soils can be also classified as well-graded or gap-graded. In the following, we focus on gap-graded soils, in particular cohesionless mixtures composed of fine and coarse particles such as mixtures of sand and gravel. The amount of fine particles is characterized by fine content f_c which is a vital parameter to study the composition of mixed soils. Sherard and Dunnigan (1989) distinguished many categories of mixtures based on the value of fine content f_c as illustrated in Figures 1.5 and 1.6. Some studies showed that fine content f_c influences the density of soils (Lade et al., 1998; Yang et al., 2006). Other studies showed that fine content f_c has a significant influence on the mechanical behavior of soils (Salgado et al., 2000; Thevanayagam et al., 2002; Nguyen, 2014; Benahmed et al., 2015). Some main results in the literature about the effect of fine content on the internal state and on the mechanical behavior of mixed soils are presented in the following.

A gap-graded soil can be considered as a multi-phase material composed of fine particles, coarse particles and voids between solid particles as illustrated in Figure 1.8(a). It has a total volume V and a total mass m. The fraction of fine particles has a mass m^f and a solid volume V_s^f; the fraction of coarse particles has a mass m^c and a volume V_s^c; and the void volume is V_v (Figure 1.9). A gap-graded soil is characterized by a fine content f_c defined as the ratio of the mass of the fine particles m_f to the total mass m ($f_c = m^f/m$ with $m = m^f + m^c$). Its density can be characterized by the global void ratio e or the global porosity n:

$$e = \frac{V_v}{V_s} = \frac{V_v}{V_s^f + V_s^c}, \text{ and } n = \frac{V_v}{V}. \tag{1.1}$$

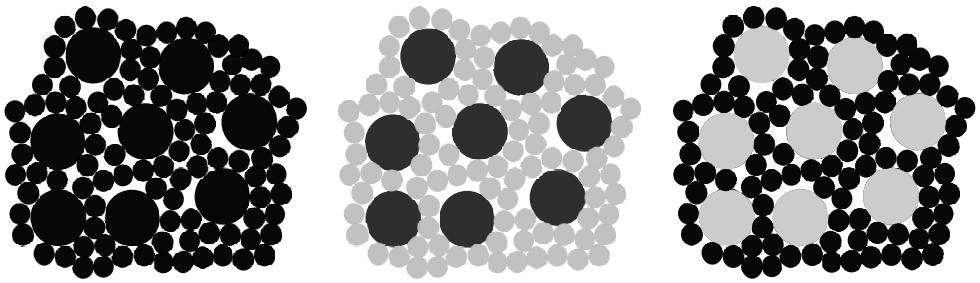

(a) (b) (c)

Figure 1.8: (a) A binary mixture, (b) the case when the fine particles are inactive (gray color) and (c) the case when the coarse particles are inactive.

In a gap-graded soil that contains a fine content smaller than a threshold value, coarse particles may constitute a solid skeleton to carry mainly the overburden stress. A significant fraction of fine particles may be confined within pores between the former ones so they may not participate in sustaining the shear stress as stated by several authors (Skempton and Brogan, 1994; Thevanayagam and Mohan, 2000). According to Thevanayagam and Mohan (2000), the global void ratio e may not adequate to describe the density of such a mixture. Therefore, the authors introduced an intergranular void ratio, e_c, and an interfine void ratio, e_f, defined as follows:

$$e_c = \frac{V_v + V_s^f}{V_s^c} = \frac{e + f_c}{1 - f_c}, \qquad e_f = \frac{V_v}{V_s^f} = \frac{e}{f_c}. \tag{1.2}$$

The intergranular void ratio e_c is defined by assuming that all the fine particles do not sustain any stress and can be considered as the intercoarse voids as illustrated in Figure 1.8.b. On the other hand, the interfine void ratio e_f is defined by assuming that the coarse particles do not participate in sustaining the loading and they can be removed from the sample as illustrated in Figure 1.8.c. According to this definition, the intergranular void ratio e_c describes the density of the coarse fraction, while the interfine void ratio e_f describes the density of the fine fraction.

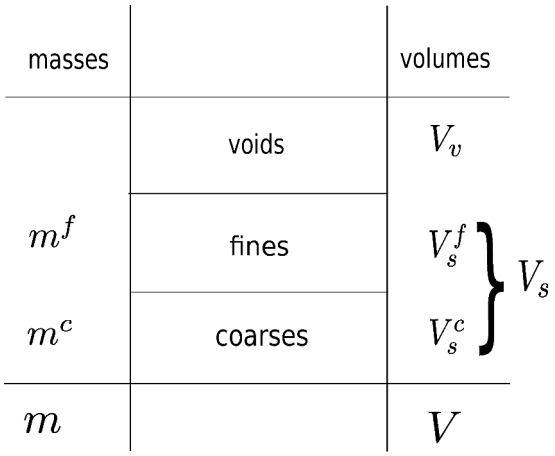

Figure 1.9: Characteristics of mixed soils.

1.3.1 Effect of fine particles on the internal state

This section aims to present several studies of the effect of fine content on the internal state of the mixture of soils. Lade et al. (1998) studied experimentally the void ratio of mixtures of coarse and fine

spherical balls. In these experiments, coarse balls of the same diameter D are mixed with fine spherical balls of the same diameter d. The coarse balls are deposited first in a container and the fine balls are added from the top, while the container is vibrated. For the binary mixtures with the ratio $D/d = 3.5$ (d_{fines}=0.91 mm), Figure 1.10(a) shows that the global void ratio e decreases when the fine content varies between 0% and 40%. This phenomenon can be explained by the fact that, when fines particles are added, they fill the voids left by the coarse particles, thus the global void ratio e decreases in this case. The minimum void ratio is obtained at fine content of 40%, above which the global void ratio increases with fine content. This means that, at f_c = 40%, fine particles fully fill the voids between coarse particles without separating them. Above this optimal fine content, fine particles tend to separate coarse ones, leaving more void space in the mixtures. It is interesting to note that in Figure 1.10(a), the minimum void ratio of mixtures decreases and tends to a limit value as the gap ratio D/d of the big ball diameter to the small ball diameter increases, due to the fact that the gap ratio is an important characteristic of the grain size distribution. In this case the minimum void ratio of the mixture depends on the grain size distribution of the mixture.

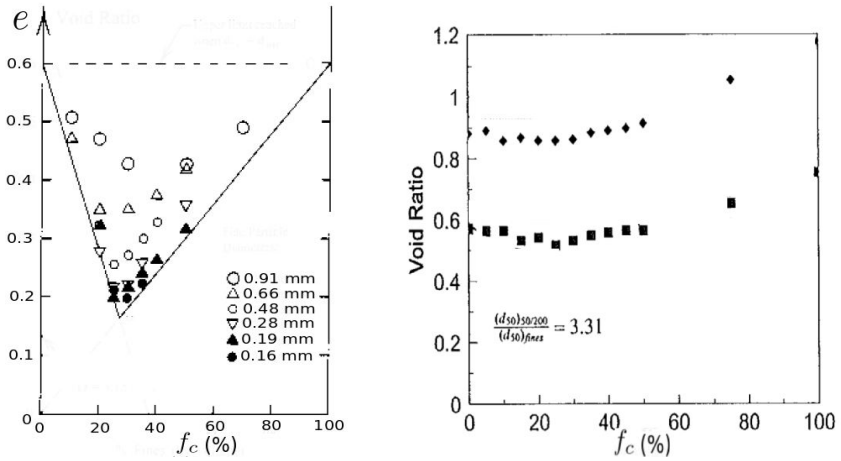

Figure 1.10: Variations of void ratios with fine content presented in Lade et al. (1998): (a) for binary mixtures of small and big spherical balls with different gap ratios D/d, and (b) for the mixtures of coarse and fine Nevada sands.

Lade et al. (1998) studied also the variation of void ratio with the fine content f_c with gap-graded mixtures of coarse Nevada sand (diameter between 0.18 mm and 0.3 mm) and fine Nevada sand (diameter between 0.075 mm and 0.18 mm) with gap ratio between the coarse and fine particles equal to 3.31. In this study, the binary mixtures was compacted according to the ASTM standards D4253-00 and D4254-00 (ASTM D4253-00, 2000; ASTM D4254-00, 2000) to obtain the minimum and the maximum void ratios $e_{\min}$ and $e_{\max}$. Figure 1.10(b) shows the variations of $e_{\min}$ and $e_{\max}$ with respect to fine content f_c. These two void ratios decrease first and then increase with fine content. The optimal fine content for these mixtures is between 20% and 25%. The gap ratio of this mixture is close to the gap-ratio of the mixture of spherical balls presented above (see Figure 1.10(a)), but the two mixtures did not have the same optimal fine content, for that, the optimal fine content can depend also on the particle shape.

Yang et al. (2006) used silt-sand mixtures whose grain size distribution curves are shown in Figure 1.11(a). In this case, the sand represents the coarse particles and the silt represents the fine particles. They studied experimentally the variation of the minimum and the maximum void ratios $e_{\min}$ and $e_{\max}$ with the fine content. As shown in Figure 1.11(b), both $e_{\min}$ and $e_{\max}$ reach their minimum values at f_c = 30% which corresponds to the optimal fine content. This optimal fine content was considered as the

transitional fine content coefficient (TFC), at which sand-dominated behavior changes to silt-dominated behavior. Nguyen (2014) considered silty-sand and found a lower optimal fine content of about 20%.

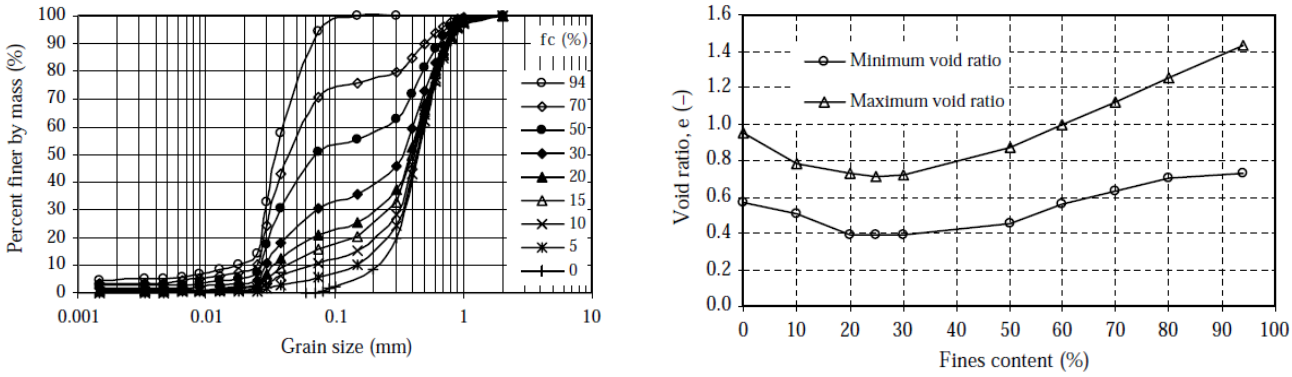

(a) (b)

Figure 1.11: (a) Grain size distributions for the silt-sand mixtures presented in Yang et al. (2006) and (b) maximum and minimum void ratios versus fine content for these silt-sand mixtures.

Thevanayagam et al. (2002) performed tests on gap-graded mixes of Ottawa sand (d between 0.09 mm and 1 mm) and silica fines ($d < 0.074$ mm) with fine content f_c varying between 0% and 100%. The particle size distribution (PSD) curves of these mixtures are shown in Figure 1.12(a). For these tests, the global void ratio e is controlled as much as possible around 0.6. Figure 1.12(b) shows the variation of the three void ratios e, e_c and e_f with fine content f_c. It can be seen that for $f_c < 25\%$, the intergranular void ratio e_c increases slightly, while the interfine void ratio e_f decreases strongly with fine content f_c. This means that, within this range of fine content, the fine particles fill the voids between the coarse particles and they also separate slightly the latter ones. Starting from 25% of fine content, the fine particles fully fill intercoarse voids. A further addition of fine particles needs to discard strongly the coarse particles to increase the void space between them. As a consequence, the intergranular void ratio e_c increases strongly, while the interfine void ratio e_f decreases slightly. The optimal fine content for this type of gap-graded soils seems to be about 30%.

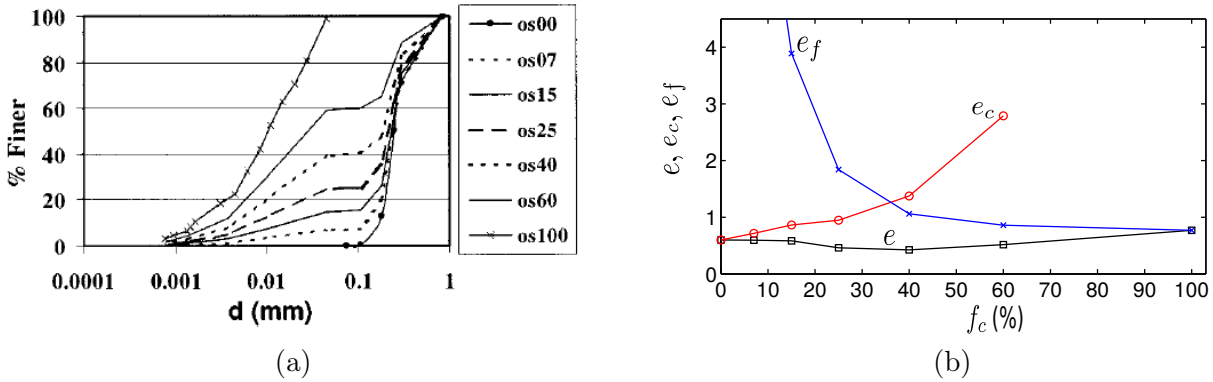

(a) (b)

Figure 1.12: (a) Grain size distributions for the silica-sand mixtures presented in Thevanayagam et al. (2002), and (b) variations of e_c and e_f of these mixtures with fine content f_c.

1.3.2 Effect of fine particles on the mechanical behavior

We have shown in the last section that fine content affects greatly the internal state of granular mixtures. In this section, we show how this parameter influences drained and undrained mechanical behaviors of granular mixtures.

1.3.2.1 Drained behavior

Salgado et al. (2000) performed triaxial drained tests on gap-graded mixtures of silt (d between 0.0006 mm and 0.07 mm) and Ottawa sand (d between 0.07 mm and 1mm), whose particle size distribution curves are presented in Figure 1.13. Loose and dense samples with fine contents varied between 0% and 20% are tested. The relative density D_r is defined by:

$$D_r = \frac{e_{\max} - e}{e_{\max} - e_{\min}} \times 100\%, \tag{1.3}$$

where $e_{\max}$ presents the void ratio of the loosest state of the mixture and $e_{\min}$ presents the densest state of the mixture. In these tests, D_r is controlled between 25% and 40% for loose samples and between 74% and 80% for dense samples.

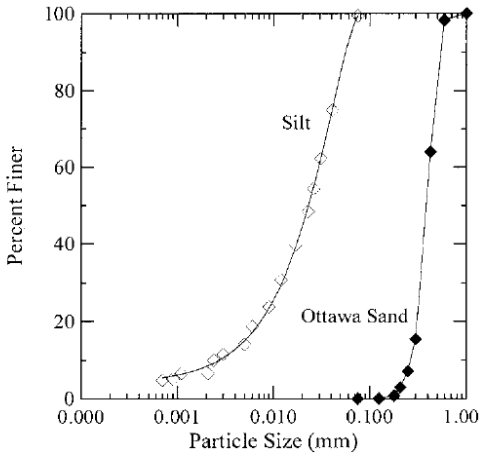

Figure 1.13: Grain size distribution of Ottawa sand and the silt considered in Salgado et al. (2000).

Figures 1.14 and 1.15 show the deviatoric stress $\sigma'_1 - \sigma'_3$ and the volumetric strain ε_v versus the axial stress for the loose and dense samples with different fine contents. It can be observed that an addition of silt to the sand leads clearly to an increase in the shear stiffness (initial slope of the stress-strain curve) and in the shear strength at the peak and critical state, particularly for the dense samples. Indeed, the critical-state friction angle is 33^o for the dense sample with 20% of fine content, significantly higher than the value of 29^o for the clean sand. The silt-sand mixtures show a more marked softening phase after the peak state than the clean sand. It can be also observed in Figure 1.15 that the dense silt-sand mixtures dilate strongly when they are subjected to shearing and their dilatancy increases as well with fine content. The authors explained these results by the fact that, for low fine contents ($\leq$ 20%), the solid skeleton is mainly constituted of the sand particles and the silt particles occupy void spaces between the sand particles, increasing particle interlocking and then making the soil more dilative and stronger.

Sterpi (2003) studied experimentally the effect of the removal of fine particles on the mechanical behavior of a well graded silty sand whose particle size distribution is presented in Figure 1.16 by the dashed line curve. The fine content, defined as the percentage by weight of particles with diameter smaller

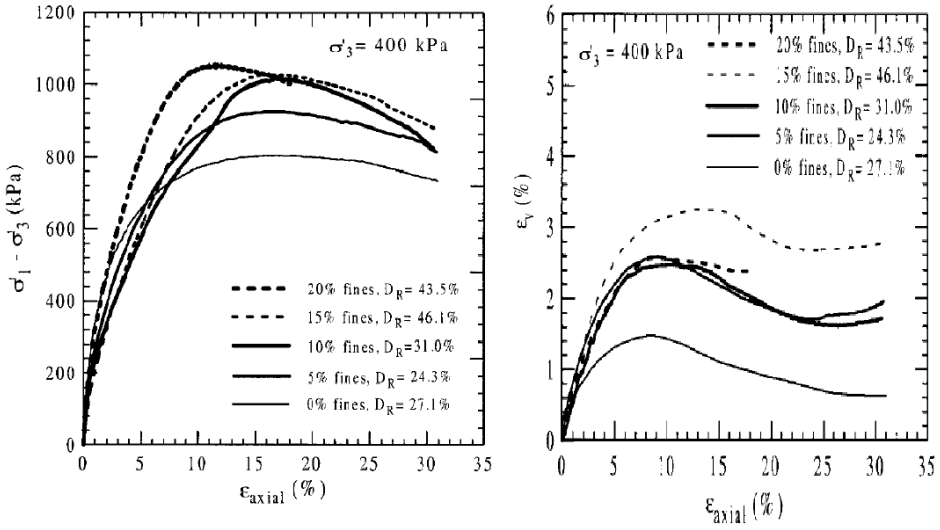

Figure 1.14: Drained triaxial compression tests on loose samples of Ottawa sand with various silt contents under moderately high effective confining stress (Salgado et al., 2000).

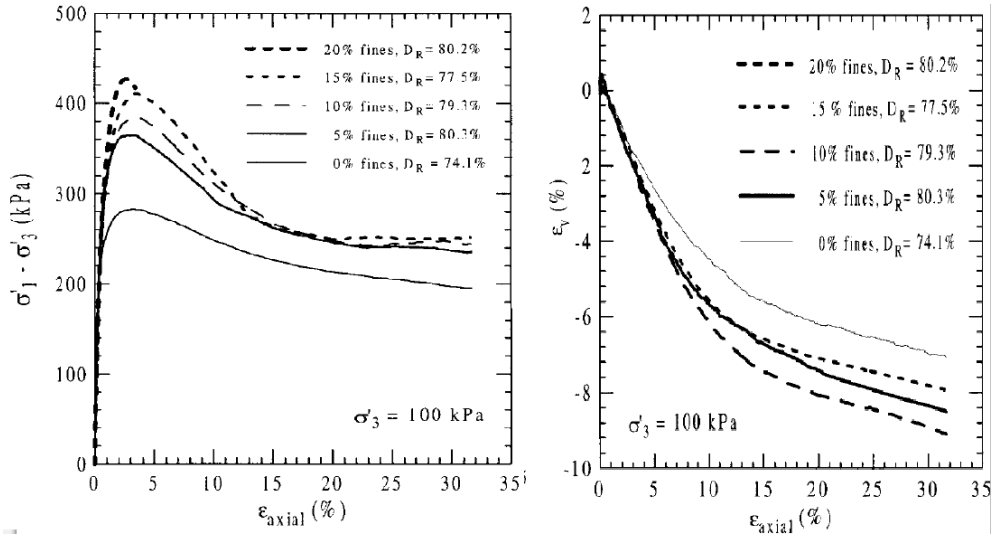

Figure 1.15: Drained triaxial compression tests on dense samples of Ottawa sand with various silt contents under low effective confining stress (Salgado et al., 2000).

than 0.0074 mm, is 20%. For the laboratory tests, only the particles with $d < 2$ mm was considered, due to the relatively small size of the experimental device. The author introduced a parameter μ_e which is the percentage by weight of fine particles removed from the original soil. It is worth mentioning that this parameter was called *percentage by weight of eroded fine particles* by the author; however, no erosion test was performed to erode fine particles to investigate the mechanical behavior of eroded soils. The author assumed that the erosion leads to a decrease in fine content and a modification of the relative density so they removed a fraction of fine particles from the original soil and reconstituted samples with a target relative density. Drained triaxial compression tests are then performed on three samples with $\mu_e = 0$, $\mu_e = 0.1$ and $\mu_e = 0.2$ corresponding to the respective fine contents of 20%, 10% and 0%. The two last samples, which correspond respectively to the soil after partial and full erosion, were compacted to relative densities of 30% and 70%. Their mechanical behaviors were compared to that of the sample with $\mu_e = 0$ (the original soil) compacted to the relative density of 70%. Figure 1.17 shows a comparison between the mechanical behavior of the original soil and those of the eroded sols with different percentages of removed

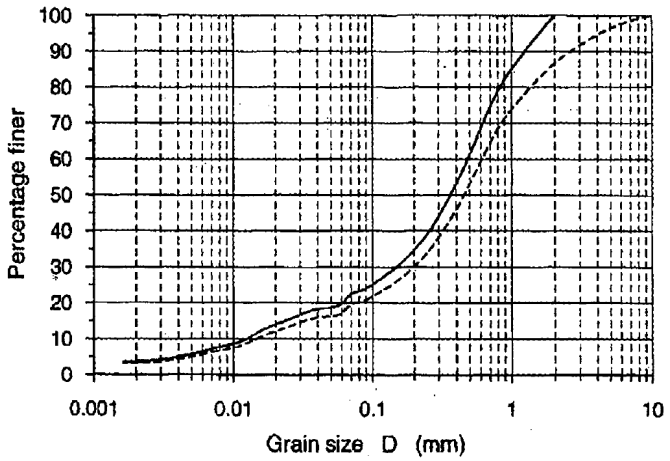

Figure 1.16: Grain size distribution for the original soil (dashed line) and for the soil used in the laboratory tests (solid line) (Sterpi, 2003).

fine particles. Surprisingly, the eroded samples with $\mu_e = 0.1$ and $\mu_e = 0.2$ show stiffer stress-strain curves and better shear strengths than those of the original sample; and the two eroded samples dilate more than the original one. Even though the eroded sample with $\mu_e = 0.2$ is at lower relative density (30%), it has a much better shear strength than the original one at the relative density of 70%. These results mean that the shear strength and dilatancy increase as fine content decreases, which contradicts the results of Salgado et al. (2000) shown above.

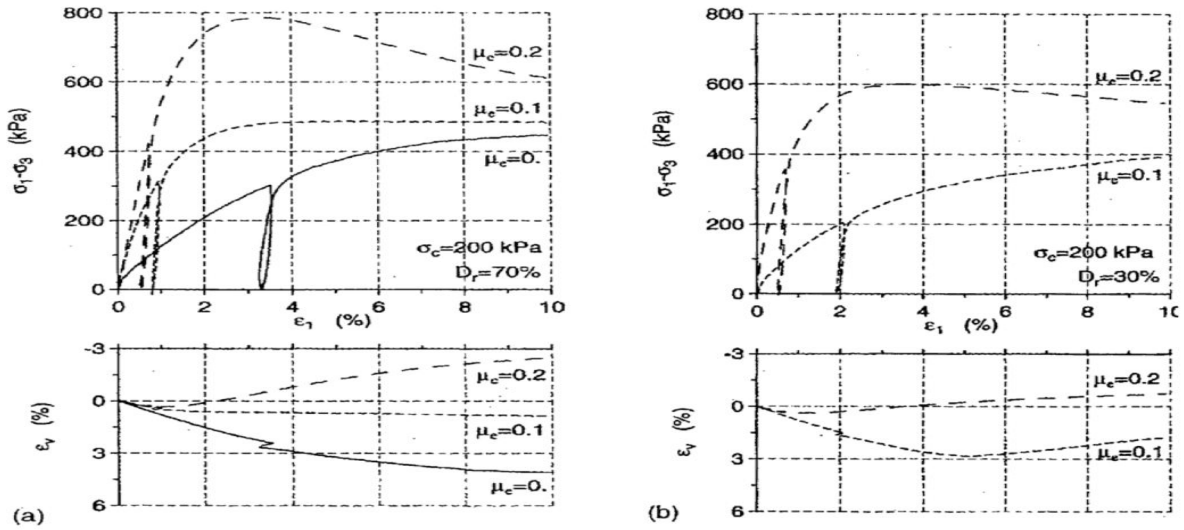

Figure 1.17: Deviatoric stress and volumetric strain versus axial strain, from triaxial compression tests on dense samples (Sterpi, 2003).

1.3.2.2 Undrained behavior

In what follows, the role of fine particles under undrained stress-strain behaviors of granular soils is studied. Thevanayagam et al. (2002) studied the effect of fine content on the mechanical behavior under undrained conditions for mixes of Ottawa sand and silica fines (see Figure 1.12 for their size distribution curves). The samples with fine content $f_c = 0$, 7 et 15% were prepared at the same global void ratio $e = 0.6$. The samples with $f_c = 25\%$, 40% and 60% are too fragile to be prepared at $e = 0.6$ so they were prepared at much lower values of e (their void ratios are 0.46, 0.425 and 0.516, respectively). The pure

silt sample ($f_c = 100\%$) was tested at $e = 0.77$. The stress-strain behavior of these samples is presented in Figure 1.18. It was found that the silty samples with $f_c \leq 25\%$ are weaker than the dense clean sand ($f_c = 0$) and this weakness increases with an increase in fine content. This is due to the fact that these samples are looser than the clean sand in terms of intergranular void ratio e_c and the interfine void ratio e_f is very high. Although the sample with $f_c = 25\%$ was prepared at $e = 0.46$, the value of e_c is 0.947 compared to the value of 0.864 for the sample with $f_c = 15\%$ prepared at $e = 0.6$. Murthy et al. (2007) also found that the silty sand with 10% of fine content is less dilative and weaker than the clean sand even though the silty sand is denser than the clean sand in terms of global void ratio e. A further increase in fine content leads, on one hand, to an increase of e_c, but on the other hand, to a strong decrease of e_f. The sample with $f_c = 40\%$ reaches a maximum value of $e_c = 1.375$, while its value of e_f reduces to 1.06. Starting from $f_c = 25\%$, the undrained shear strength increases with fine content. The sample with $f_c = 40\%$ is indeed stronger than the sample with $f_c = 25\%$. It is worth noting that the former is looser in terms of e_c but much denser in terms of e_f than the latter ($e_f = 1.06$ for $f_c = 40\%$ compared to the value of 1.84 for $f_c = 25\%$). The fine content of 25% can be considered as a threshold value, under which the undrained shear strength decreases with fine content but above which the undrained shear strength increases with fine content. It should be noted that the above statement is valid when the global void ratio e is controlled. Indeed, the undrained shear strength increases with an increase in fine content in the case where the intergranular void ratio e_c was controlled, as shown by Thevanayagam et al. (2002).

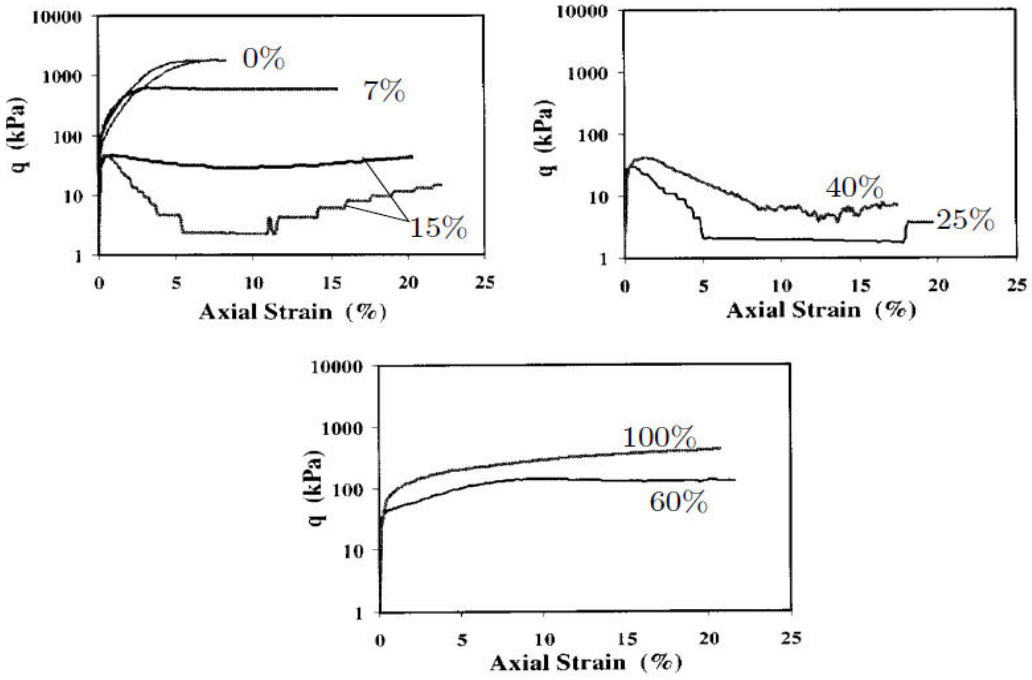

Figure 1.18: Undrained stress-strain behavior of the samples with different fine contents tested by Thevanayagam et al. (2002).

Nguyen (2014) performed two series of undrained triaxial tests on silty-sand with fine content varied between 0 and 20%. The global void ratio e is controlled to be almost the same for all the tested samples in the first series, while the intergranular void ratio e_c is controled to be almost the same for all the tested samples in the last series. Figure 1.19 shows the undrained friction angle ϕ' at the peak state versus fine content for these two series of tests. The undrained friction angle ϕ' is defined according to the Mohr-Colomb criterion $\sigma'_1 - \sigma'_3 = \sin(\phi')(\sigma'_1 + \sigma'_3) + 2c\cos(\phi')$ for a cohesive soil, but for these tests, the soils are cohesionless, and the Mohr-Colomb criterion becomes $\sigma'_1 - \sigma'_3 = \sin(\phi')(\sigma'_1 + \sigma'_3)$. It can be seen that the undrained shear strength decreases first and then increases with an increase in fine content for the

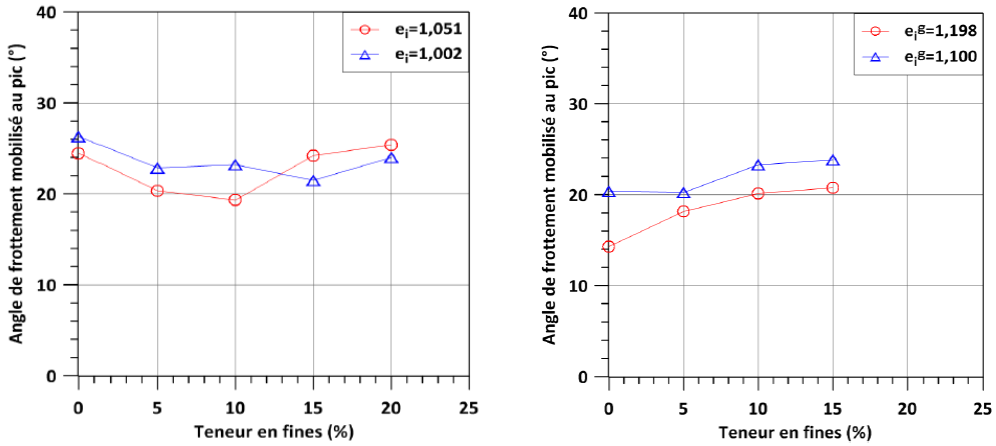

Figure 1.19: Undrained friction angle of silty sand at the peak state versus fine content: (a) global void ratio e is controlled and (b) the intergranular void ratio e_c is controlled (Nguyen, 2014).

first series, while it increases with an increase in fine content for the second series. These results are in agreement with those obtained by Thevanayagam et al. (2002) shown above.

Andrianatrehina et al. (2016) performed undrained triaxial tests on mixtures of sand (0.1 mm $< d <$ 0.315 mm) and gravel (2 mm $< d <$ 16 mm). Sand particles are considered as fines and their content varies from 5% to 30%. The relative density D_r is controlled to be around 60% for all the samples. Figure 1.20 shows the maximum deviator stress q versus fine content for two confining pressures of 100 kPa and 200 kPa. It is shown that the undrained shear strength increases with fine content. It is worth mentioning that this result is different from those obtained by Thevanayagam et al. (2002) who showed that the undrained shear strength decreases with an increase in fine content up to 25% and then increases with an increase in fine content above 25%. This might be related to the fact that the relative density D_r was controlled in the former study, while the global void ratio e was controlled in the latter one.

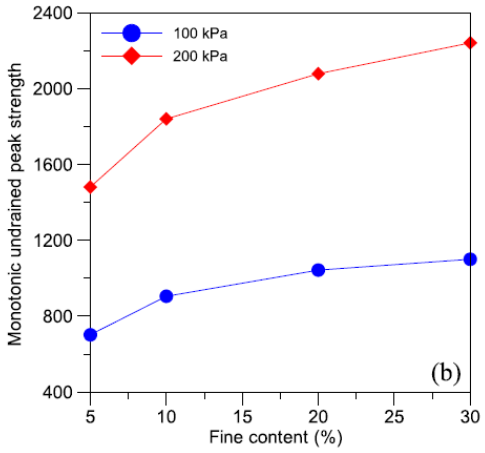

Figure 1.20: Undrained shear strength versus fine content shown in Andrianatrehina et al. (2016).

1.3.3 Discussions

In Sections 1.3.1 and 1.3.2, we presented some studies in the literature on the effect of fine particles on the global, intergranular and interfine void ratios and on the drained and undrained mechanical behaviors of mixed soils. In terms of void ratios, there exists an optimal fine content, at which the global void ratio reaches its minimum value. This optimal fine content have been found to depend on the grain size distribution and on the particle shape. In terms of mechanical behavior, different studies showed contradictory results. Salgado et al. (2000) showed that the drained shear strength increases with an increase in fine content for the loose and dense gap-graded soils. On the contrary, the drained shear strength was found by Sterpi (2003) to decrease with an increase in fine content for well graded soils. Regarding the undrained behavior, Thevanayagam et al. (2002) and Nguyen (2014) found a threshold value of fine content f_c^{th} for the case where the global void ratio is controlled to be the same: fine particles weaken granular mixtures when $f_c < f_c^{\text{th}}$ but strengthen them when $f_c > f_c^{\text{th}}$. On the other hand, Andrianatrehina et al. (2016) found that an increase in fine content between 0 and 30% leads to an increase in undrained shear strength of granular mixtures. It should be noted that the effect of fine content depends strongly on the way the initial density of mixtures is controlled. Thevanayagam et al. (2002) and Nguyen (2014) showed that when the intergranular void ratio e_c is controlled to be the same, a further addition of fine particles makes granular mixtures stronger under undrained conditions.

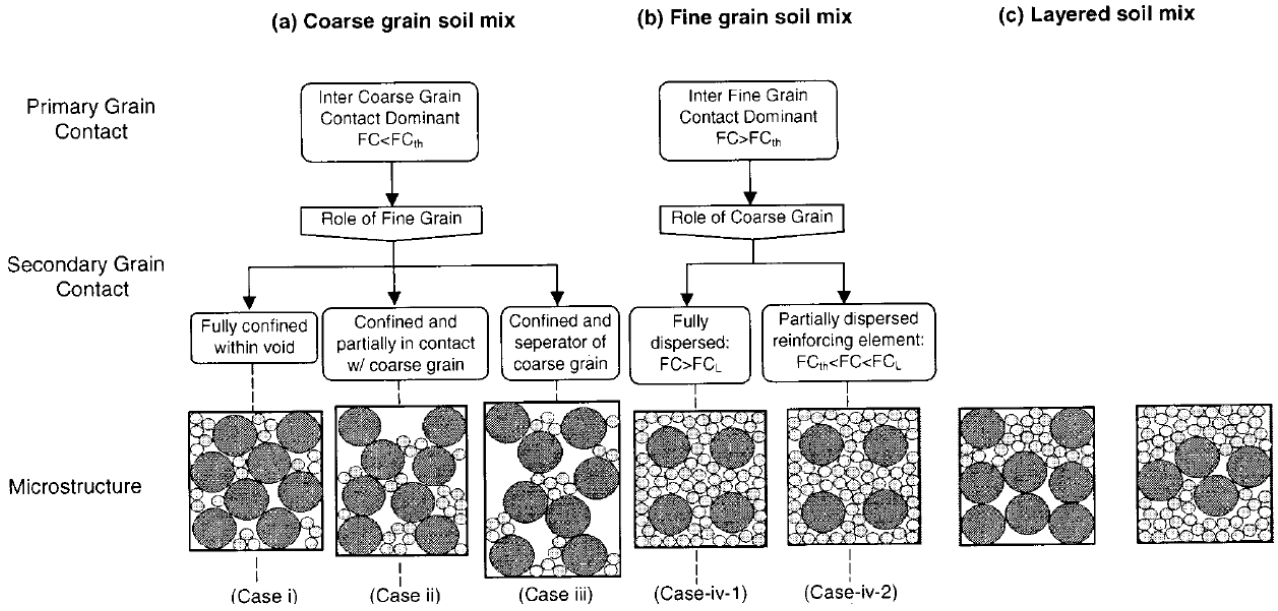

Figure 1.21: Classification of soil mixes proposed by Thevanayagam et al. (2002).

It is generally accepted that an addition of fine particles to granular mixtures leads to a variation of their microstructure. Thevanayagam et al. (2002) proposed a classification of the microstructure of granular soil mixes into three main category by using a threshold fine content f_c^{th}: (a) coarse grain soil mix when $f_c \leq f_c^{\text{th}}$, (b) fine grain soil mix when $f_c > f_c^{\text{th}}$ and (a) layered soil mix as illustrated in Figure 1.21. In soil mixes of category (a), the coarse grains are primarily in contact and they play a primary role in the soil's shear response, while the fines offer a secondary contribution. This category is also split into three subsets: the fines are confined within the void spaces between the coarse grain skeleton [case (i)]; they are partially supporting the coarse grain skeleton [case (ii)]; or they partially separate the coarse grain skeleton [case (iii)]. In category (b), the fine grains are primarily in contact with each other and they play a primary role in sustaining the shear stress, while the coarse grains are separated by the fine ones and provide a secondary reinforcement effect. For category (c), the soil mix is constituted of a layer of

fine particles and a layer of coarse particles. It should be noted that this classification of the microstructure of granular mixtures is intuitive without any investigation of granular mixtures at the particle scale. Such an investigation might be performed by using X-ray tomography imaging technology (Kim et al., 2012), however, this technique is quite delicate and expensive. To the best of our knowledge, no experimental investigation of the effect of fine content on the granular micro-structure has been performed so far.

It has been shown previously that the fine particles play an important role in the mechanical behavior of granular soil mixtures. Granular soils in earth-filled structures are usually gap graded or well graded. During the water flow through out the soils, their fine particles might be eroded by the seepage force. This phenomenon is called *suffusion* and presents an important risk of instability to earth-filled structures. The suffusion causes a reduction in fine content and a modification of the compactness and of the microstructure to eroded soils. As a consequence, their mechanical properties might change. In the next section, we introduce the suffusion phenomenon and present some studies of its consequences on the mechanical behavior of eroded soils.

1.4 Particle case of internal erosion: Suffusion

1.4.1 Definition

The internal erosion phenomenon is defined as the migration of soil particles caused by fluid flow. Internal erosion occurs when the hydraulic forces exerted by water seeping through the pores or cracks of the material in the earth structure (such as dam, dike or levee) are sufficient to detach fine particles and transport them out of the structure. Internal erosion is especially dangerous: it is one of main causes of failure in levees and in earth-filled dams. Statistical analyses showed that internal erosion is the governing failure mode of approximately half of the failures observed in embankment dams (Foster et al., 2000; Richards and Reddy, 2007).

Internal erosion can be classified into four different forms: concentrated leak erosion, backward erosion, soil contact erosion, and suffusion (Fell and Fry, 2007; Chang et al., 2012) as illustrated in Figure 1.22. While the three first forms of internal erosion occur at the interface between the soil and fluid or between the fine soil and the coarse soil, suffusion occurs inside the soil. It is characterized by a migration of fine particles caused by the seepage flow through the void space of the solid skeleton constituted of coarser particles. These migrant particles are not retained by the solid skeleton due to internal instability of grading and high enough seepage gradient. The suffusion process is illustrated in Figure 1.23.

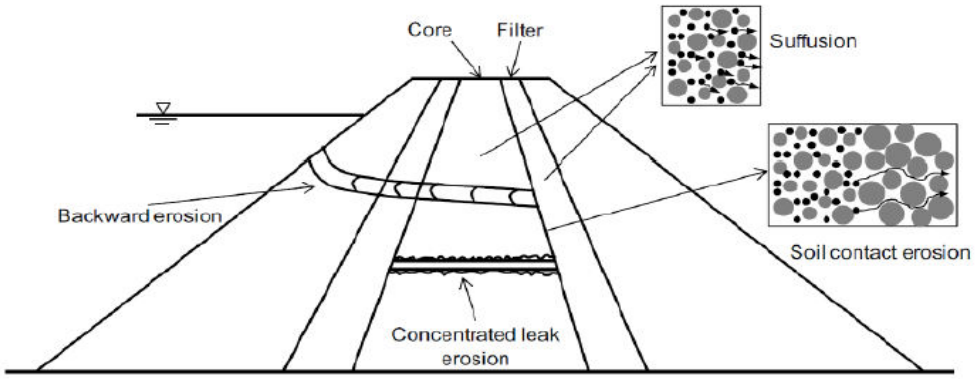

Figure 1.22: Illustration of internal erosion by four modes (Chang et al., 2012).

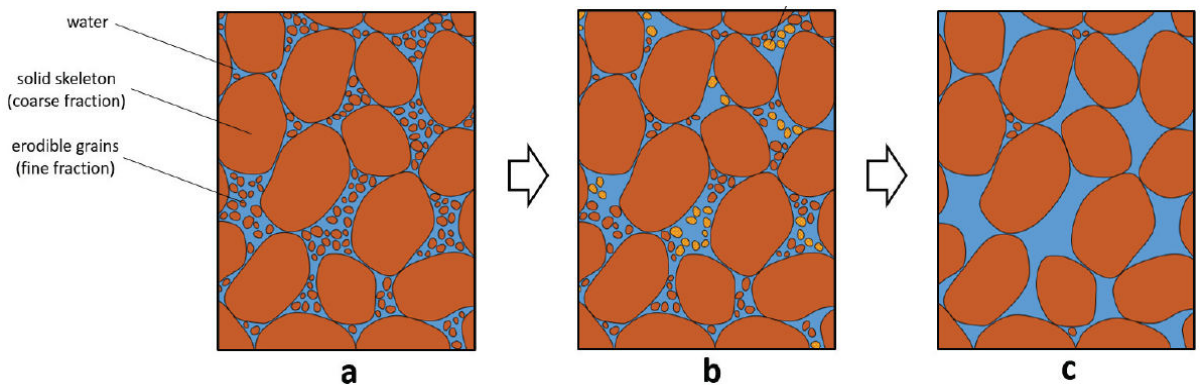

Figure 1.23: Illustration of suffusion process in a bimodal soil: a) intact sample, b) sample during suffusion process, c) sample after full erosion of the fine fraction (Yerro et al., 2017).

Suffusion comprises three main mechanisms: detachment of fine particles, transport of detached fine particles through the void space of the solid skeleton and retention of migrant fine particles by constrictions. Fine particles are detached when the seepage force is sufficiently high. If the detached fine grains are sufficiently small, they pass through constrictions of the solid skeleton formed by coarser particles. Otherwise, they are retained in the soil by constrictions.

1.4.2 Criteria for assessing suffusion

Suffusion occurs in a granular soil if three following main conditions are met according to Venn diagram shown in Figure 1.24.

- **Material susceptibility**: it is related to the ability of the soil to lose fine particles by detachment and migration of these particles. This detachment and migration are related mainly to the grain size distribution, the shape of grains and the compactness of the soil.

- **Stress condition**: it is referred to the ability to resist suffusion due to the magnitude of effective stress within the body of the soil. It is worth noting that this stress varies spatially or temporally within the body of the soil.

- **Hydraulic load**: it is associated with the action of seepage flow that is sufficient enough to detach and carry away fine particles. It can be related to the seepage gradients, velocities or hydraulic shear stress presented in the hydraulic structure.

The detachment of fine particles and their subsequent transport throughout the porous network of the soil requires that the sizes of constrictions formed by coarser particles are sufficiently large. These constriction sizes are conditioned not only by the granular size distribution, but also by the grain shape and the density of the granular packing. Lafleur et al. (1989) distinguished four main gradation curves as illustrated in Figure 1.25: uniform distribution (curve 1), upwardly convex distribution (curve 2), gap-graded distribution (curve 3) and upwardly concave distribution (curve 4). The soils whose grain size distribution curve corresponds to curves 1 or 2 are generally stable to suffusion (Lafleur et al., 1989). On the other hand, the soils whose grain size distribution curve corresponds to curves 3 or 4 are likely to suffer from suffusion (Fell and Fry, 2007; Burenkova, 1993; Wan and Fell, 2008).

Many geometric criteria have been proposed to assess the susceptibility of soil to internal erosion based on the particle size distribution curve. Sherman (1953); Istomina (1957) considered the coefficient of uniformity $C_u = D_{60}/D_{10}$ and stated that suffusion might occur in cohesionless granular materials if $C_u > 20$. Kézdi (1979) presented a method that consists in splitting the grain size distribution curve of a

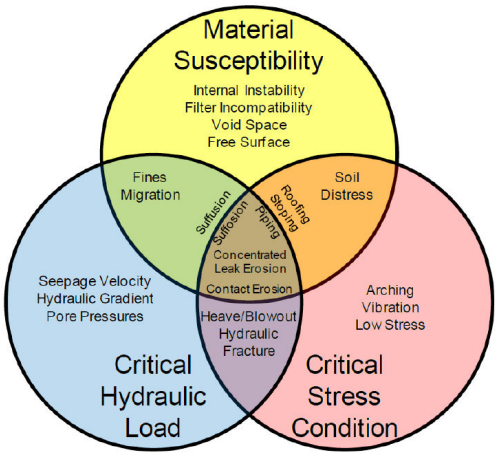

Figure 1.24: Venn diagram, showing internal erosion mechanisms for three overlapping adverse conditions (Garner and Fannin, 2010).

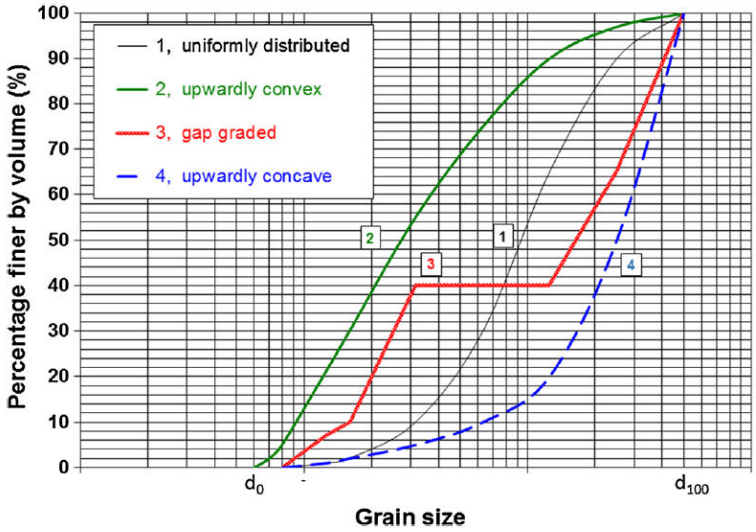

Figure 1.25: Main types of gradation curve (Lafleur et al., 1989).

cohesionless soil into coarse and fine components. The coarse particles serve as a filter to prevent erosion of the fine particles. According to this criterion, a soil is internally unstable or susceptible to internal erosion if $d_{15c}/d_{85f} > 4$, where d_{15c} is the diameter of the 15% mass passing in the coarse part and d_{85f} is the diameter of the 85% mass passing in the fine part. Moffat and Fannin (2006) found experimentally that a soil considered as stable and not susceptible to internal erosion if $d_{15c}/d_{85f} \leq 4$ and as unstable if $d_{15c}/d_{85f} \geq 7$. Kenney and Lau (1985) presented a geometric criterion based on the shape of particle size grading curve. The authors used an index ratio H/F where H is the mass fraction of grains with a diameter between D and $4D$ and F is the mass fraction of grains smaller than D. A soil is not susceptible to suffusion if $H/F > 1$.

According to Chang and Zhang (2013), the susceptibility of gap-graded soils to internal erosion is assessed by using the gap ratio defined as $G_r = d_{\max}/d_{\min}$ where $d_{\max}$ and $d_{\min}$ are the maximal and minimal particle sizes of the missing fraction, respectively. According to this criterion, a gap-graded soil is stable if $G_r < 3$ for fine content $f_c < 10\%$, if $G_r < 0.3f_c$ for $10\% \leq f_c \leq 35\%$ or if $f_c > 35\%$.

It should be noted that only consideration of the particle size distribution is not sufficient to assess if a sol is susceptible or not to suffusion. The stress and hydraulic conditions need to taken into account. Therefore, Marot et al. (2011) proposed a new method to represent the hydraulic load, based on the energy dissipated by the fluid. This energy is computed by time integration of the total flow power which takes into account the difference of head and the flow rate. Moreover, the hydraulic loading on one hand, and the induced erosion on the other hand, must be independently characterized. Thus, the energy dissipated by the water seepage (E_{flow}) and the cumulative loss of dry mass (m_{dry}) are computed respectively. Finally, at the end of each test, which corresponds to the invariability of the hydraulic conductivity and the decrease of the erosion rate, the erosion resistance index is expressed by: I_α = -log($m_{\text{dry}}/E_{\text{flow}}$). From this energy-based method, six categories of suffusion soil sensibility are proposed: from highly resistant to highly erodible (Marot et al., 2011).

1.5 Impact of suffusion on the mechanical behavior of granular soils

As mentioned above, large amount of fine particles are eroded during suffusion, which might trigger the rearrangement of soil grains into a stable packing. As a consequence, the soil structure is modified and the mechanical behavior of soil after suffusion may be strongly affected. In this section, several experimental studies in the literature on consequences of suffusion on the mechanical behavior of eroded granular materials will be presented. These experimental studies are classified into three categories: (i) studies without any suffusion test, (ii) studies with partial suffusion tests and (iii) studies with full suffusion tests.

1.5.1 Experimental studies without any suffusion test

Sterpi (2003) and Andrianatrehina et al. (2016) presented studies on mechanical properties of eroded soils by performing drained and undrained triaxial tests. In these studies, the authors made an assumption that suffusion causes only a reduction of fine content and a modification of the density to eroded soils so they reduced fine content on the particle size distribution curve and reconstituted samples with a target density. By doing so, the effect of suffusion is merely the effect of the reduction of fine content and of the modification of the density of the eroded samples. These studies have been presented in Section 1.3.2. These studies showed contradictory results. Sterpi (2003) concluded that suffusion is favorable to the drained shear strength which increases with an increase in percentage of eroded particles. On the contrary, Andrianatrehina et al. (2016) showed that suffusion is unfavorable to the undrained shear strength which decreases as the percentage of eroded particles increases.

1.5.2 Experimental studies with partial suffusion tests

The experimental study carried out by Chen et al. (2016) consists in replacing some amount of fine particles in the original soils by salt particles with the same particle size distribution. Two original soils, namely A and B, are mixtures of granite particles with 20% and 35% of fine particles whose diameter is between 0.09 mm and 0.15 mm (their PSD curves are shown in Figure 1.26). For each original soil, different samples where a certain amount of fine particles are replaced by salt particles was prepared, compacted and consolidated under an isotropic confining pressure of 50 kPa. After that, the carbon dioxide and deaired water were injected to saturate the samples and dissolve the salt. After the salt was completely dissolved, drained triaxial tests were performed on the samples. It should be noted that the salt dissolution process considered in this study does not represent fully the suffusion process. Indeed, the salt particles are randomly distributed inside the samples and their dissolution leaves local pores that are also randomly distributed. As a result, the samples issued from the dissolution process remains more or less homogeneous, compared to those obtained after a full suffusion test, which might be strongly heterogeneous. In addition, the dissolution of the salt particles imitates the loss of fine particles by suffusion so it represents

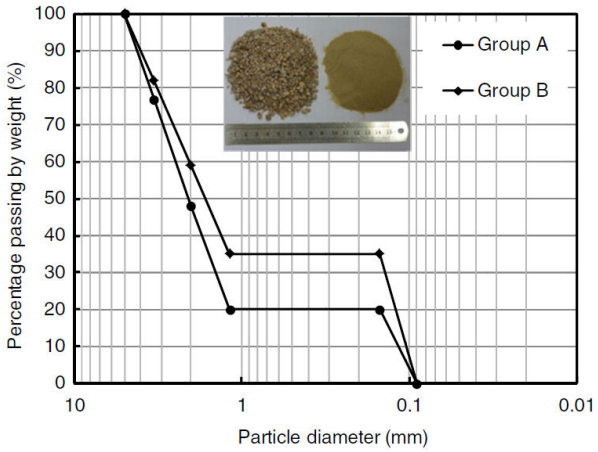

Figure 1.26: Grain size distributions of the original soils A and group B considered in (Chen et al., 2016).

only the detachment of fine particles during the suffusion process. It should be noted that a fine particle detached by the seepage flow can be transported and dropped off somewhere else in the samples, making the latter ones more heterogeneous. After the dissolution of salt, the eroded samples become much more porous compared to the original ones, despite a decrease in their porosity due to the rearrangement of particles, as shown in Table 1.1.

Table 1.1: Changes in porosity of the eroded samples after dissolution of salt.

Test identifier	Salt content (%)	Porosity before erosion	Porosity after erosion
A1	0	0.315	0.315
A2	5	0.315	0.339
A3	10	0.315	0.364
A4	15	0.315	0.391
B1	0	0.273	0.273
B2	10	0.273	0.322
B3	20	0.273	0.343
B4	30	0.273	0.372

Figure 1.27 presents the shear strength and the volumetric strain versus the axial strain for the eroded samples of the soils A and B with different percentages by mass of fine particles replaced by salt. It can be seen that the shear strength and the dilativeness decrease greatly with an increase in salt content. This is consistent to a great increase in the porosity of the eroded samples with increasing salt content after the salt dissolution. Moreover, the shear strength of the soil with 35% of fine content is much more degraded by the loss of fine particles than that with 20% of fine content. It is worth mentioning that soils containing soluble materials such as salt, limestone, gypsum, anhydrite, dolomite and halite can be found in geotechnical structures such as earth dams and reservoirs and these soils may experience internal erosion of fine particles throughout the dissolution of soluble materials (Bell, 2007).

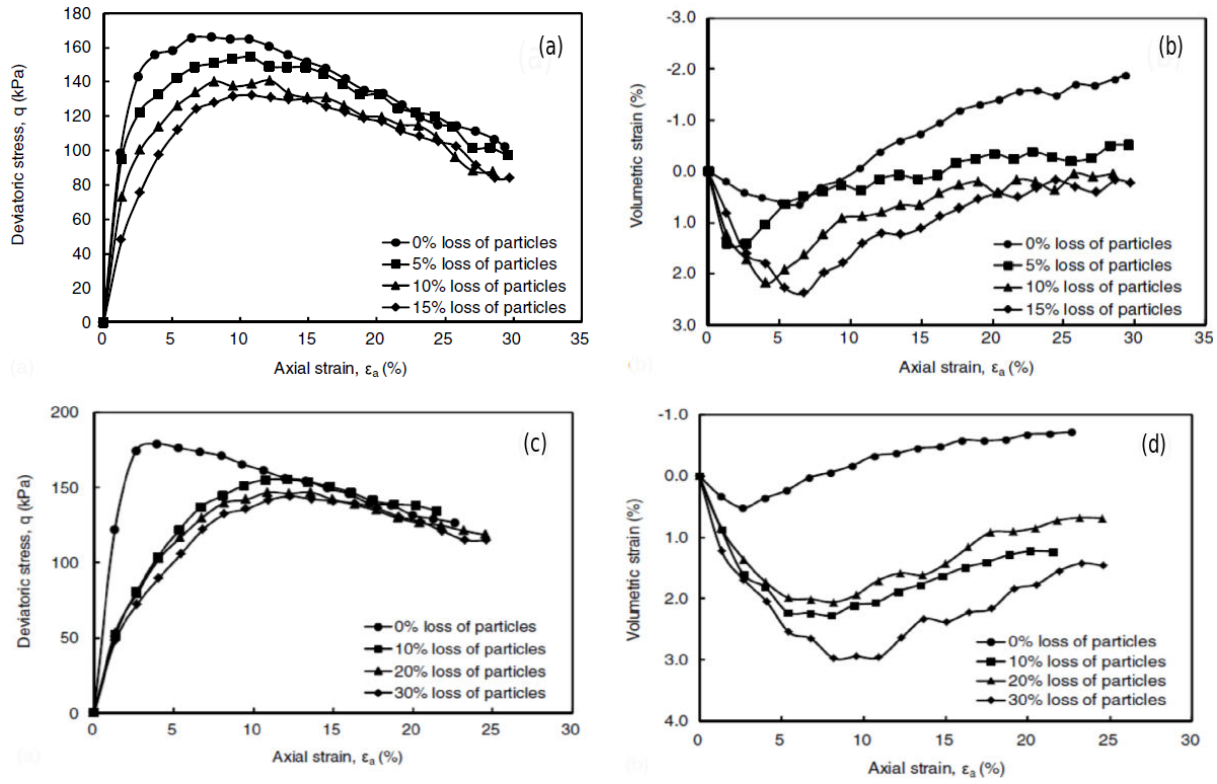

Figure 1.27: Stress-strain relationships with loss of different amounts of fine particles in the soil A: (a) and (b), and in the soil B: (c) and (d) (Chen et al., 2016).

1.5.3 Experimental studies with full suffusion tests

Chang and Zhang (2011) developed a testing apparatus that allows the authors to carry out first a suffusion test to erode a soil sample and then a triaxial compression test on the eroded sample to study the change in mechanical behavior of soils subjected to suffusion. Experimental tests were carried out on a mixture of sand and granite with a sand content of 35%. The tested samples were eroded at different stress state characterized by the effective mean stress p' and the deviatoric stress q. It was found out that the amount of eroded particles after the suffusion test depends strongly on the stress state: it increases as the deviatoric stress increases. Figure 1.28 shows the mechanical behavior of the samples eroded at different stress states. It can be seen that the tested soil changes the behavior of a dense soil before suffusion to the behavior of a loose soil after suffusion. This means that suffusion causes a reduction in the dilativeness and the shear strength to soils. This conclusion is also shared by several authors (Chang et al., 2012; Yin et al., 2014; Li et al., 2017; Aboul-Hosn, 2017).

To explain the changes in the mechanical behavior of soils subjected to suffusion, Nguyen et al. (2019) used X-ray tomography technique to experimentally characterize the impact of suffusion on a gap-graded soil microstructure. These X-ray CT can measure different physical properties during suffusion, such as fine content f, void ratio e and inter-granular void ratio e_g. Figure 1.29 presents the values of the physical properties for each scan for the whole sample. Scan 1 presents the scan after the saturation phase, scan 2 presents the scan after applying a very low flow rate, scan 3 and 4 present the scan after applying an important flow rate. It can be seen that, no visible changes of these properties is observed between scan 1 and scan 2 due to the absence of erosion of particles, then from scan 2 to scan 4, as the flow rate is increased, the fine content decreases with the development of erosion which influence the microstructure of the gap-graded sample and then the mechanical behavior of this sample.

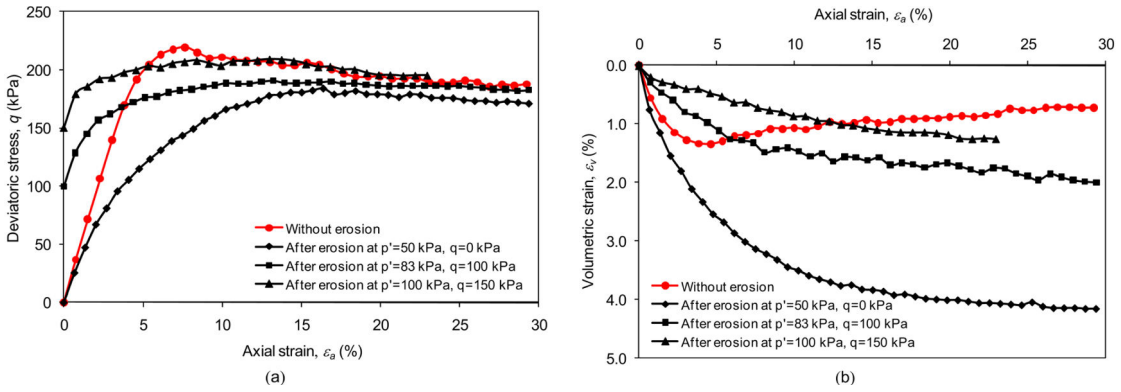

Figure 1.28: Stress-strain relationships without and with suffusion at different stress states: (a) deviatoric stress versus axial strain and (b) volumetric strain versus axial strain (Chang and Zhang, 2011).

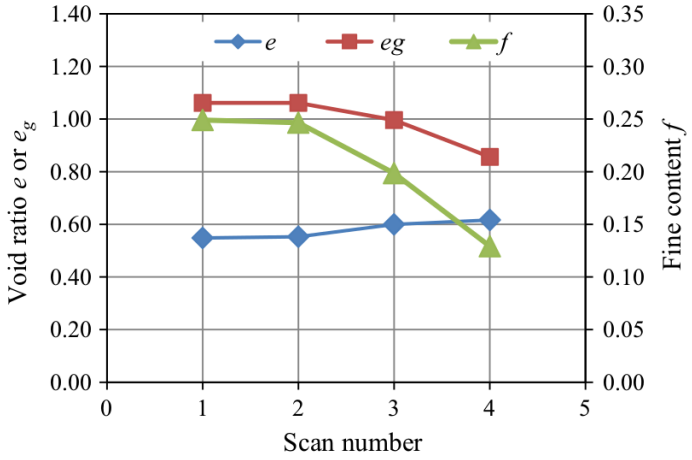

Figure 1.29: Void ratio e, inter-granular void ratio e_g and fine content f of the four successive scans (Nguyen et al., 2019).

1.6 Numerical modeling of suffusion and its mechanical consequences

It was shown in the last section that suffusion erodes fine particles from the soil solid skeleton, causing a modification of the mechanical behavior to eroded soils. In this section, we will show some numerical models in the literature which can be used to predict mechanical consequences of suffusion. These numerical models can be classified into two main categories: numerical models based on the Discrete Element Method (DEM) and numerical models based on the homogenization technique.

1.6.1 Models based on the DEM

1.6.1.1 Coupled DEM-fluid models

The DEM has been widely used to simulate numerically granular media. According to this method, a dry cohesionless granular soil is modeled as an assembly of distinct particles which are assumed to be rigid. The interaction between particles can only occur at frictional interfaces. The DEM has the two following main ingredients: (i) Newton-Euler dynamic equations to describe the translational and rotational motions of each rigid particle, and (ii) a contact law to calculate the interaction forces at the contact between two particles. An explicit or implicit time-stepping scheme is used to numerically integrate the dynamic equations. At each step, the velocity and the position of each particle are integrated up to the end of the step. At the same moment, contacts between particles are detected and contact forces are

calculated from the velocity and the position of particles in contact. There are two main approaches for the DEM, which differ from each other in the way of modeling the interaction at contact. The Molecular Dynamic (MD) approach considers a small compliance effect at the contact point so the contact force can be uniquely determined from the elastic relative displacement at the contact point Luding (2008). On the other hand, the Contact Dynamic (CD) approach neglects the compliance effect at the contact point. As a consequence, the contact force cannot be uniquely determined from the relative displacement at the contact point without considering the dynamic equations of the whole system Radjai and Richefeu (2009). In both approaches, Coulomb's friction law is used in the tangential direction to limit the tangential force. For the MD approach, an explicit integration scheme of high order can be used with a time step sufficiently small to describe accurately the dynamic process at the contact point. For the CD approach, the numerical integration can only be done implicitly, but with a time step much bigger than that used in the MD approach. The DEM was found to be able to reproduce the main features of the mechanical behavior of granular materials such as the non-linearity, the softening phase, the dilatancy and the induced anisotropy Belheine et al. (2009). One of its main advantages is that any local information at the particle scale can be accessed, which makes the DEM very suitable for investigating granular media from a micro-mechanical point of view. The DEM based on the MD method is adopted in our work and will be presented in details in Chapter 2.

In recent years, many efforts have been devoted to couple the DEM, which is used to simulate the motion of the solid particles, to a fluid model to simulate the fluid flow through the void space between the solid particles. During the simulation, the action of the fluid flow on each particle is computed by means of the fluid model and then the position of each solid particle is updated by means of the DEM. Several couplings have been developed such as DEM-CFD (coupled DEM and Computational Fluid Dynamics) (Benmezroua, 2011; Zhao and Shan, 2013), DEM-LBM (coupled DEM and lattice Boltzmann method) (Lominé et al., 2013; Tran et al., 2017) and DEM-SPH (coupled DEM and Smoothed Particle Hydrodynamics)(Sjah, 2013; Robinson et al., 2013).

The coupled DEM-CFD model consists in using the Navier-Stokes equation to model the fluid motion:

$$\rho_f \frac{\partial \boldsymbol{v}}{\partial t} + \rho_f \boldsymbol{v}.\nabla \boldsymbol{v} = -\nabla p + \mu \nabla^2 \boldsymbol{v} + \boldsymbol{f}_p, \tag{1.4}$$

where $\boldsymbol{v}$ and p are respective fluid velocity and pressure; ρ_f and μ are respective fluid mass density and viscosity; and $\boldsymbol{f}_p$ is the external force exerted on a unit volume of the fluid. The Navier-Stokes equation is solved by using a finite element discretization of the void space. To describe well the motion of the fluid, the mesh issued from the discretization must be sufficiently fine compared to the particle size as illustrated in Figure 1.30.a.

The coupled DEM-LBM model solves the simplified form of Boltzmann equation for the fluid motion:

$$\frac{\partial f}{\partial t} + \frac{\partial f}{\partial \boldsymbol{x}}.\boldsymbol{c} = -\frac{f - f^{\mathrm{eq}}}{\tau}, \tag{1.5}$$

where $f(\boldsymbol{x}, \boldsymbol{c}, t)$ is a distribution function defined as the probability density for the presence of a fluid particle at position $\boldsymbol{x}$ with velocity $\boldsymbol{c}$ and at time t; $f^{\mathrm{eq}}(\boldsymbol{x}, \boldsymbol{c}, t)$ is the distribution function at thermodynamic equilibrium; and τ is a relaxation time. The Boltzmann Equation (1.5) is discretized on a regular lattice (rectangular lattice in 2D as illustrated in Figure 1.30.b and cubic lattice in 3D). Like the coupled DEM-CFD, the coupled DEM-LBM requires a sufficiently fine mesh to obtain a good resolution of the fluid flow between solid particles.

Unlike the coupled DEM-CFD or DEM-LBM, the coupled DEM-SPH does not need a meshing of the void space. The SPH method consists in modeling the fluid as a collection of particles with their

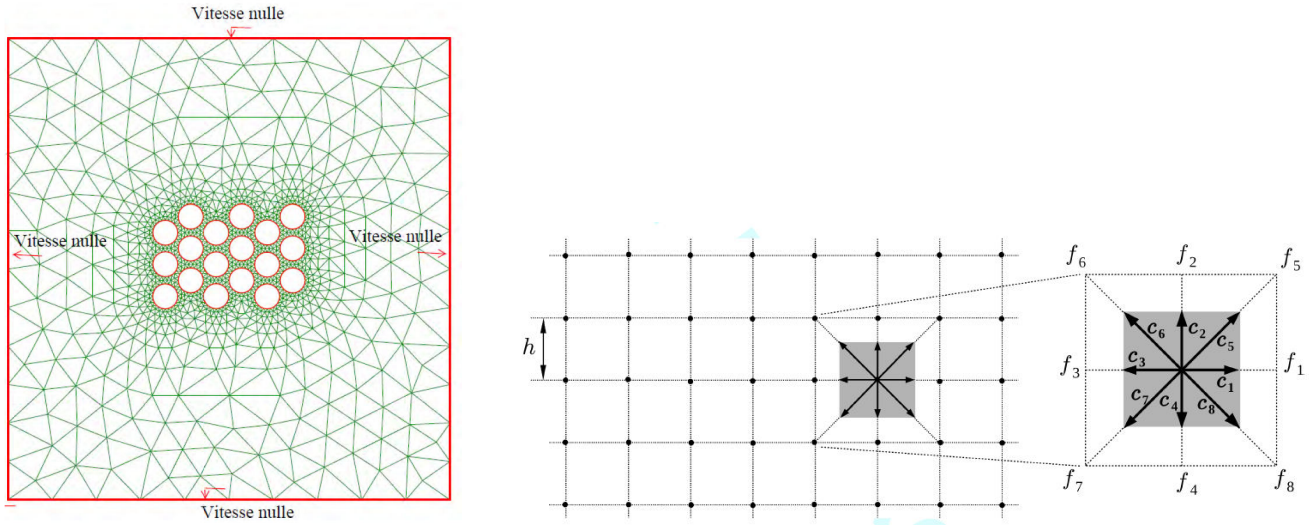

(a) (b)

Figure 1.30: (a) Mesh used in the coupled DEM-CFD (Benmezroua, 2011) and (b) regular lattice used in the coupled DEM-LBM (Tran et al., 2017)

microscopic quantities such as mass, density, volume, velocity, pressure, etc. These particles interact each other and move according to the equation of motion. Fluid quantities such as velocity and pressure at a given position are interpolated from known microscopic quantities of neighboring particles. To obtain a good resolution of the fluid flow between solid particles, the number of fluid particles needed by the SPH method must be sufficiently big. Sjah (2013) used about 120000 fluid particles to represent a fluid domain, to model a spherical solid particle free falling in this domain.

The three coupled models mentioned above has been used by several authors to simulate the internal erosion in granular materials. Lominé et al. (2013) and Tran et al. (2017) used the coupled DEM-LBM to perform 2D simulation of the piping erosion and backward erosion. Galindo-Torres et al. (2015); Harshani et al. (2015) simulated the suffusion in 3D granular media. Due to large memory requirement and computation time, the numbers of coarse and fine particles were limited to respective 30 and 13 000 and only the onset of suffusion was simulated. Up to date, it seems to be impossible to simulate a full suffusion process in a widely graded material with a full coupled DEM and fluid model.

As mentioned above, a good resolution of fluid flow in the void space between solid particles is computationally very expensive. To overcome this limitation, Chareyre et al. (2012) and Catalano et al. (2014) proposed a coupled DEM-PFV (DEM - Pore-scale Finite Volume) model, in which the void space between solid particles is partitioned into pores and every couple of adjacent pores share a throat. The regular Delaunay triangulation is used to subdivide a granular sample into tetrahedra, each of which joins the centers of four neighboring particles. The void space contained within a given tetrahedron is considered as a pore whose center is the regular Voronoi center of the tetrahedron under consideration (Figure 1.31.a). The void space on the triangular face shared by two adjacent tetrahedra defines a throat (Figure 1.31.b and c). The condition for the incompressible fluid in a pore i implies that:

$$\sum_{j=j_1}^{j_4} q_{ij} = 0, \tag{1.6}$$

where $j \in \{j_1,\ j_2,\ j_3,\ j_4\}$ are four pores adjacent to the pore i and q_{ij} is the fluid flux from the pore i to

the pore j. The relation between q_{ij} and the pressure difference between two pores i and j is expressed using a local conductance g_{ij}:

$$q_{ij} = g_{ij}\frac{p_i - p_j}{L_{ij}}, \tag{1.7}$$

where L_{ij} is the distance between the centers of pores i and j. The local conductance g_{ij} between two adjacent pores i and j is related to the geometry of the throat between them by adapting the Hagen–Poiseuille relation, which was initially derived for a fluid flow through a cylinder, to the channel of complex geometry between the two adjacent pores.

$$g_{ij} = \frac{A_{ij}{R_{ij}^h}^2}{2\mu}, \tag{1.8}$$

where A_{ij} is the void area on the throat between two pores i and j and R_{ij}^h is a hydraulic radius which is defined as the ratio between the volume Φ_{ij} occupied by the fluid in the channel and the area γ_{ij} of its solid-fluid interface.

The coupled DEM-PFV is still computationally very expensive to simulate the suffusion process despite a great simplification of the fluid model. This is due to a big number of pores to be handled when a widely graded soil is considered. In addition, during the suffusion process, fine particles move greatly so the Delaunay triangulation and the Voronoi decomposition must be updated frequently during the simulation. Aboul-Hosn (2017) used coupled DEM-PFV to simulate only the onset of the suffusion for a widely graded sample composed of 10000 particles. Wautier et al. (2019) used also a coupled DEM-PFV to simulate the suffusion for a widely graded sample composed of 5000 particles to investigate the microstructure modifications during suffusion, such as force chain orientation and transport of particles distances.

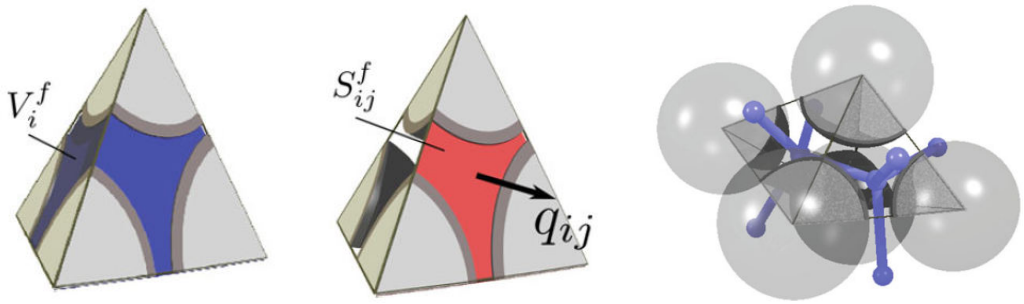

(a) (b) (c)

Figure 1.31: (a) Pore and (b) throat and (c) pore network defined in the coupled DEM-PFV model (Chareyre et al., 2012).

There exist also some simplified versions of the coupled DEM-CFD to reduce the computational cost (Shafipour and Soroush, 2008; Zhao and Shan, 2013; Hu et al., 2019; Kawano et al., 2018; Pirnia et al., 2019). In these simplified versions, instead of solving the Navier-Stokes equation (1.4) on a mesh sufficiently fine in the void space between solid particles, the Navier-Stokes equation and mass conservation equation are integrated on a coarse mesh of cells whose size is several times larger than the mean particle diameter. The main issue in this resolution is how the interaction force between the solid particles and fluid in each cell (force $\boldsymbol{f}_p$) is estimated. No clear relation has been established so different empirical relations were used. Like the coupled DEM-PFV, these simplified version of the coupled DEM-CFD are computationally expensive so they were used by some authors (Hu et al., 2019; Kawano et al., 2018; Pirnia et al., 2019) to simulate only the early stage of the suffusion process.

The coupled particle-fluid models, which have been developed up to date, are used in different domains such as mechanical and chemical, like the transport of fluid-particles in iron pipes and dissolution of solid particles in a fluid. But these models are computationally very expensive to simulate a complete suffusion process. In order to investigate numerically the impact of suffusion on the mechanical behavior of eroded soils, some authors proposed to represent the internal state of an eroded soil by removing some fraction of fine particles from the original soil (Wood and Maeda, 2008; Wood et al., 2010; Scholtès et al., 2010). These approaches will be presented in the next section.

1.6.1.2 DEM with particle removal

Wood and Maeda (2008) and Wood et al. (2010) proposed to remove progressively a fraction of the smallest particles from an original sample to represent the internal state of the sample after suffusion. According to this approach, a sample composed of disks with a given well-graded particle size distribution is first isotropically compressed and then sheared to a certain stress state. At the target stress state, the smallest particle is removed from the sample to mimic the detachment of fine particles by the seepage force. The removal of this particle might perturb the equilibrium of the sample so it is next stabilized while external stresses are controlled and kept constant. The sample reaches then a new equilibrium state and some deformations are induced by this perturbation. This process of removing particles is repeated until reaching 25% of the axial strain or 5% of removed particles. Figure 1.32 shows the behavior of the original sample and that of the sample during the process of particle removal at different stress-ratio states (τ_m/σ_m), where τ_m and σ_m are the shear and the isotropic stresses applied on the sample. It can be seen that the removal of particles leads to a contractive volumetric deformation at a low stress ratio but to a dilative volumetric deformation at a high stress ratio.

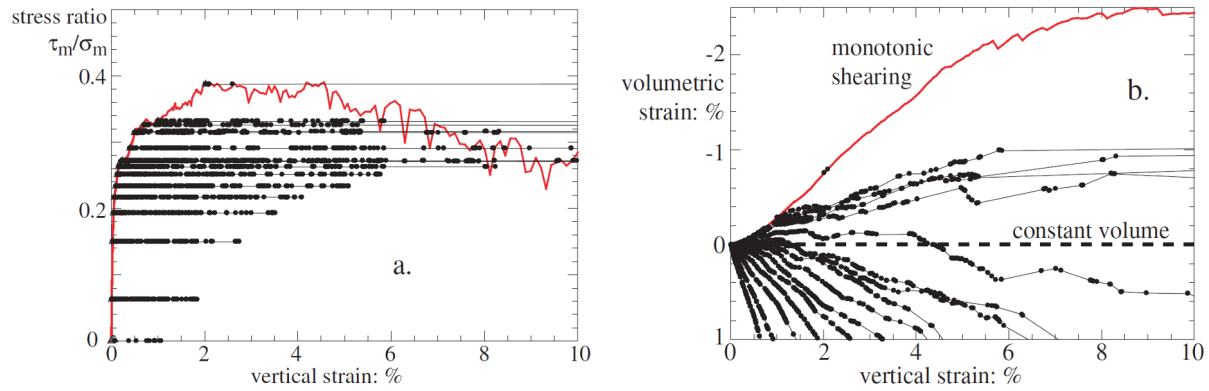

Figure 1.32: Tests with particle removal : (a) stress ratio; (b) volumetric strain (Wood and Maeda, 2008).

In a widely graded granular sample subjected to a shear stress state, some fine particles are not stressed or weakly stressed, while other fine particles are highly stressed. The seepage flow tends to wash out preferentially the less stressed fine particles from the solid skeleton as stated by Skempton and Brogan (1994). Scholtès et al. (2010) proposed to consider not only the size but also the degree of interlocking of each fine particle in the process of particle removal. To quantify the degree of interlocking, an internal moment tensor $\boldsymbol{M}^p$ is defined for each particle (Staron et al., 2005):

$$M_{ij}^p = \sum_{c \in p} r_i^c f_j^c, \tag{1.9}$$

where subscript c runs over all contacts on particle p; $\boldsymbol{r}^c$ is the vector connecting the center of particle p to the contact point and $\boldsymbol{f}^c$ is the contact force. The mean internal moment m^p ($m^p = \mathrm{tr}(\boldsymbol{M}^p)$) defines the degree of interlocking of particle p. Among the smallest particles, the one with the lowest degree of

interlocking is removed from the sample. A stabilization is performed so that the sample reaches a new equilibrium state before removing the next particle. This process of particle removal is repeated until the percentage of removed particles is up to 5%.

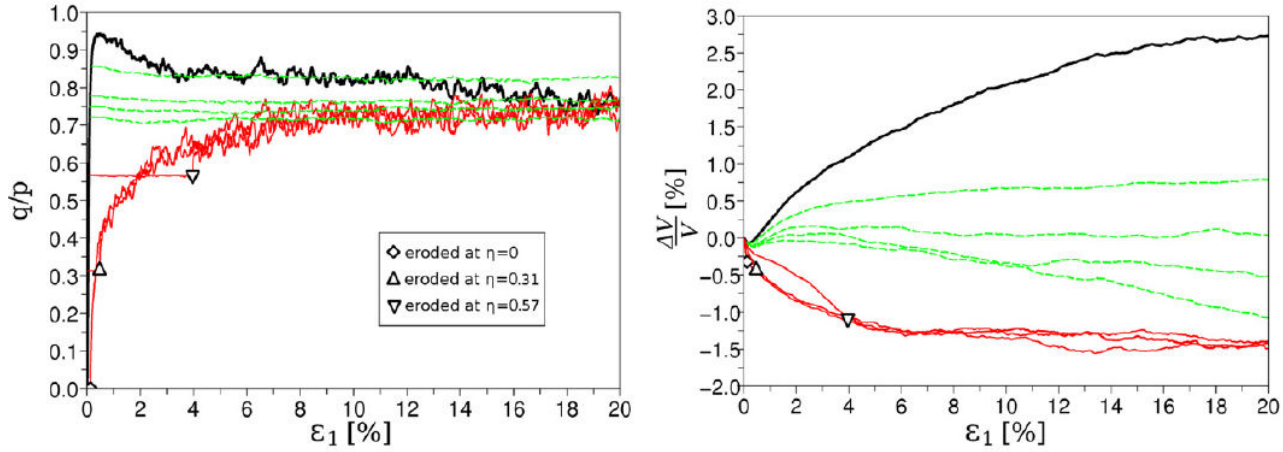

Figure 1.33: Particle extraction at different value of stress ratio $\eta = q/p$ (0, 0.31, 0.57, 0.72, 0.75, 0.78, 0.86) followed by a triaxial compressions. The thick black line corresponds to the initial dense sample (Scholtès et al., 2010).

Figure 1.33 shows the evolutions of the stress ratio $\eta = q/p$ of and of the volumetric strain during the process of particle removal and during the triaxial compression. The authors found that the behavior of the sample is strongly influenced by the stress state at which fine particles are removed. Indeed, the soil shows a contractive behavior if the extraction process was performed at low stress ratios $\eta = 0$, 0.31 and 0.57 (red lines in Figure 1.33), but a dilative behavior if the extraction process was performed at high stress ratios η= 0.72, 0.75, 0.78 and 0.86 (green lines in Figure 1.33). Figure 1.33 also shows that the loss of fine particles leads to a reduction in shear strength and dilativeness, which is in good agreement with the experimental results presented in Section 1.5.

Another approach for removing fine particles was proposed by Aboul-Hosn (2017). The coupled DEM-PFV presented above was used to simulate the onset of suffusion in a widely graded sample. The equilibrium of each solid particle subjected to contact forces exerted by its neighbors and to the fluid force is checked by comparing the magnitude of the unbalanced force on the particle with the magnitude of the contact forces. The magnitude of the unbalanced force on a particle p is defined as:

$$f^p_{\text{unb}} = \left\| \sum_{c \in p} \boldsymbol{f}^c + \boldsymbol{f}^p_f \right\|, \tag{1.10}$$

where c runs over all contacts of particle p; $\boldsymbol{f}^c$ is the contact force; $\boldsymbol{f}^p_f$ is the force exerted by fluid on particle p; and $\|.\|$ denotes the norm of a vector. A particle is considered to be out of equilibrium if the unbalanced force is significant compared to the mean magnitude of the contact forces according to the following criterion:

$$f^p_{\text{unb}} > \lambda \langle \|\boldsymbol{f}^c\| \rangle, \quad \text{for } c \in p, \tag{1.11}$$

where $\langle . \rangle$ denotes the average operator; and λ is a threshold value that was chosen to be equal to 0.1. A particle out of equilibrium is considered to be detached from the solid skeleton. It is then considered to be transported by fluid through the interstitial space if its diameter is smaller than an empirical value taken as D_{c35} which is the constriction size for which 35% of constrictions are smaller than this size. If a

particle is considered to be detached and transported by fluid, it is removed from the sample.

Figure 1.34 shows a comparison between the behavior of samples eroded at different hydraulic gradients and that of a dense initial sample (NE) during drained triaxial tests. The eroded samples show clearly a significant reduction in shear strength at the peak state and dilativeness, particularly when the hydraulic gradient is bigger than 6 (group 2).

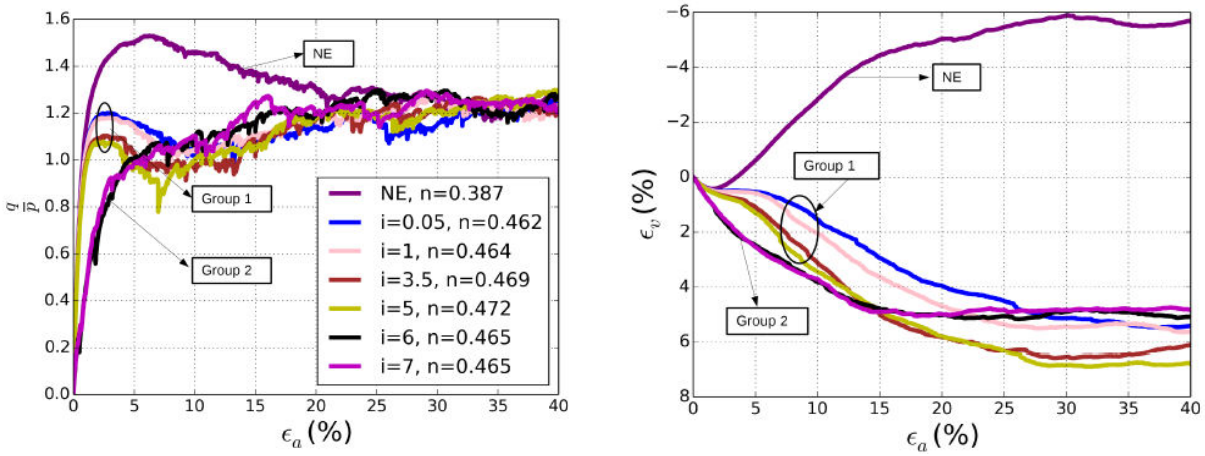

(a) (b)

Figure 1.34: (a) Stress ratio q/p and (b) volumetric strain ϵ_v versus the axial strain for samples eroded at different hydraulic gradients i, compared to that of the intact sample (NE) (Aboul-Hosn, 2017).

The methods presented above allow us to represent the internal state of an eroded soil by removing a fraction of its fine particles and then to study the impact of this particle removal on the mechanical behavior of eroded samples from a micro-mechanical point of view. However, these methods based on the DEM are limited to the sample scale and cannot be extended to the scale of earth-filled structures to predict the consequences of suffusion on their mechanical stability. In the next section, we present a model based on the homogenization technique, which allows us to take into consideration the impact of suffusion in a constitutive law for eroded soils. The latter can be used in a finite element modeling to predict the impact of suffusion on the mechanical behavior of an earth-filled structure.

1.6.2 Models based on the homogenization technique

The goal of a homogenization technique is to establish a link the macroscopic behavior of a material at the scale of a representative element volume (REV) to the local properties of the material. For a granular material, the local scale is usually defined at contacts between particles. Figure 1.35 shows the scheme of a homogenization technique for granular materials. According to this scheme, the macroscopic stresses ($\boldsymbol{\sigma}$) and strains ($\boldsymbol{\varepsilon}$) can be determined from the forces of contact ($\boldsymbol{f}^c$) and the relative displacements at contact points ($\boldsymbol{u}^c$) at the local scale using homogenization operators. Inversely, we can use the localization operators to determine the microscopic quantities from the macroscopic ones. The contact force $\boldsymbol{f}^c$ and the relative displacement at contact point $\boldsymbol{u}^c$ are related by a microscopic constitutive law.

Hicher (2012, 2013) proposed a homogenization technique to take into account the structural changes resulting from the loss of fine particles caused by suffusion. The basic idea of this model is to view a granular material as a set of microsystems which correspond to the contact planes with different orientations. A local constitutive law is introduced to relate interparticle forces and displacements along a set of contact

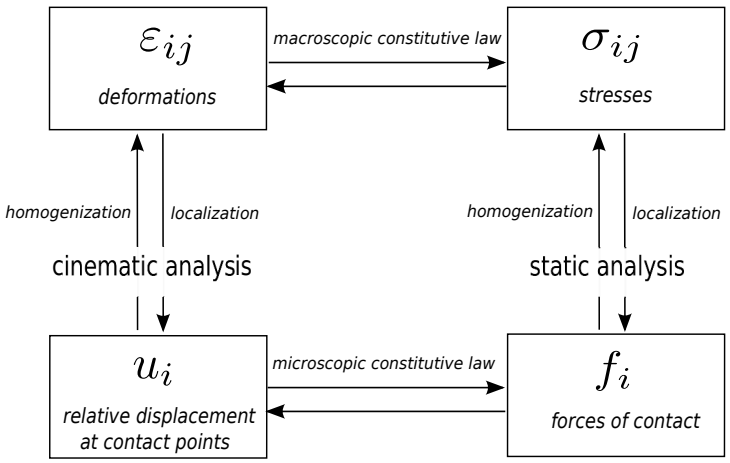

Figure 1.35: Scheme of a homogenization technique for granular media (Jean and Cambou, 2001).

planes. The overall stres–strain relationship is then obtained from averaging the contact plane behavior. This model is summarized below. Interested readers can refer to Hicher (2012, 2013) for more details.

- Starting from a macroscopic stress increment $\delta\boldsymbol{\sigma}$, the force on each contact plane is localized:

$$\delta f_j^c = \delta\sigma_{ij} A_{ik}^{-1} l_k^c V, \tag{1.12}$$

  where $\boldsymbol{l}^c$ is the vector joining the centers of two particles at contact c; V is the total volume of the REV; and $\boldsymbol{A}$ a fabric tensor describing the micro-structure of the material under consideration:

$$A_{ik} = \sum_{c=1}^{N} l_i^c l_k^c, \tag{1.13}$$

  where N is the number of contacts.

- The local behavior at each contact plane is modeled by an elasto-plastic law, from which contact force $\delta\boldsymbol{f}^c$ and inter-particle displacement $\delta\boldsymbol{u}^c$ are related by

$$\delta f_i^c = k_{ij}^c \delta u_j^c, \tag{1.14}$$

  where $\boldsymbol{k}^c$ is an elasto-plastic stiffness tensor (see Chang and Hicher (2005) for a detailed expression of this tensor). In this local constitutive law, the initial global void ratio e_0 is considered as a state parameter of the soil. The author assumed that the loss of fine particles leads to an increase in void ratio so the void ratio of an eroded soil is calculated as $e_0 = (e_0)_{\text{ne}} + (\Delta e)_{\text{er}}$ where $(e_0)_{\text{ne}}$ is the initial void ratio of the corresponding intact soil and $(\Delta e)_{\text{er}}$ is the increase in void ratio due to the loss of fine particles f_e: $(\Delta e)_{\text{er}} = f_e(1+(e_0)_{\text{ne}})/(1-f_e)$ with f_e being the fraction of eroded particles.

- The local displacement $\delta\boldsymbol{u}^c$ at each contact plane is calculated from the contact force $\delta\boldsymbol{f}^c$ by using the local constitutive relation (1.14).

- The macroscopic strain $\delta\boldsymbol{\varepsilon}$ is calculated by averaging local inter-particle displacements by using the following homogenization operator:

$$\delta u_{j,i} = A_{ik}^{-1} \sum_{c=1}^{N} \delta u_j^c l_k^c \quad \text{and} \quad \delta\varepsilon_{ij} = \frac{1}{2}(\delta u_{j,i} + \delta u_{i,j}) \tag{1.15}$$

The author compared the results obtained with the above model with those given by the DEM simulations. For this comparison, the parameters of this model are calibrated on the numerical samples presented in Scholtès et al. (2010) for which a fraction of fine particles are removed to mimic the loss of fine particles due to suffusion. As shown in Figure 1.36, the model based on the homogenization technique is capable of reproducing the reduction in shear strength and the contractive behavior of eroded samples.

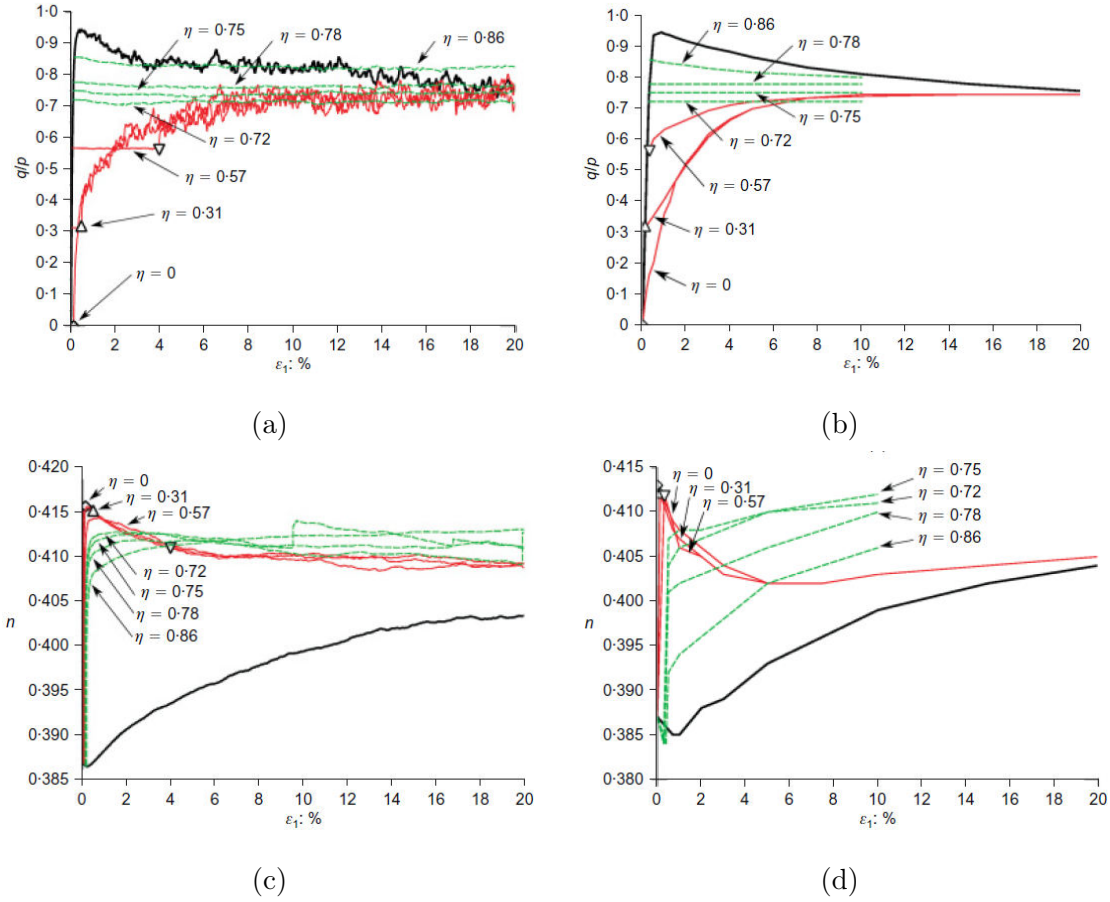

Figure 1.36: Comparison between the results obtained with the DEM simulations (a and c) with those given by the homogenization technique presented in Hicher (2013) (b and d).

It should be noted that the above model assumes that the main effect of suffusion is the increase in void ratio due to the loss of a solid fraction. As the void ratio increases after suffusion, the shear strength of eroded soils decreases according to this model. The erosion of fine particles from the solid skeleton triggers a rearrangement of the microstructure and also an increases of the heterogeneity of the eroded soil. Even though the above model takes into account this rearrangement of particles, it does not take into account the heterogeneity of the eroded soil caused by suffusion.

1.7 Conclusions

We have presented above a literature review of the role of fine particles in the mechanical behavior of widely graded granular soils and the consequences of the loss of fine particles caused by suffusion on the mechanical properties of eroded soils. We also presented several approaches based on the DEM and on the homogenization technique to model suffusion and its impact on the mechanical behavior of eroded soils. The following conclusions can be drawn:

- A presence of fine particles affects greatly the density of mixed soils. There exists an optimal fine content where a mixed soil reaches its minimum void ratio. An addition of fine particles leads to a decrease in void ratio if fine content is smaller than this threshold value but to an increase in void ratio otherwise.

- Fine particles play an important role in the mechanical behavior of a mixed soil. An increase in fine content might lead to an increase or a decrease in shear strength and dilativeness of mixed soils, depending on the particle size distribution curve, on the way the initial density is controlled, and so on.

- When a mixed soil is subjected to suffusion, some fraction of fine particles is eroded by the fluid flow. This loss of fine particles might change greatly the mechanical behavior of eroded soils. Up to date, mechanical consequences of suffusion are not well understood yet. Some preliminary studies have showed that suffusion causes a reduction in shear strength and in dilativeness to eroded soils. Further investigation on this topic are needed.

- Several coupled DEM-fluid models have been developed to simulate fluid flow through a granular soil. These models are computationally very expensive; therefore they have been used to simulate only the onset of suffusion. Up to date, it is difficult to simulate the whole suffusion process with these coupled DEM-fluid models.

- Models based on the DEM with particle removal have been proposed to mimic the loss of fine particles of a given sample caused by suffusion. These models consist in removing the smallest and the less loaded particles from the sample at a target stress state. Numerical simulations with these models show a reduction in shear strength and in dilativeness of eroded samples, which are qualitatively in agreement with the experimental finding. It should be noted that only the detachment of fine particles among three main mechanisms of suffusion is taken into account in this kind of model.

- Models based on the homogenization technique have been introduced to predict the impact of suffusion on the mechanical behavior of eroded soils. In this kind of models, the increase in void ratio caused by the loss of a solid fraction is assumed to be the main effect of suffusion. The validity of such an assumption is questioned.

In this work, we aim to bring a better understanding of consequences of the loss of fine particles on the mechanical behavior of eroded soils by performing numerical simulations with the DEM. This work is divided into two parts. The first part is dedicated to a study of the effect of fine content on the mechanical behavior of mixed soils at the macro-scale and at the particle scale. This study will be presented in Chapters 2 and 3. In the second part, we aim to study the mechanical behavior of eroded soils. We do not use a coupled particle-fluid model to simulate a full suffusion process. Instead, we propose three following levels for representing the internal state of eroded soils:

- **Level 1**: at this level, the effect of suffusion is assumed to be a reduction in fine content on the particle size distribution (PSD) curve. Starting from an initial PSD, a fine content is removed from this initial PSD curve and a sample is generated according to the new PSD curve, which is considered as the eroded sample.

- **Level 2**: this level consists in removing some fraction of fine particles from an original sample to obtain an eroded sample. We use different methods to remove fine particles. We propose a new method to identify the fine particles which are susceptible to be detached by the seepage flow.

- **Level 3**: we aim to take into account the transport of fine particles and the blockage of fine particles by constrictions of the pore network to represent the internal state of eroded soils.

The second part of our work will be presented in Chapters 4 and 5.

Chapter 2

Discrete element simulations of gap-graded soils

2.1 Introduction

Granular materials are composed of distinct rigid particles which interact each other through contacts between them. These materials are strongly discontinuous and heterogeneous. Their macroscopic properties are then governed by properties at the particle scale such as friction at contacts, particle shape and arrangement of particles. The Discrete Element Method (DEM) has been introduced to model this kind of material as a collection of rigid distinct elements (Cundall and Strack, 1979; Luding, 2008). Each element can move independently according to Newton-Euler equations of motion and the interaction between them occurs only at their contact according to a contact law. One of the main advantages of this method is that it is capable to modeling the complex behavior of a granular medium with few parameters. As every local information at the particle scale (particle position, particle velocity and contact force, etc.) can be accessed during simulation, the DEM is a powerful tool to study the behavior of granular material at the particle scale. It should be noted that such a study is difficult to be carried out experimentally. In this work, we perform numerical simulations with the DEM to investigate the effect of the fine particles on the mechanical behavior of gap-graded soils and consequences of a loss of fine content on their macroscopic properties at the particle scale.

This chapter starts by a brief presentation of the DEM in Section 2.2. After that, numerical samples simulated in our work are presented in Section 2.3. It is vital to highlight that the DEM is computationally very expensive so the number of particles should be carefully chosen to gain the computation time, while guaranteeing the representativity of the simulated samples. Section 2.4 is thus dedicated to an analysis of the representativity of the simulated samples in our simulations. In Section 2.5, we study the effect of fine content on the compactness and on the mechanical behavior of loose and dense gap-graded samples.

2.2 A brief review of the Discrete Element Method (DEM)

There are two main approaches for the DEM: Molecular Dynamic (MD) approach and Contact Dynamic (CD) approach. Both approaches model a granular material as a collection of distinct rigid particles whose motion follows the Newton-Euler law but they differ from each other in the way of modeling the interaction at contact. The Molecular Dynamic (MD) approach considers a small compliance effect at the contact point so the contact force can be uniquely determined from the elastic relative displacement at the contact point Luding (2008). On the other hand, the Contact Dynamic (CD) approach neglects the compliance effect at the contact point. As a consequence, the contact force cannot be uniquely determined from the relative displacement at the contact point without considering the dynamic equations of the whole system

Radjai and Richefeu (2009). In addition, as particles are assumed to be perfectly rigid, a discontinuity of the particle velocity occurs when two particles collide each other. This discontinuity render the numerical resolution of the CD approach much more complex than that of the MD approach. The DEM based on the MD approach is chosen in our work in view of its simplicity in the numerical resolution. The main ingredients of the MD approach are presented below.

2.2.1 Particle shapes

Most studies based on the DEM have used simplified particle shapes as disks or spheres. The main advantages of these simple shapes are that the contact between two adjacent circular or spherical particles occurs at only one point and the distance between them is easily calculated. However, circular or spherical particles roll easily on each other and cannot represent the real soil. Many studies tried to consider complex shapes such as polygons or polyhedra (Szarf et al., 2011; Radjaï and Dubois, 2011). For these complex shapes, a great computational effort is required to detect contacts and to calculate contact forces and torques. An alternative approach makes use of clumps of spherical particles to represent a real particle shape (Salot, 2007; Das, 2007). As shown by Das (2007), a real particle shape can be approximated by a cluster of overlapping spheres (Figure 2.1). However, many spheres are needed to model a real particle, increasing greatly the computation time to simulate a real soil sample. Belheine et al. (2009); Oda and Iwashita (2000) pointed out that the behavior of a real granular material such as sand can be reproduced by simulating a numerical sample composed of spherical particles with an appropriate contact model to take into account the rolling and twisting resistances at contacts between two non-spherical particles.

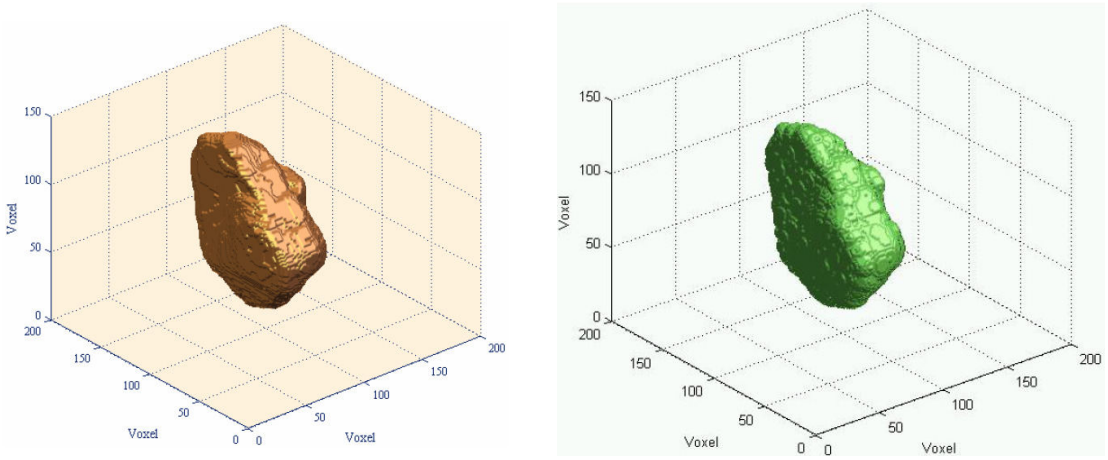

(a) (b)

Figure 2.1: (a) A real sand particle and (b) particle shape obtained by clustering overlapping spheres (Das, 2007).

In this study, we aim to study the mechanical behavior of gap-graded soils composed of fine particles and coarse particles. To simulate such granular materials, a great number of particles is needed so the simulation is very time-consuming. Spherical particles are considered in our simulations to keep the computation time reasonable.

2.2.2 Newton-Euler equations

Each particle p in the DEM has six degrees of freedom: three translational displacements and three rotations. Its position is located by the vector $\boldsymbol{x}^p = [x_1^p,\ x_2^p,\ x_3^p]$ and its three rotations along the three axes

1, 2 and 3 are denoted by the vector $\boldsymbol{\theta}^p = [\theta_1^p,\ \theta_2^p,\ \theta_3^p]$ (Figure 2.2). Its dynamics follows the Newton-Euler equations of motion:

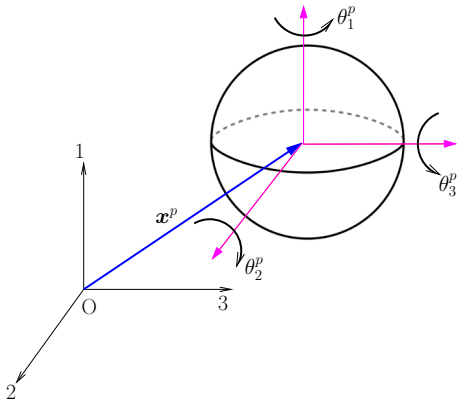

Figure 2.2: Position vector $\boldsymbol{x}^p$ and three rotations θ_1^p, θ_2^p and θ_3^p of each particle.

$$\begin{cases} m^p \ddot{x}_i^p = \sum\limits_{c \in \mathcal{C}^p} f_i^c + f_i^{\text{ext},p}, \text{ for } i = 1, 2, 3 \\ I^p \ddot{\theta}_i^p = \sum\limits_{c \in \mathcal{C}^p} M_i^c + M_i^{\text{ext},p}, \end{cases} \tag{2.1}$$

where:

- $\ddot{\boldsymbol{x}}^p$ and $\ddot{\boldsymbol{\theta}}^p$ denote the translational and rotational accelerations, respectively;
- m^p and I^p are the mass and the moment of inertia of particle p, respectively;
- superscript c runs over the set of contacts $\mathcal{C}^p$ of particle p;
- $\boldsymbol{f}^c$ and $\boldsymbol{M}^c$ are the contact force and the moment of the contact force with respect to the particle center, respectively; and
- $\boldsymbol{F}^{\text{ext},p}$ and $\boldsymbol{M}^{\text{ext},p}$ are the exterior force and moment applied on particle p, respectively.

The system of Equations (2.1) combined with the initial conditions $\boldsymbol{x}^p(t=0) = \boldsymbol{x}_0^p$, $\boldsymbol{\theta}^p(t=0) = \boldsymbol{\theta}_0^p$, $\dot{\boldsymbol{x}}^p(t=0) = \dot{\boldsymbol{x}}_0^p$ and $\dot{\boldsymbol{\theta}}^p(t=0) = \dot{\boldsymbol{\theta}}_0^p$ constitutes an initial value problem to be solved. It can be numerically integrated by using the central-difference method with a time increment Δt as follows:

- Translational and rotational accelerations $\ddot{x}_i^p$ and $\ddot{\theta}_i^p$ at time t are calculated with Equation 2.1;
- Then, the translational and rotational velocities $\dot{x}_i^p$ and $\dot{\theta}_i^p$ at time $t + \Delta t/2$ are calculated from those calculated at time $t - \Delta t/2$:

$$\begin{cases} \dot{x}_i^p(t + \Delta t/2) = \dot{x}_i^p(t - \Delta t/2) + \ddot{x}_i^p(t)\Delta t \\ \dot{\theta}_i^p(t + \Delta t/2) = \dot{\theta}_i^p(t - \Delta t/2) + \ddot{\theta}_i^p(t)\Delta t; \end{cases} \tag{2.2}$$

- Finally, the position of the particle center x_i^p and rotation θ_i^p at time $t + \Delta t$ are calculated from those calculated at time t:

$$\begin{cases} x_i^p(t + \Delta t) = x_i^p(t) + \dot{x}_i^p(t + \Delta t/2)\Delta t \\ \theta_i^p(t + \Delta t) = \theta_i^p(t) + \dot{\theta}_i^p(t + \Delta t/2)\Delta t. \end{cases} \tag{2.3}$$

2.2.3 Interaction law at contacts

When two particles touch each other, a contact model is needed to calculate the force at the contact. The DEM based on the MD approach allows a small overlap at contact although the particles are assumed

to be rigid as illustrated in Figure 2.3.b. The overlap δ_c at the contact between two spherical particles i and j with respective diameters R^i and R^j is calculated as:

$$\delta^c = (R^i + R^j) - \|\boldsymbol{x}^i - \boldsymbol{x}^j\|. \tag{2.4}$$

Two particles are in contact if $\delta^c \geq 0$. In this case, we use a simple model illustrated in Figure 2.3.a for their interaction at the contact. This model consists in modeling the normal interaction by a normal spring with stiffness K_n^c and the tangential interaction by a tangential spring with stiffness K_t^c and a slider that represents friction at the contact point. This model does not take into account the rolling and twisting resistances at contacts between two spherical particles.

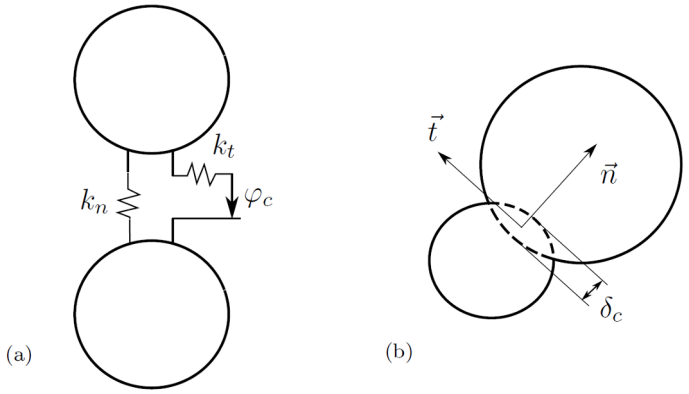

Figure 2.3: (a) Interaction law according to (Cundall and Strack, 1979), (b) overlap δ^c at the contact.

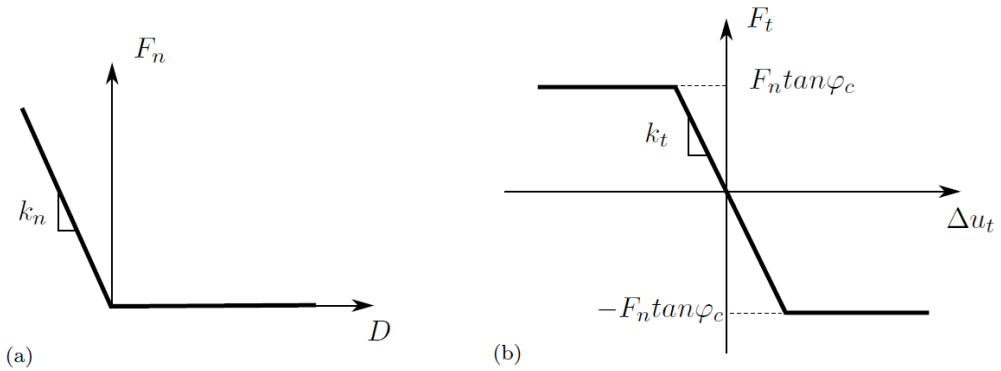

Figure 2.4: Force–displacement relations (a) in the normal direction and (b) in the tangential direction.

Figure 2.4 illustrates the force-displacement relations obtained with a linear contact model adopted in our work. According to this contact model, the normal force f_n^c at the contact is given by:

$$f_n^c = \max(0, K_n^c \delta^c), \tag{2.5}$$

and the tangential force is calculated incrementally:

$$\delta f_t = K_t^c \delta u_t^c, \tag{2.6}$$

where u_t^c is the relative tangential displacement. Coulomb's friction law limits the tangential force f_t:

$$\mid f_t^c \mid \leq f_n^c \tan\varphi, \tag{2.7}$$

where φ is the friction angle at the contact.

The contact normal and tangential stiffnesses K_n^c and K_t^c used in Equations (2.5) and (2.6) are calculated from the respective particle stiffnesses k_n and k_t of two contacting particles i and j by assuming that the latter ones are connected in series in each direction:

$$K_n^c = \frac{k_n^i k_n^j}{k_n^i + k_n^j}, \quad K_t^c = \frac{k_t^i k_t^j}{k_t^i + k_t^j} \tag{2.8}$$

2.2.4 Computation cycle

The computation in the DEM is performed in a stepping manner as illustrated in Figure 2.5. Each step corresponds to an interval of time $[t,\ t + \Delta t]$. At the beginning of each computation step, all local information such as particle position, particle velocities and contact forces are known from the previous step. The Newton-Euler equations of motion are first integrated according to the method presented in Section 2.2.2 to compute the particle positions and velocities at the end of the step. All contacts between particles are next detected to update the list of contacts. Finally, interaction forces at each contact are calculated according to the contact model presented in Section 2.2.3. This computation cycle is repeated until the end of our simulation.

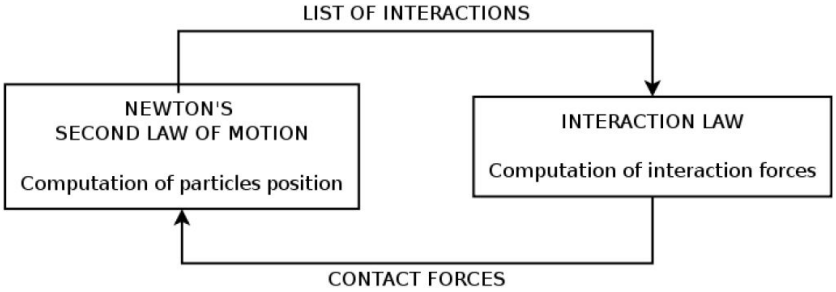

Figure 2.5: Computation cycle of the DEM.

2.2.5 Time step

A granular material is modeled by the DEM is a system composed of masses and springs joining every couple of masses. For such an oscillating system, the stability of the central difference scheme presented in Section 2.2.2 is guaranteed if the time step Δt is sufficiently small to allow the propagation of waves in the system. Indeed, the time step Δt must be chosen to be sufficiently small compared to the natural period T_N of each oscillating mode in the system. The natural period is expressed by the following relation (Catalano, 2012):

$$T_N = \sqrt{\frac{m_i}{K_i^j}}, \tag{2.9}$$

where m_i is the mass of particle i; and K_j^i is an equivalent stiffness that is evaluated by considering all the contacts of particle i for each degree of freedom $j = 1$, 2, 3 and 4 ($j = 4$ corresponds to the rotational stiffness). The critical time step is defined as the minimum natural period:

$$\Delta t_{\text{crit}} = \min_{(i,j)} \sqrt{\frac{m_i}{K_i^j}}. \tag{2.10}$$

The time step is chosen as $\Delta t = \alpha \Delta t_{\text{crit}}$ with $\alpha < 1$ is a coefficient of safety.

2.2.6 Numerical damping

The DEM is a dynamic method that consists in solving the Newton's second law of dynamics for each particle as presented in Section 2.2.2. Thus, any action applied to the system generates waves that propagate throughout the medium. When simulating a quasi-static granular sample, these wave must be damped such that the system remains in a quasi-equilibrium state. This damping can be achieved by adding dashpots in series with the springs in the normal and tangential directions at each contact. For this *viscous damping*, it is not easy to choose values of the normal and tangential viscosities to avoid the over-damping. Cundall and Strack (1979) proposed a *non-viscous* numerical damping by adding a damping force $\boldsymbol{F}^{d,p}$ and a damping moment, $\boldsymbol{M}^{d,p}$ to the right hand side of Equation 2.1:

$$\begin{cases} F_i^{d,p} = -\zeta \mid F_i^p \mid \text{sign}(\dot{x}_i^p), \\ M_i^{d,p} = -\zeta \mid M_i^p \mid \text{sign}(\dot{\theta}_i^p), \end{cases} \tag{2.11}$$

where ζ is the damping coefficient which can be chosen between 0 and 1; $\boldsymbol{F}^p$ and $\boldsymbol{M}^p$ are resultant force and moment acting on particle p.

2.3 Numerical simulations of binary mixtures

In our study, we simulate triaxial compression tests on 3D granular samples by using the open-source software YADE which is an C++ open-source for the DEM framework (Šmilauer et al., 2015). In the following, we first discuss how parameters are chosen in our simulations and then we present how numerical samples are generated, compacted and sheared by triaxial compression tests.

2.3.1 Parameters

The numerical samples simulated in our work are composed of spherical particles whose sizes are selected to match the gap-graded PSD curve shown in Figure 2.6(a). This gap-graded curve is characterized by a gap ratio $G_r = D_{\min}/d_{\max}$ where $D_{\min}$ is the minimum diameter of coarse particles and $d_{\max}$ is the maximum diameter of fine particles. According to Chang and Zhang (2013), internal instability for internal erosion due to seepage flow for a gap-graded material might occur for a gap ratio $G_r \geq 3$. In our simulations, the gap ratio $G_r = 3$ is chosen to keep the computation time reasonable since a higher value of G_r leads to a larger number of particles and then to a very long computation time. The fine content f_c is varied from 0% to 100%. Figure 2.6(b) illustrates a simulated gap-graded sample.

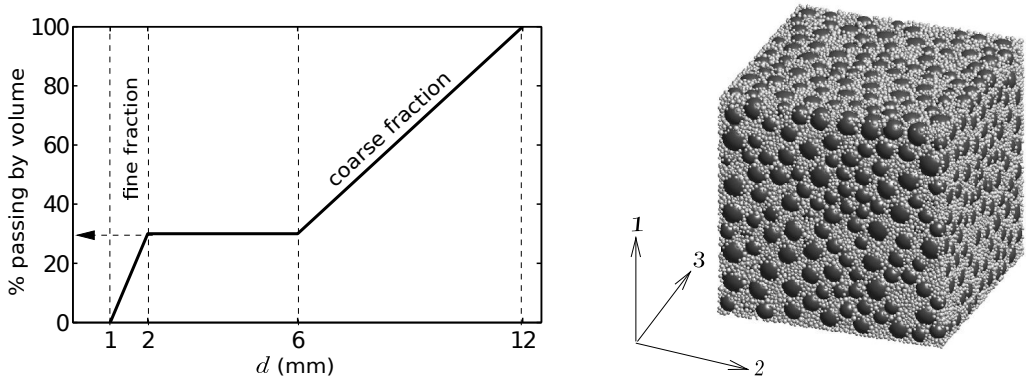

(a) (b)

Figure 2.6: (a) The considered gap-graded grain size distribution and (b) a simulated granular mixture.

The parameters used in the simulated samples are shown in Table 2.1. The microscopic parameters used in the contact model are identical to those used in the paper of Scholtès et al. (2010). It should be noted that the normal particle stiffness k_n must be sufficiently large so that the particles can be considered to be rigid. The particle rigidity can be assessed by using the following dimensionless number κ:

$$\kappa = \frac{k_n}{D.p}, \tag{2.12}$$

where D is the average particle diameter and p is the confining pressure. The value of $k_n/D = 250$ MPa shown in Table 2.1 and a confining pressure $p = 100$ kPa result in $\kappa = 2500$. Combe (2001) recommended a value of κ between 500 to 40 000. In our simulations, $\kappa = 2500$ is sufficient to consider that the particles are rigid. The inter-granular friction angle $\varphi = 35°$ is chosen in our simulations to obtain a reasonable shear resistance of the simulated samples with spherical particles.

Table 2.1: Chosen values of the numerical parameters.

Local parameters	**Value**
Mass density ρ	2600 kg/m^3
Particle stiffness k_n/D	250 MPa
Particle stiffnesses ratio k_t/k_n	0.5
Inter-granular friction angle φ	35°
Damping coefficient ζ	0.3
Safety coefficient of the time step α	0.8

2.3.2 Sample generation and compaction

Particles are first randomly instantaneously generated into a cube composed of six rigid walls. At this stage, each particle diameter is reduced by a factor of 2.0. Particles are then progressively expanded to reach the target size distribution. After that, the box dimensions are slowly reduced until the stresses σ_i (i = 1, 2, 3) reach a target confining stress of 100 kPa. To promote the arrangement of particles, the inter-granular friction angle φ is reduced during the compaction process. As shown by O'Sullivan (2011), the void ratio largely varies as the inter-granular friction angle φ decreases. The loosest state is obtained with $\varphi = 35°$ and the densest state is obtained with $\varphi = 0$. At the end of the compaction, the initial value of the friction angle must be reset. The gravity is set to zero to avoid an anisotropic arrangement of particles during the generation and compaction of the samples. The above generation and compaction methods allow us to obtain isotropic and homogeneous samples.

2.3.3 Triaxial compression tests

After the compaction, triaxial compression tests are performed on the numerical samples. During these tests, a strain rate $\dot{\varepsilon}_1$ is imposed in direction 1, while the stresses σ_2 and σ_3 in the respective lateral directions 2 and 3 are kept constant and equal to 100 kPa. The strain rate $\dot{\varepsilon}_1$ must be low enough such that the dynamic effect induced by the shearing is low and then the simulated samples remain in a quasi-static regime. The dynamic effect can be quantified by an inertia number I defined as:

$$I = \dot{\varepsilon}_1 \sqrt{\frac{m}{D.p}}, \tag{2.13}$$

where m is the average particle mass, D is the average particle diameter and p is the confining pressure. A strain rate $\dot{\varepsilon}_1 = 0.01$ s^{-1} is chosen in our simulations, which corresponds to an inertia number I about 10^{-4}. Sibille (2006) recommended a value of I smaller than 10^{-2} for a quasi-static test. Figure 2.7 shows the behavior of a simulated loose sample of 8 000 particles with zero fine content during the triaxial compression. It can be seen that, the behavior of this loose sample is dilative but, normally, loose samples have contractive behavior. This contradiction can be explained by the fact that in numerical samples, the particles are spherical which are different than the real ones. The rolling between these particles is easier in comparison with that of the real particles. For that, we can see a dilative behavior for some loose samples.

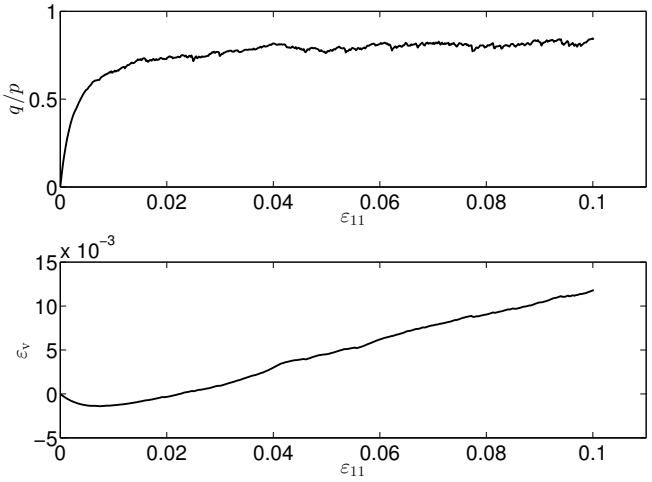

Figure 2.7: Stress ratio q/p and volumetric strain ε_v versus axial strain ε_1 for a loose sample.

For a simulated sample, it is important to choose a number of particles sufficient such that the conditions of a representative elementary volume (REV) are achieved and the computation time is reasonable. This point will be discussed in the next section.

2.4 REV for gap-graded soils under triaxial compression tests

2.4.1 REV in the DEM

The REV is a key concept for studying random heterogeneous materials such as granular materials. The REV is a sample that contains the constituents of the heterogeneous material under consideration (solid phase, fluid phase, voids, etc.). On one hand, this sample must be sufficiently small compared to the size of the structure such that the REV can be considered as a point at the structure scale. On the other hand, it must be sufficiently big compared to the size of the local constituents such that it can be considered to be representative of the material under consideration. Figure 2.8 shows a conceptual representation of the change in a material property as the sample size V increases. If the the sample size is smaller than a threshold value $V_{\min}$, the material property fluctuates. In this case, we obverse the material at the microscopic scale at which the material is very heterogeneous. When $V > V_{\min}$, the material property does not change with the sample size as long as the sample size is smaller than a second threshold value $V_{\max}$. The sample in this case contains a sufficiently large number of microscopic constituents so an average of the corresponding property of the microscopic constituents leads to only minor fluctuations. A further increase in V beyond $V_{\max}$ leads to a change in the material property. In this case, the sample is not representative of the material at a point in the structure since it includes the spacial variability at the structure scale. The REV size must be then between $V_{\min}$ and $V_{\max}$.

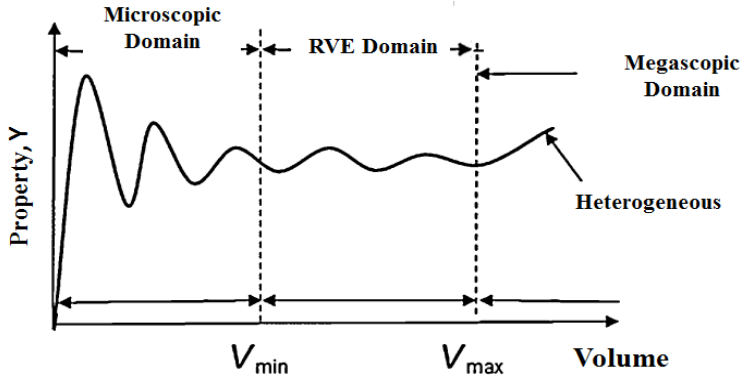

Figure 2.8: Conceptualization of the representative elementary volume (REV) (Brown et al., 2000).

The REV size depends mainly on the material under consideration and on the property that we want to study. A sample can be considered as a REV if the two following conditions are satisfied:

- An increase in its size does not lead to a significant change in the material property under consideration;

- Different random generations of microscopic constituents give close values of the material properties under consideration.

The choice of the sample size when performing experimental tests on granular soils is usually based on experimental standards. The ASTM standard (ASTM D4767-88, 1988) recommends that the ratio of the specimen diameter to the largest particle size is larger than 6, while the French standard (NFP 94-074, 1994) recommends a value larger than 5 for widely graded soils and 10 for uniformly graded soils. Al-Raoush and Papadopoulos (2010) studied the REV for a sand by using the X-ray microtomography. The authors considered different material properties such as porosity, particle size distribution and coordination number (average number of contacts per particle) to determine the REV size. They found that the minimum sizes of the REV obtained for the particle size distribution and coordination number are larger than that for the porosity. On the whole, the ratio of the REV volume to the volume of a sphere with diameter D_{50} must be greater than 2×10^4. This means that the REV diameter must be 27 times greater than the particle diameter D_{50}. Moreover, a larger size of the REV is required as the uniformity coefficient $C_u = D_{60}/D_{10}$ is increased.

For DEM numerical simulations, no clear rule has been established. Wiącek and Molenda (2016) showed that for polydisperse granular packings which are not widely graded and are subjected to uniaxial compression, the REV size is about 15 times the average particle diameter, i.e. the sample must include at least $15 \times 15 \times 15 = 3375$ particles. Salot (2007) found out that the REV size for simulating a triaxial compression test on samples having a tight and uniform PSD is about 8000 particles. Other studies considered samples composed of 10000 particles (Plassiard et al., 2009; Belheine et al., 2009; Widuliński et al., 2009; Wang and Li, 2014). For a gap-graded PSD, the number of particles required for a REV must be varied with fine content, and 10000 particles are, in general, not enough. Shire et al. (2014a) stated that a gap-graded sample with a minimum of 500 coarse particles can be considered as a REV when simulating an isotropic compression. Kawano et al. (2016) used 30000 particles in their simulations of gap-graded samples subjected to isotropic compression. In numerical simulations of isotropic compression tests performed by Minh et al. (2014), the number of particles for binary mixtures is varied with fine content. A shear loading might require a larger number of coarse particles to achieve a RVE. It is worth noting that the RVE size for granular materials is determined in a statistical sense. This means that differ-

ent random generations of samples with the same size must give close results as stated by Chareyre (2003).

In the next section, we will show a study of the REV size when simulating triaxial compression tests on gap-graded soils with the PSD shown in Figure 2.6. For each value of fine content, several samples with different sizes are simulated and for each sample size, different random generations of particles are performed. Different macroscopic and microscopic properties such as porosity, peak stress ratio $(q/p)_{\max}$ and coordination number are considered for determining the REV size. The dilatation angle which characterizes the volumetric strain of samples is not considered in this study due to the difficulty in its determination. The coordination number, defined as the average number of contacts per particle, is usually used to describe the density of a granular sample at the micro-scale. This microscopic variable is not adequate for a binary mixture for which the number of contacts per coarse particle is very different from the number of contacts per fine particle. For such a system, a coordination number for the coarse fraction should be separated from the one defined for the fine fraction as suggested by Minh and Cheng (2013). The coordination number N_C^{C-C} for the coarse fraction, which is defined as the average number of coarse-coarse contacts per coarse particle, is considered in our study. As the computation time is very long when simulating gap-graded samples, fine content f_c is limited between 0 and 20%. Based on the obtained results, we propose a relation between the REV size and fine content f_c to extrapolate the REV size for greater values of fine content. In the following, the variation of the considered properties with the sample size and the dispersion of these properties for a given sample size but with different random generations will be studied for loose samples. It should be noted that if the REV conditions are satisfied by a sample at the loose state, they are obviously satisfied at the dense state as dense materials show lower dispersion of their properties than loose materials.

2.4.1.1 Variation of the sample properties with the sample size

For this study, triaxial compression tests are performed on loose samples with gap ratio $G_r = 3$ which are obtained by setting the inter-granular friction angle $\varphi = 35°$ during the compaction phase presented in Section 2.3.2. For each sample size, from 5 to 10 samples with random generations of particles are simulated and a mean value is determined for each property (porosity, shear resistance $(q/p)_{\max}$ and the coordination number N_C^{C-C}). Figure 2.9 shows the variation of the mean values of the porosity n and of the coordination number N_C^{C-C} with respect to the ratio $L/D_{\max}$ of the sample size L to the maximum diameter $D_{\max}$. The variation of the peak shear strength $(q/p)_{\max}$ with sample size is shown in Figure 2.10. It can be seen that the porosity n decreases and the coordination number N_C^{C-C} increases with the sample size and tend to reach constant values when the sample size is big enough. The shear strength $(q/p)_{\max}$ fluctuates strongly when the sample size is small and tends to reach a constant value as the sample size is increased. For the samples composed of only coarse particles ($f_c = 0$), a slight variation of these properties is observed when the sample size $L/D_{\max}$ is greater than 10.62. This value is agreement with the results found by several authors who stated that the REV size must be, at least, 10 times bigger than the mean particle diameter (Radjai, 2001). For binary mixtures, as a whole, these properties do not fluctuate significantly when $L/D_{\max} > 6$. This means that the REV size for a binary mixture might be much smaller than that for a uniformly graded sample.

To quantify the variation of a given sample property, namely x, with respect to the sample size, we define a variation measure ϵ:

$$\epsilon = \frac{\mid x_i - x_{i+1} \mid}{x_i} \times 100\%, \tag{2.14}$$

where x_i is the value of the considered property obtained for a given sample size L_i and x_{i+1} is the value obtained for the next sample size L_{i+1} considered in our simulations. This variation measure ϵ is calculated for the porosity n, the coordination number N_C^{C-C} and the shear strength $(q/p)_{\max}$ at different sample sizes. Figure 2.11 shows the obtained results for different fine contents. This figure confirms a stronger

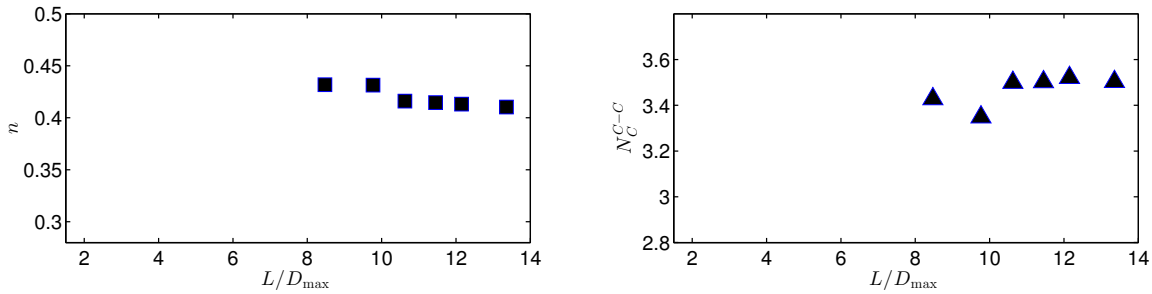

(a)$f_c = 0\%$

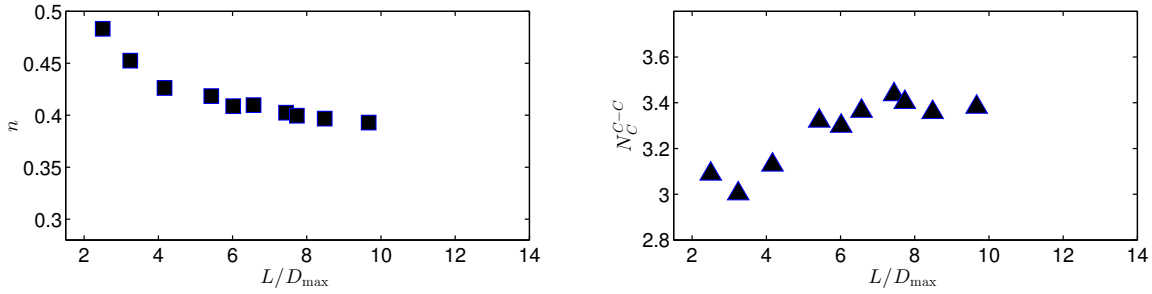

(b) $f_c = 5\%$

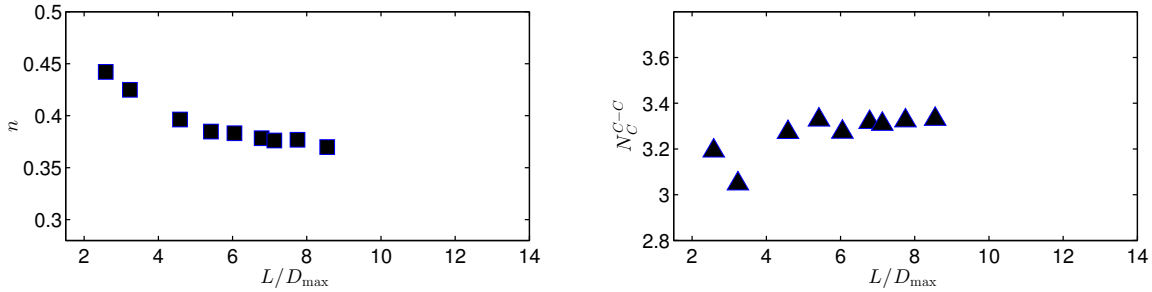

(c) $f_c = 10\%$

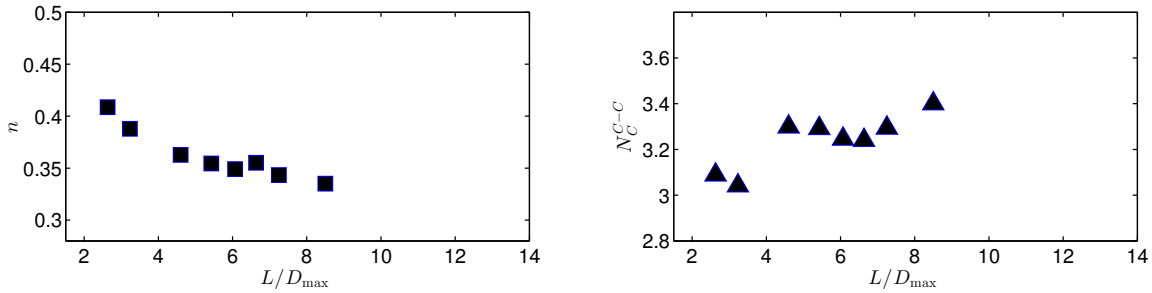

(d) $f_c = 15\%$

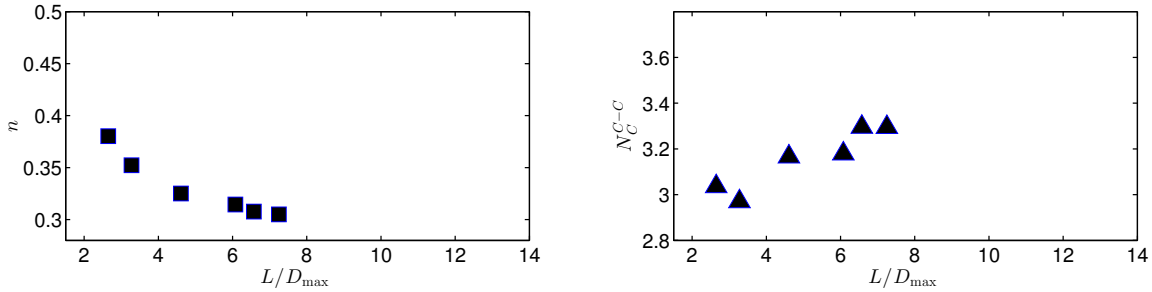

(e) $f_c = 20\%$

Figure 2.9: Mean values of the porosity n and of the coordination number N_C^{C-C} versus sample size: a) $f_c = 0\%$, b) $f_c = 5\%$, c) $f_c = 10\%$, d) $f_c = 15\%$, e) $f_c = 20\%$

.

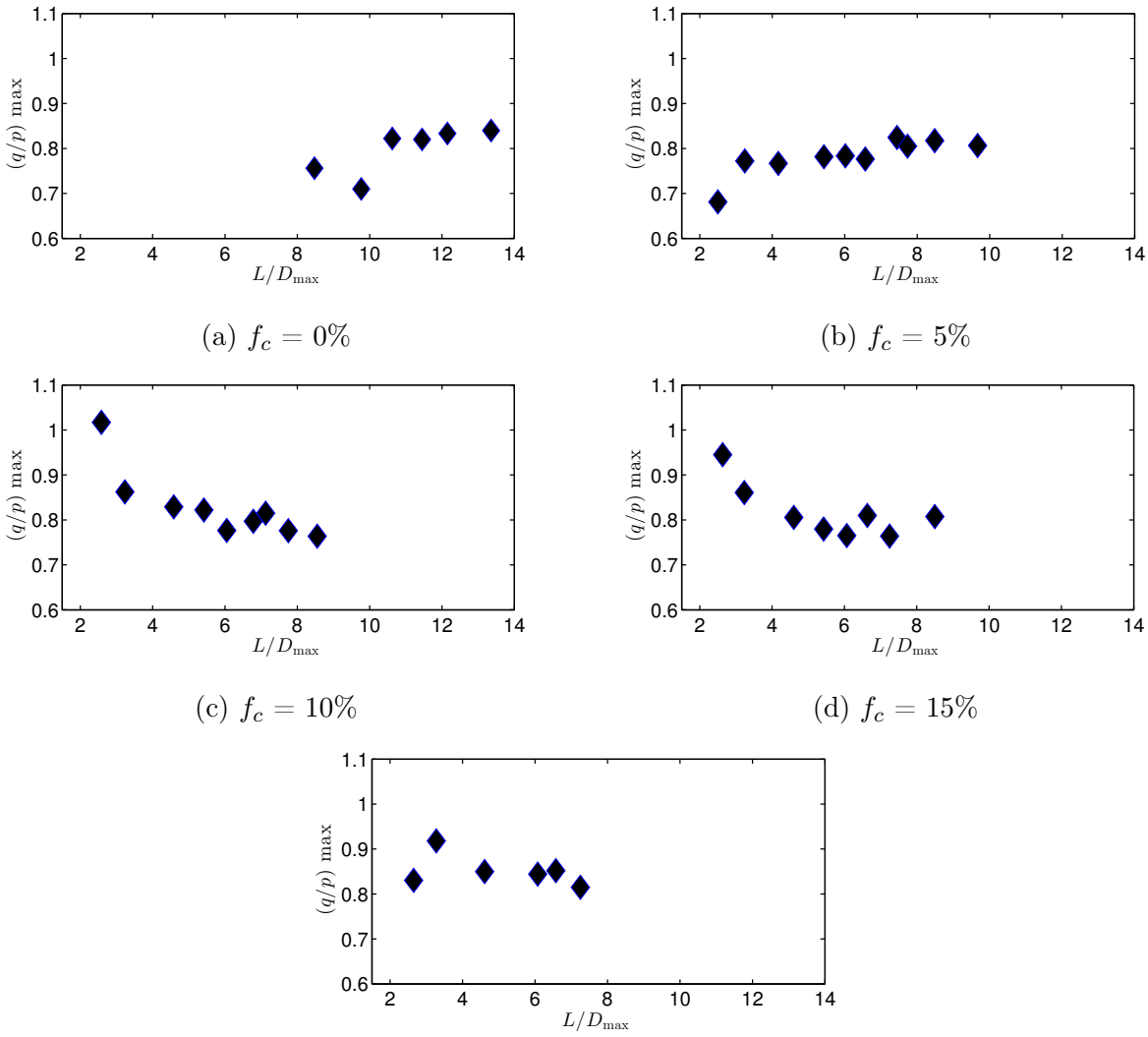

(a) $f_c = 0\%$ (b) $f_c = 5\%$

(c) $f_c = 10\%$ (d) $f_c = 15\%$

(e) $f_c = 20\%$

Figure 2.10: Mean value of the shear strength $(q/p)_{\max}$ versus sample size: a) $f_c = 0\%$, b) $f_c = 5\%$, c) $f_c = 10\%$, d) $f_c = 15\%$, e) $f_c = 20\%$

.

variation of the shear strength $(q/p)_{\max}$ with respect to the sample size, compared to those of the porosity n and the coordination number. This means that the REV size must be defined by considering the shear strength $(q/p)_{\max}$. We define a minimum REV size for a given fine content if the variation measure ϵ for $(q/p)_{\max}$ does not exceed 5%. Figure 2.12 shows the minimum REV sizes determined for fine contents f_c from 0 to 20%. It is clear that the minimum REV size tends to decrease with an increase in fine content.

2.4.1.2 Dispersion of sample properties

For a given sample size, we simulate different samples generated randomly to study the dispersion of their porosity n, of their coordination number N_C^{C-C} and of their peak shear strength $(q/p)_{\max}$. Random samples with different sample sizes and different fine contents are simulated with a gap ratio $G_r = 3$.

Figure 2.13 shows the dispersion of the stress-strain curves of 10 random loose samples with $f_c = 0$ for different sample sizes $L/D_{\max}$. We can see that the dispersion is very high for $L/D_{\max} = 8.47$ which corresponds to 2000 particles, and this dispersion decreases as the sample size is increased. It becomes

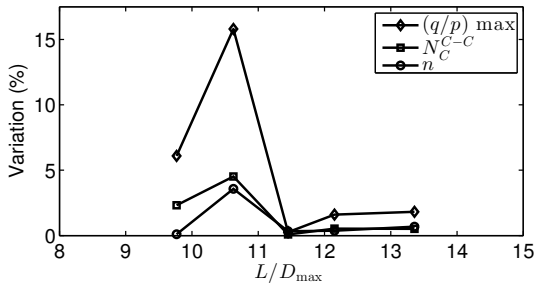

(a) $f_c = 0\%$

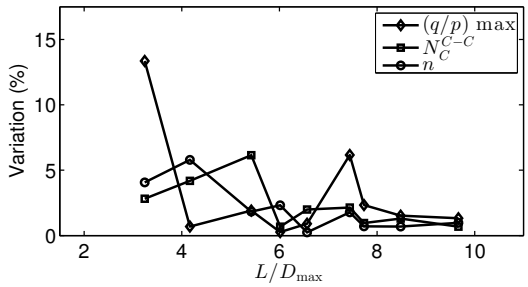

(b) $f_c = 5\%$

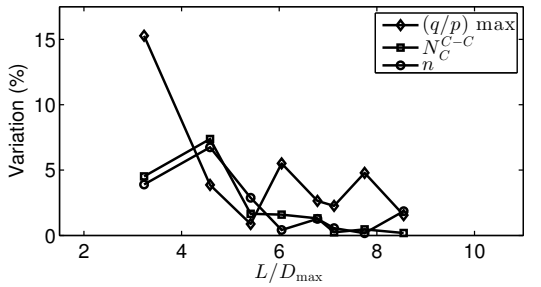

(c) $f_c = 10\%$

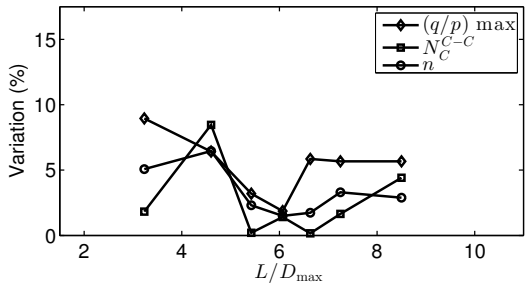

(d) $f_c = 15\%$

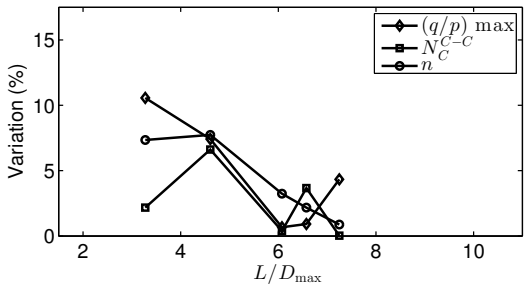

(e) $f_c = 20\%$

Figure 2.11: Variation measure ϵ of the mean values of the shear strength $(q/p)_{\max}$ versus sample size: a) $f_c = 0\%$, b) $f_c = 5\%$, c) $f_c = 10\%$, d) $f_c = 15\%$, e) $f_c = 20\%$

.

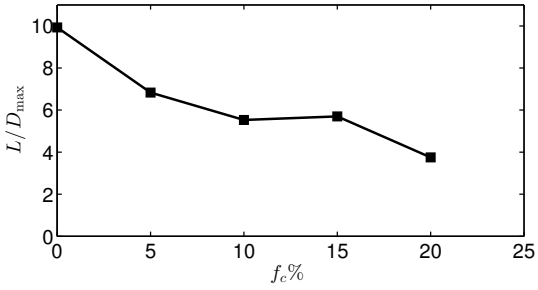

Figure 2.12: Minimum REV size versus fine content f_c.

small for $L/D_{\max} = 13.35$ which corresponds to 8000 particles.

In order to quantify the dispersion of a given property obtained for different random samples of the

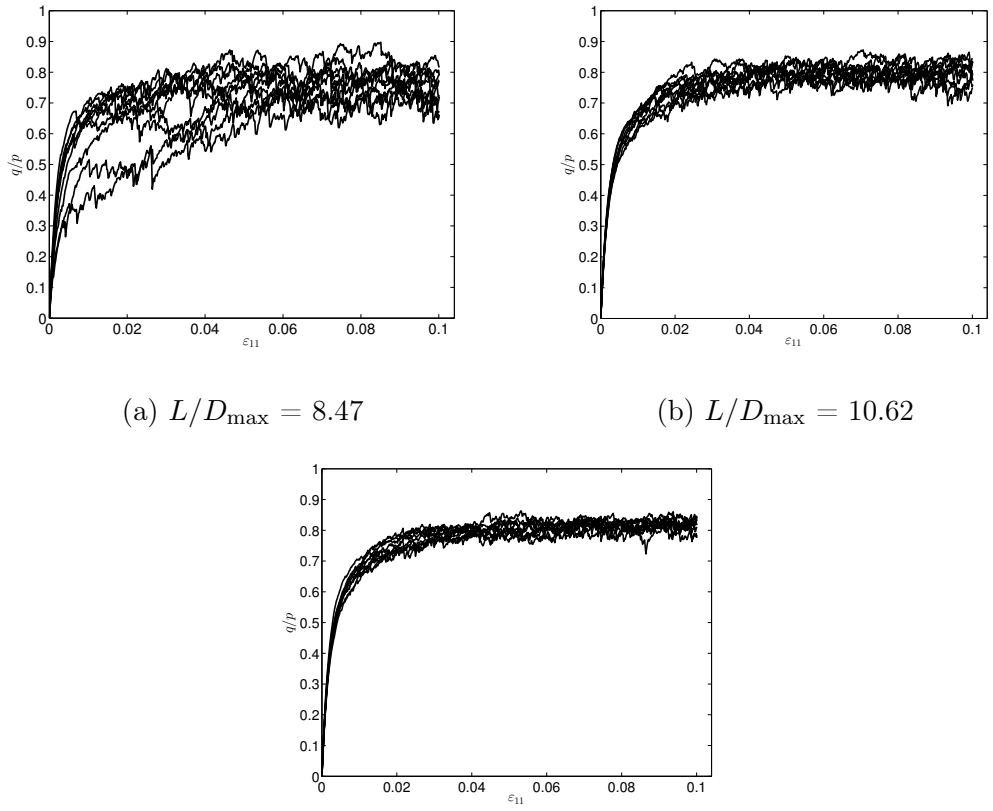

(a) $L/D_{\max} = 8.47$ (b) $L/D_{\max} = 10.62$

(c) $L/D_{\max} = 13.35$

Figure 2.13: Dispersion of the stress-strain curves for 10 samples with $f_c = 0$: (a) $L/D_{\max} = 8.47$, (b) $L/D_{\max} = 10.62$; (c) $L/D_{\max} = 13.35$

same size, we use the coefficient of dispersion C_{v} defined as $C_{\mathrm{v}} = \sigma/\mu$ where σ is the standard variation and μ is the mean value of the considered property. For the samples with $f_c = 0$ shown in Figure 2.13, the coefficient of dispersion C_{v} calculated for the shear strength $(q/p)_{\max}$ is about 9.8% for the sample size $L/D_{\max} = 8.47$, 3.0% for $L/D_{\max} = 10.62$ and 1.3% for $L/D_{\max} = 13.35$. Figure 2.14 shows the coefficient of dispersion C_{v} calculated for the porosity n, the shear strength $(q/p)_{\max}$ and the coordination number N_C^{C-C} versus the sample size for different fine contents. It can be seen that these properties disperse greatly when the sample size is small and their dispersion is attenuated as the sample size is increased. Among the three considered properties, the shear strength $(q/p)_{\max}$ shows the most important dispersion. Therefore, the shear strength $(q/p)_{\max}$ should be considered to determine the REV size for granular soils subjected to shear loading, rather than the initial porosity n at the macro-scale and the initial coordination number N_C^{C-C} at the micro-scale. If we consider that a REV must have $C_{\mathrm{v}} \leq 5\%$ for the shear strength $(q/p)_{\max}$, the minimum REV size can be determined for each fine content. Figure 2.15 shows the minimum REV size obtained with this method, compared to that obtained when the variation of the shear strength with respect to the sample size was considered (Figure 2.12). It is shown that the minimum REV size decreases with an increase in fine content. This suggests that the number of coarse particles, which determines the sample size, could be reduced when fine content is increased to keep the computation time reasonable, while the REV conditions are verified for the simulated samples. Moreover, the REV size is larger when analyzing the dispersion of the shear strength for the same sample size than when analyzing its variation with respect to the sample size. Therefore, we determine the REV size of the simulated samples by analyzing the dispersion of the shear strength $(q/p)_{\max}$.

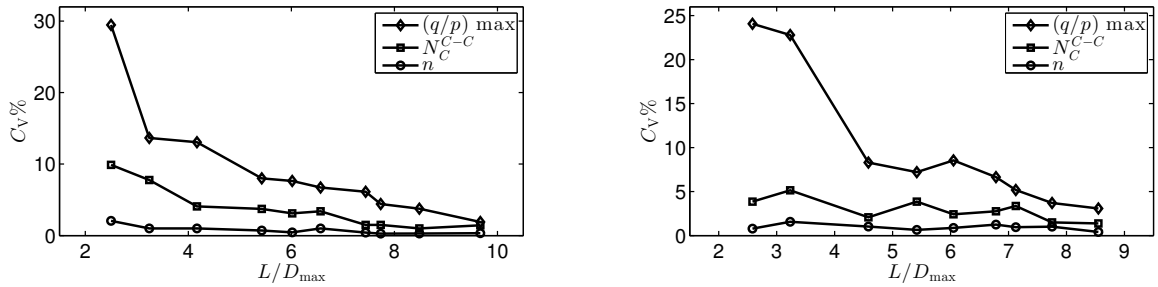

(a) $f_c = 5\%$ (b) $f_c = 10\%$

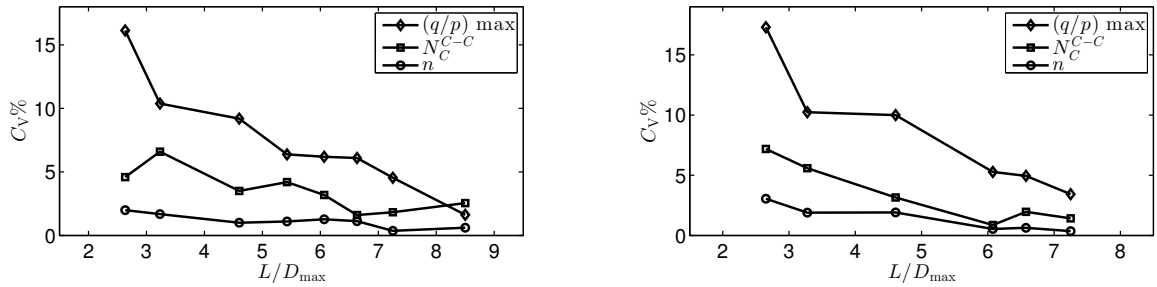

(c) $f_c = 15\%$ (d) $f_c = 20\%$

Figure 2.14: Coefficient of dispersion C_v for the porosity n, the shear strength $(q/p)_{\max}$ and the coordination number N_C^{C-C} versus the sample size: a) $f_c = 5\%$, b) $f_c = 10\%$, c) $f_c = 15\%$, d) f_c =20%

.

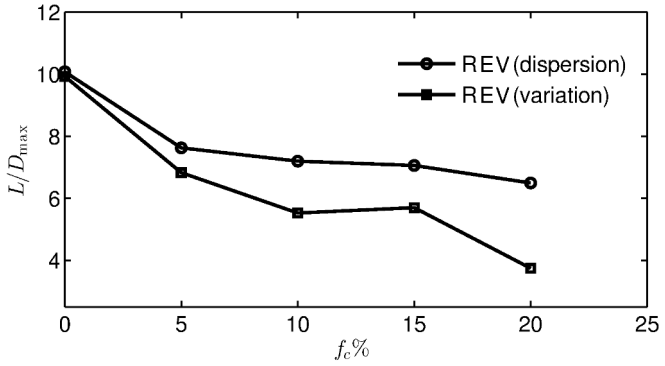

Figure 2.15: Minimum REV size versus fine content $f_c = 5\%$ to 20% obtained when analyzing the dispersion and the variation of the shear strength with the sample size.

For $f_c > 20\%$, the above study is difficult to be carried out since the computation time for samples with $f_c > 20\%$ is very long. A question is how to determine the REV size for these large values of fine content. We propose to extrapolate the REV size for $f_c > 20\%$ from the values determined for $f_c \leq 20\%$. To do so, we determine a relation of the coefficient of dispersion $C_{\rm v}$ calculated for the shear strength $(q/p)_{\max}$ to the sample size $L/D_{\max}$ and fine content f_c by performing a linear regression on the data obtained from the simulated samples with $G_r = 3$ and $f_c \leq 20\%/$. The following relation is obtained:

$$C_{\rm v} = -2.0(L/D_{\max}) - 0.196 f_c + 21.8, \tag{2.15}$$

where $C_{\rm v}$ and f_c are expressed in percentage. The coefficient of correlation R^2 is 0.93, meaning a good quality of the linear regression. This is confirmed in Figure 2.16 where values of $C_{\rm v}$ calculated with

Equation (2.15) are plotted versus the corresponding values in the brute data. The plotted points are located more or less on the diagonal of the figure. Equation (2.15) indicates that the dispersion of the shear strength $(q/p)_{\max}$ decreases with an increase in the sample size $L/D_{\max}$ and with an increase in fine content f_c. It allows us to estimate the REV size for a given fine content by defining an admissible value of the coefficient of dispersion C_{v}. For example, if the admissible value of C_{v} is 1%, the REV size $L/D_{\max}$ for $f_c = 40\%$ must be greater than 6.5. A rough estimation gives that the REV for $f_c = 40\%$ contains at least 500 coarse particles and 62000 fine particles for a target porosity of 0.4.

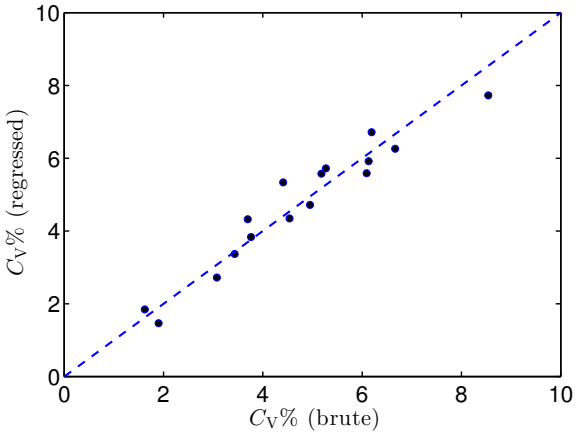

Figure 2.16: Values of C_{v} calculated with Equation (2.15) versus their corresponding brut values.

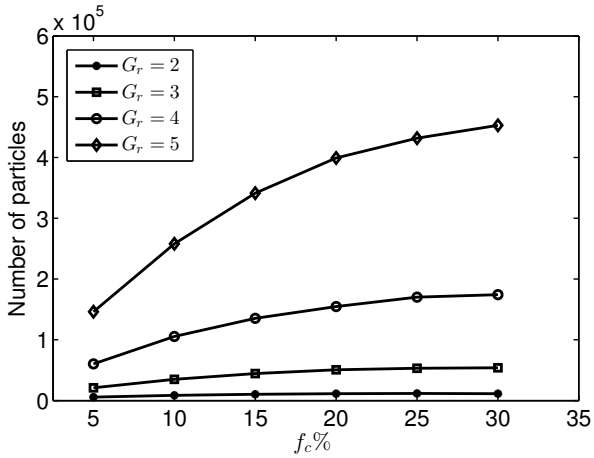

Figure 2.17: Number of particles estimated for the REV for different fine contents f_c and different gap ratios G_r.

It should be noted that Equation (2.15) is only valid for the gap ratio $G_r = 3$. In order to take into account the gap ratio G_r in such a relation for C_{v}, samples with different sizes and different random generations are simulated for $G_r = 2$ with f_c being varied from 5% to 20% and $G_r = 4$ for $f_c = 5\%$ and 10% (simulations with $G_r = 4$ are very time consuming). A linear regression gives the following relation:

$$C_{\mathrm{v}} = -2.11(L/D_{\max}) - 0.15 f_c + 1.41 G_r + 17.96. \tag{2.16}$$

A coefficient of correlation R^2 equal to 0.9 means that the performed linear regression works also quite well. Equation (2.16) means that the coefficient of dispersion C_{v} for the shear strength $(q/p)_{\max}$ increases with an increase in gap ratio G_r. This means that a larger REV size is required for a bigger gap ratio

G_r. Equation (2.16) can be used to roughly estimate the number of particles needed for simulating a gap-graded sample. Figure 2.17 shows a rough estimation of the number of particles required for the REV size for binary mixtures with different gap ratios G_r and different fine contents f_c by using Equation (2.16) with an admissible value of C_{v} equal to 5% and a target porosity of 0.4. We can notice that as the gap ratio G_r value increases, the number of particles increases greatly, specially for high values of fine content f_c. For $G_r = 4$ and $f_c > 10\%$, more than 100000 particles are required for a REV so the computational cost is very expensive.

2.4.2 Size of simulated loose and dense binary mixtures

Based on the previous study, we can estimate the minimum size of a binary mixture with a given fine content by using Equation (2.16) with an admissible value for the coefficient of dispersion $C_{\mathrm{v}} = 5\%$. To respect the minimum sample size recommended by French experimental norm (NFP 94-074, 1994), a minimum value of 5 is required for all simulated samples. For each simulation, the sample size is carefully chosen such that it is bigger than the minimum size roughly estimated and the number of particles is reasonable to gain the computation time. Table 2.2 shows the number of coarse particles, the number of fine particles, the sample size $L/D_{\max}$ and the estimated minimum sample size $(L/D_{\max})_{\min}$ for loose binary mixtures with fine contents between 0 and 30%.

f_c	N_c	N_f	$L/D_{\max}$	$(L/D_{\max})_{\min}$
0 %	8000	0	13.35	8.4
5 %	1533	17078	7.73	7.9
10 %	1541	36000	7.75	7.4
15 %	1324	47241	7.25	6.9
25 %	1349	93315	7.43	6.0
30 %	1407	121751	7.6	5.5

Table 2.2: Respective numbers, N_c and N_f, of coarse and fine particles, sample size $L/D_{\max}$ and the estimated minimum sample size $(L/D_{\max})_{\min}$ for different values of fine content f_c for loose samples.

For dense binary mixtures, fine content f_c is varied from 0 to 100%. To keep the computation time reasonable, the sample size is decreased when the fine content is increased. For fine contents between 0 and 20%, five random samples with the same size are simulated to calculate the coefficient of dispersion C_{v} for the shear strength $(q/p)_{\max}$. As shown in Table 2.3, the values of C_{v} for these fine contents are small, meaning that the chosen sample sizes are enough to verify the REV conditions. For $f_c \geq 25\%$, we did not perform this repeatability study because the simulation of samples with a high fine content is very time-consuming. However, the samples with $25\% \leq f_c \leq 60\%$ could be considered as REVs as their sizes are almost equal to the sample size for $f_c = 20\%$. Starting from 60% of fine content, the fine particles play a primary role in the mechanical behavior of binary mixtures as we will see in Chapter 3. The sample size is not large enough compared to the size of coarse particles, but large enough compared to the size of fine particles. As their mechanical behavior is mainly governed by fine particles, these binary mixtures could be expected to be REVs.

Table 2.3: Respective numbers, N_c and N_f, of coarse and fine particles, sample size $L/D_{\max}$, the estimated minimum sample size $(L/D_{\max})_{\min}$ and coefficient of dispersion C_{v} for different values of fine content f_c for dense samples.

f_c	N_c	N_f	$L/D_{\max}$	$(L/D_{\max})_{\min}$	C_{v}	f_c	N_c	N_f	$L/D_{\max}$	$(L/D_{\max})_{\min}$
0	6000	0	11.9	8.4	1.0%	40%	982	141198	7.2	5.0
5%	1347	15305	7.3	7.9	3.0%	50%	748	164350	7.1	5.0
10%	1266	30346	7.2	7.4	2.3%	60%	567	183529	7.0	5.0
15%	1276	48571	7.2	6.9	1.6%	70%	331	166454	6.5	5.0
20%	1273	68646	7.2	6.4	1.7%	80%	193	166016	6.3	5.0
25%	1296	93170	7.3	6.0		90%	90	173963	6.2	5.0
30%	1 246	115186	7.4	5.5		100%	0	19489	17.5	-
35%	1 063	123 386	7.2	5.0						

2.5 Macroscopic behavior of binary mixtures

To study the effect of fine content on the mechanical behavior of gap-graded soils, loose and dense numerical binary mixtures with different fine contents are considered. For the loose mixtures, the fine content f_c is varied from 0 to 30% and their size is shown in Table 2.2. For dense samples whose size is shown in Table 2.3, fine content f_c is varied from 0 to 100%. In the following, we will show first how fine content affects the density of binary mixtures. After that, the mechanical behavior of binary mixtures with different fine contents will be analyzed.

2.5.1 Void ratios

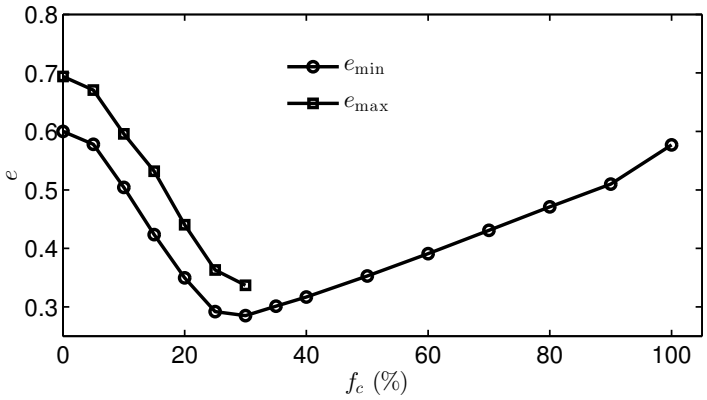

Figure 2.18: Minimum and maximum void ratios, $e_{\max}$ and $e_{\min}$, versus fine content fc.

Numerical samples are compacted by the isotropic compaction method shown in Section 2.3.2. The inter-granular friction angle φ can be varied to vary the density of a sample after compaction. We assume that the maximum and minimum void ratios, $e_{\max}$ and $e_{\min}$, is obtained by setting 35° and 0° to the friction angle φ during the compaction process, respectively. Figure 2.18 shows the variation of $e_{\max}$ and

$e_{\min}$ with fine content f_c. For the loose samples, fine content f_c is varied only between 0% and 30%. Figure 2.18 shows that, as fine content f_c is increased, $e_{\min}$ decreases first, reaches then its minimum value at fine content f_c of 32% and increases when $f_c > 32\%$. The same tendency would be obtained if loose samples with $f_c > 30\%$ were simulated. This numerical result is qualitatively in good agreement with the experimental results shown by Lade et al. (1998), Yang et al. (2006) and Thevanayagam et al. (2002). Nevertheless, the optimal fine content of 32% found in this study is a little bit bigger than the experimental values of around 25% found by Lade et al. (1998) and Yang et al. (2006) but is quite close to the value of about 30% found by Minh et al. (2014) who performed simulations of binary mixtures with the DEM. It is worth noting that this optimal fine content depends on several factors, particularly on the particle size distribution and the particle shape.

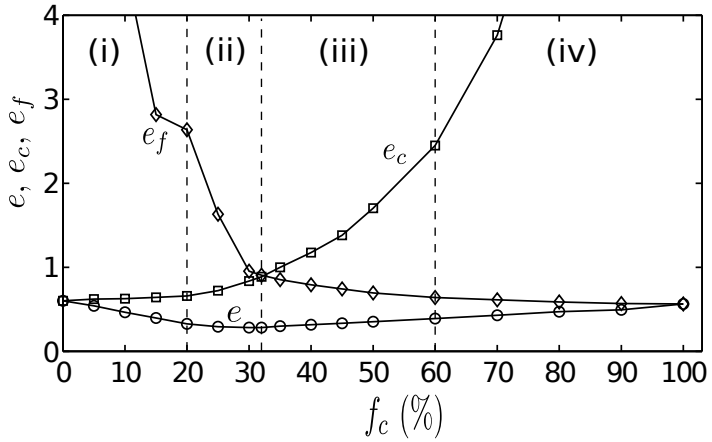

Figure 2.19: Global void ratio e, intergranular void ratio e_c and interfine void ratio e_f versus fine content fc.

Figure 2.19 presents the global void ratio e, the intergranular void ratio e_c and the interfine void ratio e_f versus fine content f_c between 0% and 100% for the dense simulated samples (see Section 1.3 for the definition of e_c and e_f). It can be seen that the intergranular void ratio e_c increases, while the interfine void ratio e_f decreases with an increase in fine content f_c. Four remarkable ranges of fine content with three threshold fine contents of 20%, 32% and 60% can be identified. For the range (i) with $f_c < 20\%$, the intergranular void ratio e_c remains more or less constant, while the interfine void ratio e_f decreases greatly with increasing fine content f_c. This means that the fine particles fill the voids left by the coarse particles without separating the latter ones. As a result, the global void ratio e decreases as the fine content increases. It is worth mentioning that the interfine void ratio e_f for this range of fine content is very high compared to the intergranular void ratio e_c and the curve for e_f cannot be fully represented in the chosen scale in Figure 2.19. Within the range (ii) with $20\% \leq f_c < 32\%$, the fine particles separate the coarse ones and occupy the void space between them. The fine-grained matrix gets denser but the coarse-grained matrix gets looser. It should be noted that, for this range of fine content, the coarse-grained matrix is still denser than the fine-grained matrix. One would expect that there exists an intermediate configuration where all the fine particles fill fully voids between coarse particles without separating them; however, this is not the case. As shown in Figure 2.19, at $f_c = 20\%$, fine particles begin to separate coarse ones but the interfine void ratio e_f is still very large. This means that intercoarse voids are not fully filled yet by the fine particles. It is interesting to note that, at the optimal fine content of 32% where the global void ratio e reaches its minimum value, the interfine void ratio e_f is equal to the intergranular one e_c. For the range (iii) with $32\% \leq f_c < 60\%$, the coarse particles are greatly separated by the fine ones and the coarse-grained matrix gets looser than the fine-grained matrix. When $f_c \geq 60\%$ (range (iv)) the intergranular void ratio e_c is very large compared to the interfine void ratio e_f which remains more or less

constant. This means that, for this range of fine content, the coarse particles are strongly dispersed by the fine ones.

It has been shown above that fine content affects greatly the void ratios of binary mixtures. By increasing fine content while keeping the same compaction procedure, the internal state of binary mixtures varies from a state where the coarse-grained matrix is much denser than the fine-grained matrix to a state where the fine-grained matrix becomes much denser than the coarse-grained matrix. When the void ratios of these two matrices are equal, the global void ratio is minimum. The variation of the internal state of binary mixtures with fine content leads to a variation of their mechanical behavior. In the next section, we will show how fine content affects the mechanical behavior of gap-graded soils.

2.5.2 Mechanical behavior

To study the mechanical behavior of gap-graded soils, we simulate triaxial compression tests on numerical binary mixtures presented in Section 2.4.2. The procedure to perform a triaxial compression test was described in Section 2.3.3. During triaxial tests, a strain rate $\dot{\varepsilon}_1 = 0.01$ s^{-1} is prescribed in the major principal stress direction 1, while the lateral stresses σ_2 and σ_3 are kept equal to 100 kPa. Two series of tests are performed: the initial relative densities D_r which are defined in Equation (1.3) are controlled to be equal to 0, 100% and 50% in the first series, while the initial intergranular void ratio e_c is controlled to be equal more or less to 0.74. In the following, we present first the results obtained for the first series of tests and then for the second series of tests.

2.5.2.1 Initial relative densities D_r controlled

The loosest and densest samples with different fine contents, whose void ratios e, e_c and e_f were analyzed in Section 2.5.1, correspond to relative densities D_r of 0 and 100%. Samples with an intermediate relative density D_r of 50% are also simulated. The samples with $f_c \leq 40\%$ are loaded until 15% of the axial strain ε_1 which is the value recommended by the ASTM standard (ASTM D4767-88, 1988) to achieve the critical state. For the samples with $f_c > 40\%$, the triaxial tests are conducted until about 10% of the axial strain due to a very long computation time for these samples.

a) $D_r = 0\%$

Figure 2.20 shows the stress ratio q/p and the volumetric strain ε_{v} versus the axial strain ε_{11} for the simulated loosest samples. The global void ratio e, the intergranular void ratio e_c and the interfine void ratio e_f, the maximum stress ratio $(q/p)_{\max}$ and the residual stress ratio $(q/p)_{\mathrm{residual}}$ at the critical state of these samples are shown in Table 2.4. Two opposite tendencies can be observed when fine content f_c increases. Indeed, an addition of fine particles weaken gap-graded materials for $f_c \leq 15\%$ but strengthen them when $f_c > 15\%$. The sample with $f_c = 15\%$ is weaker than the sample with $f_c = 0$, while the sample with $f_c = 30\%$ is much stronger than the sample with $f_c = 0$. Therefore, fine content $f_c = 15\%$ can be considered as a threshold fine content, under which gap-graded samples get weaker with an increase in fine content, but above which they get stronger. Thevanayagam et al. (2002) also observed that silty sands with fine content $f_c < 25\%$ show a lower undrained shear strength than the clean sand ($f_c = 0\%$) but they are stronger than the clean sand when $f_c > 25\%$. It is interesting to note that the sample with 30% of fine content behaves like a dense granular sample although it is at the loosest state. It shows a marked peak on the stress-strain curve, a marked softening phase and a strong dilatant behavior. It has a much higher shear strength at the peak state but a lower shear strength at the critical state than the sample with no fine particle.

By looking at the variation of the void ratios e, e_c and e_f with fine content, we can explain the above results. For fine content $f_c \leq 15\%$, the fraction of fine particles is very loose so the fine particles have no

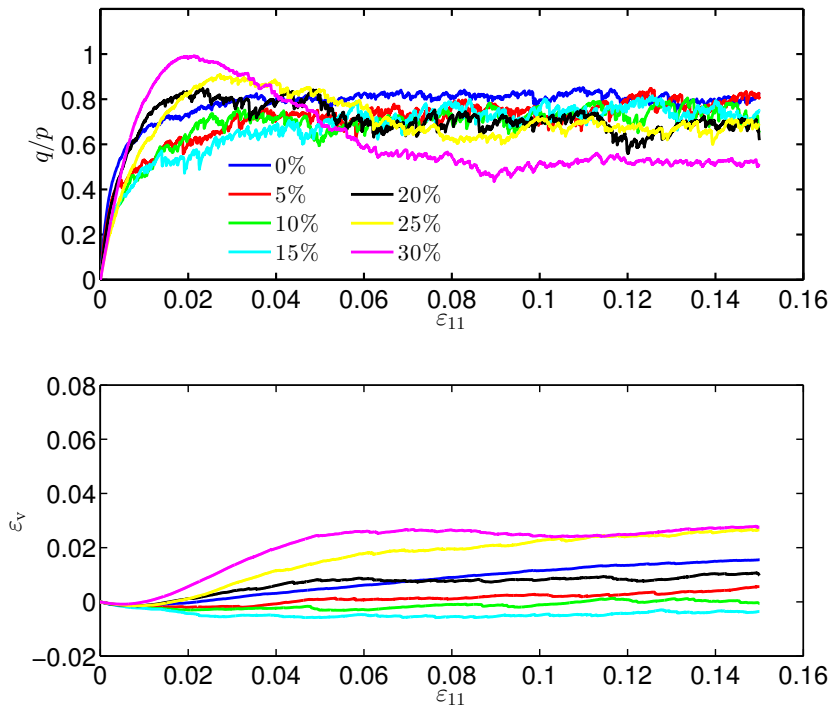

Figure 2.20: Stress ratio q/p and volumetric strain ε_v versus axial strain ε_{11} for the loose samples with different fine contents.

f_c (%)	0	5	10	15	20	25	30
e	0.69	0.67	0.60	0.53	0.44	0.36	0.34
e_c	0.69	0.76	0.77	0.78	0.79	0.81	0.91
e_f		13.3	5.9	3.5	2.1	1.5	1.1
$(q/p)_{\max}$	0.8	0.9	0.8	0.8	0.8	0.9	1
$(q/p)_{\text{residual}}$	0.8	0.8	0.7	0.8	0.6	0.7	0.5

Table 2.4: Global void ratio e, the intergranular void ratio e_c, the interfine void ratio e_f, maximum and residual stress ratios $(q/p)_{\max}$ and $(q/p)_{\text{residual}}$ for the loosest samples with fine content f_c varied from 0% to 30%

significant role in the binary mixtures, while the fraction of coarse particles becomes looser as fine content is increased because coarse particles are separated by fine ones. As a result, their shear strength decreases with an increase in fine content. When fine content $f_c > 15\%$, the fine particles are sufficiently close to each other and close to the coarse particles. Therefore, they reinforce the coarse particles and participate in carrying the shear stress.

b) $D_r = 100\%$

Figure 2.21 shows the stress ratio q/p and the volumetric strain ε_{v} versus the axial strain ε_{11} for the densest samples with fine content f_c varied from 0% to 100%. For the samples with $f_c \leq 40\%$, we perform triaxial tests until 15% of the axial strain. Due to a high computation cost, the triaxial tests for the samples with $f_c > 40\%$ are conducted until 10% of the axial strain. It should be noted that the critical state has not been achieved yet for the last tests so the residual stress ratio q/p could not be determined for the samples with $f_c > 40\%$. Table 2.5 shows the void ratios e, e_c, e_f, the maximum stress ratio $(q/p)_{\max}$ and the residual stress ratio $(q/p)_{\mathrm{residual}}$ at the critical state for these samples.

Figure 2.21(a) shows that the stress-strain behavior of the samples with $f_c < 20\%$ is not significantly affected by fine content. Unlike the loose samples, the dense samples with $f_c = 5\%$, 10% and 15% have a slightly higher shear resistance than the sample with $f_c = 0\%$. Starting from $f_c = 20\%$, fine content has opposite effects on the shear strength and dilatancy of the binary mixtures. The shear strength at the peak state and the dilatancy increase with fine content $f_c \leq 32\%$ (Figure 2.21(b)) but decrease when $f_c > 32\%$ (Figure 2.21(c)). It is interesting to note that the threshold fine content of 32% found here is also the threshold value observed in Figure 2.19(a) at which the intergranular and interfine void ratios e_c and e_f are equal and the global void ratio e is minimum. The same tendency is observed for the material dilatancy except that the threshold fine content for it is about 35%, which is also quite close to the value of 32% observed for the maximum shear strength. It can be seen in Figure 2.21(d) that the stress-strain behavior of granular mixtures is not affected by fine content $f_c \geq 60\%$.

Table 2.5: Global void ratio e, the intergranular void ratio e_c, the interfine void ratio e_f, maximum and residual stress ratios $(q/p)_{\max}$ and $(q/p)_{\mathrm{residual}}$ for the dense samples with fine content f_c from 0% to 100%.

f_c (%)	0	5	10	15	20	25	30	32	35	40	50	60	70	80	90	100
e	0.6	0.54	0.46	0.4	0.33	0.29	0.28	0.28	0.30	0.32	0.35	0.39	0.43	0.47	0.51	0.57
e_c	0.6	0.62	0.63	0.64	0.66	0.72	0.83	0.89	1.0	1.2	1.7	2.5	3.8	6.3	13.3	
e_f		11.5	4.6	2.8	2.6	1.6	0.95	0.90	0.85	0.79	0.71	0.65	0.62	0.59	0.57	0.57
$(q/p)_{\max}$	1.2	1.1	1.2	1.2	1.3	1.5	1.6	1.6	1.5	1.4	1.4	1.3	1.3	1.2	1.2	1.2
$(q/p)_{\mathrm{residual}}$	0.8	0.8	0.9	0.7	0.8	0.7	0.5	0.5	0.4	0.6						

The above result means that a reasonable fine content ($20\% \leq f_c \leq 32\%$) can make granular materials stronger and more dilatant. This is in good agreement with the experimental results of Salgado et al. (2000) who performed drained triaxial tests on mixtures of clean Ottawa sand and silt. However, in this study, the role of fine particles was clearly observed even at a low fine content ($f_c \leq 15\%$). This might be explained by the fact that the sand-silt mixtures considered in their study have continuous and broadly graded PSDs, for which fine particles might fill the void space between coarse particles even at low fine content. Figure 2.21(b) also shows that a too high fine content ($f_c > 32\%$) can be a factor unfavorable to the shear strength and dilatancy of granular mixtures. The mixture with $f_c = 40\%$ has indeed a lower shear strength and a lower dilatancy than the mixture with $f_c = 30\%$.

A dense granular sample exhibits a peak on the stress-strain curve, followed by a marked softening phase. This kind of behavior can be observed for the mixtures with $f_c \geq 20\%$. It is interesting to note in Figures 2.21(b) and (c) that the fine particles, on one hand, strengthen granular mixtures at the peak state, but on the other hand, weaken them at the critical state. Indeed, the stress ratio q/p for $f_c = 30\%$

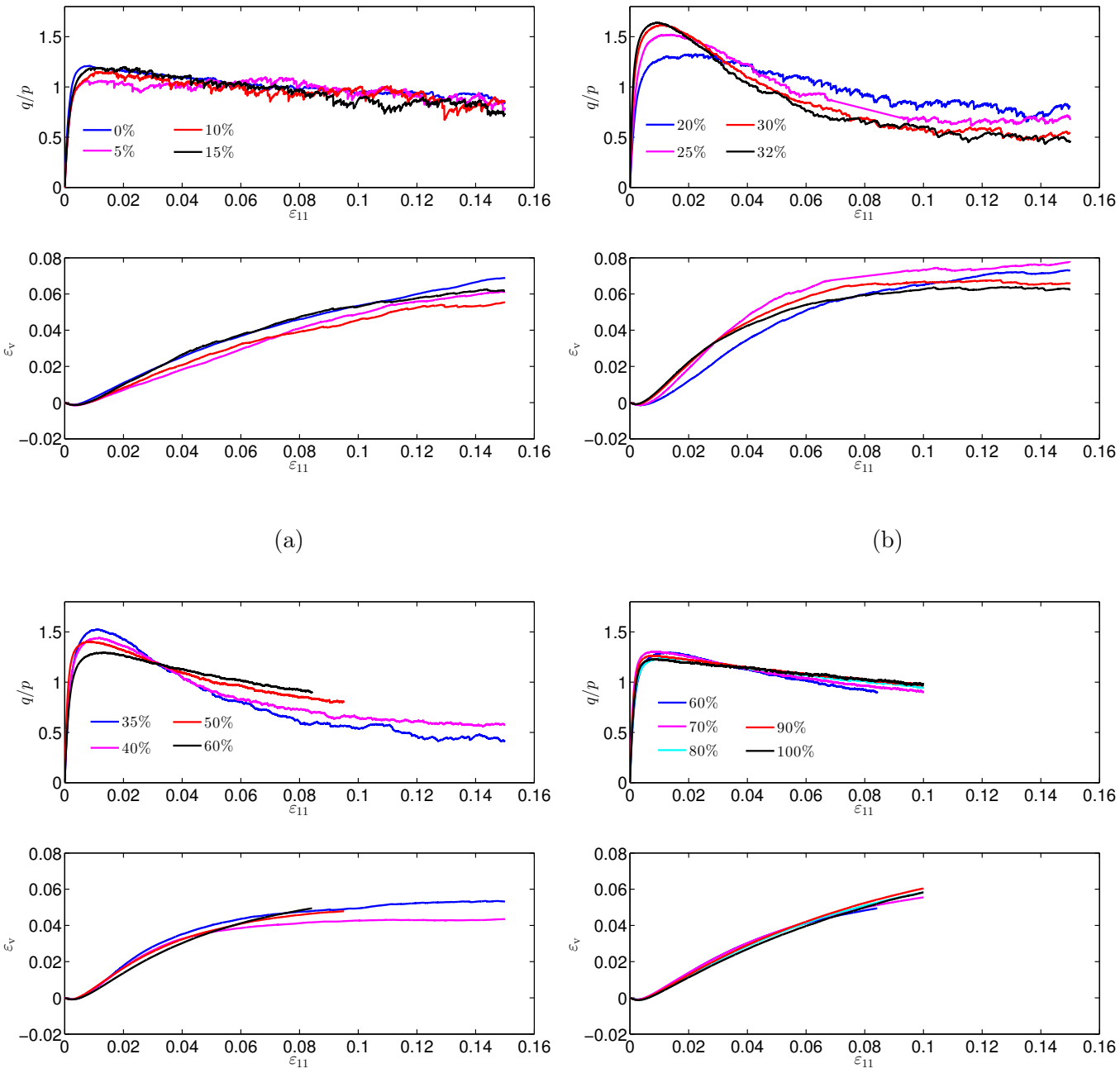

Figure 2.21: Stress ratio q/p and volumetric strain ε_{v} versus axial strain ε_{11} for the densest samples: (a) $0\% \leq f_c \leq 15\%$, (b) $20\% \leq f_c \leq 32\%$, (c) $35\% \leq f_c \leq 60\%$ and (d) $60\% \leq f_c \leq 100\%$.

is 0.5 at the critical state, much lower than the value of 1.6 at the peak state.

It can be concluded that, for the dense binary mixtures, the presence of fine particles has (i) no significant effect on the shear strength for fine content $f_c < 20\%$, (ii) a positive effect for fine content $20\% \leq f_c \leq 32\%$ but (iii) a negative effect for fine content $32\% < f_c \leq 60\%$, and (iv) no significant effect for fine content $f_c > 60\%$. One could try to explain the above result by using the dependency of the void ratios e, e_c and e_f upon fine content f_c shown in Figure 2.19. The negligible effect of the fine particles on the stress-strain behavior observed for the mixtures with $f_c < 20\%$ is related to the fact that the fine-grained matrix is very loose (range (i) in Figure 2.19) so the fine particles do not participate actively in supporting the external loading. When $f_c > 60\%$ (range (iv) in Figure 2.19), the shear strength remains more or less constant with an increase in fine content since the coarse particles are strongly dispersed by the fine ones and the mechanical behavior of the mixtures for this range of fine content is mainly governed by the fraction of fine particles. However, it is not easy to explain why the shear strength and the dilatancy increase with fine content when $f_c < 32\%$ but decrease when $f_c > 32\%$, and why a mixture with a significant fine content shows a marked softening phase. It should be noted that adding fine particles into a mixture leads to two opposing effects: on one hand, the coarse-grained matrix gets looser, which weakens the mixture, but on the other hand, the fine-grained matrix gets denser, which strengthens the mixture. It is not well understood yet which effect is more important than the other for a given fine content.

c) $D_r = 50\%$

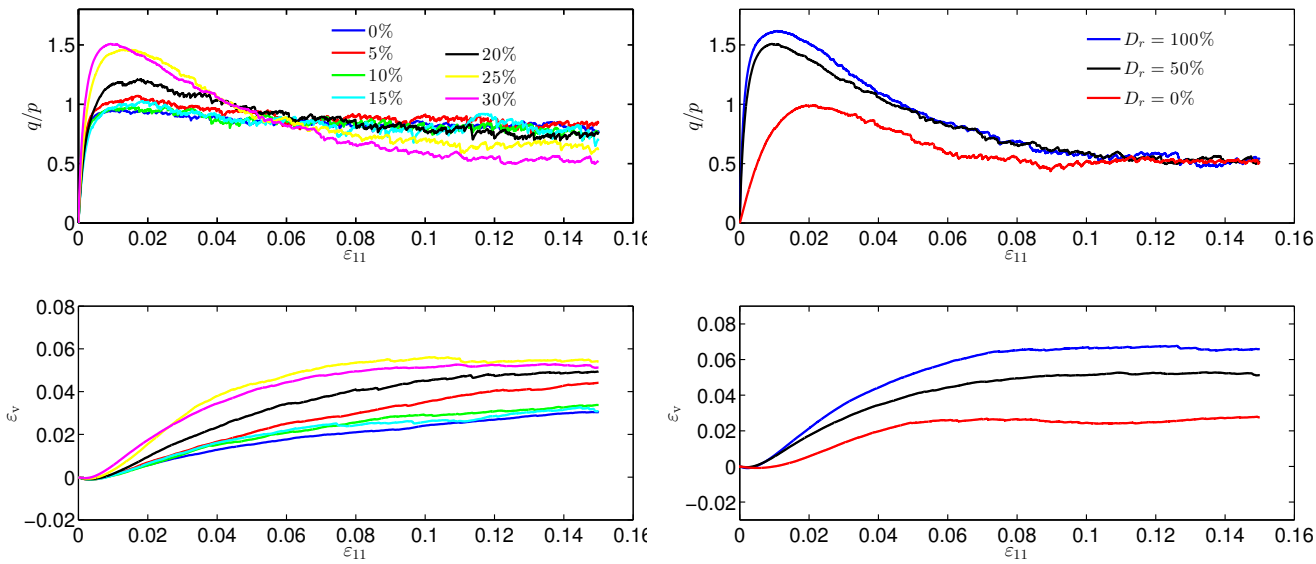

(a) (b)

Figure 2.22: Stress ratio q/p and volumetric strain ε_v versus axial strain ε_1 (a) for the samples of $D_r = 50\%$ with fine content f_c varied from 0 to 30% and (b) for the sample of $f_c = 30\%$ with $D_r = 0$, 50% and 100%.

Triaxial tests are also performed on the binary mixtures with fine content between 0 and 30% for which the initial relative density D_r is controlled to be more or less equal to 50%. Figure 2.22(a) shows the stress-strain behavior of these samples. It can be seen that the effect of fine content observed in this case is similar to that observed for the densest samples. Figure 2.22(b) shows the behavior of the sample

with 30% of fine content at three relative densities $D_r = 0$, 50% and 100%. It is shown that the behavior of this sample at $D_r = 50\%$ is very different from that at $D_r = 0\%$ but quite close to that at $D_r = 100\%$.

Table 2.6: Global void ratio e, the intergranular void ratio e_c, the interfine void ratio e_f, maximum and residual stress ratios $(q/p)_{\max}$ and $(q/p)_{\text{residual}}$ for the samples of $D_r = 50\%$ with fine content f_c varied from 0% to 30%.

f_c (%)	0	5	10	15	20	25	30
e	0.74	0.66	0.56	0.48	0.40	0.31	0.28
e_c	0.74	0.74	0.74	0.74	0.74	0.74	0.83
e_f		13.1	2.6	3.2	2.0	1.2	0.95
$(q/p)_{\max}$	0.75	0.82	0.86	0.91	1.2	1.56	1.6
$(q/p)_{\text{residual}}$	0.75	0.82	0.74	0.83	0.76	0.68	0.5

In order to compare the mechanical behavior of gap-graded samples at different values of relative density D_r, Figure 2.23 presents the maximum stress ratio $(q/p)_{\max}$ versus fine content at different values of D_r. This figure shows that, for low values of fine content ($f_c < 20\%$), the maximum stress ratio for the three relative densities $D_r = 0$, 50% and 100% are very different and the values of the maximum stress ratio for $D_r = 50\%$ are intermediary between the values of $D_r = 0\%$ and $D_r = 100\%$. But it can be seen that, for high values of fine content ($f_c \geq 20\%$), the maximum stress ratios for $D_r = 50\%$ become quite close to that at $D_r = 100\%$.

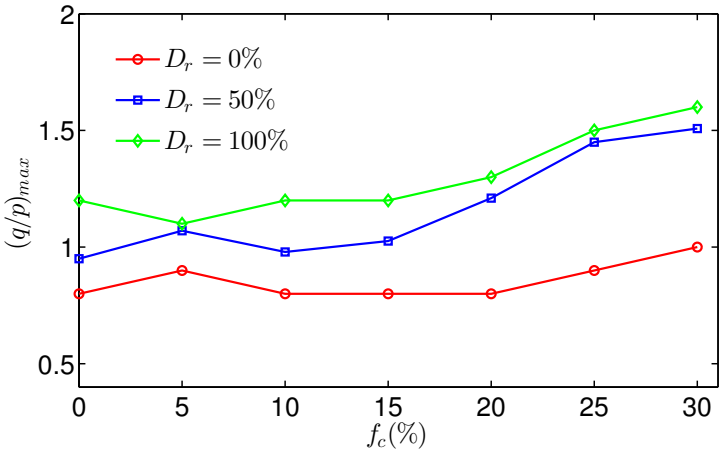

Figure 2.23: Maximum stress ratio $(q/p)_{\max}$ versus fine content for different value of relative density D_r.

2.5.2.2 Intergranular void ratio e_c controlled

As shown above, the intergranular void ratio e_c increases, while the interfine void ratio e_f decreases with an increase in fine content if the same compaction procedure is used for all the samples. In this case, the fine particles discard the coarse ones and then weaken the solid skeleton constituted of coarse particles. A question that arises here is how fine content affects the stress-strain behavior of binary mixtures if their fraction of coarse particles remains more or less undisturbed by the fine particles. To answer to

this question, we control the intergranular void ratio e_c of the binary mixtures with $0 \leq f_c \leq 30\%$ to be more or less equal to 0.74. This can be done by decreasing the intergranular friction angle φ when fine content is increased to better compact the fraction of coarse particles. As shown in Table 2.6, a constant value of e_c equal to 0.74 can be achieved for the samples with $f_c < 25\%$. However, despite the effort made to compact the sample with $f_c = 30\%$, e_c for this sample is larger than the target value since the coarse particles are strongly separated by the fine ones and it is very hard to reduce further the intergranular void ratio e_c. Thevanayagam et al. (2002) controlled the intergranular void ratio e_c of mixed soils in their experimental study of the effect of fine content on the undrained shear strength. The authors encountered also difficulties to obtain a constant value of e_c for all fine contents.

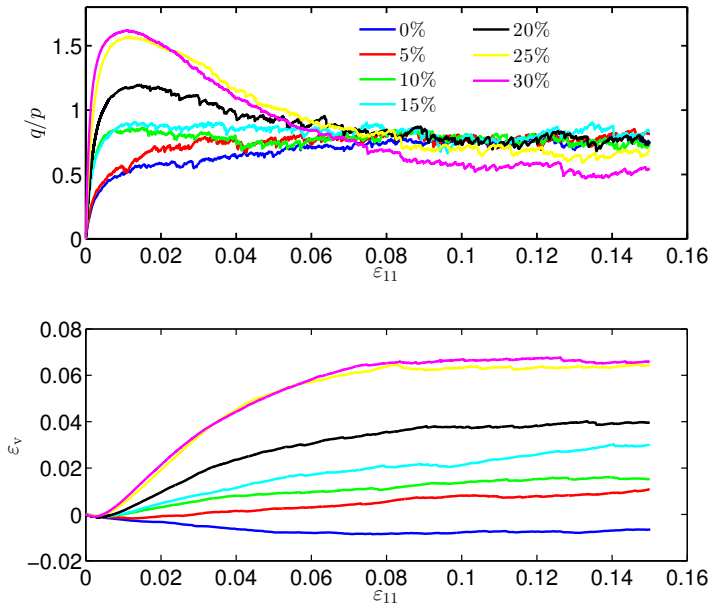

Figure 2.24: Stress ratio q/p and volumetric strain ε_v versus axial strain ε_{11} for f_c varied between 0 and 30%. For these samples, the intergranular void ratio e_c is controlled to be more or less equal to 0.74.

As can be seen in Figure 2.24, the effect of fine content on the mechanical behavior of the binary mixtures considered in this case is clearly observed even at low fine contents. These binary mixtures get stronger and more dilatant when fine particles are added between the coarse particles. In this case, the fine particles reinforce greatly the solid skeleton constituted of coarse particles, which remains more or less undisturbed. Thevanayagam et al. (2002) also showed that the undrained shear strength of silty sands increases with an increase in fine content when their intergranular void ratios are controlled to be more or less the same.

2.6 Conclusions

This chapter presented numerical simulations of the mechanical behavior of gap-graded granular soils by using the DEM based on the molecular dynamic approach. As a great number of particles is needed to simulate gap-graded soils, spherical particles are considered to keep the computation time reasonable.

Gap-graded granular samples with a gap ratio of 3 and fine content varied between 0 and 100% are simulated. A study on the representative elementary volume (REV) of the simulated samples was pre-

sented to determine the sample size to guarantee the conditions required for the REV. With the chosen sample sizes $L/D_{\max} > 7.0$, the REV conditions are achieved for the simulated mixtures with fine content $f_c \leq 60\%$. For fine content $f_c > 60\%$, the sample size $L/D_{\max}$ is reduced to keep the computational time reasonable. For this range of fine content, the mechanical behavior of the binary mixtures is mainly governed by the fraction of fine particles. Consequently, the binary mixtures for $f_c > 60\%$ could be expected to be the REVs.

Based on variations of the global void ratio e, of the intergranular void ratio e_c and of the interfine void ratio e_f with fine content f_c, four ranges of fine content f_c were observed. For the range (i) with $f_c < 20\%$, the fine particles are very loose and do not disturb the coarse particles. The fine particles separate the coarse ones and get denser for the range (ii) with $20\% < f_c \leq 32\%$. For this range of fine content, the coarse fraction is denser than the fine fraction. For the range (iii) with $32\% < f_c \leq 60\%$, the fine particles separate strongly the coarse ones and they become denser than the coarse ones. The coarse particles are fully dispersed by the fine particles for the range (iv) of fine content with $f_c > 60\%$.

Two series of triaxial compression tests were performed on gap-graded samples. In the first series, the relative density D_r of the tested samples was controlled to be equal to 0 (loosest state), 50% (intermediate state) and 100% (densest state). In the second series, the intergranular void ratio e_c was controlled to be almost the same for all the tested samples. For the first series of tests, on the whole, fine content in the range (i) does not have a significant effect on the stress-strain behavior of gap-graded samples. The dilatancy and the shear strength increase with an increase in fine content in the range (ii), but decrease with an increase in fine content in the range (iii). For the range (iv) of fine content, the stress-strain behavior of gap-graded samples is almost independent of fine content. For the second series of tests, the effect of fine content is visible even at low fine content: the shear strength and dilatancy increase clearly with an increase in fine content.

Chapter 3

Micro-mechanical behavior of gap-graded granular soils

3.1 Introduction

The literature review presented in Section 1.3 showed that the fine particles play an important role in the mechanical behavior of widely graded soils: they strength or weaken these materials depending on their fine content, on their density, etc. The numerical simulations presented in Section 2.5 confirmed this statement. To explain this result from a micro-mechanical point of view, Thevanayagam et al. (2002) made a conjecture that, with an increase in fine content, the micro-structure of granular mixtures can change from a category where contacts between coarse grains are dominant to a category where contacts between fine grains are dominant. This conjecture should be verified by investigating experimentally the granular micro-structure. Such an investigation might be performed by using X-ray tomography imaging technology (Kim et al., 2012), however, this technique is quite delicate and expensive. To the best of our knowledge, no experimental investigation of the effect of fine content on the granular micro-structure has been performed so far.

One of the main advantages of the DEM is that any local information at the particle scale can be accessed, which makes the DEM very suitable for investigating granular media from a micro-mechanical point of view. This method has been recently used by some authors to investigate the micro-structure and the micro-mechanical behavior of granular mixtures. Minh et al. (2014); Minh and Cheng (2016) studied the contact force distribution and the force networks in granular mixtures under one-dimensional compression. Shire and O'Sullivan (2013); Shire et al. (2016) investigated the micro-structure and micro-properties of granular mixtures under isotropic compression. It is worth mentioning that a granular material subjected to a one-dimensional or an isotropic compression shows only a contractive behavior and never reaches the failure. Voivret et al. (2009) studied the shear behavior and force transmission in highly polydisperse 2D granular materials composed of disks by simulating direct simple shear tests. Surprisingly, the authors found that the shear strength is almost independent of the particle size polydispersity although the solid fraction increases with the latter parameter. As the polydispersity increases, more and more large particles but less and less small particles are included in strong force chains which sustain primarily the shear stress. Dai et al. (2015) also found in their simulations of undrained biaxial tests that fine particles leave the solid skeleton as fine content increases, resulting in a decrease in undrained shear strength. It is noteworthy that these findings at the micro-scale cannot explain why the drained shear strength increases with fine content as reported by several authors mentioned previously. Aboul-Hosn (2017) simulated triaxial tests on 3D granular mixtures with fine content from 5% to 15% and found a slight increase of the shear strength with fine content. At the micro-scale, the author observed that more coarse-fine contacts and fine-fine contacts are created with increasing fine content to support the shear stress. These preliminary results need to be

completed with higher fine contents and with a profound micro-mechanical investigation to shed light on the role of fine particles in sustaining the shear loading.

In this chapter, we present a numerical study of the effect of fine content on the micro-mechanical behavior of granular mixtures during triaxial compression tests. The micro-mechanical investigation focuses on (i) the role of fine particles in the granular micro-structure (Section 3.2), (ii) the stress transmission through the contact network and the force networks in a granular mixture (Sections 3.3 and 3.4), and (iii) the contribution of the fine particles in carrying the overburden stress (Section 3.5). Based on this study, a classification of binary mixtures in terms of their micro-structure is proposed in Section 3.6.

3.2 Micro-structure

3.2.1 Coordination numbers

Coordination number, denoted by $\mathcal{N}$, is defined as the average number of contacts per particle. It is usually used to describe the density of a granular assembly at the micro-scale. However, this definition of the coordination number is not appropriate for a mixture of coarse and fine particles because the number of contacts per coarse particle is very different from that per fine particle. As mentioned previously, a binary granular mixture can be thought of being a multi-phase medium which is composed of the coarse-grained matrix, the fine grained matrix and the interface between them. The interaction between particles in each phase occurs through $C-C$ contacts (between two coarse particles), $F-F$ contacts (between two fine particles), respectively; and these two phases interact each other through $C-F$ contacts (between a coarse and a fine particle). Describing the local density of the coarse-grained and fine-grained matrices and the interface between them needs thus three coordination numbers, denoted by $\mathcal{N}_C^{C-C}$, $\mathcal{N}_F^{F-F}$ and $\mathcal{N}_C^{C-F}$, which are defined as the respective average numbers of $C-C$ contacts per coarse particle, of $F-F$ contacts per fine particle, and of $C-F$ contacts per coarse particle:

$$\mathcal{N}_C^{C-C} = \frac{2N_c^{C-C}}{N_p^C}, \quad \mathcal{N}_C^{C-F} = \frac{2N_c^{C-F}}{N_p^C}, \quad \text{and} \quad \mathcal{N}_F^{F-F} = \frac{2N_c^{F-F}}{N_p^F}, \tag{3.1}$$

where N_c^{C-C}, N_c^{C-F} and N_c^{F-F} are respective numbers of $C-C$, $C-F$ and $F-F$ contacts; and N_p^C and N_p^F are respective numbers of coarse and fine particles. Minh and Cheng (2013), Shire et al. (2014a) and Shire et al. (2016) also defined similar coordination numbers to study the micro-structure of granular mixtures.

Figure 3.1 presents the evolution of the three coordination numbers $\mathcal{N}_C^{C-C}$, $\mathcal{N}_C^{C-F}$ and $\mathcal{N}_F^{F-F}$ during triaxial compression test for three dense mixtures with $f_c = 20\%$, 30% and 40%. It can be seen that these three coordination numbers decrease during the shear loading. This is due to the fact that when a dense sample is sheared, it dilates to resist the shearing and this dilatant behavior leads to a loss of contacts between particles. This loss of contacts during shearing is responsible for the softening phase on the stress-strain curve after the peak stated as observed in Figure 2.21. For $f_c = 30\%$, high values of $\mathcal{N}_C^{C-F}$ and $\mathcal{N}_F^{F-F}$ at the initial state, mean that the fraction of fine particles in this mixture is initially dense. Moreover, the strongest decrease in $\mathcal{N}_C^{C-C}$ and $\mathcal{N}_C^{C-F}$ during the shear loading is observed for this mixture: $\mathcal{N}_C^{C-C}$ and $\mathcal{N}_C^{C-F}$ decrease from 3.8 and 44.9 at the initial state to 1.8 and 9.1 at the critical state, respectively. This drastic drop in these coordination numbers is in good agreement with the strongest dilatancy observed for the mixture with $f_c = 30\%$ (Figure 2.21(b)). This means that the micro-structure of this mixture is strongly altered after the peak state, which explains why it exhibits a marked softening phase as shown in Figure 2.21(b).

Starting with the dense samples presented in Section 2.5 having $D_r = 100\%$, Figures 3.2(a), (b) and (c) show the respective coordination numbers $\mathcal{N}_C^{C-C}$, $\mathcal{N}_C^{C-F}$ and $\mathcal{N}_F^{F-F}$ versus fine content f_c at the

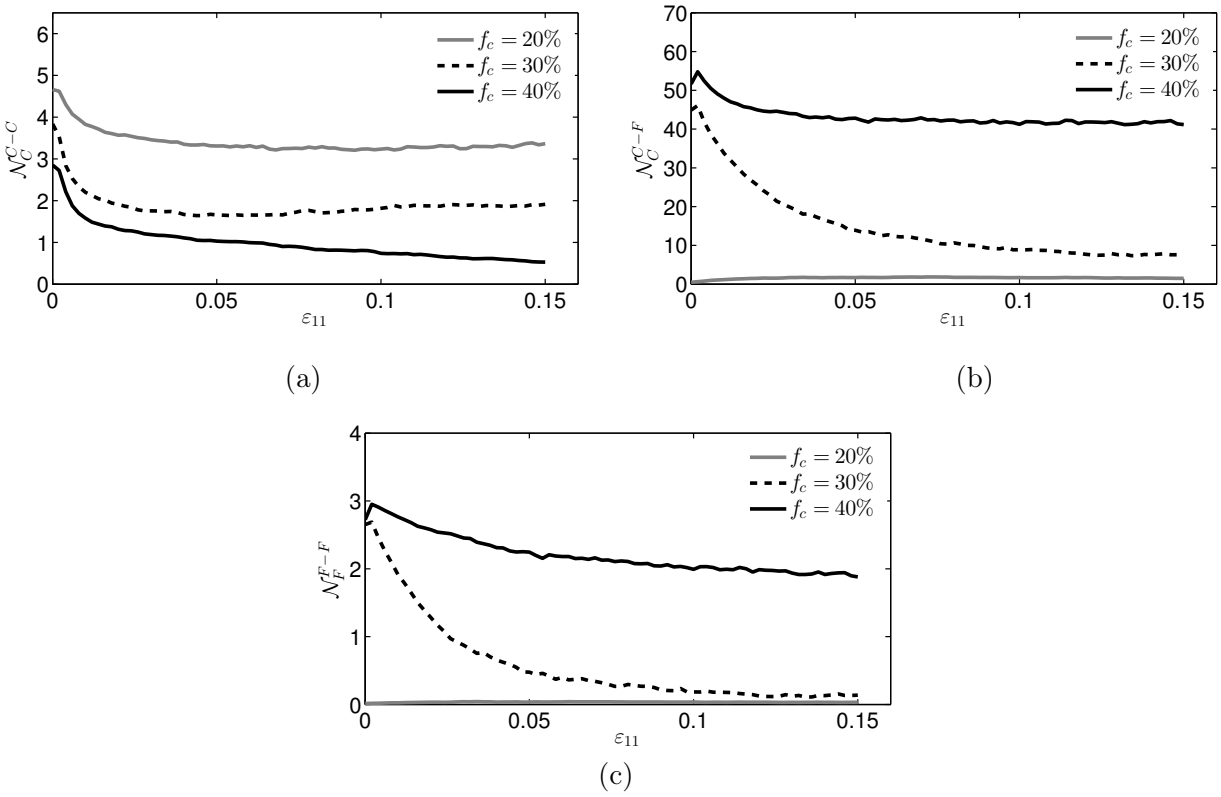

Figure 3.1: Coordination numbers (a) $\mathcal{N}_C^{C-C}$, (b) $\mathcal{N}_C^{C-F}$ and (c) $\mathcal{N}_F^{F-F}$ versus axial strain ε_{11} for $f_c =$ 20%, 30% and 40%.

initial, peak and critical states. It is clear that the average number of contacts per coarse particle is much bigger than that per fine particle. At the initial state, the coordination number $\mathcal{N}_C^{C-C}$ remains more or less constant and the coordination numbers $\mathcal{N}_F^{F-F}$ and $\mathcal{N}_C^{C-F}$ are very small for $f_c < 20\%$. This confirms the statement made in Section 2.5.1 that the fine particles are almost floating within voids between coarse ones and they do not modify the granular skeleton which is mainly constituted of coarse particles. Starting from 20% of fine content, a further addition of fine particles leads, on the whole, to a strong increase in $\mathcal{N}_C^{C-F}$ and $\mathcal{N}_F^{F-F}$, particularly for $\mathcal{N}_C^{C-F}$, but to a remarkable decrease in $\mathcal{N}_C^{C-C}$. This means that the presence of an important fine content in a granular material induces two opposing effects. Fine particles disrupt contacts between coarse ones so they weaken the coarse fraction. On the other hand, a significant quantity of fine particles around each coarse particle reinforce the interface between the coarse-grained and fine-grained matrices. Furthermore, more contacts between fine particles are created, allowing the shear stress to be transmitted through the fine-grained matrix as will be shown in the next section. Shire et al. (2014a) also observed a decrease in number of contacts par coarse particle and an increase in number of contacts per fine particle with increasing fine content for granular mixtures with bigger values of the gap ratio G_r. The best shear strength at the peak state for $f_c = 30\%$ shown in Figure 2.21(b) can be attributed to the fact that the coarse particles are strongly reinforced by an important number of fine particles around them (about 50 fine particles, on average), despite the fact that they are slightly weakened by a loss of contacts between them.

When $f_c > 60\%$, the coordination number $\mathcal{N}_C^{C-C}$ becomes very small, while the coordination numbers $\mathcal{N}_C^{C-F}$ and $\mathcal{N}_F^{F-F}$ become very high: $\mathcal{N}_C^{C-F}$ can reach of a value of 100, meaning that there are, on average, 100 fine particles in contact with each coarse particle which will be verified in the next section using analytical estimation. The coarse particles are strongly dispersed by the fine particles which constitute a

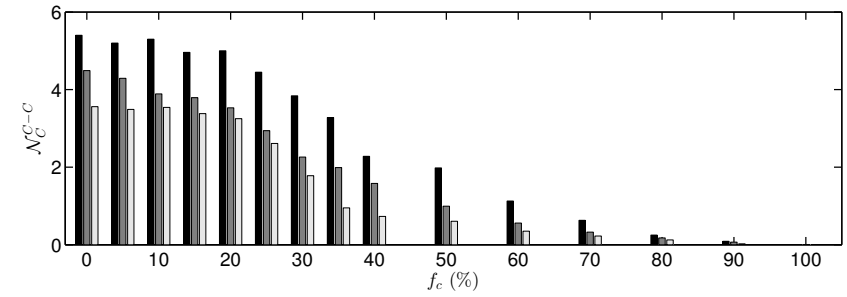

(a)

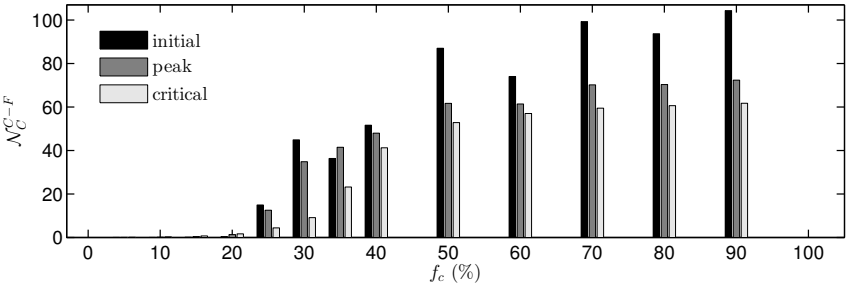

(b)

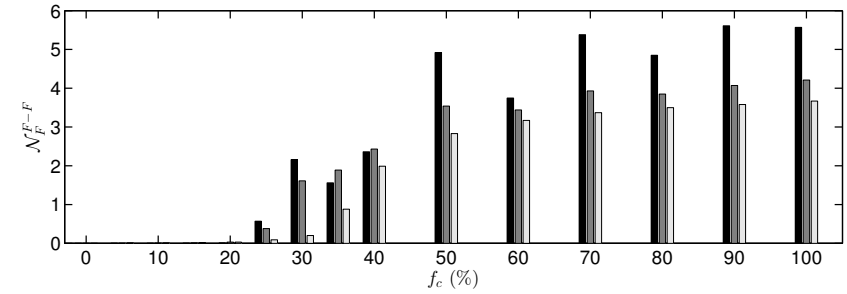

(c)

Figure 3.2: Coordination numbers (a) $\mathcal{N}_C^{C-C}$, (b) $\mathcal{N}_C^{C-F}$ and (c) $\mathcal{N}_F^{F-F}$ versus fine content f_c at the initial, peak and critical states for dense samples.

dense packing for this range of fine content. This result in terms of coordination numbers is in good agreement with the result in terms of intergranular and interfine void ratios observed for the range (iv) of fine content in Figure 2.19, for which the intergranular void ratio e_c becomes much larger than the interfine void ratio e_f. In this case, the solid skeleton is mainly constituted of fine particles. Moreover, values more or less constant of $\mathcal{N}_C^{C-F}$ and $\mathcal{N}_F^{F-F}$ indicate that the solid skeleton remains more or less constant with an increase in fine content. This explains why the stress-strain behavior of the binary mixtures with $f_c > 60\%$ is not significantly affected by fine content as shown in Figure 2.21(d). It should be noted that, in this study, the fine and the coarse particles are instantaneously generated, which means that the coarse particles are not fixed. With the addition of fine particles, the coarse particles can be separated from each other, for that, we can see that the three coordination numbers and specially $\mathcal{N}_C^{C-C}$ are variable with respect to fine content f_c. But with another generation mode of samples, for example, if the coarse particles are firstly generated and they are fixed, then after that the fine particles are added, in this case the coordination number $\mathcal{N}_C^{C-C}$ will not vary with respect to fine content f_c. So we can say that the variations of coordinations numbers with respect the fine content depend on the generation mode of the samples.

The coordination number $\mathcal{N}_C^{C-F}$ reached a high value of 100, which means that there exist about 100 fine particles in contact with each coarse particle. To verify this large number of fine particles, an analytical estimation which is presented in 2D in Figure 3.3, will be used. The solid angle ω is equal to the area of the fine particle divided by diameter of coarse particle plus the diameter of fine particle ($\omega = s/(D+d)^2$). If we have an hexagonal arrangement, in this case the number of fine particles in contact with one coarse particle is maximum and the solid angle ω = 0.91x4xπxN, where N represents the number of fine particles in contact with one coarse particle. Using the two previous equations, N is found to be equal to 0.91x4x$(D+d^2)/d^2$, and for our case $D = 9$ mm (average diameter of coarse particles) and $d = 1.5$ mm (average diameter of fine particles), by calculation, N = 178 fine particles. So for the densest numerical samples with high fine content, $\mathcal{N}_C^{C-F} = 100$ can be an acceptable value.

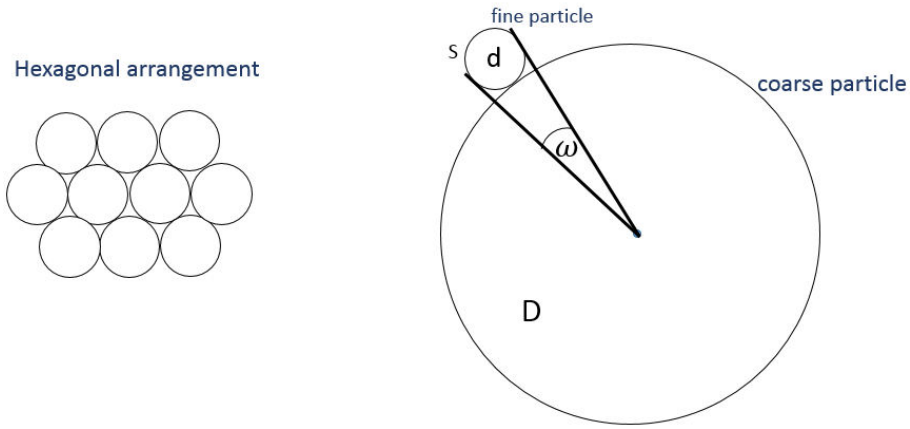

Figure 3.3: Analytical interpretation of the big number of fine particles in contact with one coarse particle.

For the loose samples having $D_r = 0\%$, Figures 3.4(a), (b) and (c) show the respective coordination numbers $\mathcal{N}_C^{C-C}$, $\mathcal{N}_C^{C-F}$ and $\mathcal{N}_F^{F-F}$ versus fine content f_c at the initial, peak and critical states for $f_c \leq 30\%$. It is clear that the average number of contacts per coarse particle is much bigger than that per fine particle. At the initial state, the coordination number $\mathcal{N}_C^{C-C}$ remains more or less constant and the coordination numbers $\mathcal{N}_F^{F-F}$ and $\mathcal{N}_C^{C-F}$ are very small for $f_c < 20\%$. That means that the variations of the three coordination numbers for the loose samples are almost the same of dense samples for $f_c < 20\%$. For $f_c \geq 20\%$, a further addition of fine particles leads to a strong increase in $\mathcal{N}_C^{C-F}$ and $\mathcal{N}_F^{F-F}$, particularly for $\mathcal{N}_C^{C-F}$, but a remarkable decrease in $\mathcal{N}_C^{C-C}$. So we can see that these variations of the tree coordination numbers are almost the same of those of dense samples for $f_c \geq 20\%$. But the difference between the coordination numbers of loose samples and those of dense samples is that those of dense samples are much bigger than those of loose samples, where this variation is normal because in dense sample the particles are close to each other where a big number of contacts between the particles can be obtained. But generally, we can say that loose samples and dense samples have almost a close variation of the micro-structure with respect to fine content. Next we are going to present the micro-structure properties for only the dense samples having $D_r = 100\%$.

3.2.2 Anisotropy

Different fabric tensors have been proposed in the literature to describe the fabric of granular materials in terms of orientation of contacts (Satake, 1982). For a binary mixture composed of fine and coarse spherical particles, we use the following fabric tensor:

$$H_{ij} = \sum_k l^k n_i^k n_j^k, \tag{3.2}$$

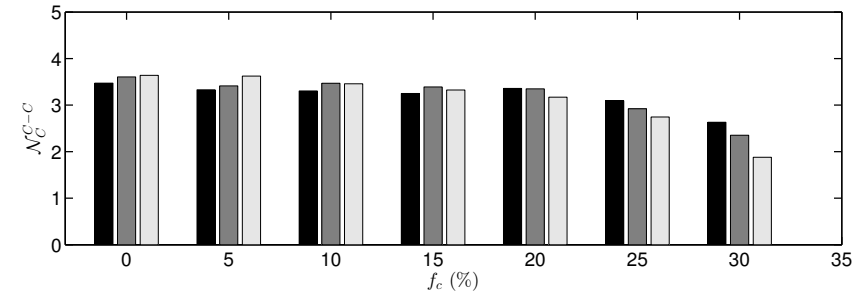

(a)

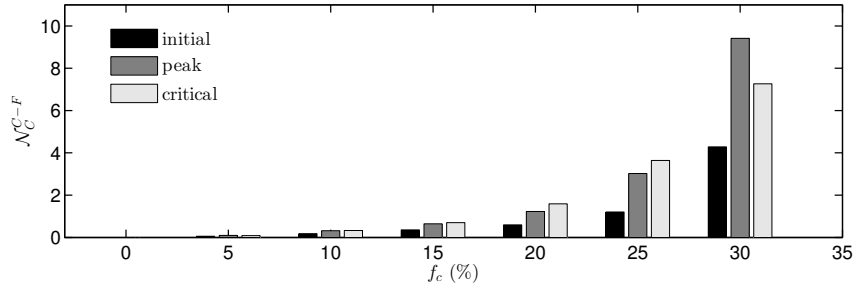

(b)

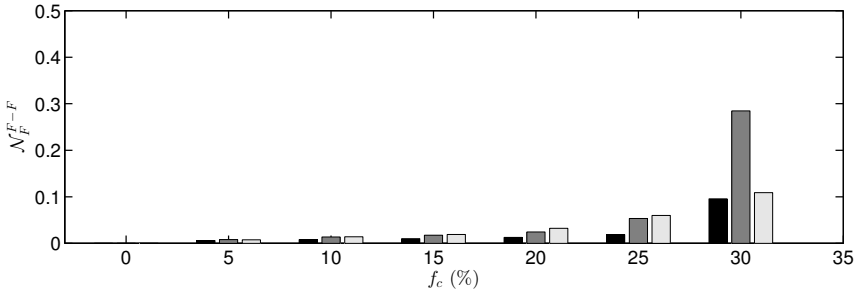

(c)

Figure 3.4: Coordination numbers (a) $\mathcal{N}_C^{C-C}$, (b) $\mathcal{N}_C^{C-F}$ and (c) $\mathcal{N}_F^{F-F}$ versus fine content f_c at the initial, peak and critical states for loose samples.

where superscript k runs over all the contacts in the volume under consideration; $\boldsymbol{n}^k$ is the unit normal vector at contact k; and l^k is the length of the branch joining the centers of two particles in contact. If the fabric tensor $\boldsymbol{H}$ is isotropic, the granular material under consideration is isotropic, i.e., the contacts are uniformly oriented. When a sample is subjected to a triaxial compression test, contacts tend to be preferentially oriented in the major principal direction of the stress (direction 1), causing the anisotropy to the sample. As a result, H_1 increases, while H_2 and H_3 are almost equal and decrease during the test. The anisotropy of the sample is quantified by the following index:

$$H_d = \frac{H_1 - H_3}{\mathrm{tr}(\boldsymbol{H})}, \quad \text{and} \quad \mathrm{tr}(\boldsymbol{H}) = \sum_k l^k. \tag{3.3}$$

The fabric tensor defined by (3.2) can split into three parts $\boldsymbol{H}^{C-C}$, $\boldsymbol{H}^{C-F}$ and $\boldsymbol{H}^{F-F}$ which are the contributions of the three respective categories of $C-C$, $C-F$ and $F-F$ contacts:

$$\boldsymbol{H} = \boldsymbol{H}^{C-C} + \boldsymbol{H}^{C-F} + \boldsymbol{H}^{F-F}. \tag{3.4}$$

For example, the part $\boldsymbol{H}^{C-C}$ relative to the $C-C$ contacts is defined as:

$$H_{ij}^{C-C} = \sum_{k \in C-C} l^k n_i^k n_j^k, \tag{3.5}$$

where superscript k runs only over the set of $C-C$ contacts. The contribution of the $C-C$ contacts to the anisotropy index H_d defined in (3.3) is $(H_1^{C-C} - H_3^{C-C})/\mathrm{tr}(\boldsymbol{H})$.

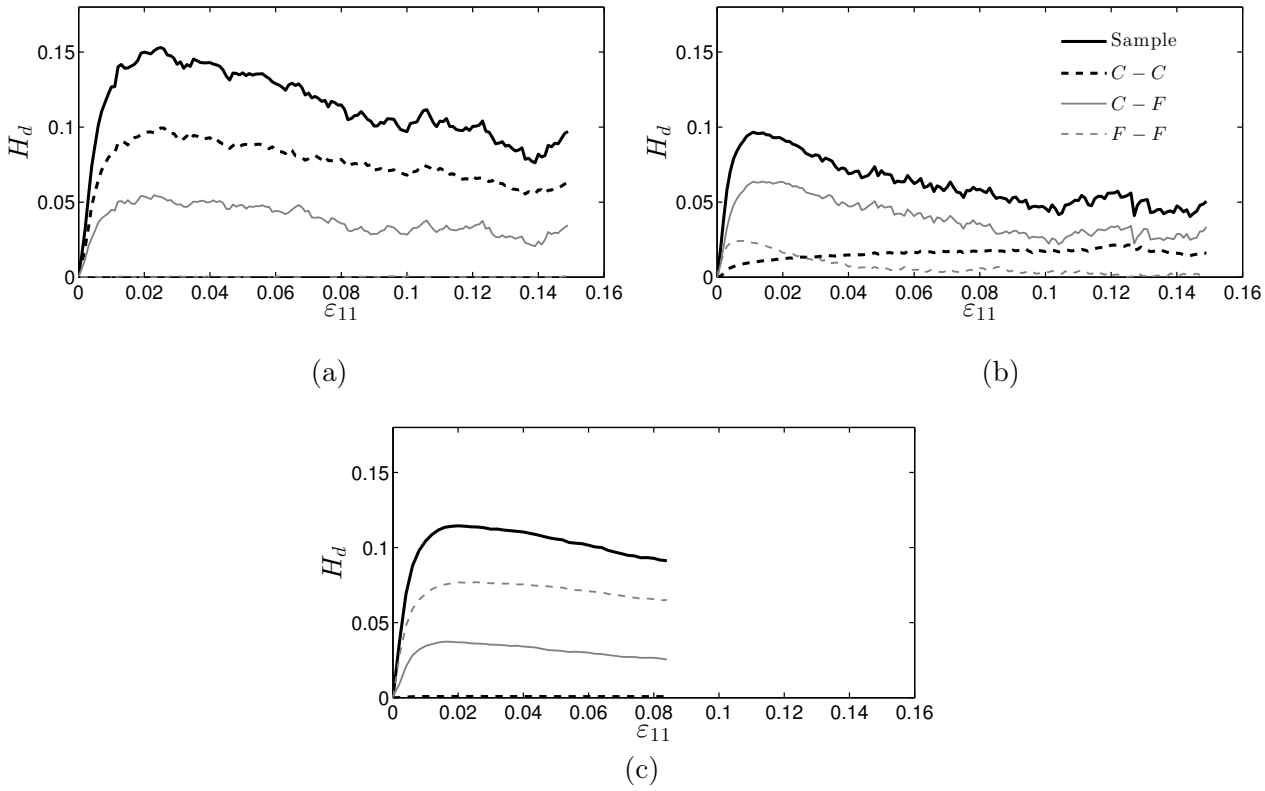

Figure 3.5: Contributions of the $C-C$, $C-F$ and $F-F$ contacts to the anisotropy index H_d versus axial strain ε_{11} for (a) $f_c = 20\%$, (b) $f_c = 30\%$ and (c) $f_c = 60\%$.

Figure 3.5 shows the evolution of the anisotropy index H_d and the contributions of the $C-C$, $C-F$ and $F-F$ contacts during the triaxial compression tests for fine contents of 20%, 30% and 60%. It can be seen that the anisotropy develops during the shearing and reaches the maximum value almost at the peak state where the shear strength reaches its maximum value. After the peak state, the solid skeleton collapses and a rearrangement of the micro-structure is triggered, leading to a decrease in anisotropy. Figure 3.5 indicates that the contributions of the $C-C$, $C-F$ and $F-F$ contacts to the anisotropy depend strongly on fine content. The $C-C$ contacts contribute primarily to the anisotropy for fine content of 20%, while the $C-F$ contacts contribute primarily for fine content of 30%. The contribution of the $F-F$ contacts is quite small for fine contents of 20% and 30% but it becomes primary for fine content of 60%.

Figure 3.6 shows the anisotropy index H_d at the peak state and the contributions of the $C-C$, $C-F$ and $F-F$ contacts to the anisotropy versus fine content f_c. It is shown that the anisotropy of binary mixtures induced by the shearing results primarily from the distribution of the $C-C$ contacts at low fine contents ($f_c < 20\%$) but results primarily from the distribution of the $F-F$ contacts at very high fine contents ($f_c > 60\%$). Between fine contents of 20% and 60%, the role of the $C-F$ contacts in the anisotropy becomes important. Furthermore, the contribution of the $C-F$ contacts increases as fine

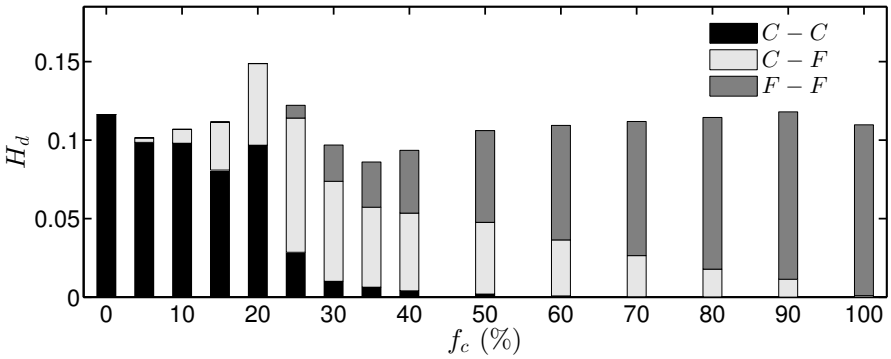

Figure 3.6: Anisotropy index H_d at the peak state and the contributions of the $C-C$, $C-F$ and $F-F$ contacts versus fine content f_c.

content is increased up to around 25%; after this fine content, the contribution of the $C-F$ contacts decreases with an increase in fine content. It is interesting to note that the anisotropy is minimum for the mixture of $f_c = 35\%$, which is quite close to the optimum fine content of 32% for which the shear strength is the best (Figure 2.21(b)). This suggests that the micro-structure of this mixture is so strong that it can bear the deviatoric loading without developing greatly the anisotropy.

By using the fabric tensor defined for each category of contacts, the anisotropy index relative to this category of contacts can be calculated. For example, the anisotropy index for the $C-C$ contacts is calculated from the tensor $\boldsymbol{H}^{C-C}$ defined in (3.5):

$$H_d^{C-C} = \frac{H_1^{C-C} - H_3^{C-C}}{\mathrm{tr}(\boldsymbol{H}^{C-C})}. \tag{3.6}$$

This anisotropy index gives information about the distribution of orientation of the $C-C$ contacts. If $H_d^{C-C} = 0$, the $C-C$ contacts are uniformly oriented; and if $H_d^{C-C} > 0$, these contacts are preferentially oriented in the major principal direction of the stress tensor. Due to small number of $F-F$ contacts, H_d^{F-F} is not calculated for $f_c \leq 20\%$, while H_d^{C-C} is not calculated for $f_c > 70\%$ due to a small number of $C-C$ contacts.

In Figure 3.7, the three anisotropy indexes H_d^{C-C}, H_d^{C-F} and H_d^{F-F} defined for the respective categories of $C-C$, $C-F$ and $F-F$ contacts are plotted versus the axial strain ε_{11} for three fine contents of 20%, 30% and 60%. In addition, Figure 3.8 presents the isotropic index H_d for each category of contacts at the peak state versus fine content f_c. It can be seen that the distribution of orientation of contacts depends strongly on the category of contacts and on fine content. For $f_c < 20\%$, the global anisotropy is mainly governed by the $C-C$ contacts and the anisotropy of these contacts remains more or less constant. Starting from 20% of fine content, the anisotropy of the $C-C$ contacts increases quickly with an increase in fine content, while the anisotropy of the $C-F$ and $F-F$ contacts remains more or less constant. This means that the $C-C$ contacts tend to be more preferentially oriented in the major principal direction of the stress as fine content is increased. Among three categories of contacts, the distribution of orientation of the $C-C$ contacts is the most anisotropic. Despite this fact, these contacts do not contribute primarily to the global anisotropy for $f_c > 20\%$ (Figure 3.6), because the number of these contacts is small compared to the number of $C-F$ and $F-F$ contacts. Analyses of force networks presented in Section 3.4 will allow us to explain why the $C-C$ contacts develop strongly the anisotropy.

The above study of the variation of the three coordination numbers $\mathcal{N}_C^{C-C}$, $\mathcal{N}_C^{C-F}$ and $\mathcal{N}_F^{F-F}$ and the anisotropy of the three categories of contacts with fine content allows us to confirm that:

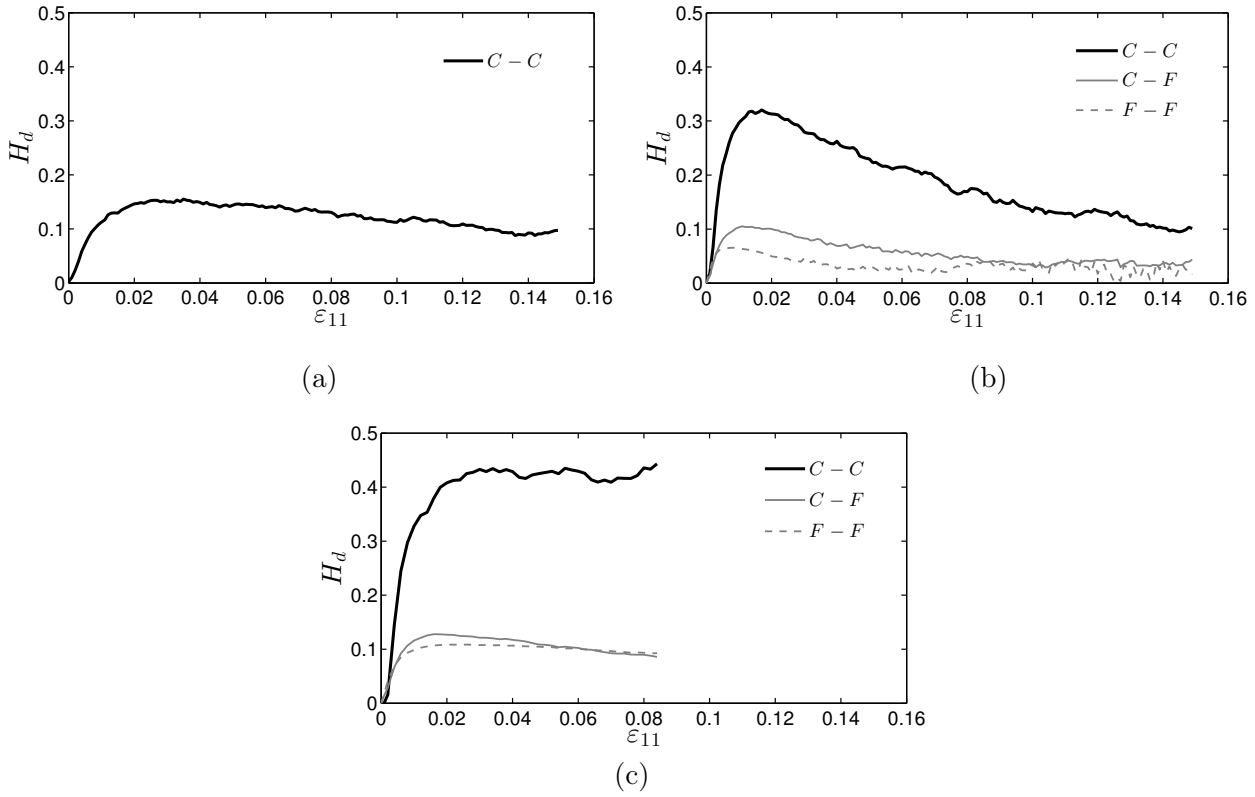

Figure 3.7: Anisotropy index H_d calculated for the $C-C$, $C-F$ and $F-F$ contacts versus axial strain ε_{11} for (a) $f_c = 20\%$, (b) $f_c = 30\%$ and (c) $f_c = 60\%$.

- the solid skeleton of the binary mixtures with $f_c < 20\%$ (range (i) of fine content) is mainly constituted of coarse particles so fine content has a negligible effect on the mechanical behavior of these mixtures;

- the solid skeleton of the binary mixtures with $f_c > 60\%$ (range (iv) of fine content) is mainly constituted of fine particles and it remains more or less constant with an increase in fine content. As a consequence, the mechanical behavior of the mixtures with $f_c > 60\%$ does not change with an increase in fine content.

It is not clear yet why the shear strength increases with an increase in fine content when $f_c < 30\%$ but decreases when $f_c > 30\%$. To explain this, we will study how the shear stress is transmitted through the coarse-coarse, coarse-fine and fine-fine contacts in granular mixtures in the next section.

3.3 Stress transmission through the contact network

When a granular sample is subjected to an external loading, contacts between particles participate in transferring forces (Thornton, 1997; Radjai and Wolf, 1998). The stress tensor at the macro-scale can be defined from contact forces at the micro-scale. Let's consider a volume V that contains a number of solid particles as illustrated in Figure 3.9. The boundary of the volume V is assumed to be tangent to the particles that are close to it. The macroscopic stress $\boldsymbol{\sigma}$ defined on the volume V can be expressed as an average stress of the field of the microscopic stress $\boldsymbol{\sigma}(\boldsymbol{x})$ defined at each point in the volume:

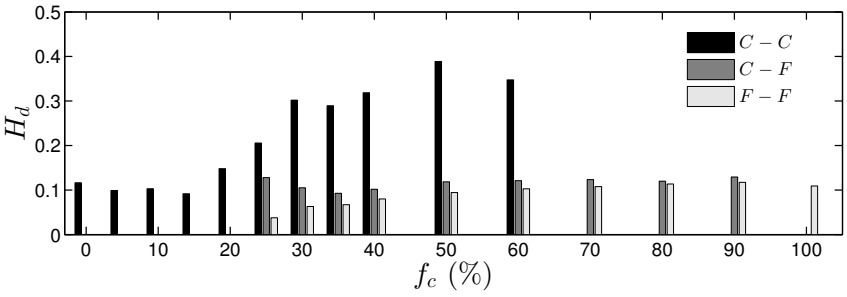

Figure 3.8: Anisotropy index H_d for each category of contacts at the peak state versus fine content f_c.

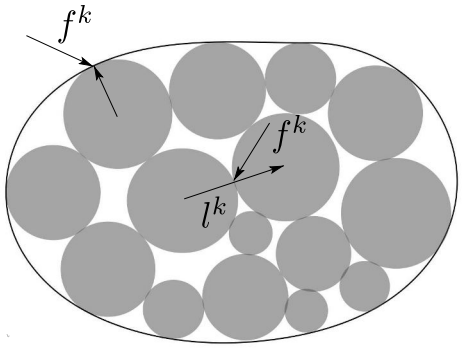

Figure 3.9: Illustration of a volume on which the stress tensor $\boldsymbol{\sigma}$ is defined.

$$\sigma_{ij} = \frac{1}{V}\int_V \sigma_{ij}(\boldsymbol{x})dV. \tag{3.7}$$

For a dry granular assembly, the microscopic stress $\boldsymbol{\sigma}(\boldsymbol{x})$ is not zero only for the solid particles. It follows that Equation (3.7) can be rewritten as:

$$\sigma_{ij} = \frac{1}{V}\sum_{p\in V}\Big(\int_{V_s^p}\sigma_{ij}(\boldsymbol{x})dV\Big) = \frac{1}{V}\sum_{p\in V} M_{ij}^p, \tag{3.8}$$

where superscript p runs over all the solid particles included in the volume V; and the tensor $\boldsymbol{M}^p$ is defined over each particle as follows:

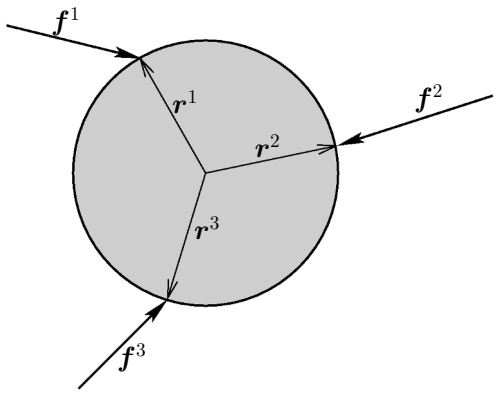

Figure 3.10: Contact forces $\boldsymbol{f}^k$ and contact vectors $\boldsymbol{r}^k$ on a particle.

$$M_{ij}^p = \int_{V_s^p} \sigma_{ij}(\boldsymbol{x}) dV. \tag{3.9}$$

where V_s^p is the solid volume of each particle.

Each solid particle is assumed to be a continuum in equilibrium. Therefore, the equilibrium condition $\text{div}\boldsymbol{\sigma}(\boldsymbol{x}) = \mathbf{0}$ is verified at every point $\boldsymbol{x}$ in this continuum. By using this equilibrium condition and Gauss-Ostrogradski theorem, the volume integral (3.9) can be transformed into a surface integral:

$$M_{ij}^p = \int_{\partial V_s^p} f_i x_j dS, \tag{3.10}$$

where ∂V_s^p denotes the boundary of the particle volume; $\boldsymbol{f} = \boldsymbol{\sigma}.\boldsymbol{n}$ is the stress vector at a point $\boldsymbol{x}$ on the boundary where the outward normal vector is $\boldsymbol{n}$. For a particle subjected to some contact forces as illustrated in Figure (3.10), Equation (3.10) can be rewritten in a discrete form as follows:

$$M_{ij}^p = \sum_{k \in p} f_i^k x_j^k, \tag{3.11}$$

where superscript k runs over all the contacts of particle p.

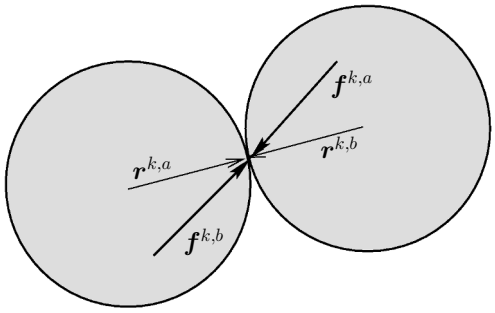

Figure 3.11: Contact forces $\boldsymbol{f}^k$ and contact vectors $\boldsymbol{r}^k$ at a given contact shared by two particles.

It can be proven that when the particle is in equilibrium, the tensor $\boldsymbol{M}^p$ defined by (3.11) does not depend on the choice of the origin of the coordinate system and it is symmetric. We can choose the particle center as the origin of the coordinate system; as a result, Equation (3.11) becomes:

$$M_{ij}^p = \sum_{k \in p} f_i^k r_j^k, \tag{3.12}$$

where $\boldsymbol{r}^k$ is a contact vector that joins the particle center to the contact point. The tensor $\boldsymbol{M}^p$ is called *internal moment tensor* by Moreau (1996). The mean stress tensor $\boldsymbol{\sigma}^p$ over each particle is defined as:

$$\sigma_{ij}^p = \frac{1}{V_s^p} \int_{V_s^p} \sigma_{ij}(\boldsymbol{x}) dV. \tag{3.13}$$

By comparing Equations (3.9) and (3.13), we have $\boldsymbol{\sigma}^p = \boldsymbol{M}^p / V_s^p$ so the physical meaning of the internal moment tensor $\boldsymbol{M}^p$ is similar to that of the mean stress tensor $\boldsymbol{\sigma}^p$.

For a given contact k shared by two particles a and b, the two contact vectors on particles a and b are denoted by the respective vectors $\boldsymbol{r}^{k,a}$ and $\boldsymbol{r}^{k,b}$; and the two contact forces exerted on particle a by particle b and on particle b by particle a are denoted by the respective vectors $\boldsymbol{f}^{k,a}$ and $\boldsymbol{f}^{k,b}$ with $\boldsymbol{f}^{k,b} = -\boldsymbol{f}^{k,a}$ as illustrated in Figure 3.11. It is easy to obtain that:

$$f_i^{k,a} r_j^{k,a} + f_i^{k,b} r_j^{k,b} = f_i^{k,a} r_j^{k,a} - f_i^{k,a} r_j^{k,b} = f_i^a (r_j^{k,a} - r_j^{k,b}) = f_i^{k,a} l_j^k = f_i^k l_j^k \tag{3.14}$$

where $\boldsymbol{l}^k$ is a branch vector that joins the center of particle a to the center of particle b (Figure 3.9). We can also replace $f_i^{k,a}$ by f_i^k which is the contact force exerted by particle b on particle a. By using Equations (3.12) and (3.14), Equation (3.8) becomes:

$$\sigma_{ij} = \frac{1}{V} \sum_{k \in V} f_i^k l_j^k, \tag{3.15}$$

where superscript k runs over not only all contacts between particles (interior contacts) but also all contacts between particles and the boundary. For a contact between two particles, $\boldsymbol{f}^k$ is the contact force and $\boldsymbol{l}^k$ is the branch vector joining two particle centers at this contact. For a contact between a particle and the boundary, $\boldsymbol{f}^k$ is the force exerted by the exterior to the particle and the vector $\boldsymbol{l}^k$ joins the particle center to the contact point (Figure 3.9). Equation (3.15) is the well known static homogenization operator which have been established by different approaches and different authors (Christoffersen et al., 1981; Moreau, 1996).

It has been well known in the literature that the static homogenization operator (3.15) gives a good estimation of the macroscopic stress tensor if the volume under consideration contains a sufficient number of particles. This can be confirmed in Figure 3.12 where the mean stress p estimated with (3.15) is compared to the value of 100 kPa applied on the boundary at the initial state for different values of fine content f_c. Figure 3.12 also shows that the contribution of the contacts on the boundary (the rigid walls in our simulations) to the macroscopic stress tensor $\boldsymbol{\sigma}$ is not negligible (about 10% for $f_c \leq 20\%$) and it decreases as fine content f_c increases (about 4.5% for $f_c = 40\%$). This is due to the fact that the sample sizes L chosen for the simulated samples (Table 2.3) are not too large compared to the maximum particle size $D_{\max}$ so the number of contacts on the boundary is not negligible compared to the number of interior contacts. It is expected that the stress part relative to the contacts on the boundary is negligible compared to that relative to the interior contacts when the sample size is big enough compared to the particle size. In Figure 3.13, the relative error of the mean stress p obtained by Equation (3.15) by considering only the interior contacts, compared to the value of 100 kPa applied on the boundary of the sample with $f_c = 0\%$ is plotted against the sample size $L/D_{\max}$. It can be seen that the part relative to the contacts on the boundary decreases as the sample size is increased and it is smaller than 2% of the macro-stress when $L/D_{\max} = 38$. But to decrease this error for the samples having low values of $L/D_{\max}$, we must replace the total volume of the sample V used in Equation (3.15) by a reduced volume which represents the packing without taking into account the contacts between the particles and the boundary of the sample, but the difficulty is how we can determine the contour of this new volume.

The stress part relative to the contacts between particles can be split into three parts $\boldsymbol{\sigma}^{C-C}$, $\boldsymbol{\sigma}^{C-F}$ and $\boldsymbol{\sigma}^{F-F}$ which correspond to the contributions of the respective categories of $C-C$, $C-F$ and $F-F$ contacts. For example, the contribution of the set of $C-C$ contacts to the stress tensor $\boldsymbol{\sigma}$ is computed as:

$$\sigma_{ij}^{C-C} = \frac{1}{V} \sum_{k \in C-C} f_i^k l_j^k. \tag{3.16}$$

The stress tensors $\boldsymbol{\sigma}^{C-C}$, $\boldsymbol{\sigma}^{C-F}$ and $\boldsymbol{\sigma}^{F-F}$ have the same principal directions as those of the macro-stress tensor $\boldsymbol{\sigma}$. The contributions of each category of contacts to the macroscopic mean and deviatoric stresses, p and q, can be calculated, for example $p^{C-C} = (\sigma_{11}^{C-C} + 2\sigma_{33}^{C-C})/3$ and $q^{C-C} = \sigma_{11}^{C-C} - \sigma_{33}^{C-C}$. Minh et al. (2014) used the same stress decomposition to study the contributions of each category of contacts to the macro-stress for binary mixtures under one-dimensional compression.

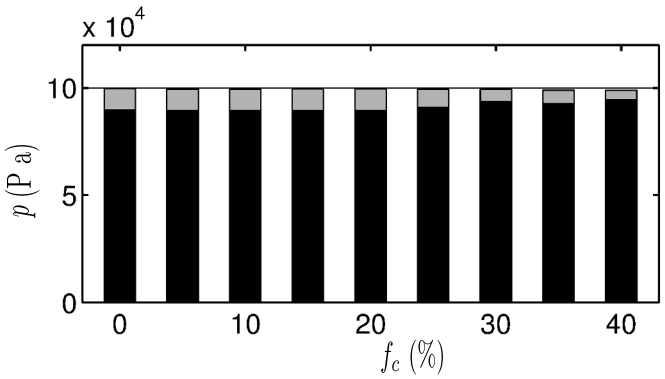

Figure 3.12: The mean stress p estimated with (3.15) at the initial state is compared to the mean stress $p = 100$ kPa applied on the boundary of samples with different values of fine content f_c. Black and gray colors represent the contributions of the interior contacts and of the contacts on the boundary, respectively.

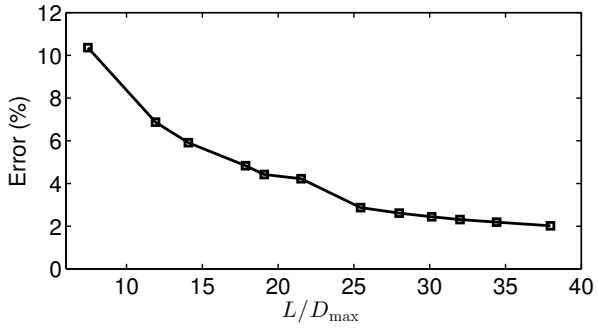

Figure 3.13: The relative error of the mean stress p estimated with (3.15) at the initial state for the sample with $f_c = 0$ versus sample size $L/D_{\max}$.

The contributions of the three categories of $C-C$, $C-F$ and $F-F$ contacts to the macroscopic mean and deviatoric stresses, p and q, are plotted versus the axial strain ε_{11} in Figure 3.14 for fine contents of 20%, 30%, 60% and 80%. Their values at the peak and critical states are plotted versus fine content f_c in Figure 3.15. It can be seen that for $f_c < 20\%$, the $C-F$ and $F-F$ contacts do not contribute significantly to the macro-stress. For instance, for $f_c = 15\%$, all the $C-F$ contacts contribute to only 4% of the macroscopic mean and deviatoric stresses at the peak state. A major part of the macro-stress is carried by the $C-C$ contacts and it remains more or less constant for $f_c < 20\%$. This is in agreement with the result shown in Figure 3.2 where the coordination numbers $\mathcal{N}_C^{C-F}$ and $\mathcal{N}_F^{F-F}$ are negligible compared to $\mathcal{N}_C^{C-C}$ which is not affected by a low fine content.

Starting from $f_c = 20\%$, the $C-F$ contacts contribute to supporting the shear stress (see also Figure 3.14(a)). For this threshold value, the $C-F$ contacts carry about 10% of the macro-stress despite a low value of $\mathcal{N}_C^{C-F}$, while the stress part carried by the $C-C$ contacts is almost the same as that for the samples with $f_c < 20\%$. This explains why the effect of fine content on the shear strength is visible starting from 20% (Figure 2.21(b)). It is worth mentioning that it is not easy to explain this if we look only at the void ratios in Figure 2.19 and at the coordination numbers in Figure 3.2. The $C-F$ and $F-F$ contacts participate more and more in sharing the macro-stress as f_c increases from 20% as shown in Figure 3.15. At $f_c = 30\%$, the $C-F$ contacts actually contribute to the deviatoric stress q as much as the $C-C$ contacts (see also Figure 3.14(b)). Interestingly, they contribute even more to the mean stress p than the latter ones. The role of the $C-F$ contacts becomes more important than the role of the $C-C$ contacts at $f_c = 40\%$ at which the former ones contribute to about 53% of the deviatoric stress q at the peak state, compared to

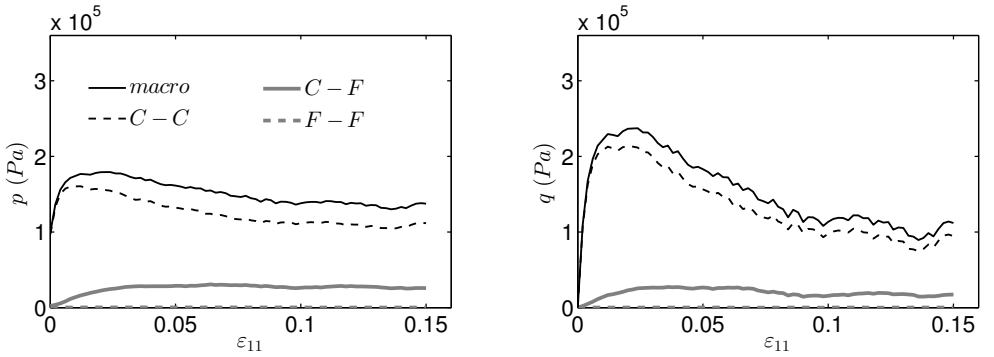

(a) $f_c = 20\%$

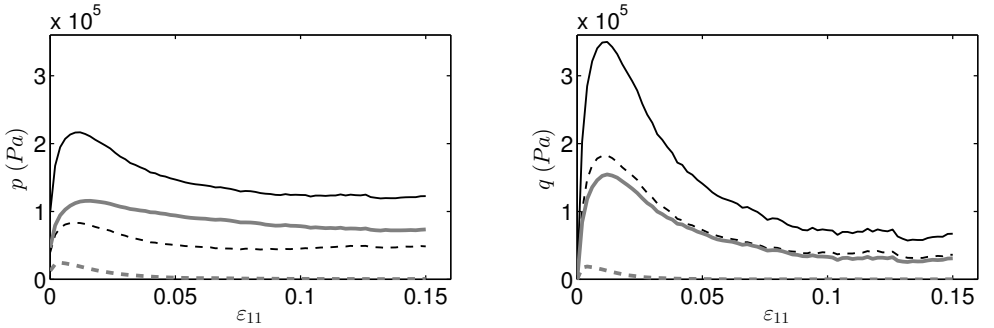

(b) $f_c = 30\%$

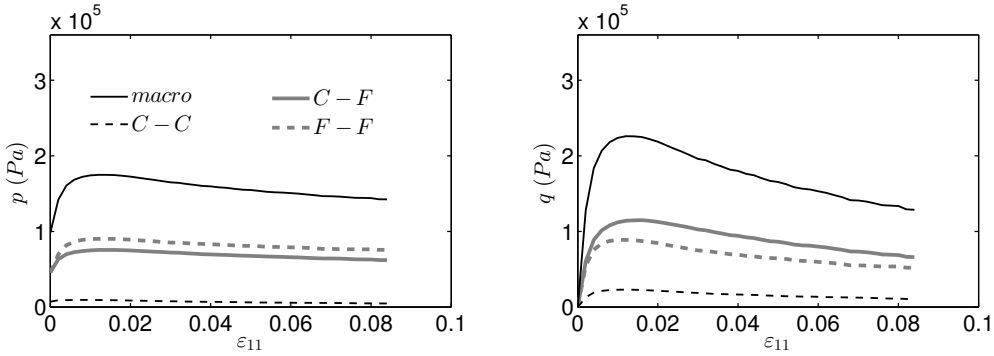

(c) $f_c = 60\%$

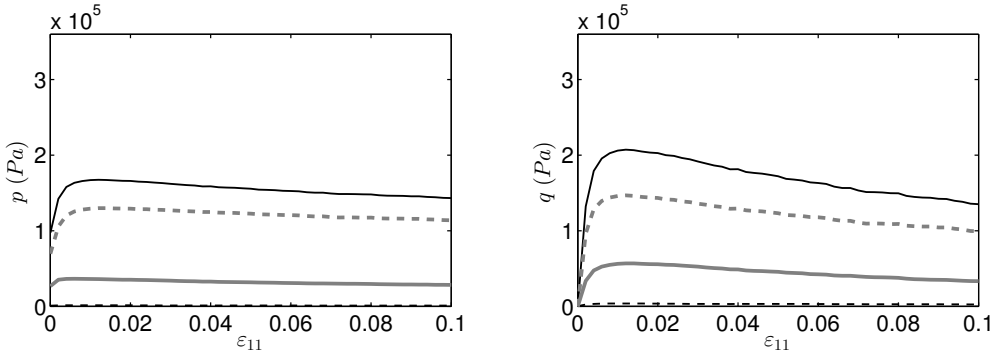

(d) $f_c = 80\%$

Figure 3.14: Contributions of the three categories of $C-C$, $C-F$ and $F-F$ contacts to the macroscopic mean and deviatoric stresses, p and q, versus axial strain ε_{11} for (a) $f_c = 20\%$, (b) $f_c = 30\%$, (c) $f_c = 60\%$, (d) $f_c = 80\%$.

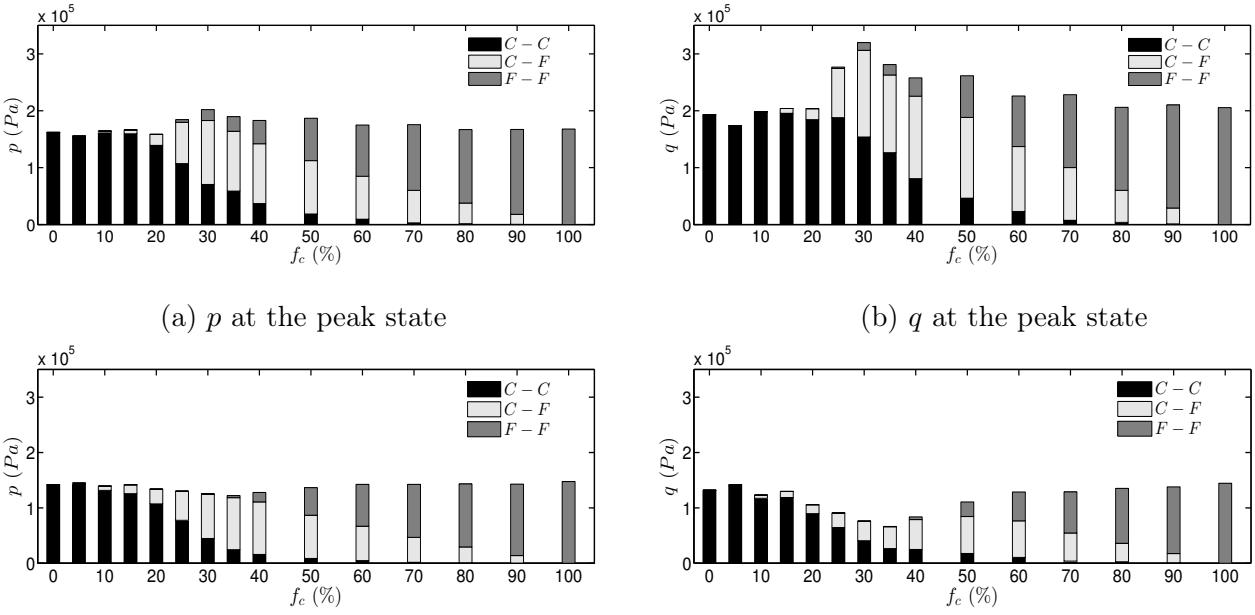

(a) p at the peak state

(b) q at the peak state

(c) p at the critical state

(d) q at the critical state

Figure 3.15: Contributions of the three categories of contacts to the macroscopic mean and deviatoric stresses versus f_c: (a) and (b) at the peak state and (c) and (d) at the critical state.

a value of 35% for the latter ones. The increasing role of the $C-F$ contacts and the decreasing role of the $C-C$ contacts with an increase in fine content in the range $20\% \leq f_c \leq 30\%$ are related to the increase in the coordination number $\mathcal{N}_C^{C-F}$ and to the decrease in the coordination number $\mathcal{N}_C^{C-C}$, respectively, as shown in Figure 3.2. Starting from 30% of fine content, despite the fact that the coordination number $\mathcal{N}_C^{C-F}$ continues to increase, the stress part carried by the $C-F$ contacts start to decrease. At the same time, the $F-F$ contacts participate more and more in carrying the shear stress. The contribution of the $F-F$ contacts to the macro-stress even becomes greater than that of the $C-F$ contacts for $f_c > 60\%$.

One can remark that the $C-C$ and $C-F$ contacts reverse their roles in sustaining the shear stress at the threshold fine content of 30%: above this value, the latter ones sustain more the shear stress than the former ones. We can explain why the best shear strength is obtained at fine content of 30% as follows. The contribution of the $C-F$ contacts to the macro-stress increases quickly with $f_c \leq 30\%$, which compensates a decrease in the contribution of the $C-C$ contacts. As a consequence, the shear strength at the peak state increases with fine content $f_c \leq 30\%$. However, an increase in fine content f_c from 30% does not lead to a significant increase in the stress part carried by the $C-F$ contacts but leads to a strong decrease in the stress part carried by the $C-C$ contacts. Consequently, the shear strength at the peak state decreases with fine content $f_c > 30\%$. It is interesting to note that, Minh et al. (2014) also observed a transition at 30% of fine content for binary mixtures subjected to one-dimensional compression with a gap ratio of 4.0, above which the $C-F$ contacts overtake the $C-C$ contacts in carrying the shear stress.

Starting from a fine content of 60%, the $C-C$ contacts do not contribute significantly to the macro-stress. For instance, all the $C-C$ contacts contribute to only 5% of the macroscopic mean stress and to only 10% of the macroscopic deviatoric stress at the peak state for $f_c = 60\%$. This result is in agreement with the result shown in Figure 3.2, where the coordination number $\mathcal{N}_C^{C-C}$ is negligible compared to the coordination numbers $\mathcal{N}_C^{C-F}$ and $\mathcal{N}_F^{F-F}$ for $f_c \geq 60\%$. The $F-F$ contacts primarily carry the shear stress for this range of fine content and the stress part carried by the $C-F$ contacts decreases with an increase in fine content. The solid skeleton is mainly constituted of $F-F$ contacts, which sustain primarily the

shear stress. Consequently, the shear strength remains more or less constant in this range of fine content as shown in Figure 2.21(d).

Figure 3.15 also shows a marked decrease in the deviatoric stresses supported by the three categories of contacts at the critical state for the samples with $f_c \geq 30\%$. The most drastic drop is observed for the sample with 30% of fine content where the deviatoric stresses supported by the $C-C$ and $C-F$ contacts are reduced by a factor > 3 from the peak state to the critical state. As a consequence, its shear strength is greatly reduced at the critical state, which is consistent with the great degradation of its micro structure after the peak state as shown in Figure 3.2. The deviatoric stress carried by the $C-C$ contacts for the sample with $f_c = 30\%$ becomes much lower than that for the sample with $f_c = 0\%$ at the critical state. In addition, the $C-F$ contacts in the former sample suffer a great softening phase. This explains why the residual shear strength for $f_c = 30\%$ is lower than that for $f_c = 0\%$ (Table 2.5). It is interesting to note in Figure 3.15 that the mean stress at the critical state is then primarily carried by the $C-F$ contacts for $f_c \geq 30\%$, and the $F-F$ contacts carry almost no stress at this state.

We have shown in this section that the external stress applied to a binary mixture is primarily transmitted through the $C-C$ contacts for the range of fine content $< 20\%$, while it is primarily transmitted through the $F-F$ contacts for the range of fine content $> 60\%$. For a fine content between 20% and 60%, the shear stress is mainly shared by the $C-C$ and $C-F$ contacts and the stress part carried by the $C-F$ contacts becomes greater than that carried by the $C-C$ contacts starting from 30% of fine content. It should be noted that all the contacts in each category do not carry in the same manner the external stress since force transmission through a granular medium is well known to be very heterogeneous. In the same system, there exist strong and weak force networks with different roles in sustaining the shear stress. In the next section, we analyze how the contacts in each category constitute the strong and weak force networks.

3.4 Strong and weak force networks

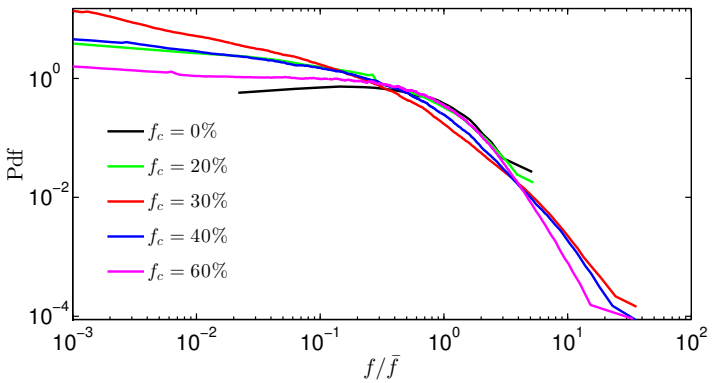

Figure 3.16: Probability density function (Pdf) of contacts forces, normalized by the average force $\bar{f}$, for different fine contents.

Dantu (1957) observed in his experiment on granular assemblies composed of photoelastic disks that forces at contacts are very heterogeneous: some contacts carry strong forces, while the others carry a weak forces. This observation is confirmed for binary mixtures in Figure 3.16 where the probability density function of contact forces is plotted for different fine contents. It can be seen that there are much more contacts that carry weak forces (weak contacts) than contacts that carry strong forces in binary mixtures

(strong contacts). In addition, the proportion of weak contacts tends to increase with an increase in fine content for $f_c \leq 30\%$. Voivret et al. (2009) also found in their numerical simulations of highly polydisperse assemblies composed of disks that the force transmission through contacts becomes more heterogeneous as the polydispersity is increased. It is interesting to note that the fine content of 30% is also a threshold value in terms of distribution of contacts forces. The heterogeneity of the force transmission is the highest at this fine content and decreases as fine content is further increased. This result means that the binary mixture of 30% of fine content contains the biggest number of weak contacts. Voivret et al. (2009) did not found such a threshold fine content in their study. We can also observe that the turning points observed for the curves in Figure 3.16 correspond to values of $f/\bar{f}$ close to 1.0, which is also the value found by several authors (Radjai and Wolf, 1998).

Radjai and Wolf (1998) distinguished two force networks, namely weak and strong force networks, which are composed of the contacts where the contact force f^c is smaller and bigger than the average contact force $\bar{f}$, respectively. The authors found that the strong network sustains almost the shear stress and the weak network behaves like a liquid without bearing any shear stress. The same result is obtained for the binary mixtures considered in this study as shown in Figure 3.17, in which the mean and deviatoric stresses carried by the weak and strong force networks at the peak state are plotted against fine content. It can be seen that the weak network sustains a small part of the mean stress p but a negligible part of the deviatoric stress q for any fine content, despite the fact that the number of weak contacts in binary mixtures is dominant compared to the number of strong contacts as shown in Figure 3.18. It is interesting to note that the percentage of weak contacts is maximum for a fine content about 30%, at which the shear strength is the best. This means that the shear strength is not proportional to the percentage of contacts in the strong force network: fewer strong contacts can carry a bigger shear stress. This does not mean that the weak contacts do not play any role in the micro-structure. On the contrary, they play an important role in sustaining laterally the strong force network, allowing the latter one to support better the shear stress.

Figure 3.19 shows the fraction of $C-C$, $C-F$ and $F-F$ contacts in the strong network versus fine content f_c at the peak state. For example, the fraction of $C-C$ contacts in the strong force network is defined as the ratio of the number of $C-C$ contacts in the strong force network to the total number of $C-C$ contacts. It can be seen that, at low fine content ($f_c < 20\%$), the strong force network is constituted of about 40% of $C-C$ contacts and a much smaller fraction of $C-F$ contacts. As fine content increases, more $C-C$ contacts participate in the strong force network. Interestingly, more than 95% of $C-C$ contacts actually take part in the strong force network for $30\% \leq f_c \leq 90\%$. Voivret et al. (2009) also showed that the strong force network passes preferentially through coarse particles in highly polydisperse samples. This result can be explained by the fact that the presence of fine particles around coarse ones makes contacts between coarse particles stronger so they carry a much bigger force. It does not mean, however, that the $C-C$ contacts can carry a bigger stress: they carry, indeed, a lower stress at $f_c = 30\%$ than at $f_c = 10\%$ (Figure 3.15) because more $C-C$ contacts are disrupted by fine particles at $f_c = 30\%$. Figure 3.19 also shows that an increasing fraction of $C-F$ and $F-F$ contacts take part in the strong force network as fine content increases so they sustain more the shear stress. However, a major fraction of these contacts are located in the weak force network (more than half of $C-F$ and $F-F$ contacts). Minh et al. (2014) obtained similar results for binary mixtures under one-dimensional compression.

The above analyzes have shown how the macroscopic stress is transmitted through the contact network in a granular mixture but they do not show how much stresses the coarse-grained and fine-grained matrices carry. According to Skempton and Brogan (1994), the stress carried by the fine fraction is an important factor that influences the susceptibility of a granular material to internal erosion. In the next section, we define first the stresses carried by each matrix, and then we show how they depend on fine content.

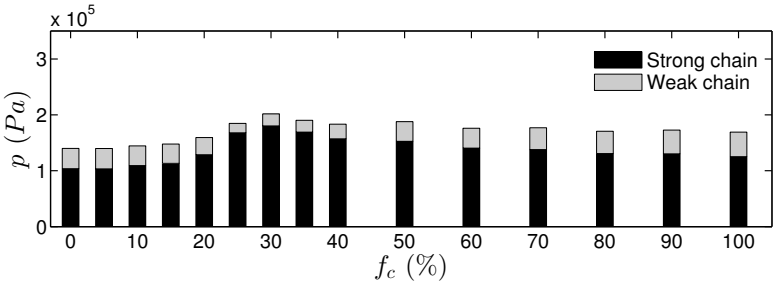

(a) Mean stress p

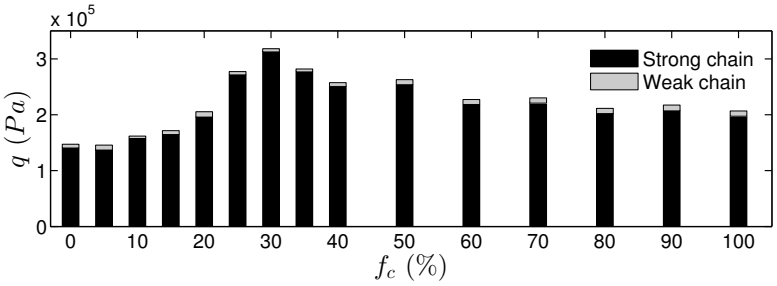

(b) Deviatoric stress q

Figure 3.17: Contributions of the strong and weak force chains to the mean stress p and the deviatoric stress q at the peak state versus fine content f_c.

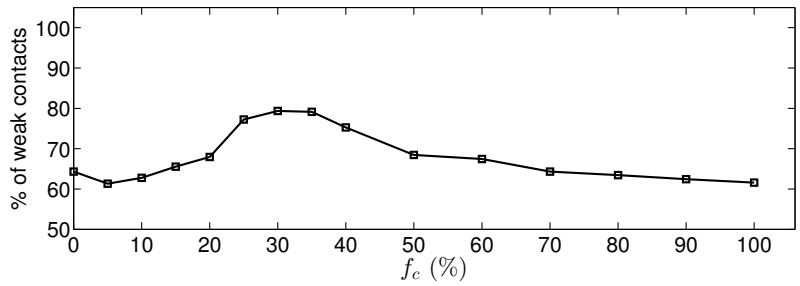

Figure 3.18: Percentage of weak contacts at the peak state versus fine content f_c.

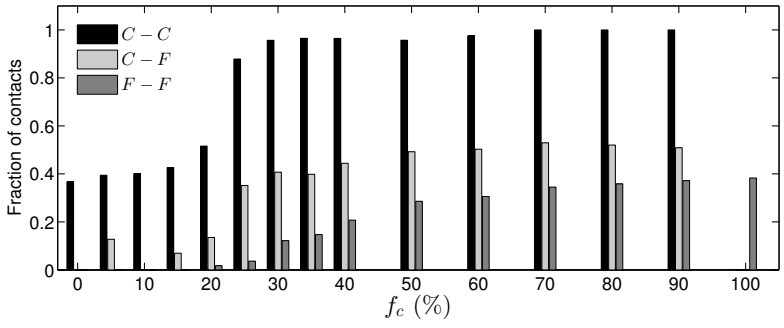

Figure 3.19: Fraction of $C-C$, $C-F$ and $F-F$ contacts in the strong network at the peak state.

3.5 Stress carried by the fine and coarse fractions

In addition to the coarse-grained matrix (C) and the fine-grained matrix (F) in a granular mixture, voids (V), which can be filled by water or not, are present between solid particles. By homogenizing

the stress field in this heterogeneous medium, the macroscopic stress can be defined from its counterpart within each phase:

$$\sigma_{ij} = \sum_{\alpha\in\{F,C,V\}} \phi^\alpha \sigma_{ij}^\alpha = \sum_{\alpha\in\{F,C,V\}} \widehat{\sigma}_{ij}^\alpha. \tag{3.17}$$

For each phase α, ϕ^α is its volume fraction, i.e. the ratio of its volume V^α to the total volume V. The *intrinsic averaged stress* $\boldsymbol{\sigma}^\alpha$ is defined as the average of the microscopic stress field $\boldsymbol{\sigma}(\boldsymbol{x})$ which prevails in the phase under consideration:

$$\sigma_{ij}^\alpha = \frac{1}{V^\alpha}\int_{\boldsymbol{x}\in V^\alpha} \sigma_{ij}(\boldsymbol{x})dV. \tag{3.18}$$

According to the mixture theory, the tensor $\widehat{\boldsymbol{\sigma}}^\alpha = \phi^\alpha\boldsymbol{\sigma}^\alpha$, called *partial stress*, is defined as:

$$\widehat{\sigma_{ij}}^\alpha = \frac{1}{V}\int_{\boldsymbol{x}\in V^\alpha} \sigma_{ij}(\boldsymbol{x})dV. \tag{3.19}$$

The partial stress $\widehat{\boldsymbol{\sigma}}^\alpha$ can be understood as the contribution of the phase under consideration to the macroscopic stress $\boldsymbol{\sigma}$. It should be noted that it is the intrinsic averaged stress $\boldsymbol{\sigma}^\alpha$ that gives information on how much the phase under consideration is stressed. For a dry mixture, voids bear zero-stress so we obtain:

$$\sigma_{ij} = \phi^F\sigma_{ij}^F + \phi^C\sigma_{ij}^C = (1-n)[f_c\sigma_{ij}^F + (1-f_c)\sigma_{ij}^C]. \tag{3.20}$$

The volume fraction ϕ^F of the fine fraction is related to fine content f_c and the porosity n by $\phi^F = (1-n)f_c$.

Using the definition (3.18) and following the transformations presented in Section 3.3, the intrinsic averaged stresses $\boldsymbol{\sigma}^F$ and $\boldsymbol{\sigma}^C$ in the fine and coarse fractions can be expressed as follows:

$$\sigma_{ij}^F = \frac{1}{V_s^F}\sum_{p\in F} M_{ij}^p, \quad \sigma_{ij}^C = \frac{1}{V_s^C}\sum_{p\in C} M_{ij}^p, \tag{3.21}$$

where superscript p runs over all the particles in each fraction; V_s^F and V_s^C are the respective total solid volumes of the fine and coarse fractions; and the internal moment tensor $\boldsymbol{M}^p$ is defined in (3.12) for each particle p. Equation (3.21) can also be transformed to

$$\sigma_{ij}^F = \frac{1}{V_s^F}\sum_{p\in F} \sigma_{ij}^p V_s^p, \quad \sigma_{ij}^C = \frac{1}{V_s^C}\sum_{p\in C} \sigma_{ij}^p V_s^p, \tag{3.22}$$

where $\boldsymbol{\sigma}^p$ is the mean stress tensor defined for each particle in (3.13).

In the same manner, the partial stresses $\widehat{\boldsymbol{\sigma}}^F$ and $\widehat{\boldsymbol{\sigma}}^C$ of the fine and coarse fractions can be expressed as follows by using the definition (3.19):

$$\widehat{\sigma}_{ij}^F = \frac{1}{V}\sum_{p\in F} M_{ij}^p, \quad \widehat{\sigma}_{ij}^C = \frac{1}{V}\sum_{p\in C} M_{ij}^p. \tag{3.23}$$

Based on the stress tensors $\boldsymbol{\sigma}^F$ and $\boldsymbol{\sigma}^C$, the mean and deviatoric stresses carried by the fine and coarse fractions can be calculated. Inspired from the stress reduction factor α that was introduced by Skempton and Brogan (1994), we define a stress reduction factor α for the fine fraction as $\alpha = p^F/p$ where p^F is the mean stress in the fraction of fine particles and p is the macroscopic mean stress. It is worth mentioning that if both fractions carried the same stress, the stress reduction factor would be $\alpha = 1/(1-n)$. Shire et al. (2014b) defined a similar stress reduction factor for the fine fraction. The authors computed the averaged stress $\boldsymbol{\sigma}^F$ in the fine fraction using the definition (3.22). However, instead of considering the solid volume

V_s^p of each particle, the authors associated to each particle an amount of void surrounding it, so the volume considered for each particle when computing the averaged stress $\boldsymbol{\sigma}^p$ is $V^p = V_s^p/(1-n)$. By doing so, a binary mixture is considered as a biphasic material: the fine and coarse fractions with the respective total volumes $V^F = V_s^F/(1-n)$ and $V^C = V_s^C/(1-n)$. As a consequence, the resulting stress tensor $\boldsymbol{\sigma}^F$ is no longer intrinsic to the solid fraction of the fine particles according to (3.18) and the resulting stress factor α is lower than that defined in the current study. A low value of the stress reduction factor α means that the fine particles are not sufficiently stressed and they are susceptible to be washed out by the seepage flow.

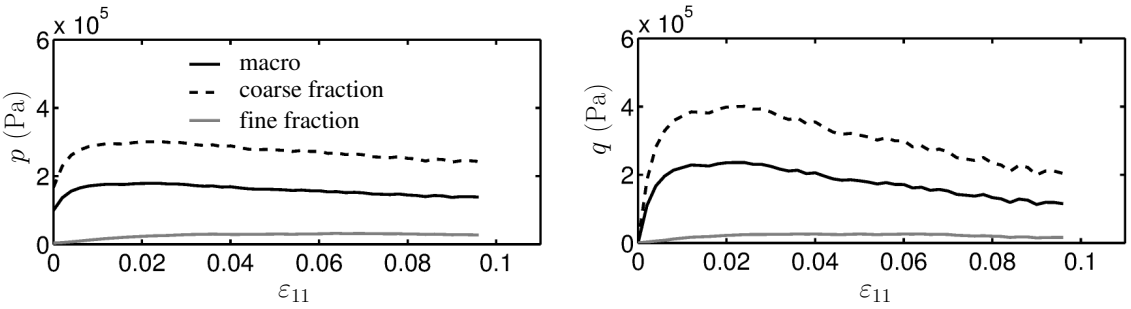

(a) $f_c = 20\%$

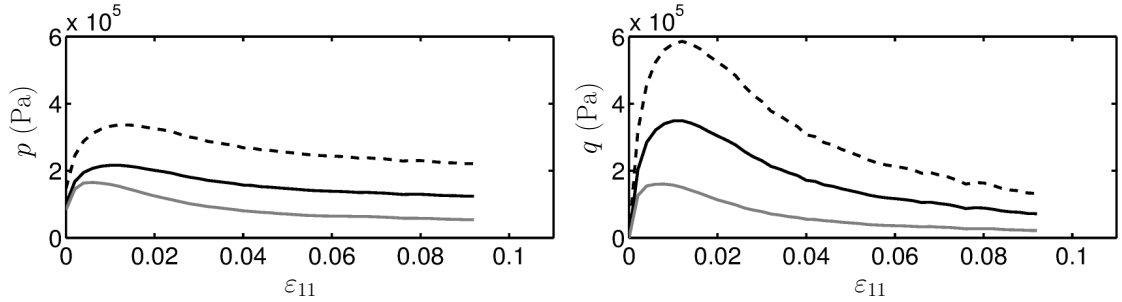

(b) $f_c = 30\%$

Figure 3.20: The mean stress p and the deviatoric stress q carried by the fine and coarse fractions versus axial strain for (a) $f_c = 20\%$ and (b) $f_c = 30\%$.

Figure 3.20 shows the mean and deviatoric stresses of each fraction versus the axial strain, compared to the macroscopic mean and deviatoric stresses, for $f_c = 20\%$ and 30%. Their values at the peak state are plotted against fine content in Figure 3.21. The stress reduction factor α at the initial, peak and critical states is plotted against fine content in Figure 3.22. It can be seen that at a low fine content ($f_c \leq 20\%$), the fine fraction carries almost zero-stress. This confirms that the fine particles are almost floating in voids between coarse particles and carry low stress. According to Skempton and Brogan (1994), a significant proportion of fine particles in this case can be easily washed out by water flow even at low hydraulic gradient – in other words, these mixtures are internally unstable. It should be noted that a low stress carried by the fine fraction is just a necessary condition for the internal instability. This just means that fine particles can be easily detached by water flow. The sufficient condition is whether or not the primary fabric formed by solid particles allow detached fine particles to migrate within the interstices of this framework.

At a higher fine content, the fine particles participate in carrying the applied stress, and its participation increases with fine content. It is interesting to note in Figure 3.21 that the fine fraction plays a more important role in carrying the mean stress than in carrying the deviatoric stress: at $f_c = 40\%$, $p^F/p = 1.0$ compared to $q^F/q = 0.6$ at the peak state. Shire et al. (2014b) also found that the stress reduction factor

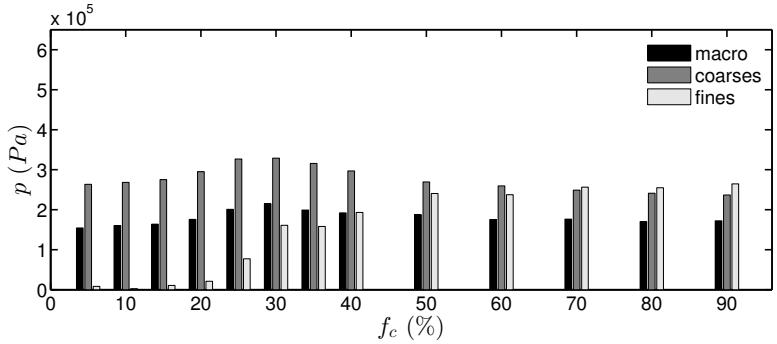

(a)

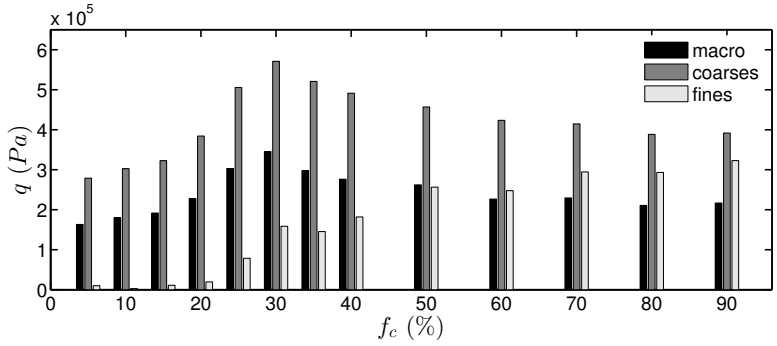

(b)

Figure 3.21: The mean stress p (a) and the deviatoric stress q (b) of the fine and coarse fractions at the peak state versus fine content f_c.

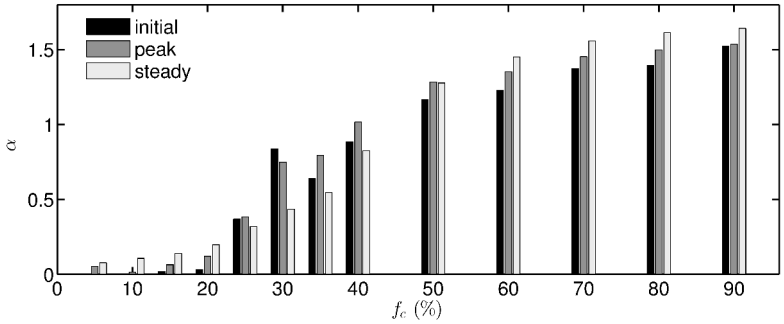

Figure 3.22: The stress reduction factor α at the initial, peak and critical states versus fine content f_c.

α at the isotropic stress state increases with fine content; moreover it depends significantly on the gap ratio G_{r}. By investigating the stress factor α during the shear loading, we find that the shearing leads to a significant reduction in the stress carried by the fine fraction (Figure 3.22). For the mixture with $f_c = 30\%$, which exhibits the most marked softening behavior as shown in Figure 2.21(b), the stress reduction factor α reduces indeed from 0.84 at the initial state to 0.43 at the critical state. This result indicates that the fine particles are softened by the shear loading, which might make them more vulnerable to internal erosion.

Concerning the coarse fraction, since voids do not carry any stress and the fine fraction carries a stress smaller than the macroscopic stress, it carries a stress much bigger than the macroscopic stress. As shown in Figure 3.21, the stress carried by the coarse fraction is indeed about 1.6 times the macroscopic stress.

Furthermore, it increases with fine content for $f_c \leq 30\%$ but decreases for $f_c > 30\%$ (Figure 3.21). This result confirms the optimal fine content $f_c = 30\%$ under which the coarse fraction is reinforced by fine particles but above which the coarse fraction is weakened since fine particles strongly separate them. Even at a very high fine content, the shear stress in the fraction of coarse particles is higher than the stress in the fraction of fine particles.

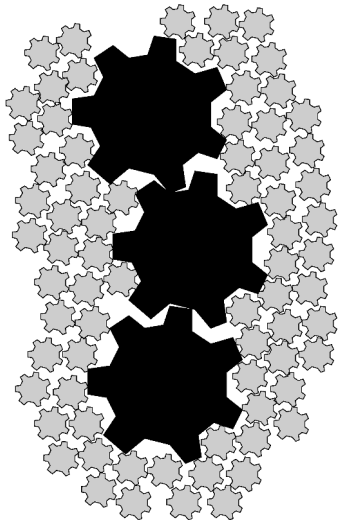

Figure 3.23: A granular binary mixture is assimilated to a system of gears. Black and gray gears correspond to particles included in the strong and weak force networks, respectively.

Let us now give an explanation of why the stress carried by the coarse fraction as well as the shear strength of granular binary mixtures increase with fine content f_c between 20% and 30%. Solid particles with frictional surface can be thought of as gears in a mechanical transmission system so a granular binary sample can be assimilated to a system of small gears and big gears (Figure 3.23). Black and gray gears correspond to particles included in the strong and weak force networks, respectively. For $f_c \leq 30\%$, the strong force network is primarily constituted of big gears. In such a system, small gears have the two following important roles. Firstly, small gears intercalated between strong force columns serve as a bracing system to laterally stabilize the latter ones: without them, strong force columns would collapse. Secondly, an important number of small gears around big gears wedge the latter ones, thus prevent greatly their rotation. In this case, sliding and rolling at contacts between big gears are greatly reduced; thus, the coarse fraction gets stronger and the shear strength of granular mixtures increases with increasing fine content. Indeed, Calvetti et al. (2003) and Belheine et al. (2009) showed that a granular sample resists better shearing if the particle rotation is prohibited or reduced.

The partial stresses $\widehat{\boldsymbol{\sigma}}^F$ and $\widehat{\boldsymbol{\sigma}}^C$ defined in (3.23) give the contribution of each fraction to the macroscopic stress. If the solid fraction was homogeneous, the contribution of the fine fraction would be proportional to fine content f_c, e.g. 40% of fine content would contribute to 40% of the macroscopic stress. Figure 3.24 shows that the contribution of the fine fraction to the macroscopic stress is far from being proportional to fine content for $f_c \leq 50\%$ but it is proportional to fine content for $f_c > 50\%$. More precisely, the fine particles do not significantly contribute to the macroscopic stress when $f_c < 20\%$. For this range of fine content, the shear stress is mainly carried by the coarse particles. For the range of fine content between 20% and 60%, the fine particles participate actively in carrying the shear stress. Interestingly, they contribute more to the mean stress p than to the deviatoric stress q: for $f_c = 40\%$, 21.5% of the deviatoric stress q is provided by the fine particles, which is much lower than the value of 30.9% of the mean stress p. For this range of fine content, the coarse particles constitute primarily the solid skeleton,

while the fine particles play the role of a matrix that reinforces the solid skeleton. For a fine content higher than 60%, the fine particles primarily carry the shear stress and the coarse particles play the role of inclusions in the matrix formed by the fine particles.

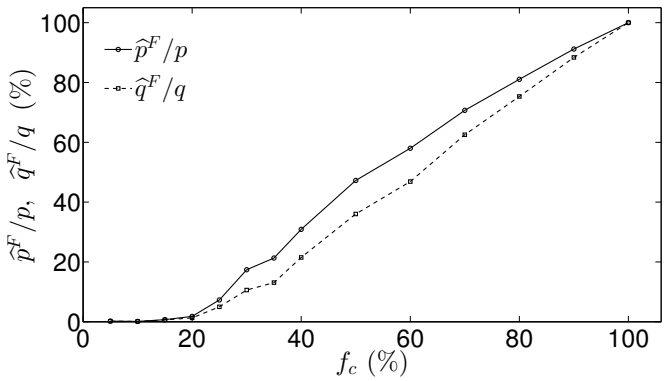

Figure 3.24: Contributions of the fine fraction to the macroscopic mean and deviatoric stresses, p and q, at the peak state versus fine content f_c.

3.6 Classification of granular mixtures

According to Thevanayagam et al. (2002), the micro-structure of granular mixtures can be constituted in many different ways, depending on fine content. The authors proposed three limiting categories of micro-structure: (a) the coarse-coarse contacts are dominant, (b) the fine-fine contacts are dominant, and (c) the fine and coarse particles form a layered system. The current study brought several interesting insights into the variation of the granular micro-structure and how the coarse-coarse, coarse-fine and fine-fine contacts participate in sustaining the shear stress, depending on fine content. It turns out that the fine-coarse contacts play an important role in the micro-structure and there exists an intermediate category between (a) and (b), where these contacts primarily bear the shear stress. We propose, therefore, the following classification of granular mixtures into four limiting categories of micro-structure with three threshold values as illustrated in Figure 3.25.

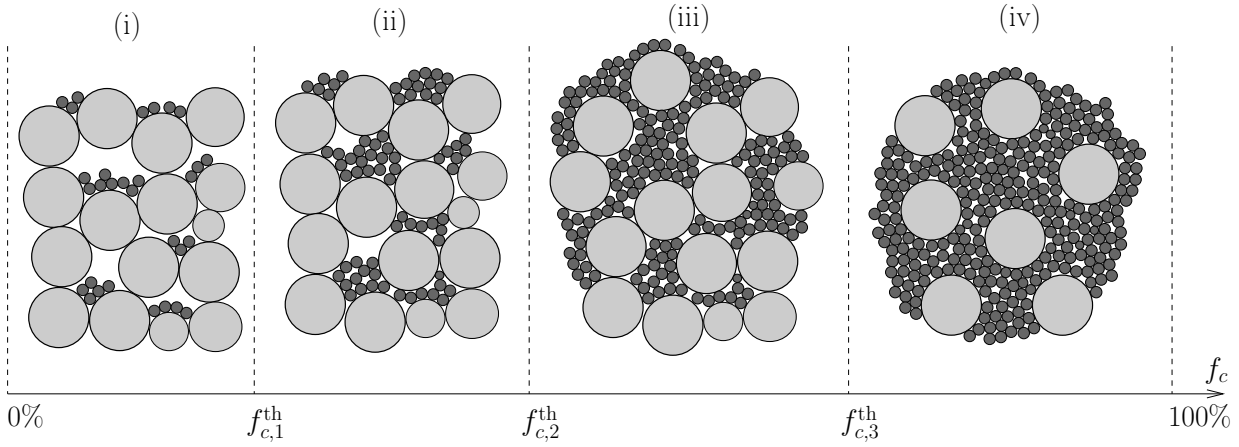

Figure 3.25: Four categories of micro-structure for granular gap-graded soils

- Category (i) for $f_c < f_{c,1}^{\text{th}}$: the fine particles are almost floating within intercoarse voids, hence they

have a little contribution to supporting the shear stress. The shear strength is then not affected by fine content.

- Category (ii) for $f_{c,1}^{\text{th}} \leq f_c < f_{c,2}^{\text{th}}$: the fine particles partially fill intercoarse voids but they partially separate coarse ones. The fine-coarse contacts are created and contribute to transmitting the shear stress. However, contacts between coarse particles primarily carry the shear stress. In this case, the shear strength increases with fine content.

- Category (iii) for $f_{c,2}^{\text{th}} \leq f_c < f_{c,3}^{\text{th}}$: the fine particles fully fill intercoarse voids and greatly destroy coarse-coarse contacts. The fine-fine contacts participate in carrying the shear stress. The major contribution to the shear stress is provided by the fine-coarse contacts. In this case, the shear strength decreases with fine content.

- Category (iv) for $f_c \geq f_{c,3}^{\text{th}}$: the coarse particles are fully dispersed by the fine ones. The behavior of granular mixtures of this category is mainly governed by the fine particles. The shear strength is independent of fine content in this case.

It is should be noted that this classification does not include the category (c) of layered micro-structure considered by Thevanayagam et al. (2002) For the binary mixtures considered in our study, the first and second threshold values, $f_{c,1}^{\text{th}}$ and $f_{c,2}^{\text{th}}$, are about 20% and 30%, respectively. For the third threshold value $f_{c,3}^{\text{th}}$, we found this value is about 60% which is also the value founded by Minh et al. (2014) for binary mixtures under one-dimensional compression with a gap ratio about 4.0.

3.7 Conclusions

In this chapter, we have presented a study on the effect of fine content on the mechanical behavior of granular gap-graded materials subjected to shear loading. Numerical samples composed of fine and coarse spherical particles with fine content varied from 0 to 100% are simulated using the DEM. Triaxial compression tests are then performed on these samples and their behavior is investigated at the micro-scale. This study brought a lot of insights into the granular micro-structure and the stress transmission in granular mixtures, which allowed us to explain why the fine particles can have no effect, positive effect or negative effect on their stress-strain behavior, depending on fine content. At a low fine content ($f_c < 20\%$), the fine particles are almost floating within the void space between the coarse particles so they do not participate significantly in carrying the shear stress. Starting from 20% of fine content, the fine particles cause two opposite effects to the granular micro-structure: on one hand, they come into contact with coarse particles and reinforce the micro-structure, but on the other hand, they separate coarse particles and then weaken the micro-structure. As a consequence, the shear stress is transmitted more and more through the coarse-fine contacts but less and less through the coarse-coarse contacts as fine content increases. The optimal fine content is about 30% under which the coarse-coarse contacts primarily support the shear stress. A decrease in the stress part carried by them is compensated by a strong increase in the stress part carried by the coarse-fine contacts. As a result, the shear strength increases with fine content. Above this optimal fine content, the coarse-fine contacts overtake the coarse-coarse contacts in carrying the shear stress. The coarse fraction is greatly weakened and is not sufficiently reinforced by the coarse-fine contacts, hence the shear strength decreases. The fine-fine contacts have little contribution to the macro-stress for a fine content smaller than 40% but their contribution is significant and increases with an increase in fine content $> 40\%$. Starting from 60%, the fine-fine contacts primarily sustain the shear stress. It was also found that the strong force network in the studied granular mixtures includes almost all the coarse-coarse contacts but no more than 50% of coarse-fine contacts. Furthermore, a major fraction of fine-fine contacts are located in the weak force network.

For fine content $< 20\%$, the coarse particles constitute primarily the solid skeleton to resist to shear loading, leaving the fine particles under lower stress. For the range of fine content between 20% and 60%, the fine particles participate actively in sustaining the shear stress. They play the role of a matrix that reinforces the solid skeleton primarily constituted of coarse particles. Above 60% of fine content, the fine particles carries primarily the shear stress and the coarse particles play the role of inclusions in the matrix formed by the fine particles.

Based on this study, a classification of binary mixtures into four limiting categories of micro-structure was proposed. The particularity of the proposed classification is that it considers the importance of the coarse-fine contacts in the micro-structure. By increasing fine content, the micro-structure of binary mixture can change from a category where the coarse-coarse contacts primarily constitute the solid skeleton, to a category where the coarse-fine contacts primarily constitute the solid skeleton, and finally to a category where the fine-fine contacts are dominant in the solid skeleton.

Chapter 4

Behavior of samples eroded by removal of fine particles

4.1 Introduction

As mentioned in Section 1.6.1, several coupled particle-fluid models such DEM-CFD, DEM-LBM, DEM-SPH and DEM-PFV have been developed to simulate the fluid flow through granular materials. However, these models are computationally very expensive to simulate a full suffusion process on widely graded granular materials. Alternative methods based on particle removal have been then proposed by several authors (Wood and Maeda, 2008; Wood et al., 2010; Scholtès et al., 2010; Aboul-Hosn, 2017) to represent the internal state of the soil after internal erosion. These methods consist in removing the smallest and the less loaded fine particles from an original sample at a given stress state to mimic the loss of fine particles caused by suffusion. We use a similar method to represent the internal state of eroded soils and then to investigate the mechanical consequences of the loss of fine particles on the mechanical behavior of gap-graded soils.

We propose a representation of the internal state of eroded soils at different levels as mentioned in Section 1.7:

- **Level 1**: an eroded sample is obtained by reducing fine content of the original sample and then reconstituting the eroded sample at a given density. We assumed that the eroded sample has the same relative density as that of the original sample. For example, if the original soil is at the densest state and contains 30% of fine content, an erosion of 10% of fine content results in an eroded sample with 20% of fine content and at the densest state. Sterpi (2003) used a similar method to investigate experimentally the mechanical consequences of suffusion. It should be noted that only the reduction in fine content caused by suffusion is taken into consideration and none of the three main mechanisms of suffusion (detachment, transport and retention of fine particles) is considered at this level. Studying the effect of suffusion by adopting this level is similar to the study of the effect of fine content on the mechanical behavior of gap-graded soils, which was presented in Chapter 2 at the macro-scale and Chapter 3 at the micro-scale.

- **Level 2**: a fraction of fine particles is removed from the original sample at a given stress state. The key point in this level is how to identify the fine particles to be removed. Two different particle removal methods are proposed. In the first method, a fraction of fine particles is randomly removed from the original sample. This method is inspired from the experimental study of Chen et al. (2016), in which a fraction of fine particles was randomly replaced by salt and are then dissolved when the water is injected into the original sample (see Section 1.5.2 for more details about this

study). The second method consists in removing a fraction of fine particles which is located in the weak force network. It is worth mentioning that only the detachment of fine particles is taken into consideration at this level.

- **Level 3**: Among all fine particles susceptible to be removed at the level 2, only those who can move through the pore network formed by the coarse particles are moved from the original sample. We propose, for this level, a model for the transport and retention of fine particles in the pore network.

This chapter focuses on the level 2 for a representation of the internal state of eroded soils and is divided into three main sections. In Section 4.2, we present the method based on the random extraction of fine particles. In Section 4.3, we propose another method to identify the fine particles susceptible to be removed by considering the weak force network in the original sample. Section 4.4 is dedicated to a comparison between different extraction methods. The densest gap-graded samples presented in Chapter 2 having $D_r = 100\%$ are considered as original samples and fine particles are extracted only at the isotropic stress state ($q/p = 0$).

4.2 Random extraction of fine particles

According to this method, fine particles are randomly removed from an original sample by successive extraction steps. For each extraction step, a fraction $\Delta\mu_e$ of fine particles is randomly removed from the original sample and a sufficient number of computation cycles is performed to bring the sample to the equilibrium while its stress state is kept constant. This extraction process is repeated until we reach a target fraction μ_e of removed fine particles, which is defined as the ratio of the mass of the removed fine particles to the total solid mass of the corresponding original sample. For example, $\mu_e = 10\%$ means that the original sample loses 10% of its solid mass due to the removal of fine particles. The fraction $\Delta\mu_e$ of fine particles removed at each extraction step can be thought of as the rate of erosion. Indeed, to erode experimentally the same mass from a sample, we can apply a high hydraulic gradient to erode quickly the sample but we can also erode slowly the sample by applying a moderate hydraulic gradient. In the study of Scholtès et al. (2010), only one fine particle is removed at each extraction process. This *particle by particle* extraction process requires very long computational time. In this study, we aim at increasing the rate of extraction to lessen the computational time of the extraction process. The influence of the parameter $\Delta\mu_e$ on the mechanical behavior of eroded samples is studied in the next section.

4.2.1 Effect of the extraction rate $\Delta\mu_e$

We considered first the well-graded sample presented in Scholtès et al. (2010), on which the extraction method proposed by Scholtès et al. (2010) (see Section 1.6.1.2) is used. Instead of removing fine particles one by one as done by Scholtès et al. (2010), we remove 1% of fine particles ($\Delta\mu_e = 1\%$) at each extraction step until 5% of fine particles is removed from the original sample. As a result, we need only 5 extraction steps to achieve the 5% of removed fine particles and 5 times for stabilizing the sample, compared to 2000 times when we extract one by one fine particles. Figure 4.1 shows stress-strain behavior of the intact sample and that of the eroded samples obtained with one by one particle extraction and with $\Delta\mu_e = 1\%$. It can be seen that the extracting each time 1% of fine particles from the original sample gives the same result as that obtained when fine particles are removed from the original sample one by one. In addition, the former method allows us to reduce significantly the computation time.

Figure 4.2 shows the stress-strain behavior of the original sample with $f_c = 30\%$ and that of the samples with 5% and 20% of eroded mass. Different extraction rates $\Delta\mu_e = 0.1\%$, 1%, 2.5% and 5% are used. The symbol f_c is used to refer to fine content of the original sample. It can be seen that a high value of $\Delta\mu_e = 5\%$ induces a greater fluctuation of the stress-strain curve of eroded samples. However,

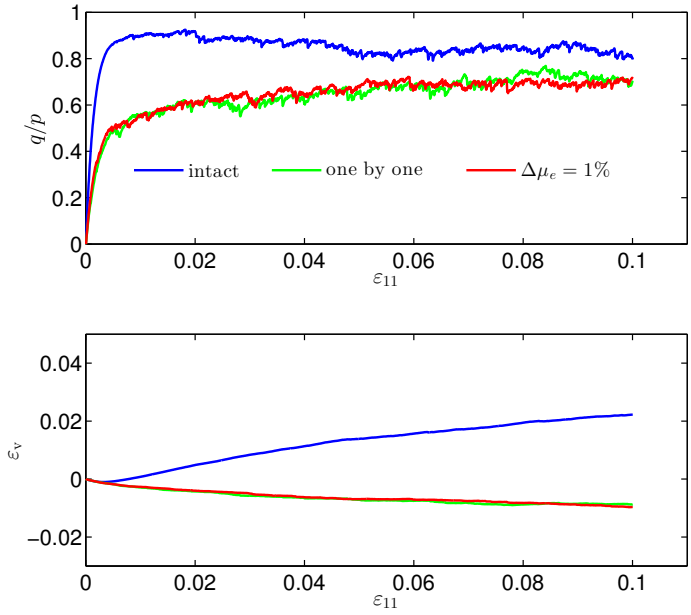

Figure 4.1: Stress ratio q/p and volumetric strain ε_v versus axial strain ε_{11} of the original sample considered in Scholtès et al. (2010) and of the eroded samples obtained with one by one particle extraction and with $\Delta\mu_e = 1\%$.

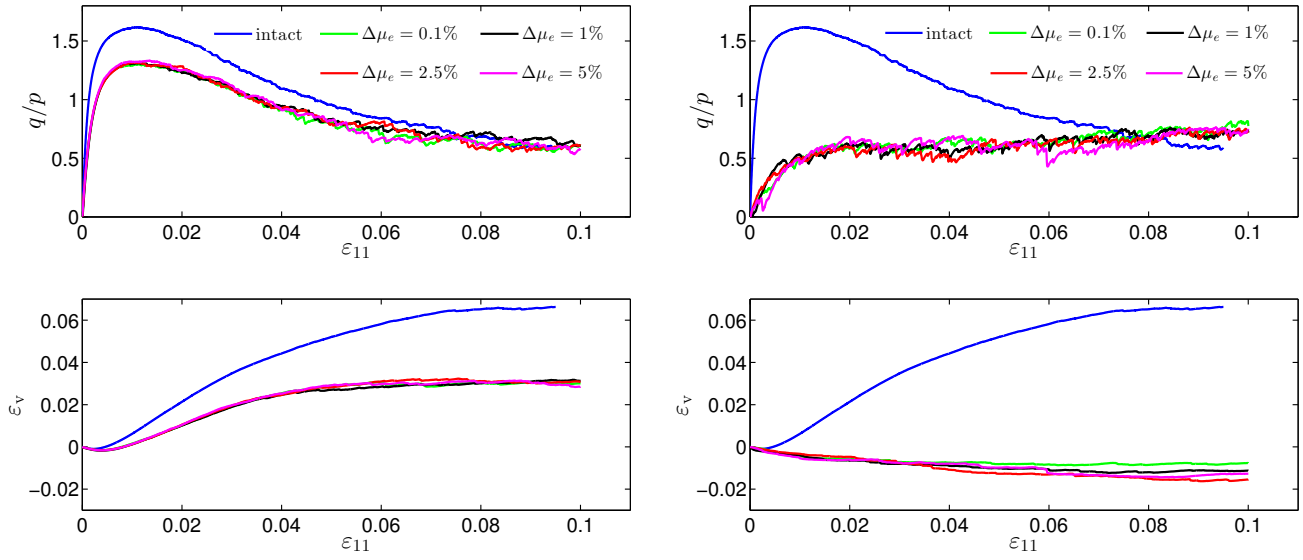

(a) $\mu_e = 5\%$ (b) $\mu_e = 20\%$

Figure 4.2: Stress-strain behavior of the original sample with $f_c = 30\%$ and of the samples eroded with different extraction rates $\Delta\mu_e$: (a) for 5% of eroded mass and (b) for 20% of eroded mass.

the extraction rate $\Delta\mu_e$ has a negligible effect on the mechanical behavior of the eroded samples. The same result is observed for the original samples $f_c = 10\%$ and 20% and with different fractions of eroded mass.

A study on the computational cost of the extraction of fine particles using different values of extraction rate $\Delta\mu_e$ is needed. Figure 4.3 presents the number of iterations of the extraction process of $\mu_e = 5\%$ and 10% of fine particles for the sample of $f_c = 30\%$ with different values of extraction rate $\Delta\mu_e$. It can be seen that, for the two values of μ_e, the number of iterations decrease with the increase of the extraction rate $\Delta\mu_e$. This decrease becomes small after $\Delta\mu_e = 0.5\%$ and for that, $\Delta\mu_e = 1\%$ is chosen for the studies presented in the following. We can also remark that the fraction μ_e of eroded fine particles affects greatly the mechanical behavior of eroded samples. The effect of this parameter will be studied in the next section.

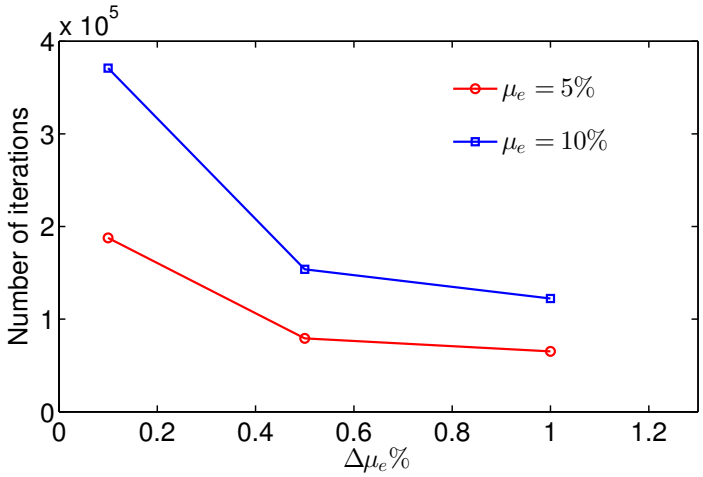

Figure 4.3: Number of iterations versus extraction rate $\Delta\mu_e$ after the extraction of 5% and 10% of fine particles from the sample of $f_c = 30\%$.

4.2.2 Macroscopic investigation

In this section, we aim to study the consequences of the random extraction of fine particles on the void ratios of eroded samples and on the mechanical behavior of eroded samples. The three densest gap-graded samples with $f_c = 10\%$, 20% and 30% whose mechanical behavior was presented in Section 2.5 are considered as the original samples. These samples are eroded by the random extraction method with different percentages μ_e of eroded fine particles. It should be noted that the parameter μ_e is defined as percentage of the mass of the fine particles removed from a given sample, compared to the total solid mass of the original sample.

Table 4.1 shows the change in the global void ratio e, the intergranular void ratio e_c and the interfine void ratio e_f for the samples with $f_c = 10\%$, 20% and 30% when different percentages μ_e of fine particles are removed from these samples. It is obvious that a removal of fine particles leads to an increase in the global void ratio e and the interfine void ratio e_f. On the other hand, the intergranular void ratio e_c remains almost constant, meaning that the extraction of fine particles does not disturb significantly the coarse particles. However, a small decrease in e_c is observed when removing 20% of fine content from the sample with $f_c = 30\%$.

Figure 4.4 shows the stress ratio q/p and the volumetric strain ε_v versus axial strain ε_{11} for the intact samples with $f_c = 10\%$ and 30% and for the eroded samples with different percentages μ_e of removed fine particles. It is shown in Figure 4.4(a) that the stress-strain behavior of the sample $f_c = 10\%$ is not significantly affected by a loss of fine particles. Even though this sample loses all the fine particles, its stress-strain behavior remains almost unchanged. This result can be explained by the fact that the fine

μ_e	$f_c = 10\%$			$f_c = 20\%$			$f_c = 30\%$		
	e	e_c	e_f	e	e_c	e_f	e	e_c	e_f
0	0.50	0.67	5.0	0.35	0.69	1.75	0.29	0.84	0.95
5%	0.58	0.67	11.0	0.42	0.69	2.67	0.35	0.83	1.34
10%	0.67	0.67	-	0.50	0.69	4.5	0.43	0.83	1.91
15%	-	-	-	0.59	0.69	10.0	0.51	0.83	2.9
20%	-	-	-	0.69	0.69	-	0.57	0.81	4.3

Table 4.1: Void ratios e, e_c and e_f for different percentages μ_e of fine particles removed from the original samples with $f_c = 10\%$, 20% and 30%.

particles in this sample are floating within voids between coarse particles and do not play a significant role in carrying the shear stress. As a result, they can be removed without changing significantly the mechanical behavior of the sample. On the other hand, a loss of fine particles leads a great change in the mechanical behavior of the sample with $f_c = 30\%$ as can be seen in Figure 4.4(b). The sample becomes looser with a decrease in shear strength and dilatancy as the percentage μ_e of eroded fine particles is increased. With a loss of 20% of fine particles, the sample with $f_c = 30\%$ changes its behavior from that of a dense sample to that of a very loose sample. Table 4.2 presents the reduction in shear strength at the peak state of the samples with $f_c = 10\%$, 20% and 30% when different percentages μ_e of fine particles are removed from them. Starting from 20%, a loss of fine particles leads to a significant reduction in shear strength at the peak state. This is related to the fact that the fine particles participate to carry the shear stress starting from 20% of fine content as shown in Chapter 3. A removal of particles that share the shear stress from a granular material makes it weaker. The sample with $f_c = 30\%$ loses half of its shear strength when 20% of fine particles is removed. Table 4.2 shows also that, with the same amount of removed fine particles, the reduction in shear strength caused by the loss of fine particles is more accentuated for a higher value of the initial fine content f_c. Indeed, the sample with $f_c = 30\%$ looses about 30% of its shear strength when it loses 10% of fine particles, while the sample with $f_c = 20\%$ loses only 12% of its shear strength with the same amount of removed fine particles. It is interesting to note in Figure 4.4 that the loss of fine particles causes a great reduction in shear strength at the peak state but not at the critical state. The shear strength at the critical state is actually more or less the same for different percentages μ_e of removed fine particles.

μ_e	$f_c = 10\%$	$f_c = 20\%$	$f_c = 30\%$
5 %	0.8	5.5	20.0
10 %	2.5	12.1	29.3
15 %	-	14.4	51.5
20 %	-	18.4	50.0

Table 4.2: Loss in percentage (%) of the maximum shear strength of the samples with $f_c = 10\%$, 20%, 30% when 5%, 10%, 15% and 20% of fine particles are removed from them.

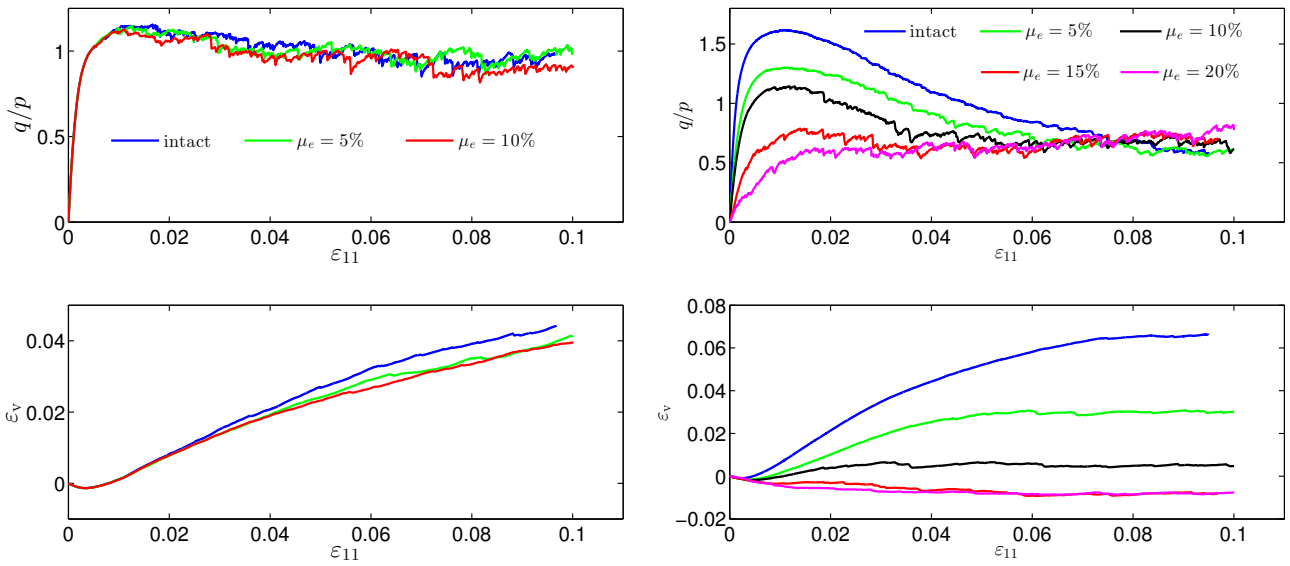

(a) $f_c = 10\%$ (b) $f_c = 30\%$

Figure 4.4: Stress-strain behavior of the intact samples and of the eroded samples with different percentages μ_e of removed fine particles: (a) for $f_c = 10\%$ and (b) for $f_c = 30\%$.

The numerical results shown above are qualitatively in good agreement with the experimental results obtained by Chen et al. (2016) (see Section 1.5.2 for some results of this study). In this study, the author replaced randomly a fraction of fine granite particles by salt particles that are dissolved when the water is injected into the samples. This experimental procedure is quite similar to the random removal of fine particles from an original sample in our simulation. The authors found that the dissolution of fine particles leads to a great reduction in shear strength at the peak of the tested granular mixtures but not at the critical state. In addition, the consequences of the loss of fine particles are more marked for the samples with 35% of fine content than for the samples with 20% of fine content.

As shown in Section 3.5, the fine particles carry no more than 20% of the shear stress applied to the sample with $f_c = 30\%$ at the peak state (Figure 3.24). A removal of fine particles does not disturb significantly the coarse particles as shown above. A question that arises here is why a removal of 20% of fine particles from this sample leads to a reduction of 50% in its shear strength at the peak state. In the next section, we will try to answer to this question by investigating the effect of the loss of fine particles at the microscopic scale.

4.2.3 Microscopic investigation

In this section we aim to study the effect of the random extraction of fine particles on the behavior of eroded samples at the micro-scale. The microscopic investigation focuses on the variation of coordination numbers with the percentage μ_e of removed fine particles and how the shear stress is carried by the fine and coarse particles in an eroded sample.

4.2.3.1 Coordination numbers

For each eroded sample, the three coordination numbers $\mathcal{N}_C^{C-C}$, $\mathcal{N}_C^{C-F}$ and $\mathcal{N}_F^{F-F}$ defined in Section 3.2.1 are calculated. As shown in Section 3.2.1, the coordination numbers $\mathcal{N}_C^{C-F}$ and $\mathcal{N}_F^{F-F}$ are very

small for the original samples $f_c \leq 20\%$. In this case, the fine particles are almost floating within the void space between the coarse particles. As a consequence, a removal of fine particles disturb slightly only the coarse particles: a slight decrease in coordination number $\mathcal{N}_C^{C-C}$ is observed when removing fine particles as shown in Table 4.3. For the original sample with $f_c = 30\%$, fine particles are in contact with coarse ones and form a strong interface between the fine and coarse fractions: the coordination number $\mathcal{N}_C^{C-C}$ equal to 45 is very high. A removal of fine particles from this sample does not destroy strongly the fraction of coarse particles but destroys strongly this interface: the coordination $\mathcal{N}_C^{C-F}$ decreases strongly with an increase in percentage μ_e of removed particles, while the coordination number $\mathcal{N}_C^{C-C}$ remains more or less constant. This means that this sample loses $C - F$ contacts between fine and coarse particles when fine particles are removed from it. It should be noted that the $C - F$ contacts play a very important role in sustaining the shear stress as shown in Section 3.3. Therefore, a loss of these contacts reduces greatly its bearing capability. In the next section, we will show how the loss of fine particles reduces the bearing capability of the coarse and fine fractions.

μ_e	$f_c = 10\%$			$f_c = 20\%$			$f_c = 30\%$		
	$\mathcal{N}_C^{C-C}$	$\mathcal{N}_C^{C-F}$	$\mathcal{N}_F^{F-F}$	$\mathcal{N}_C^{C-C}$	$\mathcal{N}_C^{C-F}$	$\mathcal{N}_F^{F-F}$	$\mathcal{N}_C^{C-C}$	$\mathcal{N}_C^{C-F}$	$\mathcal{N}_F^{F-F}$
0	5.3	0.0	0.0	5	0.4	0.0	3.8	44.9	2.2
5%	4.7	0.0	0.0	4.6	0.4	0.0	3.8	21.8	0.7
10%	4.7	0.0	0.0	4.6	0.2	0.0	3.7	11.8	0.3
15%	-	-	-	4.6	0.1	0.0	3.2	4.2	0.1
20%	-	-	-	4.6	0.0	0.0	3.2	1.3	0.1

Table 4.3: Coordination numbers $\mathcal{N}_C^{C-C}$, $\mathcal{N}_C^{C-F}$ and $\mathcal{N}_F^{F-F}$ for different percentages μ_e of fine particles removed from the original samples with $f_c = 10\%$, 20% and 30% at the initial state.

4.2.3.2 Stress carried by the fine and coarse fractions

For each eroded sample, we calculate the partial stress tensors $\widehat{\boldsymbol{\sigma}}^F$ and $\widehat{\boldsymbol{\sigma}}^C$ of the fine and coarse fractions (see Equation (3.23)) to study the stress carried by each fraction. The partial stress of each fraction is its contribution to the macroscopic stress. The mean stresses carried by these fractions are denoted by $\widehat{p}^F$ and $\widehat{p}^C$; and the deviatoric stresses carried by these fractions are denoted by $\widehat{q}^F$ and $\widehat{q}^C$. Figure 4.5 shows the mean and deviatoric stresses carried by each fraction versus the axial strain for three eroded samples obtained from the respective original samples with $f_c = 10\%$, 20% and 30% by removing 10% of fine particles. These partial stresses for each eroded sample are compared to those obtained for the corresponding original sample. Figure 4.6 shows the values of these stresses at the peak state with different percentages μ_e of extracted fine particles for two original fine contents $f_c = 20\%$ and 30%. It can be seen that even though the sample of $f_c = 10\%$ loses all fine particles, the coarse particles carry almost the same stresses as those they carry in the original sample. However, for the samples with $f_c = 20\%$ and 30%, a loss of fine particles leads to a great reduction in stresses carried by the coarse fraction. It is interesting to note that the deviatoric stress $\widehat{q}^C$ carried by the coarse fraction is much more reduced than the mean stress $\widehat{p}^C$, especially for $f_c = 30\%$. Figure 4.6(b) shows clearly that the deviatoric stress $\widehat{q}^C$ decreases strongly, while the mean stress $\widehat{p}^C$ decreases slightly with an increase in percentage μ_e of removed fine particles for $f_c = 30\%$. The coarse particles in this sample lose half of their capability to carry the deviatoric stress when it loses only 10% of fine particles. A loss of fine particles leads obviously to a reduction in stresses carried by the fine fraction as this fraction becomes looser and its solid volume

is reduced.

In order to explain why a removal of fine particles leads to a great reduction in shear strength of an eroded sample, it is important to understand the role of the removed fine particles in the corresponding original sample. For this purpose, the mean and deviatoric stresses carried by the extracted fine particles in the corresponding original sample are calculated. Their values at the peak state, normalized by the macroscopic values, are plotted versus percentage μ_e of extracted fine particles for the original samples with $f_c = 10\%$, 20% and 30% in Figure 4.7. For example, Figure 4.7 indicates that 10% of fine particles that are removed from the original sample with $f_c = 30\%$ carried initially about 12% of the mean stress p and about 7% of the deviatoric stress q applied to this original sample. The role of the removed fine particles with any value of μ_e in carrying the shear stress is small, compared to the role of the coarse fraction. If the coarse fraction kept its bearing capability, the sample with $f_c = 30\%$ would lose no more than 12% of its capability in carrying in the shear stress at the peak state when 10% of fine content is removed from it. Table 4.2 shows that this sample loses actually about 30% of its bearing capability when it losses 10% of its fine content even though the coarse fraction is not significantly disturbed by this removal of fine particles as shown in Section 4.2.3.1. In fact, for this sample, the coarse particles constitute the solid skeleton that carries primarily the shear stress and the fine particles form a matrix that reinforces the solid skeleton as shown in Chapter 3. The contacts between fine and coarse particles participate strongly in transferring the shear stress. When a fraction of fine particles is removed, the fine fraction gets looser and contacts between fine and coarse particles are disrupted. As a consequence, the coarse fraction losses the reinforcement from the fine fraction, causing a great reduction in its bearing capability.

The main drawback of the random extraction method presented above is that fine particles that are strongly loaded can be also removed. If a fine particle is strongly loaded, it is not easily detached by the seepage flow. Kenney and Lau (1985) stated that a granular soil possesses a *primary fabric*, also called *solid skeleton*, that supports primarily the shear stress. Particles within the pores of this primary fabric do not support significantly the shear stress and they are susceptible to be detached by the seepage flow. These particles are called *loose particles*. The extraction process presented above should be applied only on this loose fraction. The key point here is how loose particles are identified. In the next section, we will present two methods to identify loose particles and the consequences of a loss of loose particles on the mechanical behavior of eroded samples.

4.3 Extraction of loose particles

We discuss first the method proposed by Scholtès et al. (2010) which identifies loose particles based on the internal moment tensor $\boldsymbol{M}^p$, and another method based on the stress tensor $\boldsymbol{\sigma}^p$ defined for each fine particle in Section 3.3. We propose then another method based on the weak and strong force networks in Section 4.3.2.

4.3.1 Methods based on the internal moment tensor $\boldsymbol{M}^p$ and on the stress tensor $\boldsymbol{\sigma}^p$

The internal moment tensor $\boldsymbol{M}^p$ for each particle was defined in Equation (3.12). This tensor can be understood as the contribution of each particle to the macro-stress (see Equation (3.8)). Scholtès et al. (2010) proposed to consider the mean internal moment $m^p = \mathrm{tr}(\boldsymbol{M}^p)$ as the degree of loading of the particle under consideration. For a given sample, particles having a low degree of loading are considered as loose particles. Among the smallest particles in the sample, the authors removed the loosest ones.

The mean internal moment m^p of each particle is plotted against the particle diameter in Figure 4.8 for the sample with $f_c = 30\%$ at the initial state (Figure 4.8(a) for all particles and Figure 4.8(b) for only the fine particles). In this figure, particle diameters are sorted in an increasing order. It can be clearly seen that small particles tend to take small values of the mean internal moment m^p. This is consistent to

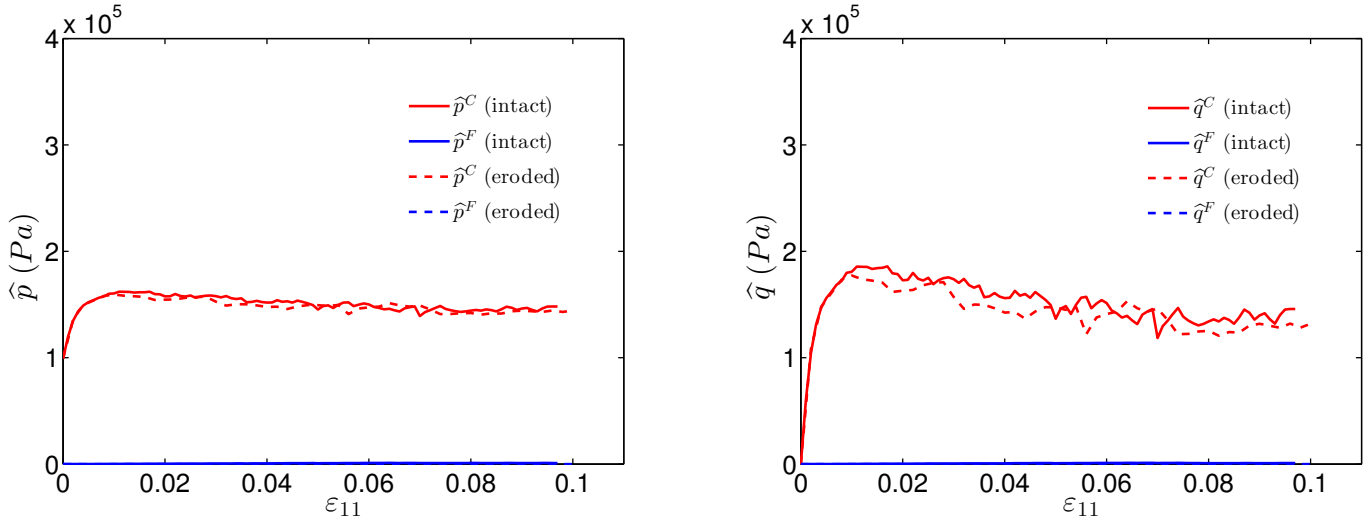

(a) $f_c = 10\%$

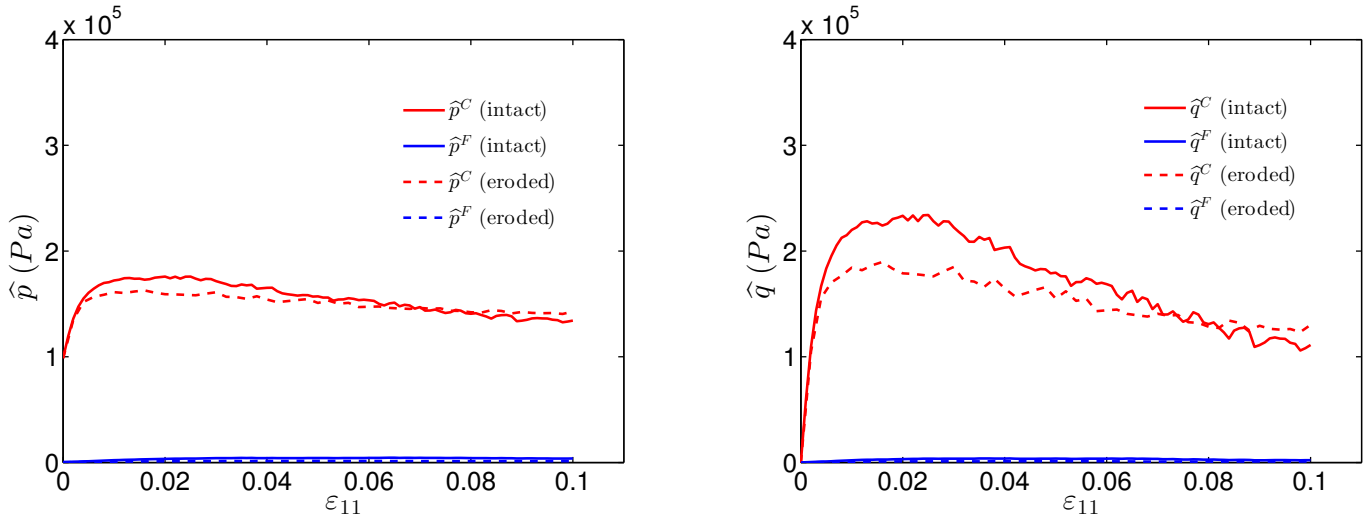

(b) $f_c = 20\%$

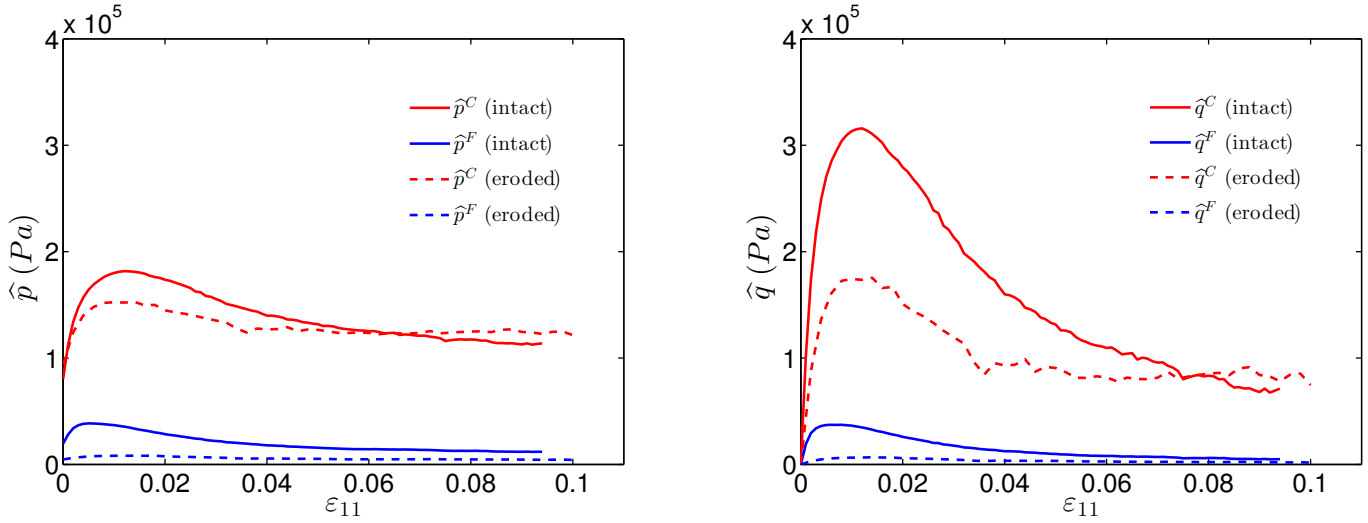

(c) $f_c = 30\%$

Figure 4.5: Mean and deviatoric stresses carried by the coarse and fine fractions versus axial strain ε_{11} for three eroded samples with $\mu_e = 10\%$ and with different initial fine contents: (a) $f_c = 10\%$, (b) $f_c = 20\%$ and (c) $f_c = 30\%$.

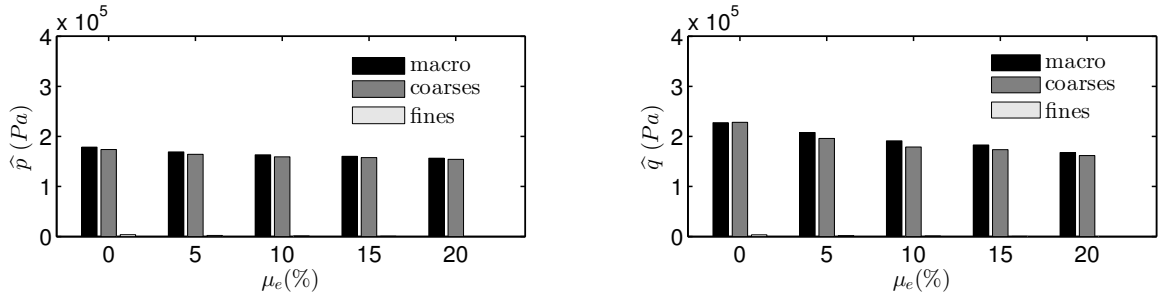

(a) $f_c = 20\%$

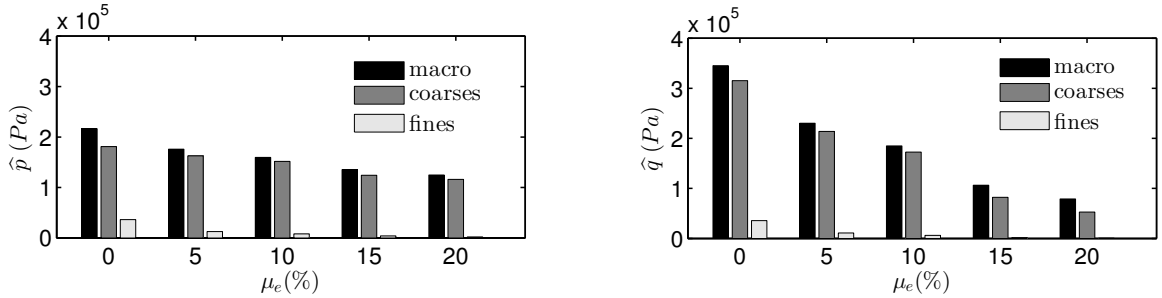

(b) $f_c = 30\%$

Figure 4.6: The mean and deviatoric stresses p and q carried by the fine and coarse fractions, compared to the macroscopic ones, versus percentage mu_e of removed fine particles at the peak state: (a) $f_c = 20\%$ and (b) $f_c = 30\%$.

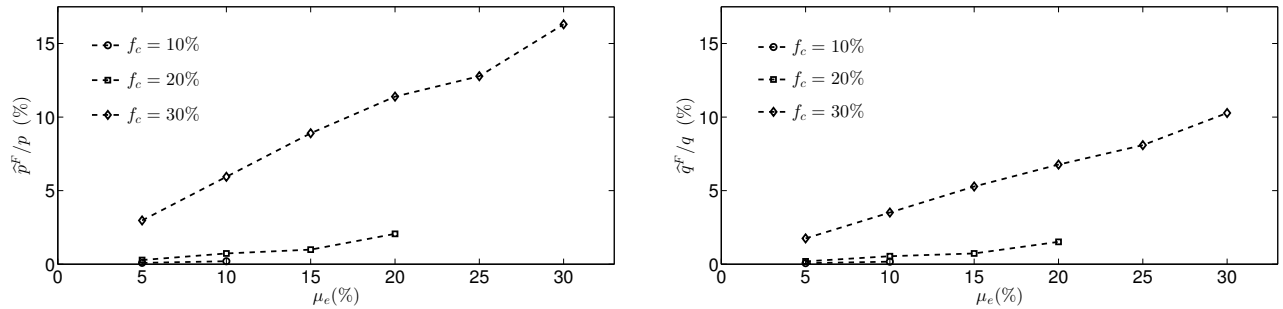

(a) Mean stress p (b) Deviatoric stress q

Figure 4.7: Mean and deviatoric stresses at the peak state carried by the extracted fine particles in the original samples with $f_c = 10\%$, 20% and 30% versus percentage μ_e of removed fine particles.

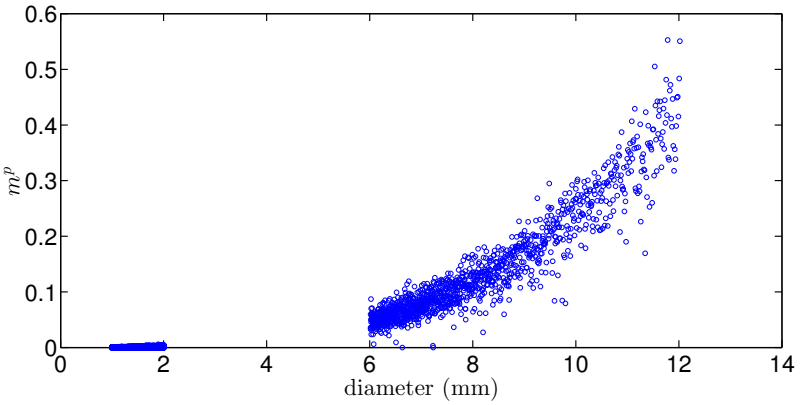

(a) for all particles

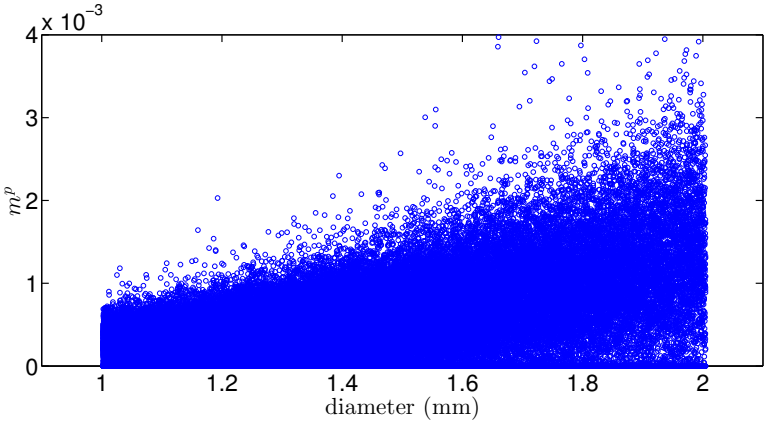

(b) for only the fine particles

Figure 4.8: Mean internal moment m^p versus the diameter of the particles in the gap-graded sample with $f_c = 30\%$ at initial state: (a) for all particles, (b) for only fine particles.

the fact that a small particle has a small contribution to the macro-stress since its size is small. Let's look at the definition of the internal moment tensor $\boldsymbol{M}^p$ in Equation (3.12). As the contact force $\boldsymbol{f}^k$ is not disproportionately scaled up with the particle radius r, the internal moment tensor $\boldsymbol{M}^p$ is indeed scaled up with r. As a consequence, a small particle that is greatly loaded can have a small value of m^p. This result means that the mean internal moment m^p might not be a relevant index for the degree of loading of fine particles since it depends closely on the particle size.

One might consider the stress tensor $\boldsymbol{\sigma}^p$ defined in Equation (3.13) to assess the degree of loading of a fine particle. Peters et al. (2005) used this stress tensor to separate strongly stressed particles from weakly stressed ones. The mean stress $\sigma_{\mathrm{m}} = \mathrm{tr}(\boldsymbol{\sigma}^p)/3$ is considered as the degree of loading for each particle. Figure 4.9 presents the mean stress σ_{m} versus the particle diameter for the sample with $f_c = 30\%$ at the initial state. This figure shows clearly that small particles tend to have high values of the mean stress σ_{m}. Let's look at the stress tensor $\boldsymbol{\sigma}^p$ in Equation (4.1) for a spherical particle:

$$\sigma_{ij}^p = \frac{1}{V_s^p} \sum_{k \in p} f_i^k r_j^k = \frac{3}{4\pi r^3} \sum_{k \in p} f_i^k r n_j^k = \frac{3}{4\pi r^2} \sum_{k \in p} f_i^k n_j^k, \tag{4.1}$$

where r is the particle radius and $\boldsymbol{n}^k$ is the unit normal vector at a contact. As the contact force $\boldsymbol{f}^k$ is not scaled down with r and the number of contacts on each fine particle is limited, the stress tensor $\boldsymbol{\sigma}^p$

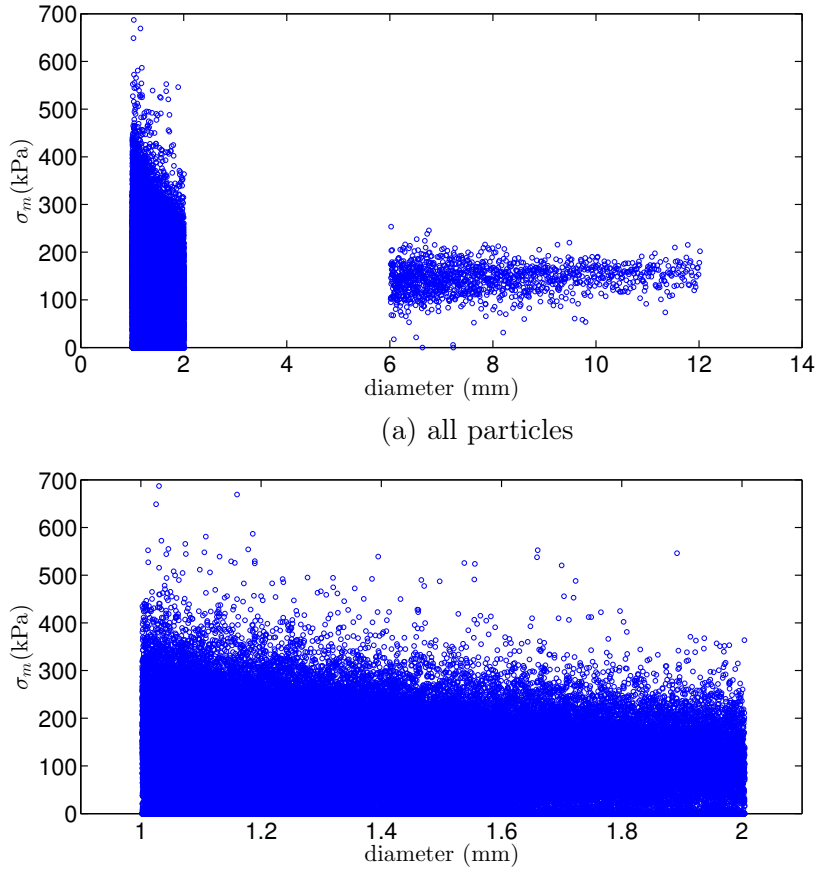

(a) all particles

(b) for only fine particles

Figure 4.9: Variation of the isotropic stress σ_{m} of each particle versus the diameter of each particle of the gap-graded sample $f_c = 30\%$ at initial state: (a) for all particles, (b) for fine particles.

defined in Equation (4.1) tends to be scaled up with $1/r^2$. It should be noted that the stress tensor $\boldsymbol{\sigma}^p$ defined in Equation (4.1) for a particle subjected to few discrete contact forces does not have the physical meaning of a Cauchy stress tensor: it is a Cauchy stress tensor only when it is used for a collection that contains a sufficient number of particles as stated by Moreau (1996).

The internal moment tensor $\boldsymbol{M}^p$ and stress tensor $\boldsymbol{\sigma}^p$ might be not adequate to assess the degree of loading of the fine particles as they depend on the particle size. In the next section, we propose another method to separate the loose fraction from the solid skeleton based on the force networks.

4.3.2 Method based on the force chain networks

The method proposed in this section consists in classifying the particles into two categories: (i) the first category contains particles that belong to the *solid skeleton*, which are considered as the non-detachable particles, and (ii) the second is the *loose fraction* which contains the weakly loaded particles. The particles in the loose fraction are considered to be detachable and they can be removed from the original sample.

4.3.2.1 Extraction method

The weak and strong force networks were defined in Section 3.4. The strong force network is composed of the strong contacts where contact force is greater than the mean contact force according to Radjai and Wolf (1998). It was also shown that the strong force network constitutes the solid skeleton that carries

primarily the shear stress applied to a granular sample. We assume that a particle belongs to this solid skeleton if the strong force network passes through it, i.e., it has at least two contacts in the strong force network. By doing so, a particle in the solid skeleton has at least two contacts with other particles in the solid skeleton as illustrated in Figure 4.10. It is worth mentioning that, to define force chains in a granular system based on the particle stress tensor defined in Equation (3.13), Peters et al. (2005) also considered that a particle in a strong force chain must have at least two strong contacts with other particles. Particles which do not belong to the solid skeleton according to the above criterion belong then to the loose fraction as illustrated in Figure 4.10.

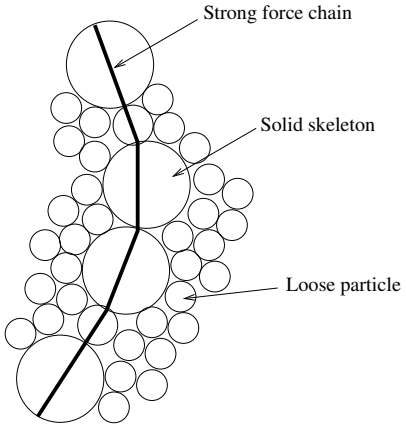

Figure 4.10: Illustration of the solid skeleton and the loose fraction in a granular assembly.

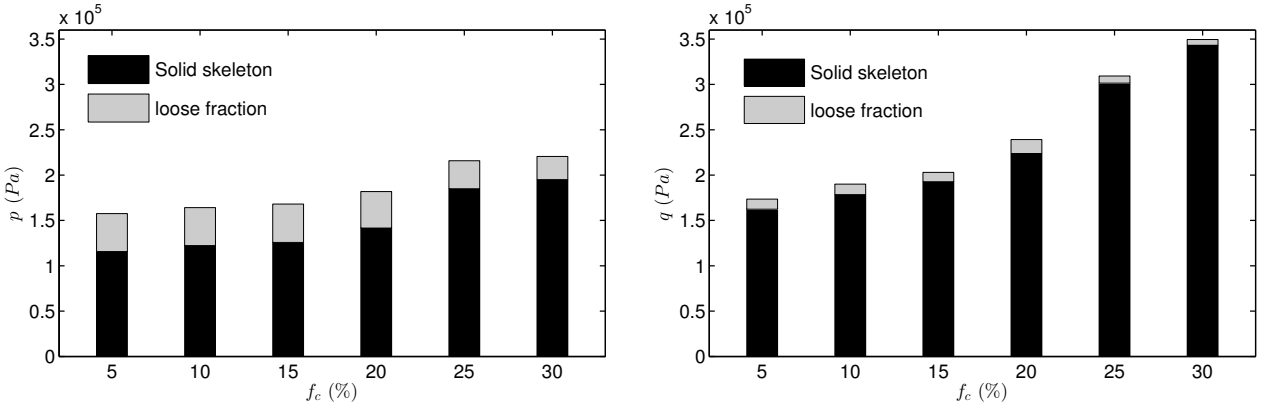

(a) Mean stress p (b) Deviatoric stress q

Figure 4.11: Mean stress p and deviatoric stress q carried by the solid skeleton and the loose fraction at the peak state versus fine content f_c.

Figure 4.11 shows the contributions of the solid skeleton and of the loose fraction to the macroscopic mean and deviatoric stresses, p and q, versus fine content f_c. This figure confirms that the solid skeleton carries primarily the shear stress. The loose fraction carries a small part of the mean stress but a negligible part of the deviatoric stress. Table 4.4 presents the percentages by mass of fine and coarse particles in the loose fraction and the percentage of floating fine particles (particles having no contact with their neighbors) for different fine contents at the initial state. These percentages are calculated with respect to the total solid mass of all the particles. It is shown that the loose fraction includes a major fraction

f_c	% of loose fines	% of loose coarses	% of floating fines
5%	5.0%	26.0%	5.0%
10%	10.0%	29.3%	10.0%
15%	15.0%	23.0%	14.9%
20%	20.0%	20.3%	19.8%
25%	24.13%	1.0%	19.12%
30%	22.0%	0.1%	10.0%

Table 4.4: Percentages by mass of fine and coarse particles in the loose fraction and that of floating fine particles for different fine contents f_c.

of fine particles but a small fraction of coarse particles. For $f_c \leq 20\%$, almost all of fine particles belong to the loose fraction and they are floating particles which carry no stress. The solid skeleton is mainly constituted of coarse particles. However, a significant fraction of coarse particles (about 30% among all the coarse particles) are located in the loose fraction. Starting from 20% of fine content, more and more fine particles participate in carrying the shear stress and then take part in the solid skeleton. Interestingly, almost all of coarse particles are included in the solid skeleton for $f_c \geq 25\%$, i.e., the loose fraction contains almost only fine particles. For 30% of fine content, a fine content of 22% is included in the loose fraction, among them 10% (with respect to the total mass) are floating particles. This means that a fine content of 8% is included in the solid skeleton.

A fraction of fine particles in the loose fraction is removed to mimic the loss of fine particles caused by suffusion. We assume that the degree of interlocking of each fine particle in the loose fraction depends on the number of contacts with its neighbors. Therefore, for each extraction step, we remove a fraction $\Delta\mu_e$ of fine particles which have the lowest number of contacts (we remove first the particles with zero contact, then those with one contact, then those with two contacts and so on). After each extraction step, the sample is stabilized until it reaches a new equilibrium at which a new solid skeleton and a new loose fraction are identified. This extraction procedure is presented in Figure 4.12.

Figure 4.13 shows the mechanical behavior of the intact sample with $f_c = 30\%$ and that of the eroded samples with 20% of fine content removed by using the above procedure. Two extraction rates $\Delta\mu_e = 0.1\%$ and 1% are used. It is shown that the extraction rate $\Delta\mu_e$ has a little effect on the mechanical behavior of eroded samples. Therefore, the extraction rate $\Delta\mu_e = 1\%$ is used in the following.

4.3.2.2 Macroscopic investigation

The macroscopic behavior of samples eroded by removing fine loose particles with the method based on the force chain networks is studied in this section. The behavior of samples eroded by this method is compared to that obtained by the random extraction method presented in Section 4.2. Figure 4.14 shows the mechanical behavior of the eroded samples with 10% and 20% of fine particles removed from the original sample with $f_c = 30\%$ by using the two aforementioned extraction methods. It is important to remind that 10% of fine particles removed refers to 10% of the total solid mass of the original sample under consideration; it does not mean 10% of the total mass of the fine particles. Like the random extraction of fine particles, the extraction of fine particles in the loose fraction leads a reduction in shear strength and in dilatancy of eroded samples. The mechanical behavior of eroded samples is more degraded with an

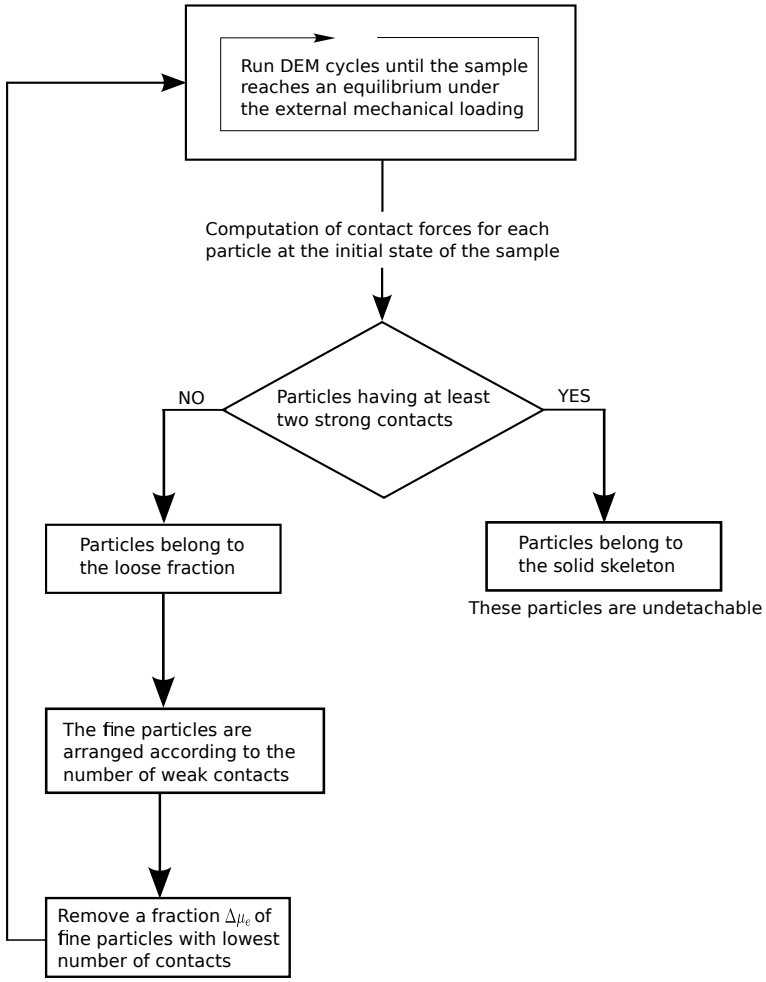

Figure 4.12: Scheme of the extraction procedure based on the force networks.

increase in the percentage μ_e of removed fine particles. It is interesting to note that the extraction of fine particles in the loose fraction disturbs less the mechanical behavior of eroded samples than the random extraction of fine particles. Indeed, with the same amount of removed fine particles, the shear strength of the samples eroded by the former method is significantly higher than that of the samples eroded by the latter method. The reduction of the peak shear strength caused by the extraction of fine particles is plotted against the percentage μ_e of removed fine particles in Figure 4.15 for $f_c = 20\%$ and 30%. It can be seen that the results given by the two extraction methods are quite close for $f_c = 20\%$. This is due to the fact that almost all of fine particles extracted from this original sample by both methods are floating particles as indicated in Table 4.4. However, these two extraction methods give different results for the sample with $f_c = 30\%$. The random extraction of 20% of fine particles causes a reduction of about 50% in shear strength to this sample, which is much higher than a value of about 28% given by the extraction of the same amount of fine particles in the loose fraction. It is clear that the difference between the results given by these methods increases with an increase in the initial fine content f_c and with an increase in the percentage μ_e of removed fine particles.

It should be noted that the floating particles in the original samples are identified at the initial state and they do not carry any stress at this state. This does not mean that these floating particles do not play any role in the mechanical behavior of the original samples. An extraction of 20% of fine particles from the original sample with $f_c = 20\%$, which are floating particles, leads indeed to a reduction of about 15% in shear strength (Figure 4.15(a)). The sample with $f_c = 30\%$ also loses about 10% of its bearing

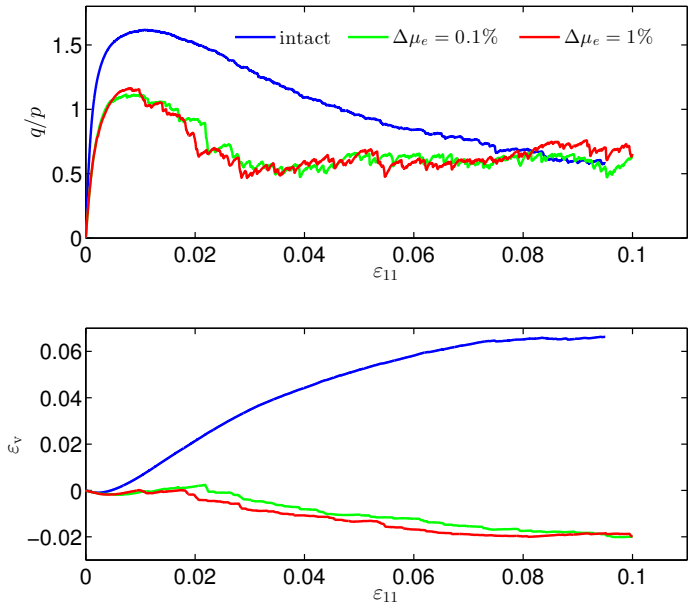

Figure 4.13: Stress ratio q/p and volumetric strain ε_v versus axial strain ε_{11} of the eroded samples with 20% of fine particles removed from the original sample with $f_c = 30\%$ by using the extraction method based on the force networks with different extraction rates $\Delta\mu_e$.

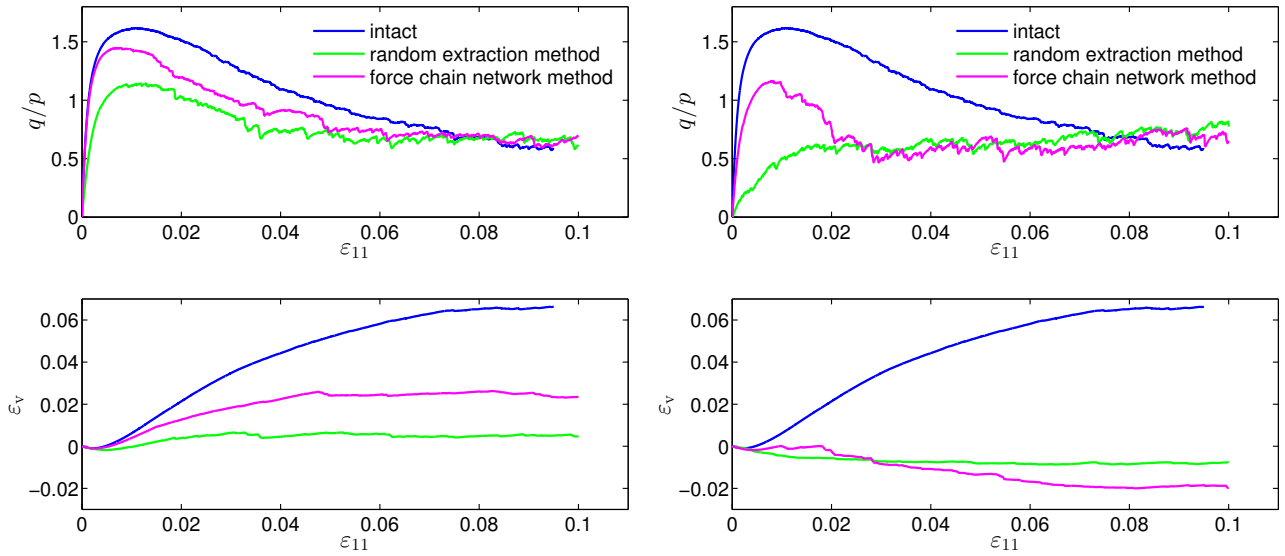

(a) $\mu_e = 10\%$ (b) $\mu_e = 20\%$

Figure 4.14: Stress ratio q/p and volumetric strain ε_v versus axial strain ε_{11} of the samples eroded from the original sample with $f_c = 30\%$ by using the random extraction method and the method based on the force chain network: (a) for $\mu_e = 10\%$ and (b) for $\mu_e = 20\%$.

capability when it loses 10% of fine particles, which are almost floating particles. Note that a particle which is floating at a given state might become active and participate then in carrying the shear stress

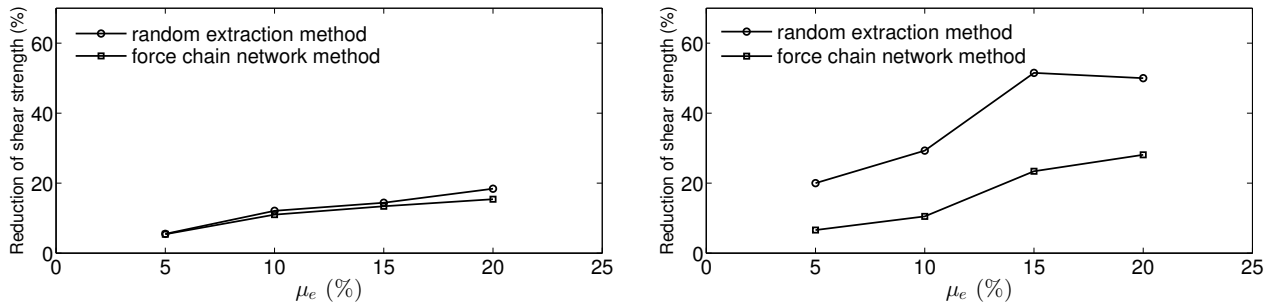

(a) $f_c = 20\%$ (b) $f_c = 30\%$

Figure 4.15: Reduction in the shear strength of the eroded samples versus the percentage μ_e of removed fine particles. The original samples with (a) $f_c = 20\%$ and (b) $f_c = 30\%$ are eroded by using the random extraction method and the method based on the force chain network.

later on. This is the reason why removing the floating particles from the original samples degrades their bearing capability.

By comparing Figures 4.15(a) and 4.15(b), one can remark that an extraction of less than 10% of fine particles in the loose fraction by using the method based on the force chain network causes almost the same reduction in shear strength (about 10%) to both samples with $f_c = 20\%$ and $f_c = 30\%$. However, an extraction of more than 10% of fine particles leads to a stronger reduction in shear strength observed for the sample with $f_c = 30\%$ than for the sample with $f_c = 20\%$. For $\mu_e = 20\%$, the former sample loses indeed about 28% its shear strength, while the latter one loses only about 15% its shear strength. It is worth mentioning that, to achieve more than 10% of extracted fine particles, we need to remove also active fine particles that carry stress from the sample with $f_c = 30\%$, while only floating particles are removed from the sample with $f_c = 20\%$. This result means that removing active fine particles that carry stress causes a greater degradation to granular samples than removing floating particles that carry no stress.

It has been shown previously that removing randomly fine particles from the original sample with $f_c = 30\%$ causes a greater reduction in shear strength than removing only loose particles which do not carry significantly stress. In the next section, we will bring some insights into this sample to explain this difference.

4.3.2.3 Microscopic investigation

The mean and deviatoric stresses carried by the fine and coarse fractions in the eroded samples obtained from the original sample $f_c = 30\%$ by removing randomly fine particles and by removing only fine particles in the loose fraction. These stresses are plotted against the axial strain for 10% and 20% of removed fine particles in Figure 4.16. It is clearly shown that a random extraction of fine particles leads to a stronger reduction in the stresses (particularly the deviatoric stress) carried by not only the fine fraction but also by the coarse fraction than an extraction of loose fine particles. This means that, with the same amount of removed particles, a random extraction of fine particles degrades more strongly the coarse fraction than an extraction of only fine particles in the loose fraction. This can be explained by the fact that fine particles in the solid skeleton are removed by the random extraction, which causes a collapse to the solid skeleton. It is worth mentioning that when fine particles in the loose fraction are removed, the solid skeleton is less disturbed although it loses the reinforcement from the fine fraction. These are the reasons which explain why a random extraction of fine particles causes a stronger reduction in shear strength to the original

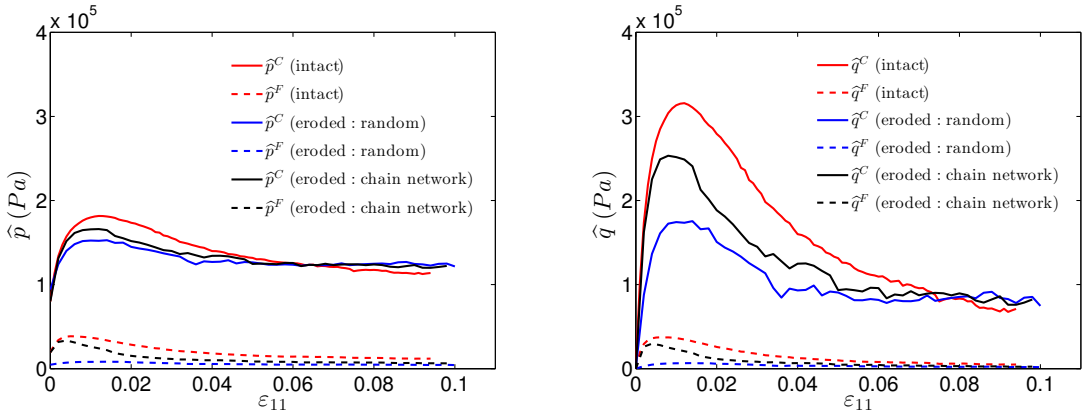

(a) $\mu_e = 10\%$

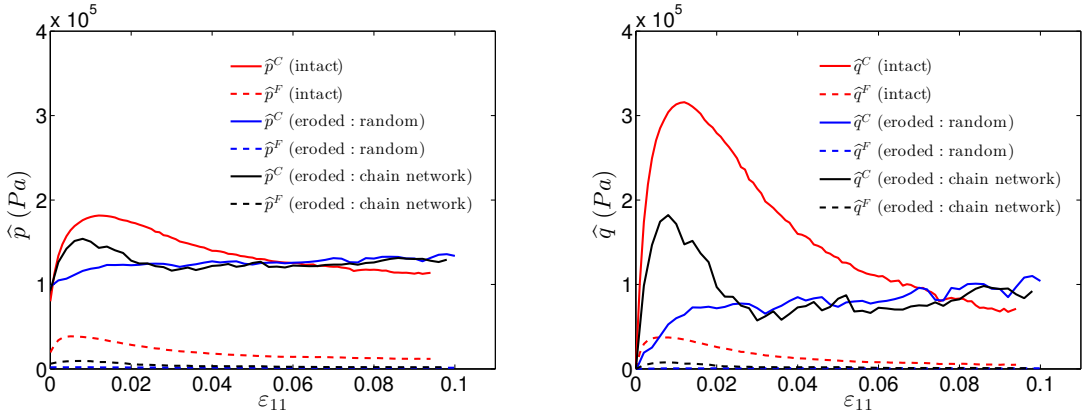

(b) $\mu_e = 20\%$

Figure 4.16: Mean and deviatoric stresses, $\widehat{p}$ and $\widehat{q}$, carried by the fine and coarse fractions in the eroded samples with (a) $\mu_e = 10\%$ and (b) $\mu_e = 20\%$ obtained from the original sample with $f_c = 30\%$.

sample with $f_c = 30\%$ than an extraction of fine particles in the loose fraction.

4.4 Comparison between different extraction methods

We presented in Sections 4.2 and 4.3.2 two particle extraction methods to mimic the loss of fine particles caused by suffusion: fine particles are randomly removed from the original sample for the first one, while only fine particles in the loose fraction, which do not carry significantly stress, are removed from the original sample for the last one. The loose fraction of a granular sample at a given state is defined based on the force chain network. A comparison between these two methods was presented in Section 4.3.2.2. In this section, we present a comparison of these two methods with the method proposed by Scholtès et al. (2010) (see Section 4.3.1) and the method of level 1 mentioned at the beginning of the chapter. For the last method, the fine content on the particle size distribution curve of a given original sample is reduced and a new sample, considered as an eroded sample, is prepared at the same relative density as that of the original sample.

Let's start this comparison by considering the well-graded sample used by Scholtès et al. (2010). Figure 4.17 shows the stress-strain behavior of the samples eroded at the initial state with 5% of removed fine particles by using the random extraction method, the extraction method based on the force chain network

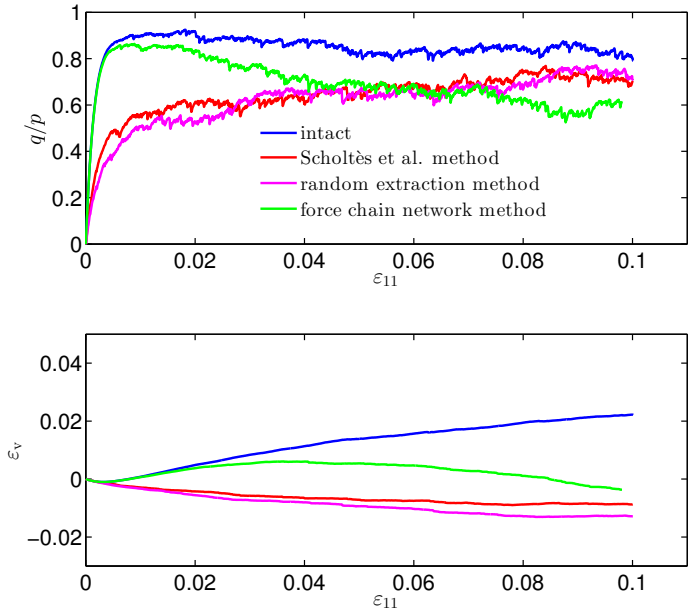

Figure 4.17: Stress ratio q/p and volumetric strain ε_v versus axial strain ε_{11} after the extraction of 5% of fine particles from the well-graded sample used by Scholtès et al. (2010) using different extraction methods.

and the method of Scholtès et al. (2010). It can be seen that the eroded samples obtained with the random extraction method and the method of Scholtès et al. (2010) show similar stress-strain behaviors but greatly different from that given by the extraction method based on the force chain network which gives a smaller change in stress-strain behavior of the eroded sample. Similar results are observed for the eroded samples obtained from the gap-graded sample with $f_c = 30\%$ as shown in Figure 4.18. The difference between the results given by these particle extraction methods increases with an increase in percentage of removed fine particles as shown in Table 4.5. For a loss of 20% of fine content, the method of Scholtès et al. (2010) gives a reduction of about 59% in shear strength, much higher than the value of about 28% given by the method based on the force chain network.

μ_e	Level 1	Scholtès et al. method	Random extraction method	Force chain network method
5 %	6.06	18.2	20.0	6.6
10 %	17.94	25.0	29.3	10.5
15 %	25.91	48.2	51.5	23.4
20 %	28.63	58.8	54.7	28.1

Table 4.5: Loss in % of the shear strength of the sample with $f_c = 30\%$ caused by an extraction of fine particles by using different methods.

As discussed in Section 4.3.1, Scholtès et al. (2010) considered the internal moment tensor $\boldsymbol{M}^p$ to identify the less loaded fine particles. The tensor $\boldsymbol{M}^p$ might get a small value for a small particle, even though it is strongly loaded and belongs to a strong force chain. This small particle might be removed from the original sample according to this method. A removal of fine particles from the strong force

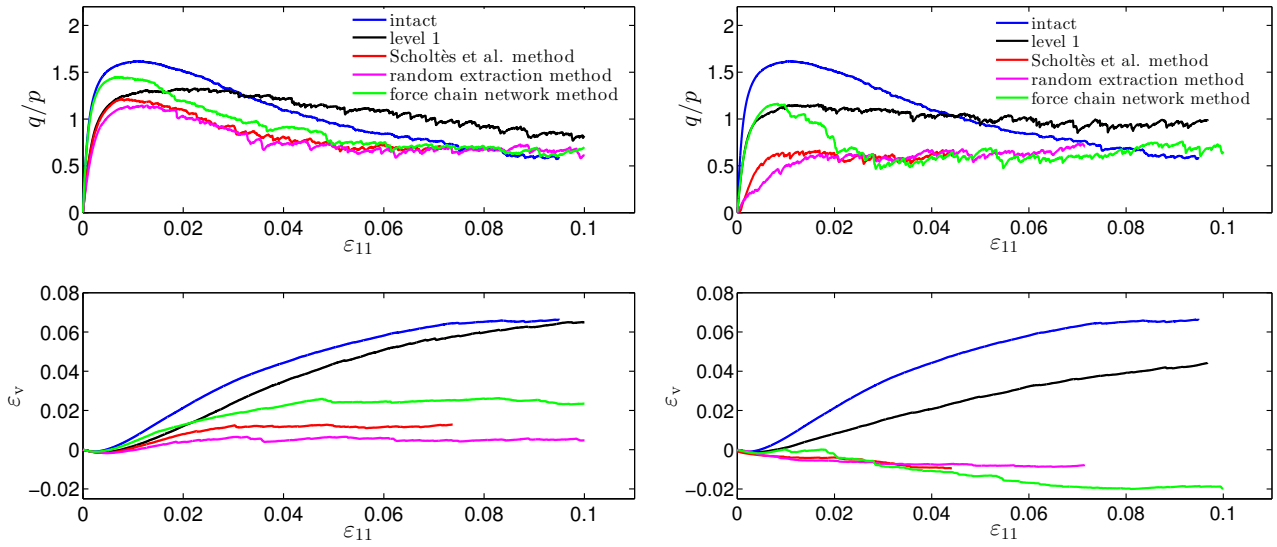

(a) $\mu_e = 10\%$ (b) $\mu_e = 20\%$

Figure 4.18: Stress ratio q/p and volumetric strain ε_v versus axial strain ε_{11} for the eroded samples with (a) 10% and (b) 20% of fine particles removed from the original sample $f_c = 30\%$ with different methods.

chains disturbs strongly the granular micro-structure, leading to a great reduction in shear strength. It is worth noting that fine particles are also removed from the strong force chains by the random extraction method. This might explain why the random extraction method and the method of Scholtès et al. (2010) give similar results. On the other hand, the method based on the force chain network removes only fine particles from the weak force network. The granular micro-structure is thus less disturbed, which explains why this method gives a smaller reduction in shear strength than the random extraction method and the method of Scholtès et al. (2010).

Method	$\mu_e = 10\%$	$\mu_e = 20\%$
Level 1	0.35	0.50
Method of Scholtès et al.	0.43	0.60
Random extraction	0.42	0.57
Force chain network method	0.43	0.60

Table 4.6: Initial global void ratio e of the eroded samples obtained with different methods from the original sample with $f_c = 30\%$.

It is also shown in Figure 4.18 that the method of level 1 gives a result greatly different from those given by the other methods. Interestingly, although the eroded samples given by this method are compacted to reach the densest state, their shear strength at the peak state is lower than that obtained with the method based on the force chain network, which are much looser. As shown in Table 4.6, the eroded sample with $\mu_e = 10\%$ obtained with the method of level 1 ($e = 0.35$) is indeed much denser than that obtained with the method based on the force chain network ($e = 0.43$); however, the former sample is

less strong than the latter sample. This might be related to the fact the original sample with $f_c = 30\%$ possesses a strong solid skeleton constituted of almost all of coarse particles and of an important fraction of fine particles. Despite a loss of fine particles in the loose fraction, an important fraction of fine particles remain in the solid skeleton and participate in carrying stress. For the eroded sample given by the method of level 1, despite a lower apparent void ratio, almost all of fine particles are floating and do not carry significantly stress. It is also interesting to note that the three eroded samples with $\mu_e = 10\%$ obtained with the method of Scholtès et al., with the random extraction method and with the method based on the force chain network have close void ratios but they show different stress-strain behaviors. Hicher (2013) assumed in his homogenization technique that the reduction in shear strength of an eroded soil results only from an increase in porosity caused by suffusion (see Section 1.6.2). The above result brings this assumption into question.

4.5 Conclusions

Different particle removal methods have been presented in this chapter to represent the internal state of a soil after suffusion. The random extraction method was inspired from the salt dissolution experiment performed by Chen et al. (2016). According to this method, fine particles are randomly removed from the original sample to mimic the loss of fine particles caused by suffusion. The shear strength of eroded soils has been found to decrease with an increase in percentage of removed fine particles for the original samples with fine content greater than 20%. This reduction in shear strength is related to the fact that the coarse fraction, which constitutes primarily the solid skeleton to carry the shear stress, loses the reinforcement from the fine fraction when fine particles are removed. The main drawback of this method is that it removes also fine particles which are strongly loaded. In fact, when a granular soil is subjected to suffusion, the seepage flow tends to wash out only slightly stressed fine particles. In order to mimic the detachment of fine particles caused by the seepage flow, it is then necessary to identify slightly loaded fine particles to be removed.

Scholtès et al. (2010) identified the less loaded fine particles by using the internal moment tensor $\boldsymbol{M}^p$ defined for each particle. However, a small particle tends to have a small value of $\boldsymbol{M}^p$, even though it is strongly loaded. Strongly loaded fine particles might be removed by this method. As a consequence, this method gives a result quite similar to that given by the random extraction method. We proposed a method to identify slightly loaded fine particles based on the force chain network. According to this method, particles that have at least two contacts in the strong force chains are considered to belong to the solid skeleton and cannot be washed out by the seepage flow. The other particles belong to the loose fraction which does not carry significantly stress. Only fine particles in the loose fraction are removed. A comparison with the random extraction method showed that removing fine particles according to this method disturbs less the solid skeleton so the impact of the loss of fine particles on the shear strength of eroded samples is reduced. It was also shown that different particle removal methods lead to different stress-strain behaviors of eroded samples although their initial void ratios are quite close. In comparison with the method of level 1, which consists in reconstituting a sample with lower fine content than the original one, the new method leads, on one hand, to a higher global void ratio of the eroded sample, but on the other hand, to higher shear strength and dilatancy of the eroded sample for the same amount of eroded fine particles.

It is worth mentioning that the three particle removal methods presented above do not take into account the transport of fine particles and the blockage of fine particles by constrictions. A fine particle detached by the seepage flow does not necessarily move out from the original sample as it might be blocked by a constriction smaller than its size. In the next chapter, we will present a strategy to take into account these two main mechanisms in a particle removal method with the aim to mimic the loss of fine particles caused by suffusion.

Chapter 5

Description of the pore network based on the Delaunay triangulation

5.1 Introduction

In Chapter 4, we have introduced two methods to represent the internal state of a soil after suffusion based on the DEM. In these methods, the representation of the internal state of an eroded soil is based on level 2, which is the removal of fine particles from the intact samples to obtain eroded samples. Fine particles are randomly removed in the first method, while only fine particles which do not participate significantly in sustaining the shear stress are removed in the last method. It should be noted that only the detachment of fine particles is considered at this level of representation. A detached fine particle can move in the void space and can be blocked by constrictions smaller than its size. Only the removal of fine particles does not represent fully the main mechanisms of suffusion.

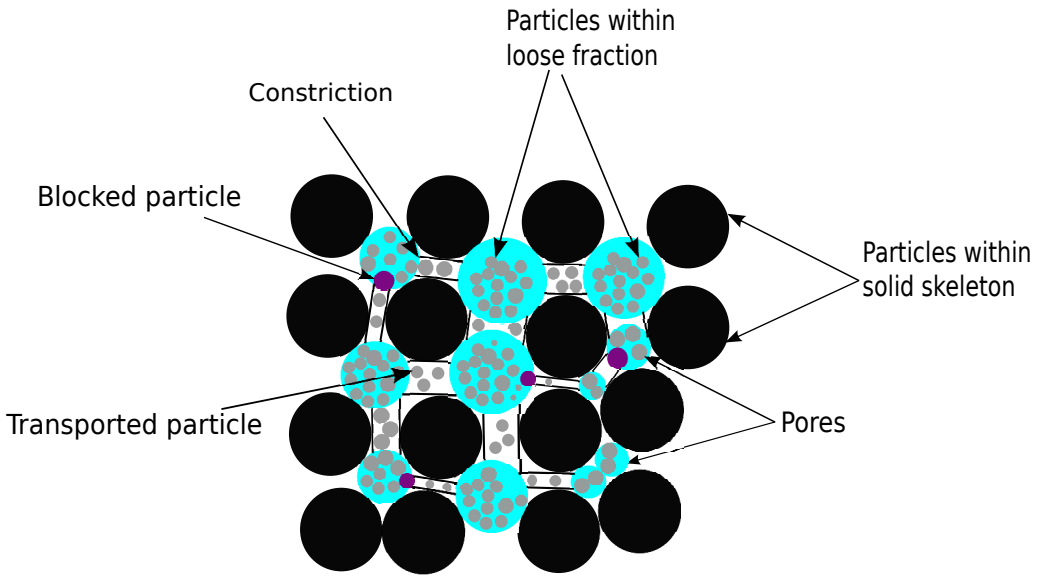

Figure 5.1: Strategy for representing the internal state of an eroded sample at level 3.

We aim to introduce a representation of level 3 for which in addition to the detachment of fine particles, the transport and the blockage of fine particles by constrictions in the pore network are taken into account. The particles are split into two categories: non-detachable particles which constitute the solid skeleton and detachable particles which belong to the loose fraction (the solid skeleton and the loose frac-

tion are defined by using the method presented in Section 4.3.2). The detachable particles are contained within pores formed by the non-detachable particles as illustrated in Figure 5.1. Each detachable particle is moved from one pore to a neighboring one according to a certain rule. If the size of the detachable particle is bigger than the constriction size, the particle is retained by the constriction. Otherwise, it passes through the constriction to go to another pore. All the detachable particles are moved within the pore network until all of them are blocked by constrictions or move out of the sample. It is important in this pore network model to define the pore network formed by the solid skeleton.

This chapter focuses mainly on the description of the pore network of a granular sample. This chapter is organized as follows. The numerical samples considered in this chapter will be first presented. A literature review of pore network models and of methods for describing the pore network of granular materials is then presented. Next, we propose a new method for defining the pore network based on the Delaunay triangulation. This method will be finally compared to other methods.

5.2 Numerical samples

The numerical samples considered in this chapter are identical to those considered by Reboul et al. (2008, 2010); Sjah and Vincens (2013); Seblany et al. (2018). They are composed of spherical particles. Two samples have a uniform particle size distribution (UG) and the two others have a gap-graded particle size distribution (GG). The particle size of the samples UG varies from 3 mm to 12 mm as shown in Figure 5.2(a) with a coefficient of uniformity $C_u = 1.7$. For the GG samples, the grain size distribution curve is presented in Figure 5.2(b) with particle size between 0.7 mm to 10 mm, a coefficient of uniformity $C_u = 3.6$ and a fine content of about 20%.

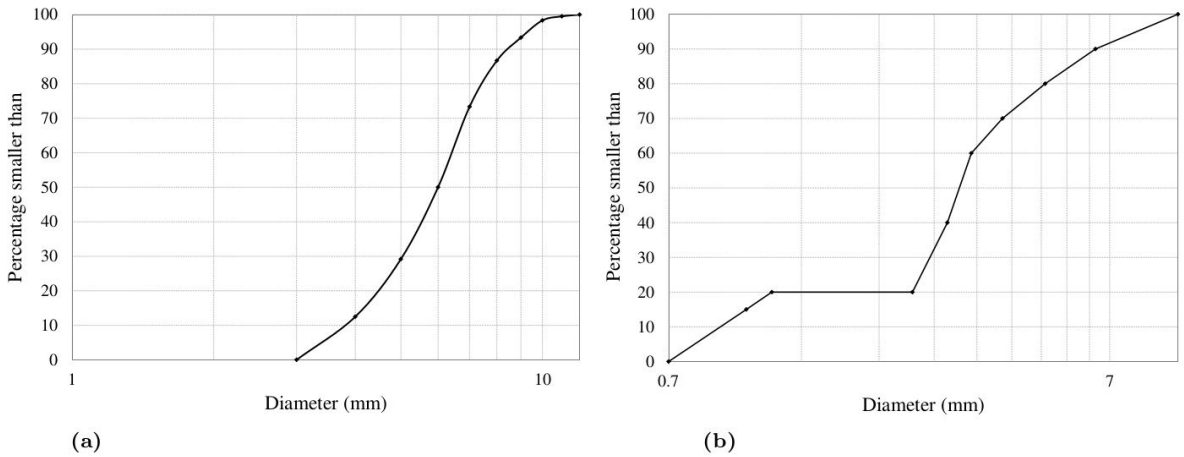

Figure 5.2: Particle size distribution for (a) UG samples and (b) GG samples (Seblany et al., 2018).

For the generation of these samples, we use the same method as the one used by Seblany et al. (2018). A loose cloud of spheres with a prescribed particles size distribution is initially generated in a box. Spheres fall freely then in the box under gravity. This process is terminated when all particles reach a quasi-static equilibrium. The loosest and the densest states are obtained by setting the inter-particle friction coefficient μ to 0.7 and 0, respectively. The parameters used for the simulated samples are shown in Table 5.1. The characteristics of the loosest and densest numerical samples UG and GG are summarized in Table 5.2.

Local parameters	**Value**
Mass density ρ	2530 kg/m^3
Particle stiffness k_n/D	250 MPa
Particle stiffnesses ratio k_t/k_n	1
Inter-particle friction φ	0.7 (loosest state) - 0 (densest state)
Damping coefficient ζ	0.7

Table 5.1: Parameters of the considered samples.

Material	**UG**	**GG**
Coefficient of uniformity (C_u)	1.7	3.6
D_0-D_{100} (mm)	3-12	0.7-10
Number of particles	6000	25000
Maximum porosity	0.4	0.34
Minimum porosity	0.34	0.25

Table 5.2: Characteristics of the numerical samples UG and GG.

5.3 Literature review

Void space in a granular soil is a continuous network of pores. Pore bodies are associated to the relatively wide portions and pore throats, also called constrictions, are the relatively narrow portions that separate the pore bodies. Vogel and Roth (2001); Reboul et al. (2008) reported that pores and constrictions constitute a partition of the void space accessible to define respectively its morphology and its topology. Seblany (2018) reported that constrictions play a major role in understanding the filtration properties of granular materials because they form the main obstacles at which the fine particles can be trapped if their diameter is bigger than the constriction diameter. Therefore, it is very important to represent pores and constrictions by a 3D network of pores interconnected by constrictions. A pore network can be used to compute important macroscopic transport properties.

There exist two ways to represent 3D networks of interconnected pores and constrictions. The first method consists in creating an equivalent network using distributions of basic morphologic parameters by idealizing the complicated soil structure. The second method is to directly map a specific porous medium onto a network structure. The fundamental difference between the two methods is that the direct mapping provides a one-to-one spatial correspondence between the porous medium structure and the network structure, whereas the pore network obtained with the first method is equivalent only in a statistical sense to the modeled system. However, the first method is simple and able to quickly generate fluid flow characteristics in a complex soil structure (heterogeneous soil). We will present some studies in literature which are based on these two methods in Sections 5.3.1 and 5.3.2

5.3.1 Idealized pore networks

To compute the probability of the fine particles passing through the constrictions, it is very important to determine the constriction size distribution (CSD) of a given granular soil, so the CSD is a parameter to assess the soil retention capability. Silveira (1965) proposed a multi-layered constriction network involving one-directional transport of fine particles. Every layer has an associated constriction size and the fine particles can cross the layer if their sizes are smaller than the associated constriction size of this layer. Kenney et al. (1985) also used a filter model consisting of a number of unit layers. Each layer is modeled by a plate containing holes that are identical in size distribution to the constriction size distribution of the filter material. Figure 5.3 represents the proposed model of the filter containing many layers. The length of flow path increases by addition of unit layers. The aim of this model is to determine D_c' which is the minimum constriction size along a flow path that governs the size of the largest particle which can be transported along that flow path. After that, they computed the maximum possible size $D_c^\star$ of particles that can be transported through a filter of specific thickness. In fact, $D_c^\star$ is equal to the maximum value of D_c' among all flow paths. In this pore network model, flow paths are only vertically aligned, which is a high simplification of the true pore network.

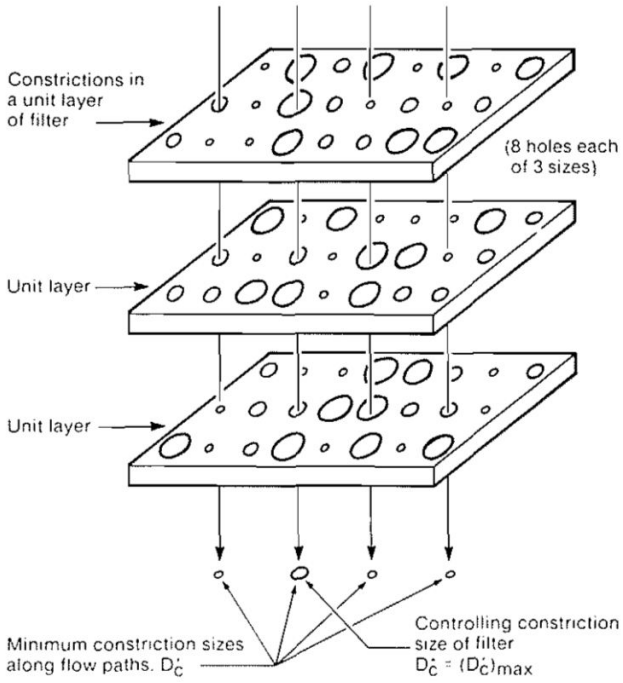

Figure 5.3: Pore network of a granular filter modeled as plates containing holes by Kenney et al. (1985).

Indraratna and Vafai (1997) used an alternative model representing the filter voids as a series of parallel channels, where the smallest constriction (D_0) controls the size of base particles that can cross the filter as illustrated in Figure 5.4.

Schuler (1996); Locke et al. (2001) used a regular cubic network model as illustrated in Figure 5.5. In such a model, each node corresponds to a pore and every two neighboring pores are connected by a tube representing a constriction. As a result, each pore is connected to its six neighboring pores by six tubes. The size of tubes is specified to match a given constriction size distribution. Sjah and Vincens (2013); Vincens et al. (2015) used this regular cubic network to determine the probability of the movement of a particle within granular filters. Recently, Shire and O'Sullivan (2017) have also used the regular cubic network to develop the pore-network model that uses an area-biased random walk approach to simulate

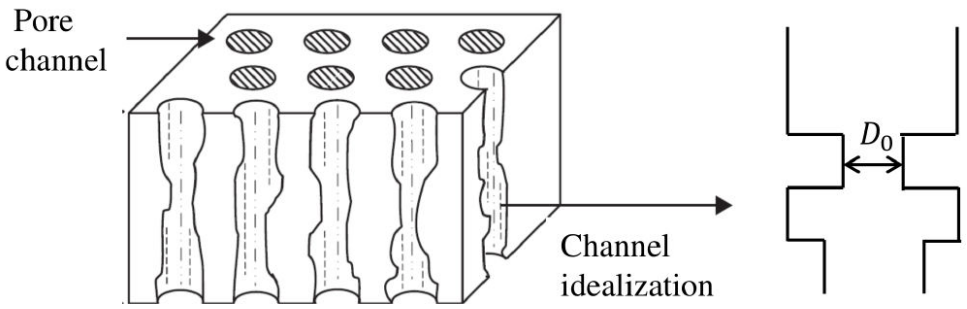

Figure 5.4: Void channel model (Indraratna and Vafai, 1997).

the percolation of a base material through a given filter using the filter constriction size distribution (CSD) and the base particle size distribution (PSD). It should be noted that the pore networks presented above are highly idealized and are far from the true pore network of a granular material. In the next section, we will present some methods to extract the true pore network.

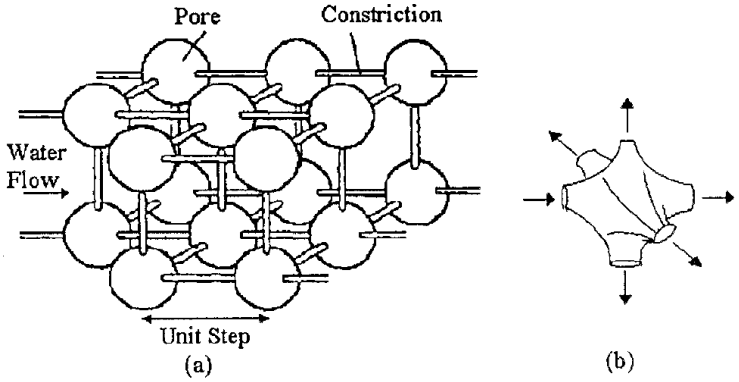

Figure 5.5: (a) Cubic network pore model; (b) single pore with six constrictions (Schuler, 1996).

5.3.2 Methods for extracting the true pore network

5.3.2.1 Methods developed for physical granular samples

Different experimental techniques have been developed to extract the pore network of a granular material. Witt (1986, 1993) used a high elastic liquid rubber to fill a gravel material until its saturation; after hardening, all grains were removed and the elastic matrix was dissected into single pores. A statistical study was carried out over these imprints to determine the pore and constriction sizes. The disadvantages of this technique are that it takes a long time to be applied, due to a large amount of pores and it is difficult to apply for materials of small particles. Another advanced technique makes use of the micro-computerized tomography scanning (micro-CT) of real soils. Figure 5.6(a) shows a 3D image of Fountainebleau sandstone obtained with the micro-CT scanning. A numerical technique is then applied to detect the portions and the sizes of the pores and constrictions from the image data. The maximal ball algorithm (Silin et al., 2003; Dong and Blunt, 2009) consists in finding the largest inscribed spheres centered on each voxel of the image that just touch the grain or the boundary and then removing spheres that are included in other spheres. The largest maximal balls identify pores while the smallest balls between pores are throats. Figure 5.6(b) shows the pore network extracted from the 3D image shown in Figure 5.6(a) by using the maximal ball algorithm. Lindow et al. (2011); Homberg et al. (2012) proposed another algorithm based on the Voronoï graph. Figures 5.7 shows the Voronoï graph for a sample composed of spherical particles.

For this graph, the edge between two Voronoï nodes is curved and run along the maximal distance to the surrounding solid spheres. The centers of pores are located where the distance to the surrounding spheres is maximal along the edge, while the centers of constrictions are located where the distance to the surrounding spheres is minimal along the edge. It should be noted that the Voronoï decomposition leads to an excessive artificial partition of the void space so neighboring pores must be merged to form single pores (Vincens et al., 2015). The criterion proposed in Seblany et al. (2018) consists in comparing the size of a given constriction $d_{C_{ij}}$ to the sizes d_{P_i} and d_{P_j} of the two adjacent pores sharing this constriction by defining a *relative diameter difference* $t_{diff}(P_i, C_{ij}, P_j) = d_P - d_{C_{ij}})/d_P$ with $d_P = \min(d_{P_i}, d_{P_j})$. The relative diameter difference t_{diff} indicates then the degree of separation between two adjacent pores. If $t_{diff} < t$ with t being a user-specified value, two adjacent pores are not sufficiently separated so they are merged together. It is worth mentioning that the two algorithms mentioned above are efficient to extract the pore network from realistic granular materials. However, they are very time-consuming and the micro-CT scanning technology is very expensive and not accessible to any research team.

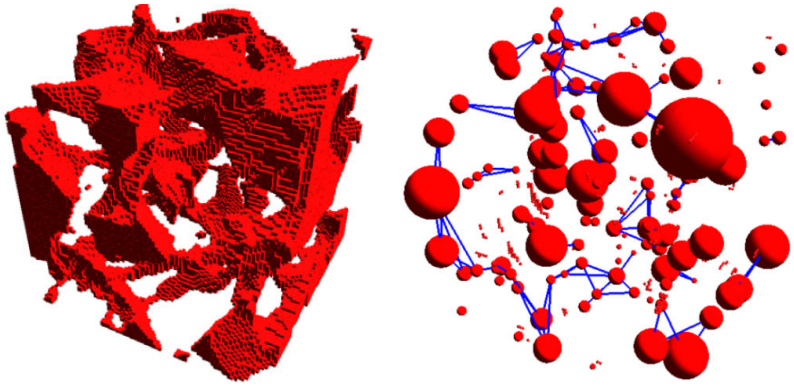

Figure 5.6: (a) A 200x200x200 voxels image of Fontainebleau sandstone and (b) the pore network extracted by the maximal ball algorithm (Silin et al., 2003).

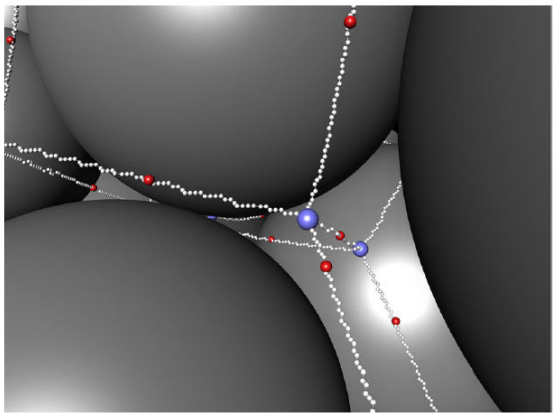

Figure 5.7: Voronoï graph indicating the center of a pore (blue sphere) and the location of the constrictions (red sphere) (Vincens et al., 2015).

5.3.2.2 Methods developed for virtual granular samples

Instead of using the micro-CT scanning to obtain a 3D image of physical granular materials, the DEM can be used to create virtual granular samples, for instance the numerical samples composed of spherical particles presented in Section 5.2. Each spherical particle is fully described by its center and its radius.

The pore network of these numerical samples can be extracted by using methods based on the Delaunay triangulation proposed by several authors (Al-Raoush et al., 2003; Reboul et al., 2008; Okabe et al., 2009; Sufian et al., 2015; Shire et al., 2016; Seblany et al., 2018).

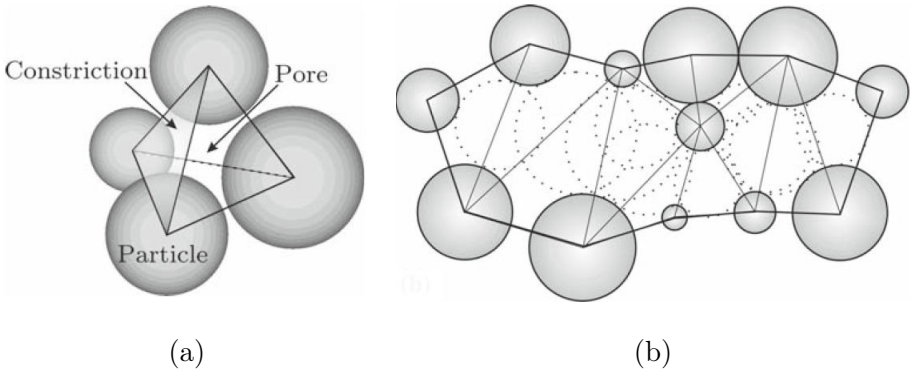

(a) (b)

Figure 5.8: (a) A 3D Delaunay tetrahedron and (b) 2D illustration of the Delaunay triangulation (Reboul et al., 2008).

The Delaunay triangulation consists in subdividing a granular volume into a set of tetrahedra whose vertices are the centers of four neighboring spheres (Figure 5.8(a)). The void volume within a tetrahedron defines a pore and the void area on each face of a tetrahedron defines a constriction. Edelsbrunner and Shah (1996) modified the classical Delaunay triangulation to the weighted Delaunay triangulation by generalizing the first one to weighted points, where weights account for the radius of spheres. It is generally accepted that the weighted Delaunay triangulation leads to an incorrect identification of pore locations and sizes since this technique tends to subdivide a single pore into multiple smaller pores as stated by Reboul et al. (2008); Vincens et al. (2015); Seblany et al. (2018). Therefore, neighboring tetrahedra need to be merged to form correct pores.

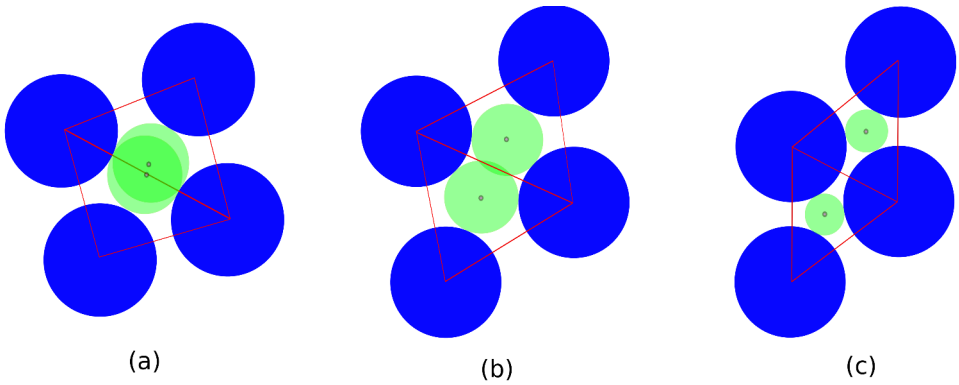

Figure 5.9: 2D illustration of three cases where two adjacent inscribed void spheres (a) overlap greatly, (b) overlap slightly and (c) do not overlap

Al-Raoush et al. (2003) introduced the concept of an *inscribed void sphere* which is tangent to the four adjacent solid spheres of each tetrahedron. A numerical technique for identifying the inscribed void sphere for each tetrahedron was presented in Reboul et al. (2008). Figure 5.8(b) shows a 2D illustration of the Delaunay triangulation: each triangle and each dashed circle correspond to a tetrahedron and an inscribed void sphere in the 3D case, respectively. We can notice that inscribed void spheres might overlap each other. Figure 5.9 shows three cases where two adjacent inscribed void spheres overlap greatly, overlap

slightly and do not overlap. The overlap between two adjacent inscribed spheres indicates the degree of interconnection between the two corresponding adjacent tetrahedra.

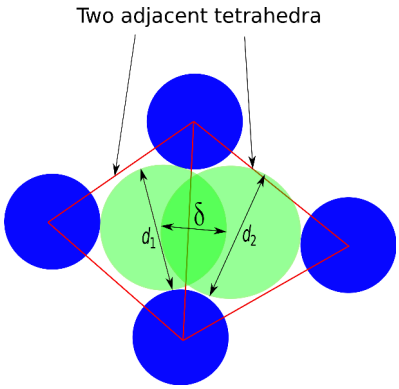

Figure 5.10: Overlap δ between two adjacent inscribed spheres.

Al-Raoush et al. (2003) proposed to merge every couple of adjacent tetrahedra if the center of an inscribed void sphere is located inside the other void sphere. By using this criterion, the two adjacent tetrahedra of case (a) in Figure 5.9 are merged together, while those of cases (b) and (c) are not merged. Sufian et al. (2015) proposed a stricter criterion for which every couple of adjacent tetrahedra are merged together if their inscribed void spheres overlap by any amount. This means that no overlap between two adjacent inscribed void spheres is allowed. According to this criterion, the couples of adjacent tetrahedra (a) and (b) in Figure 5.9 are merged together, while the couple of adjacent tetrahedra (c) are not merged. We can see that it is not easy to choose an admissible overlap between two adjacent inscribed void spheres. Therefore, Shire et al. (2016) introduced a user-specified admissible overlap. Every couple of adjacent tetrahedra are merged together if the relative overlap γ between their inscribed void spheres exceeds a user-specified value γ^{th}:

$$\gamma = \frac{\delta}{\min(d_1, d_2)} > \gamma^{\text{th}}, \tag{5.1}$$

where δ is the absolute overlap between the two adjacent inscribed spheres with diameters d_1 and d_2 (see Figure 5.10). The criterion of Al-Raoush et al. (2003) corresponds to $\gamma^{\text{th}} = 0.5$, while the criterion of Sufian et al. (2015) corresponds to $\gamma^{\text{th}} = 0$.

The size of each pore can be defined either as the diameter of an equivalent void sphere whose volume is equal to the pore volume or as the number of tetrahedra comprised in the pore. Figure 5.11 presents the pore size distributions in terms of equivalent sphere diameter and in terms of number of tetrahedra of each pore for different values of the user-specified threshold γ^{th} between 0 and 0.5 for the UG loose and dense samples. We can see that the pore size distribution changes greatly as the value of γ^{th} decreases from 0.5 to 0. For the loose UG sample, a small value of γ^{th} leads to formation of very large pores that comprise many tetrahedra (Figures 5.11(a) and (b)). For $\gamma^{th} = 0$, the number of tetrahedra of each pore varies largely and can go up to 101. Figure 5.12 shows two pores composed of 66 and 101 tetrahedra. It can be seen that they are not single pores, but rather ducts. Reboul et al. (2008); Seblany et al. (2018) also observed that merging every couple of adjacent tetrahedra whose inscribed void spheres overlap by any amount would over-merge tetrahedra. In addition, as the pore size distribution given by the criterion of Shire et al. (2016) depends hardly on the value of γ^{th}, it is not easy to choose a value of γ^{th} to obtain a good representation of the pore network. Figures 5.11(c) and (d) show that the pore size distribution for the dense UG sample is less sensitive to the threshold value γ^{th} than that for the loose sample. For such a dense sample, $\gamma^{th} = 0$ does not generate large pores with many tetrahedra.

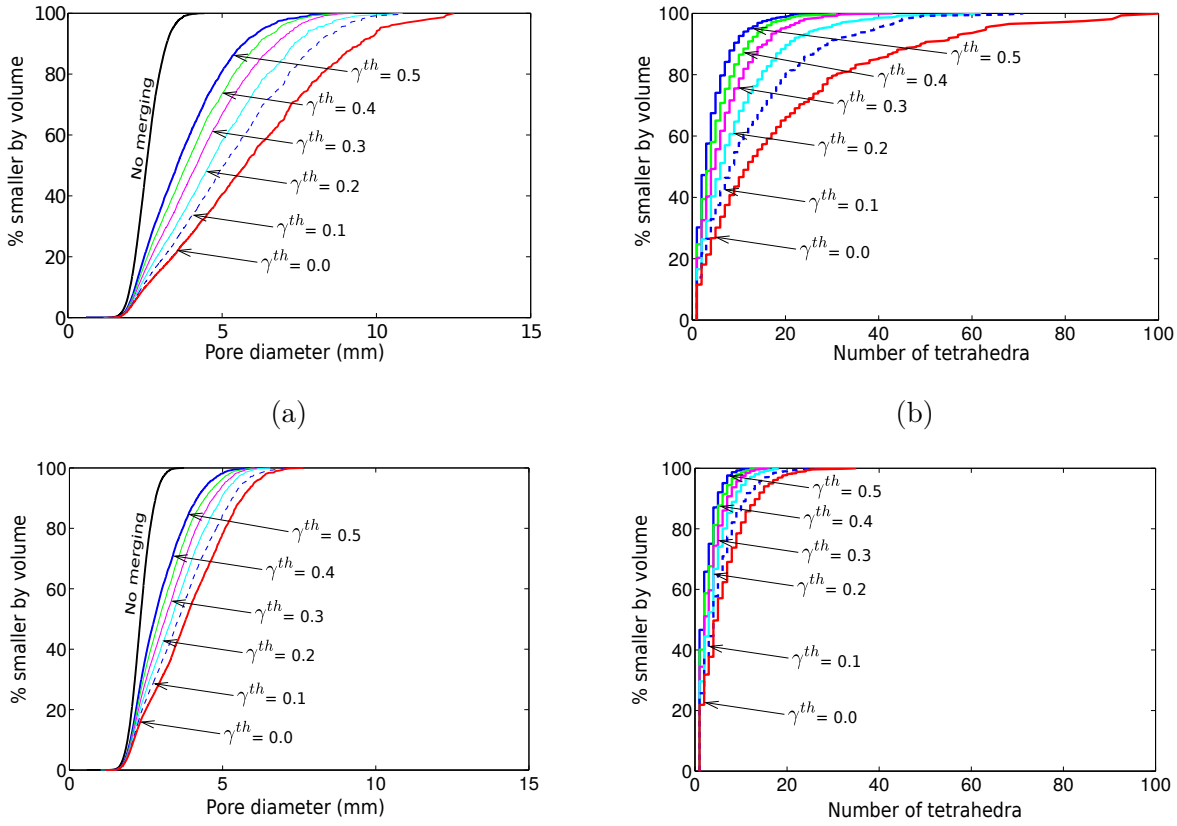

Figure 5.11: Pore size distributions obtained with the criterion of Shire et al. (2016) for different values of γ^{th} for the loose UG sample (a and b) and for the dense UG sample (c and d). The left and right columns correspond to the pore size distributions in terms of equivalent sphere diameter and of number of tetrahedra comprised in each pore, respectively.

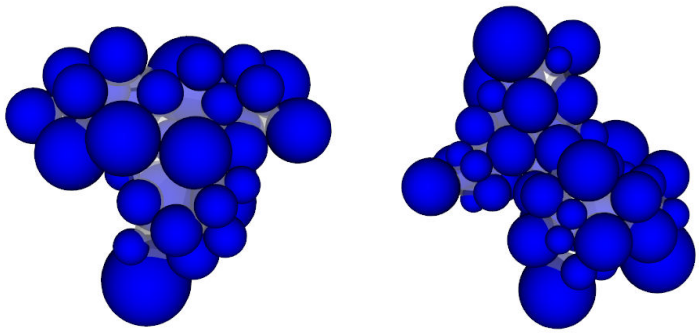

(a) 66 tetrahedra (b) 101 tetrahedra

Figure 5.12: Examples of two pores composed of (a) 66 tetrahedra and (b) 101 tetrahedra obtained with the criterion of Shire et al. (2016) with $\gamma^{th} = 0$.

Reboul et al. (2008) proposed to merge every couple of adjacent tetrahedra if their inscribed void spheres overlap by any amount ($\gamma^{th} = 0$) and introduced different merging levels to limit the pore size.

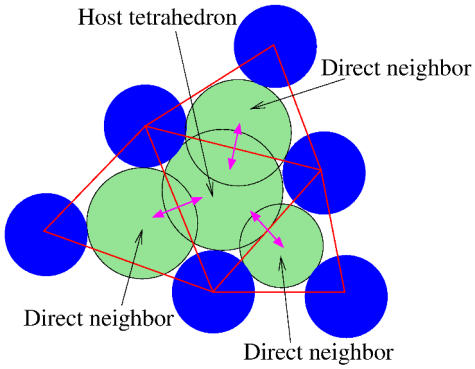

Figure 5.13: 2D illustration of the L_1 merging criterion of Reboul et al. (2008).

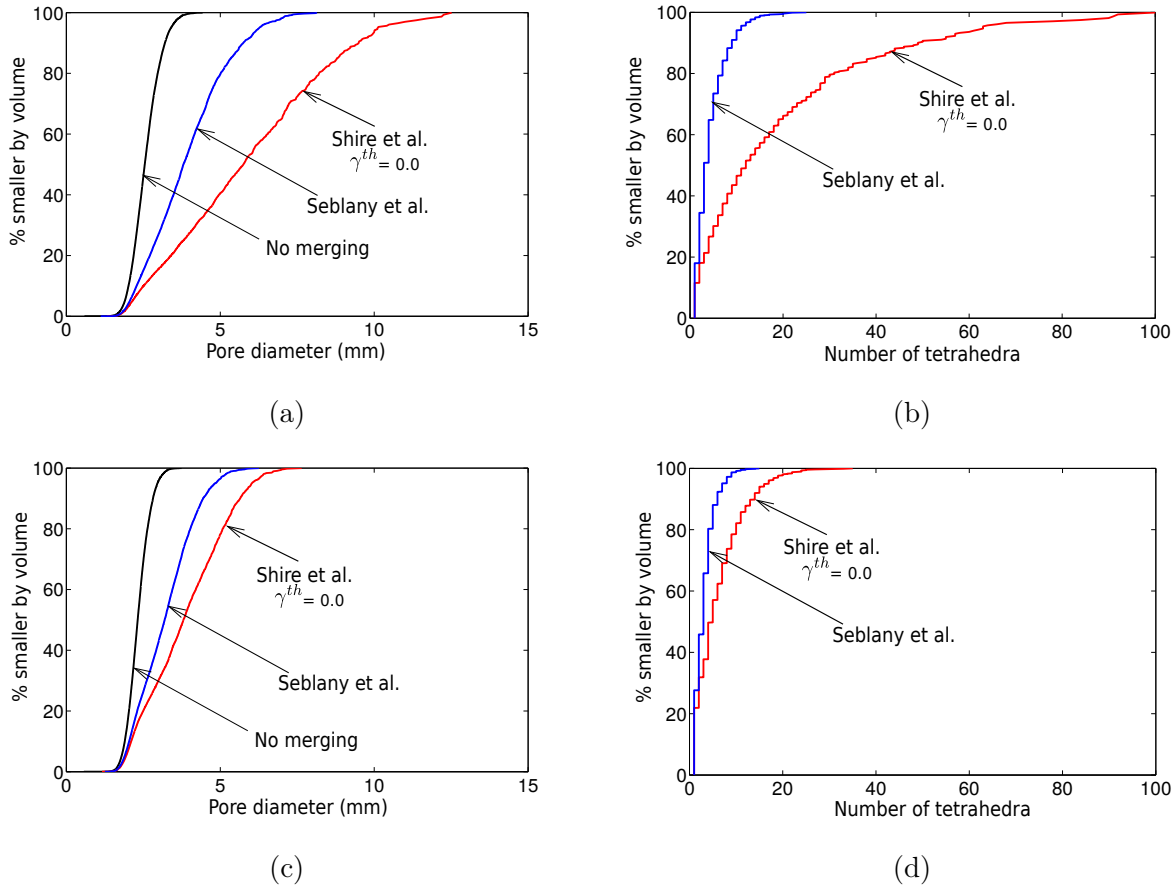

Figure 5.14: Comparison between the pore size distributions obtained with the criterion of Shire et al. (2016) for $\gamma^{th} = 0$ and with the the L_1 criterion of Seblany et al. (2018) for (a and b) the loose UG sample and for (c and d) the dense UG sample.

To form a single pore, a host tetrahedron that has the largest inscribed void sphere is first identified. Only direct neighboring tetrahedra are merged to the host tetrahedron according to the merging level L_1 as illustrated in Figure 5.13. For the level L_2, the merging can be extended to next neighbors of the host tetrahedron (neighbors of direct neighbors). Seblany et al. (2018) introduced a merging level L'_0 before applying the merging levels L_1 and L_2 to eliminate flat tetrahedra. For this level, two adjacent tetrahedra are merged together if either their inscribed void spheres almost overlap (the overlap is greater

than 99.9999%) or they share a constriction whose size is greater than the pore sizes. Figure 5.14 shows a comparison between the pore size distribution obtained with the L_1 merging criterion of Seblany et al. (2018) and that given by the criterion of Shire et al. (2016) with $\gamma^{th} = 0$ for the loose and dense UG samples. It can be seen that the L_1 merging criterion of Seblany et al. (2018) leads to smaller pores than those given by the criterion of Shire et al. (2016) and the over-merging of tetrahedra is avoided by using the former criterion. However, the L_1 merging criterion of Seblany et al. (2018) has a drawback: as the pore size is artificially limited, in some particular cases a single pore might be subdivided into several smaller pores. For instance, a single pore composed of 6 tetrahedra might be subdivided into a pore of five tetrahedra and a pore of one tetrahedron. Figure 5.15 illustrates this drawback by considering a 2D case where a single pore is subdivided into a pore of three triangles and a pore of one triangle.

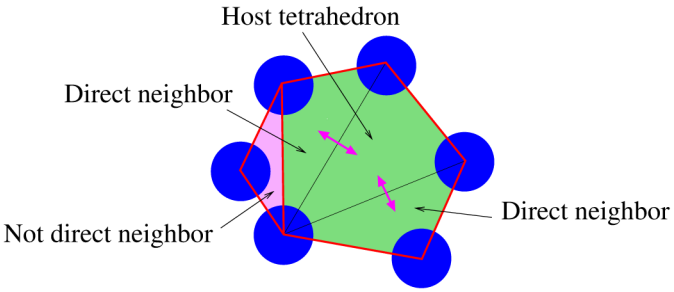

Figure 5.15: A 2D single pore might be subdivided into two smaller pores by the L_1 merging criterion of Seblany et al. (2018).

As we have shown previously, merging criteria based on the overlap between two inscribed void spheres defined for two adjacent tetrahedra have two main issues. Firstly, an admissible overlap γ^{th} between two adjacent inscribed void spheres needs to be specified as proposed by Shire et al. (2016). However, it is not easy to choose a good value of γ^{th} as the pore size distribution is quite sensitive to γ^{th}. Moreover, a small value of γ^{th} leads to an over-merging of tetrahedra and to a formation of very large pores. Secondly, to avoid the over-merging of tetrahedra, a merging level is needed to stop merging as proposed by Reboul et al. (2008) and Seblany et al. (2018). By doing so, the pore size is artificially limited and a single pore might be subdivided into several smaller pores. In the next section, we aim to propose a new merging criterion to overcome the two mentioned drawbacks.

5.4 New merging technique

In this section, we will propose a new technique to merge tetrahedra obtained from the weighted Delaunay triangulation of a numerical granular assembly. We first define what is a pore in our approach and then show how to obtain pores and constrictions. Finally, we show some results in terms of pore size and constriction size distributions obtained with the new technique.

5.4.1 Definition of a pore

The new merging technique is based on a subdivision of a granular sample into polyhedral sub-domains. Each polyhedral sub-domain can be composed of one tetrahedron or several neighboring tetrahedra, and the void space within each sub-domain defines a pore as illustrated in Figure 5.16(a) for 3D case and in 5.16(b) for 2D case. The concept of the inscribed void sphere for each tetrahedron, which was introduced by Al-Raoush et al. (2003), is generalized to each polyhedral sub-domain. The inscribed void sphere for a given sub-domain is the maximal ball that can be contained within the void space of the sub-domain (see Figure 5.16).

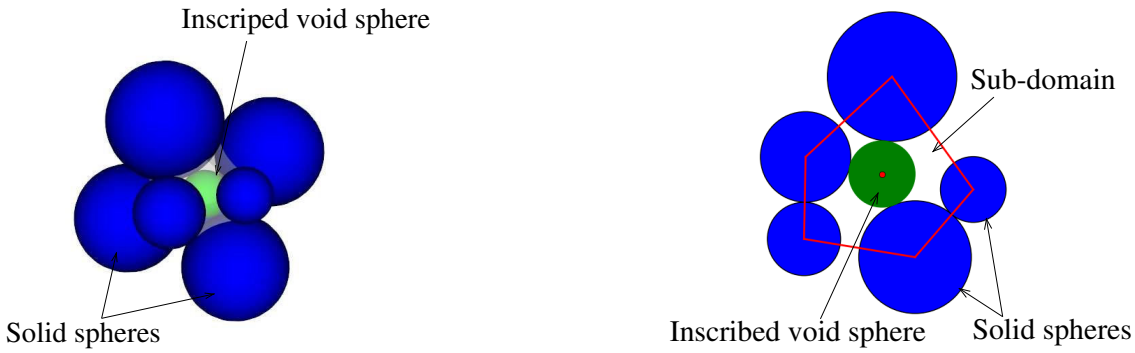

(a) A 3D sub-domain with the inscribed void sphere (b) A 2D sub-domain with the inscribed void circle

Figure 5.16: Illustration of 3D and 2D sub-domains.

The inscribed void sphere for each sub-domain is identified by a minimization procedure. Given a sphere located inside the void space of the sub-domain with center $\boldsymbol{x}$ and radius R, the distance d_i between this void sphere and a solid sphere with center $\boldsymbol{x}_i$ and radius R_i is $d_i = \mid \|\boldsymbol{x} - \boldsymbol{x}_i\| - (R + R_i) \mid$. The cost function f is defined as the sum of all distances from the void sphere to all the solid spheres of the sub-domain:

$$f = \sum_{i=1}^{N} \mid d_i \mid, \tag{5.2}$$

where the subscript i runs over all the solid particles of the sub-domains. By minimizing the cost function f, we obtain the center $\boldsymbol{x}$ and the radius R of the inscribed void sphere for the sub-domain under consideration. This minimization can be solved by using the Nelder-Mead simplex method (Gao and Han, 2012) implemented in the package SciPy. It should be noted that this minimization procedure can be used to identify the inscribed void sphere for each tetrahedron mentioned in the previous section.

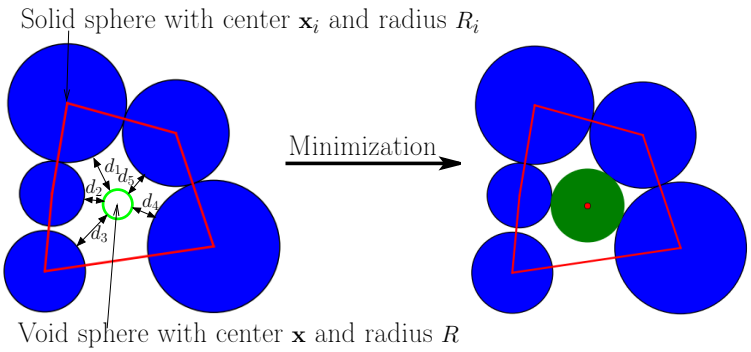

Figure 5.17: Minimization procedure to identify the inscribed void sphere for each sub-domain.

According to the new merging criterion, a pore contained within each sub-domain must fulfill three following conditions to define the pore geometry:

- **1st condition**: the inscribed void sphere of a sub-domain must not intersect solid particles of its adjacent sub-domains. If a couple of adjacent sub-domains do not fulfill this condition, they are merged together to form a new sub-domain for which a new inscribed void sphere is identified, as illustrated in Figure 5.18.

- **2nd condition**: the center of the inscribed void sphere of a sub-domain must be located inside the sub-domain. If a sub-domain fulfills this condition, it is not flat and its pore size (diameter

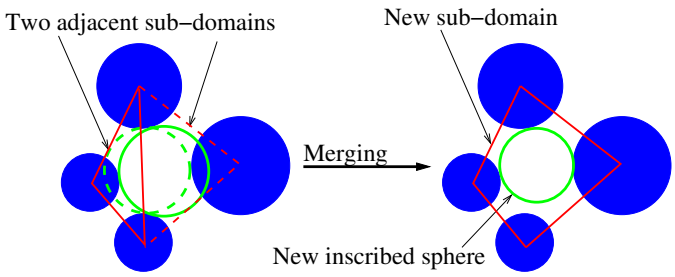

Figure 5.18: Merge a couple of adjacent sub-domains which do not fulfill the 1st condition.

of its inscribed void sphere) is bigger than the sizes of the constrictions that it shares with its neighbors (the constriction will be defined in Section 5.4.3). It should be noted that by definition the constriction size must be smaller than the sizes of the adjacent pores. For a couple of adjacent sub-domains, if the center of the inscribed void sphere of a sub-domain is located outside that sub-domain but inside the other sub-domain, they are merged together to form a new sub-domain with a new inscribed void sphere, as illustrated in Figure 5.19.

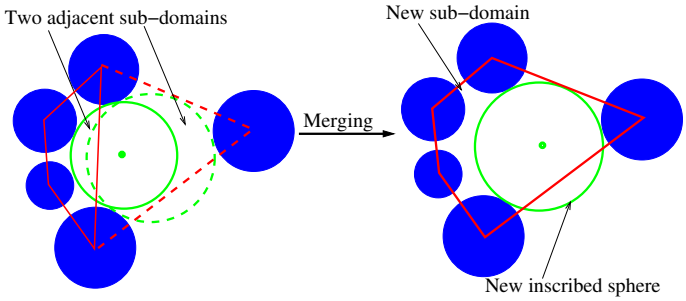

Figure 5.19: Merge a couple of adjacent sub-domains which do not fulfill the 2nd condition.

- **3rd condition**: two inscribed void spheres of two adjacent sub-domains must be sufficiently separated from each other, i.e., the overlap between them must be sufficiently small. For this condition, we use a separation criterion similar to that used by Shire et al. (2016). Two adjacent inscribed void spheres are sufficiently separated if the relative overlap $\gamma = \delta / \min(d_1, d_2) < \gamma^{th}$ (δ is the absolute overlap between the two inscribed void spheres with diameters d_1 and d_2). γ^{th} is an admissible overlap specified by the user. If two adjacent inscribed void spheres do not fulfill this condition, i.e. $\gamma \geq \gamma^{th}$, the corresponding couple of adjacent tetrahedra are merged together to obtain a new sub-domain and a new inscribed void sphere is identified as illustrated in Figure 5.20.

It is important to note that whenever a couple of adjacent sub-domains are merged together, a new inscribed void sphere is identified for the new sub-domain. The minimization procedure presented above requires guess values for the center $\boldsymbol{x}$ and the radius R of the inscribed void sphere. For this, we use the centers and the radii of the two inscribed void spheres before merging as the guess values, the global minimizer is taken as the center and the radius of the new inscribed void sphere.

5.4.2 Merging algorithm

Figure 5.21(a) presents the main merging algorithm of this new merging technique. We start the merging procedure by performing the weighted Delaunay triangulation of the granular sample under condition

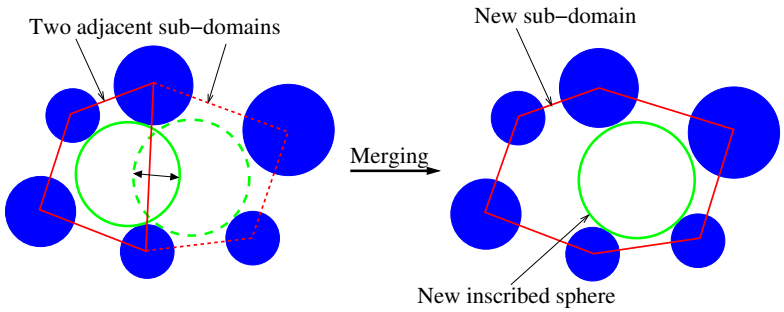

Figure 5.20: Merge a couple of adjacent sub-domains which do not fulfill the 3nd condition

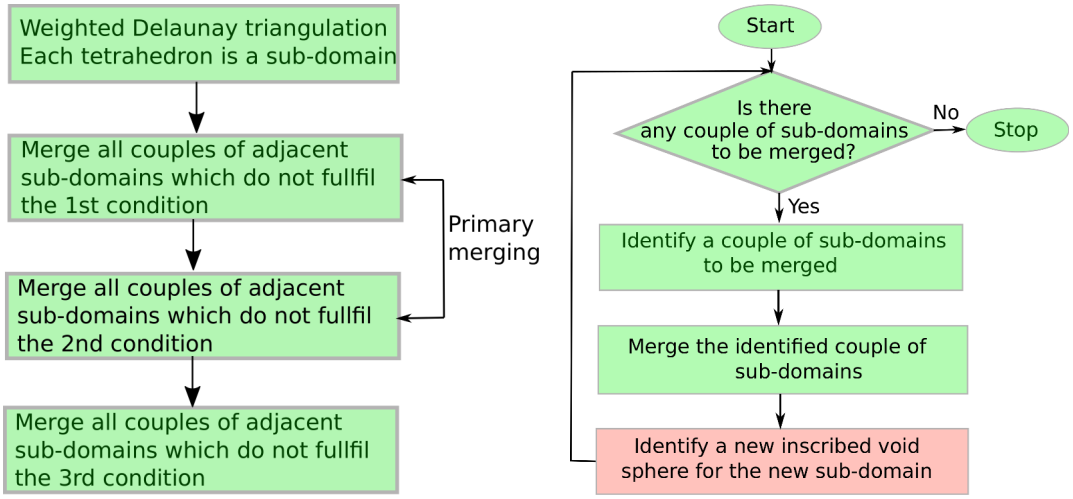

(a) Principal algorithm (b) Sub-algorithm for each merging step

Figure 5.21: Merging algorithm of the new criterion criterion.

with the package CGAL (CGAL Project, 2019). At this first step, each tetrahedron is considered as a sub-domain and an inscribed void sphere is identified for each sub-domain. The second and third steps consist in merging all the couples of adjacent sub-domains that do not fulfill the first and second conditions mentioned above, respectively. The second and third steps are called *primary merging procedure* for which no user-specified value is needed. More than 50% of tetrahedra are merged at the end of this primary merging procedure; however, the neighboring sub-domains still overlap greatly. Therefore, we merge all the couples of adjacent sub-domains that do not fulfill the third condition at the final step. At this step, a user-specified value for the admissible overlap between two adjacent inscribed void spheres is needed.

The sub-algorithm for each merging step is shown in Figure 5.21(a). At each step, we impose a condition among the three conditions mentioned above. Merging of adjacent sub-domains is performed in an iterative way. For each iteration, we first identify a couple of adjacent sub-domains that do not fulfill the condition under consideration and then merge them together. At the end of the iteration, we identify a new inscribed void sphere for the new sub-domain before moving to the next iteration. This is the key feature of the new merging technique which allows us to avoid over-merging of tetrahedra. The loop is finished when all the couples of adjacent sub-domains fulfill the condition under consideration.

For the second and final merging steps, all the couples of adjacent sub-domains are ordered according to the relative intersection ξ between inscribed void spheres and solid particles and to the relative overlap γ between two inscribed void spheres, respectively. The relative intersection between an inscribed void

sphere and a solid sphere is defined as $\xi = \delta/d$ where δ is the intersection between the void and solid spheres and d is the diameter of the void sphere. The couple of adjacent sub-domains merged at each iteration correspond to the maximal relative intersection $\xi_{\max}$ for the second step and the maximal relative overlap $\gamma_{\max}$ for the final step.

5.4.3 Definition of a constriction in the new method

We have shown previously the new merging technique to obtain pores from the weighted Delaunay triangulation. In this section, we present how constrictions that are shared by neighboring pores are defined. According to Reboul et al. (2010), the void area on each triangular face shared by two adjacent pores is a constriction. The intersection between the plane of the face and the three solid spheres whose centers are the three vertices of the face gives three solid disks on the plane. The authors defined the constriction size as the diameter of the largest empty disk that can be inscribed between the three solid disks. In some cases, this largest empty disk intersects another solid disk which is the intersection between the plane and an adjacent solid particle. In such cases, the intersected solid disk is taken into account to identify a new largest empty disk as illustrated in Figure 5.22. It is worth noting that the constriction size defined by Reboul et al. (2010) corresponds to the opening size on the plane of each triangular face. In some particular cases, if the largest empty disk is replaced by an empty sphere with the same radius and the same center, this largest empty sphere might intersect adjacent solid particles out of the plane as shown in Figure 5.23. This means that, for some particular cases, a solid spherical particle with the same size as the constriction size can not move through the constriction formed by the three particles of the face and their neighbors.

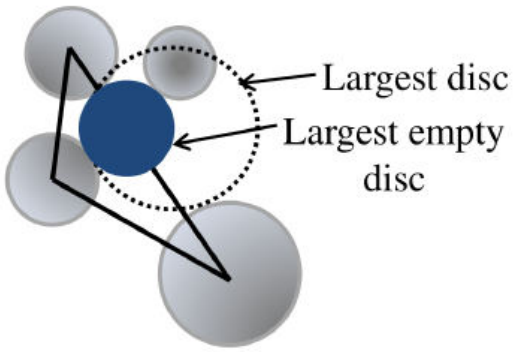

Figure 5.22: Definition of the largest empty disk on a face (Seblany et al., 2018).

We aim to correct the drawback mentioned above of the method of Reboul et al. (2010) by modifying slightly the definition of a constriction. Two adjacent pores can share one or several adjacent triangular faces; therefore a constriction can be formed by one or several triangular faces according to the new definition. Most of the constrictions have one triangular face (Figure 5.24(a)), but some of them can have two or three adjacent triangular faces (Figure 5.24(b)). This means that the centers of the solid particles that form a constriction must not necessarily lie on the same plane. The constriction size is defined as the diameter of the largest empty sphere that can pass through the void space between the solid particles of the constriction. This largest empty sphere is identified by using the same minimization procedure presented in Section 5.4.1 and by imposing that its center must be located on the planes of the triangular faces of the constriction. This largest empty sphere is illustrated in Figure 5.24(a) for a constriction formed by one triangular face and in Figure 5.24(b) for a constriction formed by two triangular faces. In the case where this largest empty sphere intersects other solid particles, these intersected ones are taken into consideration in the minimization procedure to guarantee that the largest empty sphere of a constriction does not

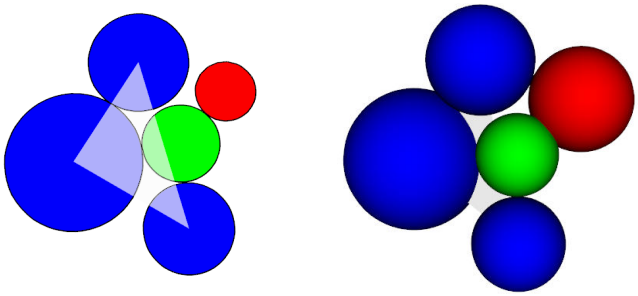

(a) (b)

Figure 5.23: (a) Largest empty disk (green one) on the plane and (b) largest empty sphere (green one) intersects the adjacent particle (red one) out of the plane.

intersect any solid particle. It is worth mentioning that the new definition of a constriction includes also a merging of several adjacent triangular faces to form a single constriction as shown in Figure 5.24(b).

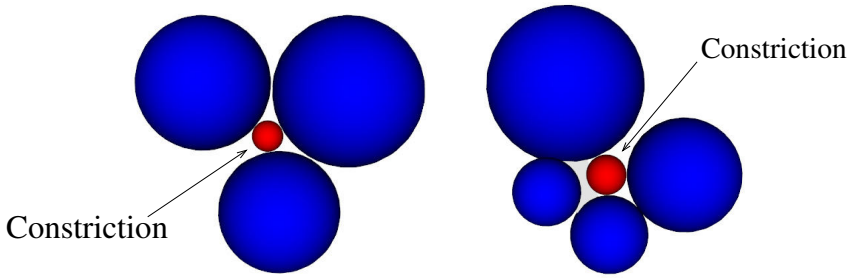

(a) (b)

Figure 5.24: Constrictions formed by (a) one or (b) two triangular faces and the largest empty sphere (red one).

Figure 5.25 shows a comparison between the constriction size distribution (CSD) obtained with the method of Reboul et al. (2010) and the CSD obtained with the new method presented above. Both methods are used for the same pore network which is extracted from the loose UG sample by using the new merging technique with an admissible overlap $\gamma^{th} = 0$. We can see that the new method leads to constrictions of smaller size, in comparison with the method of Reboul et al. (2010); nevertheless, the difference between these two methods is quite small. This means that most of the constrictions are formed by one triangular face; and for such constrictions, both methods give the same result. In the following, the new method is used to determine the constriction size.

5.4.4 Results obtained with the new merging technique

In this section, we will show some results in terms of pore size distribution and constriction size distribution obtained with the new merging technique presented above. Pore networks are extracted from the loose and dense UG samples with different user-specified values γ^{th} for the admissible overlap between two adjacent inscribed void spheres.

Figure 5.26 presents the pore size distributions in terms of equivalent sphere diameter and in terms of number of tetrahedra comprised in each pore, which are obtained with different user-specified values γ^{th}

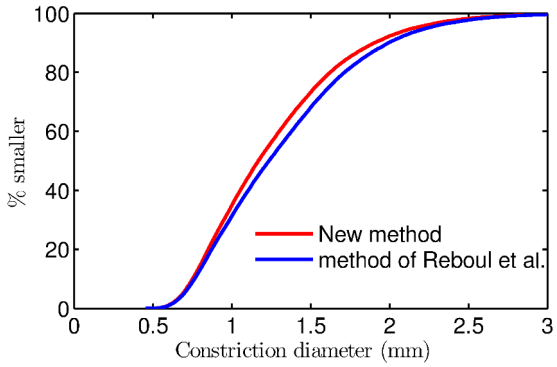

Figure 5.25: Comparison between the CSD obtained with the method of Reboul et al. (2010) and the CSD obtained with the new method. The pore network is extracted from the loose UG sample by using the new merging technique with an admissible overlap $\gamma^{th} = 0$.

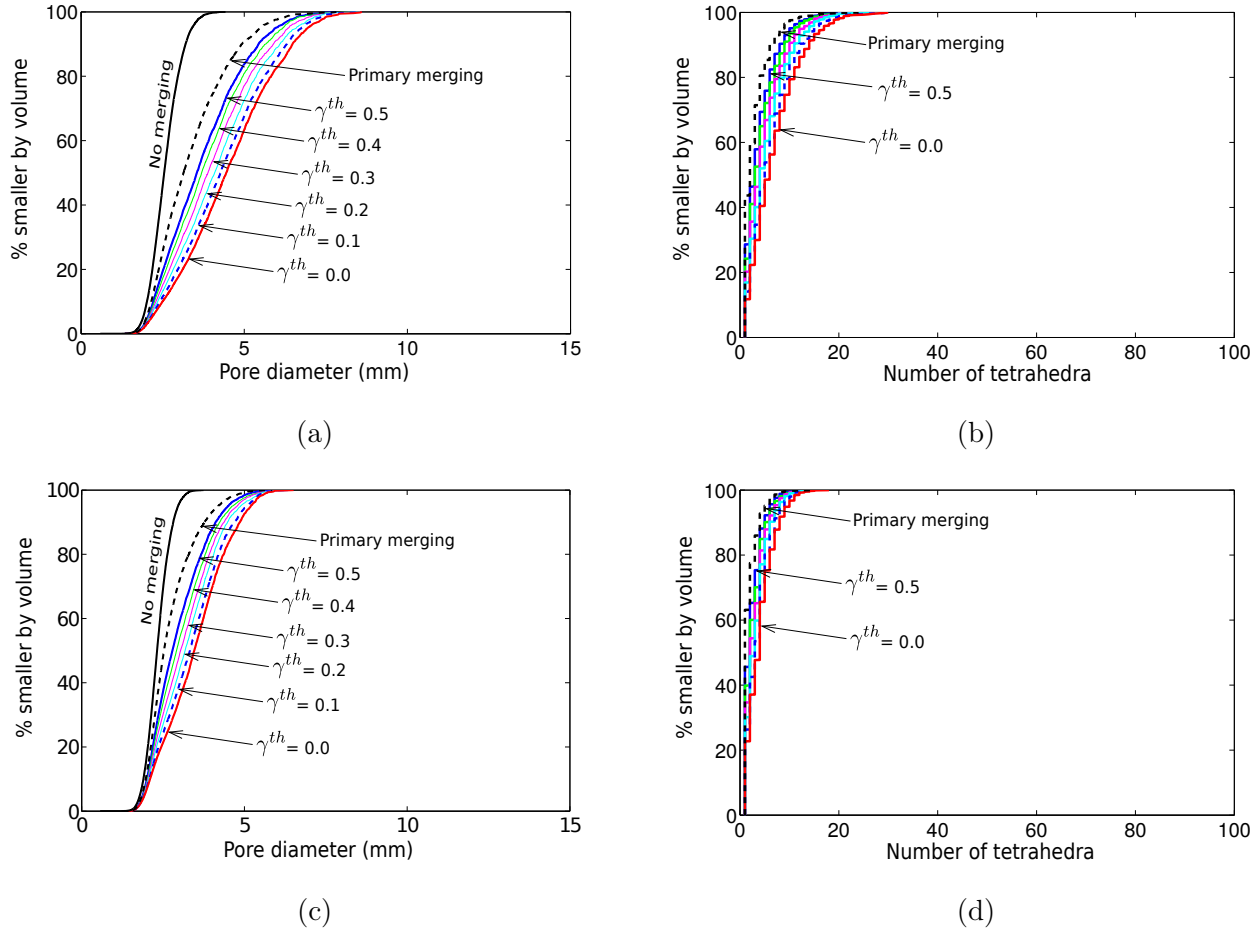

Figure 5.26: Pore size distributions obtained with the new merging technique for different values of γ^{th}: (a and b) for the loose UG sample, and (c and d) for the dense UG sample.

for the loose and dense UG samples. First of all, it can be seen that the pore size distribution changes significantly from that obtained directly from the weighted Delaunay triangulation by using only the primary merging procedure without resort to any user-specified value. Secondly, the pore size distribution continues to be shifted rightward when the pore separation condition is applied with decreasing value of

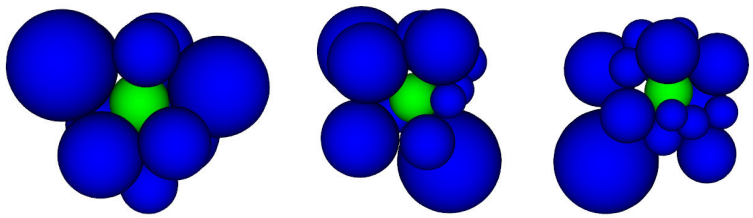

(a) (b)

Figure 5.27: Pores composed of (a) 12 tetrahedra, (b) 20 tetrahedra and (c) 30 tetrahedra. Green balls are the inscribed void spheres.

γ^{th}. By comparing Figure 5.11(a) and Figure 5.26(a), the pore size distribution obtained with the new merging technique for the loose UG sample is much less sensitive to the user-specified value γ^{th} that that obtained with the criterion of Shire et al. (2016). The new merging technique with a small value of γ^{th} does not lead to over-merging of tetrahedra, which is the main drawback of the criterion of Shire et al. (2016) (see Figure 5.26(b)). Indeed, the biggest pore obtained with the new merging technique with $\gamma^{th} = 0$ is composed of 30 tetrahedra and large pores do not have duct shapes as shown in Figure 5.27. Lastly, the pore size distribution for the dense UG sample is much less sensitive to γ^{th} than for the loose UG sample and the largest pore is composed of 20 tetrahedra.

Let's new analyze the constriction size distribution (CSD) obtained with the new merging technique. Figure 5.28 shows the CSD curves obtained with different values of the admissible overlap γ^{th} for the loose and dense UG samples. It can be seen that the CSD curve is slightly shifted leftward as γ^{th} decreases from 0.5 to 0. In comparison with the pore size distribution shown in Figure 5.26, the constriction size distribution obtained with the new merging technique is less sensitive to γ^{th}. Figure 5.29 shows the CSD curves obtained with the criterion of Shire et al. (2016) for the loose and dense UG samples. It can be seen that the CSD obtained with the new merging technique is significantly less sensitive to γ^{th} than that obtained with the criterion of Shire et al. (2016), particularly for the loose sample.

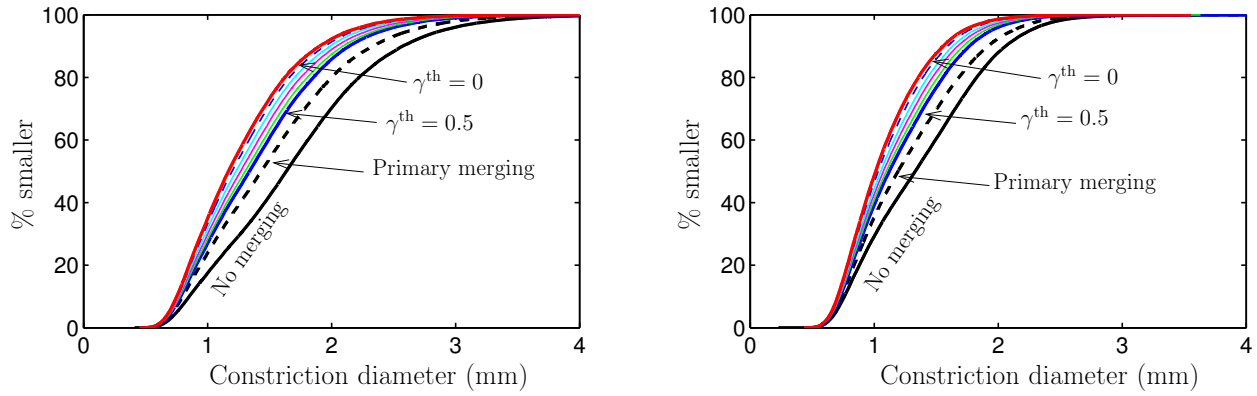

(a) (b)

Figure 5.28: CSD curves for different values of γ^{th} obtained with the new merging technique (a) for the loose UG sample and (b) for the dense UG sample.

We have presented above a new technique to merge tetrahedra obtained from the weighted Delaunay triangulation. We have demonstrated two main advantages of this new merging technique. Firstly, it

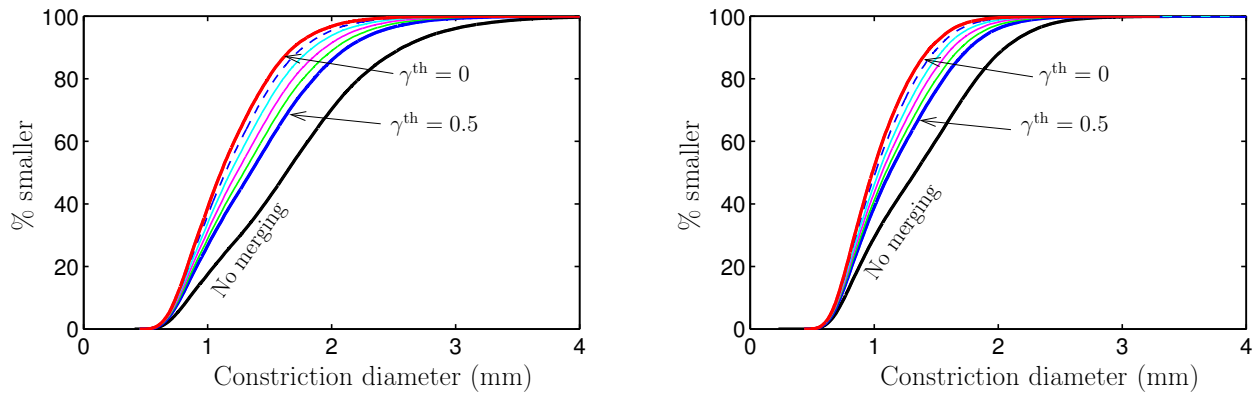

Figure 5.29: CSD curves for different values of γ^{th} obtained with the criterion of Shire et al. (2016) (a) for the loose UG sample and (b) for the dense UG sample.

allows us to avoid the over-merging of tetrahedra, a drawback observed for the criterion of Shire et al. (2016), without using any stopping criterion as proposed by Reboul et al. (2008); Seblany et al. (2018), which would be an artificial limitation of the pore size. Secondly, both particle and constriction size distributions given by the new merging technique are significantly less sensitive to the user-specified value of the admissible overlap γ^{th} than those given by the criterion of Shire et al. (2016).

5.4.5 Comparison between different merging criteria

In this section, we will compare the new merging criterion proposed above with the merging criterion of Shire et al. (2016) and the L_1 merging criterion proposed by Reboul et al. (2008), subsequently modified by Seblany et al. (2018). The admissible overlap γ^{th} between two adjacent inscribed void spheres is set to 0 for both new criterion and that of Shire et al. (2016). This comparison is made on the UG (uniform particle size distribution) and GG (gap-graded particle size distribution) samples at the loose and dense states presented in Section 5.2.

Let's consider first the UG samples for this comparison. Figure 5.30 shows the pore size distributions extracted from these samples by using the three merging criteria mentioned above. It can be seen that these three merging criteria give different results for the loose UG sample. The criterion of Shire et al. (2016) leads to formation of very large pores due to an over-merging of tetrahedra. The criterion of Seblany et al. (2018). limits the pore size so smaller pores are formed. The new criterion gives a pore size distribution curve intermediate between those given by the two other criteria. It should be noted that the pore size distribution given by the new criterion is quite close to that given by the criterion of Seblany et al. (2018). but very far from that given by the criterion of Shire et al. (2016). We can also remark that the difference between the results obtained with these three criteria gets smaller for the dense UG sample.

Figure 5.31 shows the constriction size distributions (CSD) given by the three considered criteria. In comparison to the difference in pore size distribution shown above, the difference in CSD obtained with the three criteria is less marked. The CSD given by the new criterion is intermediate between those given by the two other criteria. Unlike the pore size distribution, the CSD curve given by the new criterion is closer to that given by the criterion of Shire et al. (2016) than that given by Seblany et al. (2018). This might be due to the fact that the criterion of Seblany et al. (2018). might subdivide a single pore into several smaller pores, resulting in constrictions of large size. Regarding the criterion of Shire et al. (2016), it over-merges tetrahedra, resulting in constrictions of smaller size. It should be noted that merging tetrahedra obtained

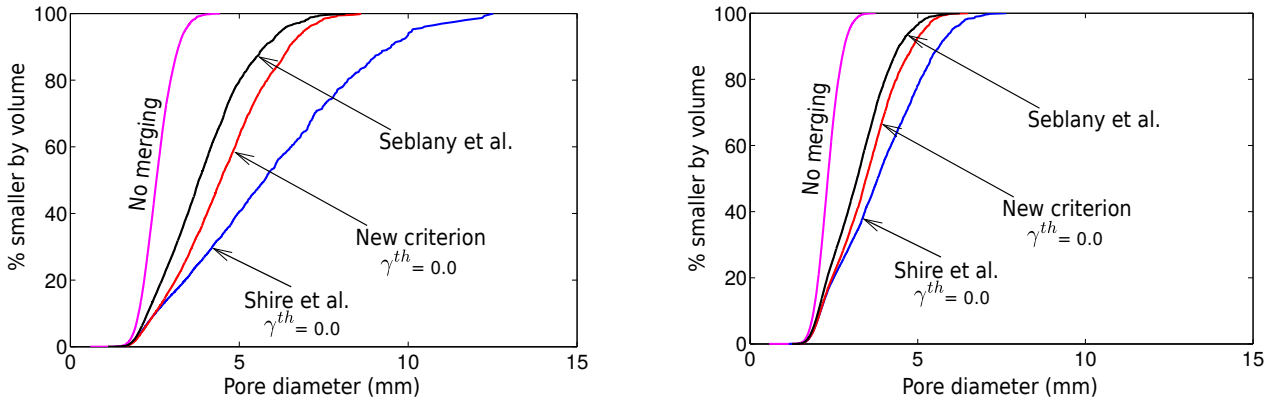

Figure 5.30: Pore size distributions obtained with the three merging criteria for (a) the loose UG sample and (b) the dense UG sample.

from the weighted Delaunay triangulation aims not only to form single pores and but also to eliminate large constrictions which are artifacts of the weighted Delaunay triangulation. We can also remark that the difference between the CSD curves given by the three considered criteria is quite small for the dense UG sample.

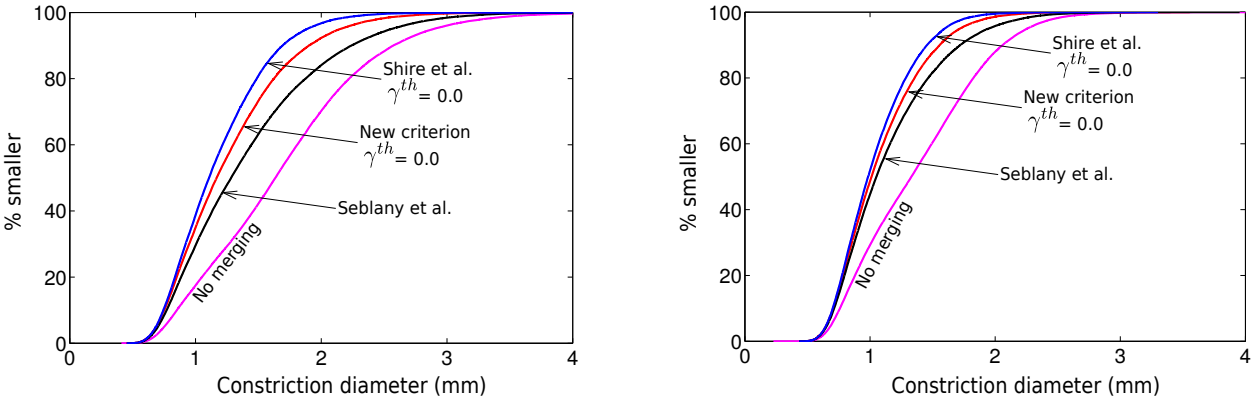

Figure 5.31: Constriction size distributions obtained with the three merging criteria for (a) the loose UG sample and (b) the dense UG sample.

Let's now consider the GG samples with a gap-graded particle size distribution for the comparison. Figures 5.32 and 5.33 show the respective pore size and constriction size distributions obtained with the three considered merging criteria for the loose and dense GG samples. In comparison to the results shown above for the UG samples, these three merging criteria give similar results for the GG samples. However, the new criterion gives, on one hand, a pore size distribution curve closer to the one given by the criterion of Seblany et al. (2018), and on the other hand, a constriction size distribution closer to the one given by the criterion of Shire et al. (2016) for the GG loose sample, compared to those obtained for the UG loose sample. We can also remark that the difference in terms of constriction size distributions given by the three criteria is quite small for the GG samples, even for the loose one; and the three criteria give close pore size and constriction size distributions for the dense one.

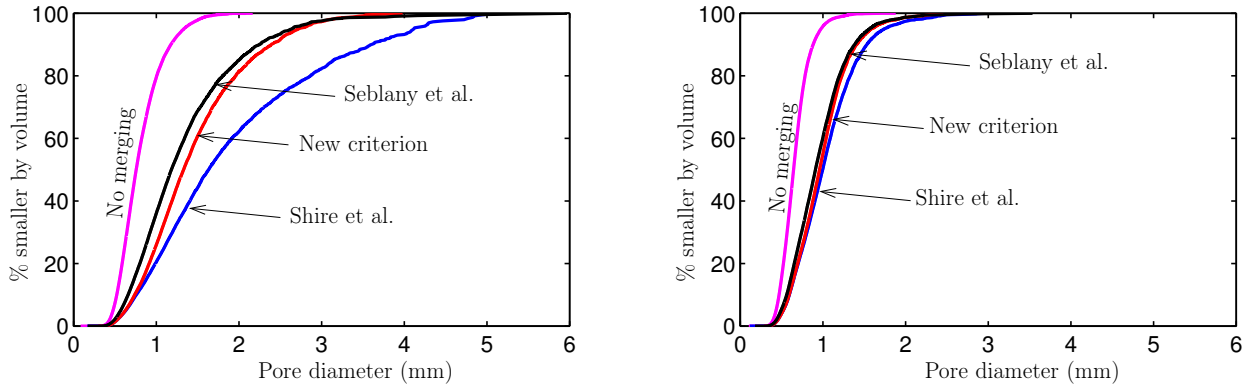

Figure 5.32: Pore size distributions obtained with the three merging criteria for (a) the loose GG sample and (b) the dense GG sample.

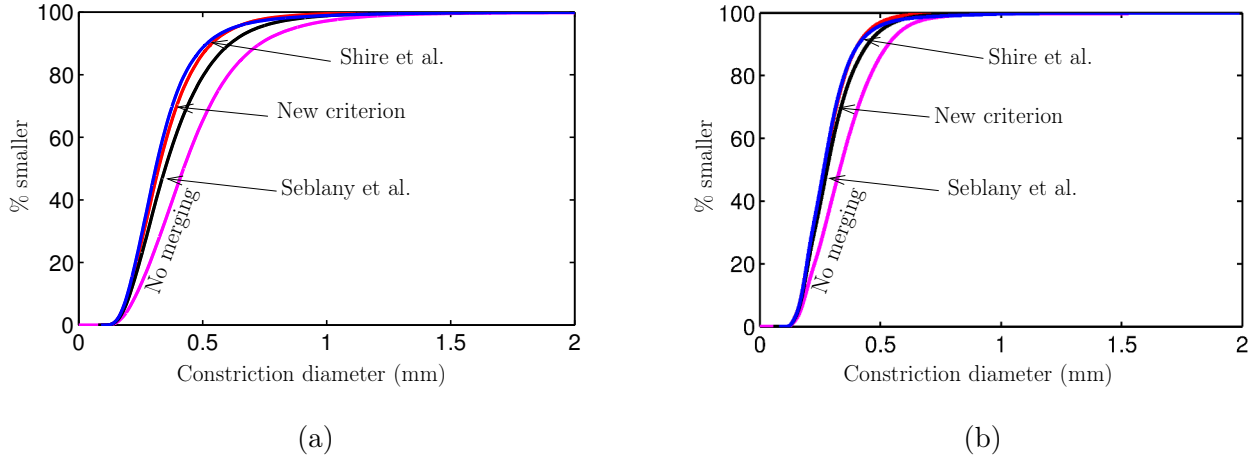

Figure 5.33: Constriction size distributions obtained with the three merging criteria for (a) the loose GG sample and (b) the dense GG sample.

5.5 Conclusions

In this chapter, we introduced a representation of the internal state of a granular soil after suffusion at level 3 by using a pore network model. For such a model, the granular soil is constituted of a solid skeleton and a loose fraction that contains the erodible particles. The solid skeleton forms the pore network, and the erodible particles are moved within this pore network until they are either blocked by constrictions or leave the pore network. The key point in such model is how to construct the pore network of the solid skeleton, which is the main concern of this chapter.

We analyzed then two techniques based on the weighted Delaunay triangulation to extract the pore network from a numerical sample. The main drawback of the first technique proposed by Shire et al. (2016) is that it leads to an over-merging of tetrahedra, hence a formation of ducts if the value for the admissible overlap γ^{th} between adjacent inscribed void spheres is small. This drawback is remediated by the second technique proposed by Reboul et al. (2008), subsequently modified by Seblany et al. (2018), in which different merging levels were used. However, this technique might lead to a sub-division of single pores to several smaller pores as it limits artificially the pore size.

We proposed then a new merging technique to remediate the drawbacks of the two techniques mentioned above. We introduced the concept of polyhedral sub-domains for each of which an inscribed void sphere is identified by using a minimization procedure. We imposed three conditions that each sub-domain must fulfill to define the pore geometry. If a sub-domain does not fulfill a condition, it is merged to its neighbors. With the new technique, tetrahedra issued from the weighted Delaunay triangulation are merged in an iterative and progressive manner. We also proposed a new definition of constrictions between two adjacent pores based on the concept of a largest empty sphere that can pass through a constriction and a new procedure to determine the constriction size.

Like the technique of Shire et al. (2016), a user-specified value γ^{th} for the admissible overlap between inscribed void spheres is needed in the new technique. It was shown that the pore size and constriction size distributions obtained with the new technique change with γ^{th}. However, they are much less sensitive to this user-specified value than those given by the criterion of Shire et al. (2016). In addition, the new merging technique allows us to avoid the over-merging of tetrahedra even for $\gamma^{th} = 0$ without resort to a stopping criterion as the ones proposed by Reboul et al. (2008).

A comparison between these three merging criteria was made on the UG (uniformly graded) and GG (gap-graded) samples at the loose and dense states. It was observed that the new merging technique gives a pore size distribution closer to that obtained with the criterion of Seblany et al. (2018) than to that given by the criterion of Seblany et al. (2018). An opposite result was found for the constriction size distributions given by these three merging techniques. This difference is well marked for the loose samples but becomes smaller for the dense samples. For the gap-graded samples, these three different techniques give close constriction size distribution curves, particularly for the dense one.

The results shown in this chapter demonstrated a good capability of the new merging technique to construct the pore network from a numerical sample based on the Delaunay triangulation. The constructed pore network will be included in the pore network model that we envisage developing to take into account the transport and blockage of erodible particles in the void space formed by the non-erodible particles. Taha et al. (2019) and Taha et al. (2017)

Conclusions and Perspectives

In this PhD thesis report, we presented a study of the consequences of suffusion on the mechanical behavior of gap-graded soils by using the Discrete Element Method (DEM). A DEM-fluid coupled model was not used to simulate the suffusion process due to a very high computational cost. Instead, the internal state of granular soils subjected to suffusion is represented at three different levels by making some simplistic assumptions. At the level 1, a sample considered as eroded is prepared and compacted in the same way as the intact sample but with fine content lower than the original one. The level 2 consists in removing a fraction of fine particles from the intact sample to mimic the loss of fine particles caused by suffusion. For the level 3, a pore network was introduced to take into consideration the transport and the blockage of fine particles with the void space formed by the solid skeleton.

Gap-graded samples with a gap ratio of 3 and fine contents between 0 and 100% were simulated using the DEM. These samples were compacted in different ways to obtain the loosest and densest states. It was shown that, by adding fine particles in binary mixtures, the coarse fraction gets looser, while the fine fraction gets denser. Based on the variations of the global void ratio e, the intergranular void ratio e_c and the interfine void ratio e_f with fine content f_c, four ranges of fine content can be distinguished: (i) $f_c \leq 20\%$ where the fine fraction is very loose and does not disturb the coarse fraction; (ii) $20\% < f_c \leq 32\%$ where the global void ratio e decreases with f_c and the fine fraction is looser than the coarse one; (iii) $32\% < f_c \leq 60\%$ where the global void ratio e increases with f_c and the fine fraction becomes denser than the coarse one; and (iv) $f_c > 60\%$ where the coarse fraction is very loose, compared to the fine fraction.

Triaxial tests were performed on the binary mixtures. The stress-strain behavior of binary mixtures was found to remain almost unchanged with an increase in fine content in the ranges (i) and (iv). The shear strength and dilatancy of binary mixtures increase with fine content f_c in the range (ii), while they decrease with f_c in the range (iii). At the optimal fine content of 32% where the global void ratio e is minimum; the shear strength and dilatancy are highest.

The micro-structure of binary mixtures varies greatly with an increase in fine content starting from 20%. Fine particles, on one hand, come into contact with coarse particles and reinforce the micro-structure, but on the other hand, they separate coarse particles and then weaken the micro-structure. As a consequence, the shear stress is transmitted more and more through the coarse-fine contacts but less and less through the coarse-coarse contacts as fine content increases. The coarse-coarse contacts primarily support the shear stress for the range (ii) of fine content, while the coarse-fine contacts primarily carry the shear stress for the range (iii) of fine content. For the range (iv) of fine content, coarse particles are strongly separated by fine ones and fine-fine contacts primarily sustain the shear stress.

As fine particles play an important role in the micro-structure and in carrying the shear stress in granular mixtures, a loss of fine particles has great consequences on the stress-strain behavior of these materials. The internal state of binary mixtures after suffusion is represented at the level 2 by two particle removal methods. A fraction of fine particles are randomly removed from the original sample for the first method, while only fine particles in the loose fraction, which belong to the weak force chains, are removed for the

second method. Both methods predicted a reduction in shear strength of eroded samples starting from 20% of fine content. This reduction in shear strength is more marked for gap-graded samples with high fine content and increases with an increase in percentage of removed fine particles. A random removal of fine particles causes a much stronger degradation to eroded samples than a removal of loose fine particles. A loss of fine particles does not destroy greatly the contact network between coarse particles; however, it causes a great reduction in bearing capability to the coarse fraction due to the loss of contacts between coarse particles and removed fine particles. A removal of loose particles was found to disturb less the coarse fraction than a random removal of fine particles.

A pore network model was introduced to take into consideration the transport and blockage of detached particles within the void space of the solid skeleton to represent the internal state of soils after suffusion at the level 3. A new method was proposed to extract the pore network from a numerical sample by using the Delaunay triangulation. This method makes use of a concept of polyhedral sub-domains, for each of which a inscribed void sphere is identified. Three different conditions are required for each sub-domain such that the void space within it can be considered as a single pore. If a given sub-domain does not fulfill one of these three conditions, it is merged to its neighbors. A comparison of this new merging technique to the techniques of Shire et al. (2016) and of Seblany et al. (2018) showed that it is capable of extracting the pore network from a numerical sample without leading to an over-merging of tetrahedra and without any artificial limitation of the pore size.

The studies presented in this report, has opened new research paths that can be interesting. In what follows, recommendations for future research work are presented which concerns the numerical approach.

We have represented the suffusion under different levels to study its consequences on the mechanical behavior of gap-graded soils. In the future works, it is important to study these consequences on other type of soils specially soils which are susceptible to suffusion like soils whose grain size distribution corresponds to upwardly concave curve.

In this study, we used a simplified particle shapes such as spherical, and the main advantage of these shapes is that the contact between two adjacent spherical particles occurs only at one point and the distance between them is easily calculated. But these shapes cannot represent the real soil.Therefore, to better represent the real soil, complex shapes such as polygons or polyhedra can be tackled.

According to the literature review, the effect of the fine content on the mechanical behavior of soils, are not always the same under drained and undrained stress-strain conditions, for that, it is very important to study this effect under undrained conditions, since in our study we have considered only the drained conditions.

In some cases, there exist a difficulty to study the mechanical behavior of coarse-grained soils by the classical testing devices due to the presence of large particles that disturb or prevent the performance of tests. So to study the mechanical behavior using the classical lab devices, we must clip or substitute a part of these coarse particles, and this clipping may result the increase of fine content. For that, it is important to compare the variation of the shear strength with the increase of fine content presented in level 1 and the variation of the shear strength with the increase of fine content due to the clipping of some coarse particles.

In chapter 4, we presented two particle-removal methods, at which the extraction of particles was in the initial stress state of gap-graded samples, but according to Scholtès et al. (2010), the behavior of eroded samples is strongly influenced by the stress state at which fine particles are removed. For that, we can study the influence of removal of fine particles at different stress states using the two methods of particle removal.

The pore network model has not been completed yet in this PhD thesis. Nevertheless, the pore network of the solid skeleton can be correctly built by using the new method mentioned above; this constitutes an important advance to develop such a model. To complete this pore network model, a procedure to move particles in the pore network needs to be established.

List of publications

Papers in international journals

H. Taha, N.-S. Nguyen, D. Marot, A. Hijazi, and K. Abou-Saleh. Micro-scale investigation of the role of finer grains in the behavior of bidisperse granular materials. *Granular Matter*, 21(2):28, 2019.

Papers in international conferences

H. Taha, N.-S. Nguyen, D. Marot, A. Hijazi, and K. Abou-Saleh. Micro-mechanical investigation of the effect of fine content on mechanical behavior of gap-graded granular materials using DEM. In *EPJ Web of Conferences*, volume 140, page 15009, 2017.

N.-S. Nguyen, H. Taha, D. Marot, A. Hijazi, and K. Abou-Saleh. Description of the Pore Network in Granular Media Using the Delaunay Triangulation. In *the* 27^{th} *Annual Meeting of the European Working Group on International Erosion EWG-IE, Vancouver, Canada*, pages 89-90, 2019.

Papers in national conferences

Habib Taha, Ngoc-Son Nguyen, Didier Marot, Abbas Hijazi, and Khalil Abou-Saleh. On the effect of fines content on the micro-mechanical behavior of gap-graded materials. In *the* 35^{mes} *Rencontres de l'AUGC, ECN/UN, Nantes, France*, 2017.

Bibliography

R. Aboul-Hosn. *Suffusion and its effects on the mechanical behavior of granular soils: numerical and experimental investigations*. PhD thesis, Grenoble Alpes, 2017.

R. Al-Raoush and A. Papadopoulos. Representative elementary volume analysis of porous media using x-ray computed tomography. *Powder technology*, 200(1):69–77, 2010.

R. Al-Raoush, K. Thompson, and C.S. Willson. Comparison of network generation techniques for unconsolidated porous media. *Soil Science Society of America Journal*, 67(6):1687–1700, 2003.

N.L. Andrianatrehina, H. Souli, J. Rech, J.-J. Fry, J.-M. Fleureau, and S. Taibi. Influence of the percentage of sand on the behavior of gap-graded cohesionless soils. *Comptes Rendus Mécanique*, 344(8):539–546, 2016.

ASTM D4253-00. Standard test methods for maximum index density and unit weight of soils using a vibratory table. *ASTM International, West Conshohocken, PA*, 2000. URL `www.astm.org`.

ASTM D4254-00. Standard test methods for minimum index density and unit weight of soils and calculation of relative density. *ASTM International, West Conshohocken, PA*, 2000. URL `www.astm.org`.

ASTM D4767-88. Standard test method for unconsolidated-undrained triaxial compression test on cohesive soils. *ASTM International, West Conshohocken, PA*, 1988. URL `www.astm.org`.

N. Belheine, J.P. Plassiard, F.V. Donzé, F. Darve, and A. Seridi. Numerical simulation of drained triaxial test using 3D discrete element modeling. *Computers and Geotechnics*, 36(1):320–331, 2009.

F.G. Bell. *Basic environmental and engineering geology*. Number 631.47 B433. Whittles Publishing, 2007.

N. Benahmed, T.K. Nguyen, P.-Y. Hicher, and M. Nicolas. An experimental investigation into the effects of low plastic fines content on the behaviour of sand/silt mixtures. *European Journal of environmental and civil engineering*, 19(1):109–128, 2015.

B. Benmezroua. *Etude numérique et expérimentale, à l'échelle microstructurelle, du transport granulaire dans les matériaux poreux saturés*. PhD thesis, INSA de Rennes, 2011.

G. Brown, H.T. Hsieh, and D.A. Lucero. Evaluation of laboratory dolomite core sample size using representative elementary volume concepts. *Water resources research*, 36(5):1199–1207, 2000.

V.V. Burenkova. Assessment of suffusion in non-cohesive and graded soils. *Filters in geotechnical and hydraulic engineering*, pages 357–360, 1993.

F. Calvetti, G. Viggiani, and C. Tamagnini. A numerical investigation of the incremental behavior of granular soils. *Rivista italiana di geotecnica*, 37(3):11–29, 2003.

E. Catalano, B. Chareyre, and E. Barthélemy. Pore-scale modeling of fluid-particles interaction and emerging poromechanical effects. *International Journal for Numerical and Analytical Methods in Geomechanics*, 38(1):51–71, 2014.

Emanuele Catalano. *A pore–scale coupled hydromechanical model for biphasic granular media. Application to granular sediment hydrodynamics*. PhD thesis, PhD thesis, Université de Grenoble, 2012.

CGAL Project. CGAL user and reference manual. *CGAL Editorial Board*, 4.14 edition, 2019.

C.S. Chang and P.-Y. Hicher. An elasto-plastic model for granular materials with microstructural consideration. *International journal of solids and structures*, 42(14):4258–4277, 2005.

D.S. Chang and L.M. Zhang. A stress-controlled erosion apparatus for studying internal erosion in soils. *Geotechnical Testing Journal*, 34(6):579–589, 2011.

D.S. Chang and L.M. Zhang. Extended internal stability criteria for soils under seepage. *Soils and Foundations*, 53(4):569–583, 2013.

D.S. Chang, L.M. Zhang, and T.H. Xu. Laboratory investigation of initiation and development of internal erosion in soils under complex stress states. In *6th Conference on Scour and Erosion*, pages 895–902, 2012.

B. Chareyre. *Modelisation du comportement d'ouvrages composites sol-geosynthetique par elements discrets: application aux ancrages en tranchees en tete de talus*. PhD thesis, Universite Joseph-Fourier-Grenoble I, 2003.

B. Chareyre, A. Cortis, E. Catalano, and E. Barthélemy. Pore-scale modeling of viscous flow and induced forces in dense sphere packings. *Transport in porous media*, 94(2):595–615, 2012.

C. Chen, L.M. Zhang, and D.S. Chang. Stress-strain behavior of granular soils subjected to internal erosion. *Journal of Geotechnical and Geoenvironmental Engineering*, 142(12):06016014, 2016.

J. Christoffersen, M.M. Mehrabadi, and S. Nemat-Nasser. A micromechanical description of granular material behavior. *Journal of applied mechanics*, 48(2):339–344, 1981.

G. Combe. *Origines géométriques du comportement quasi-statique des assemblages granulaires denses: Etude par simulations numériques*. PhD thesis, Marne-la-vallée, ENPC, 2001.

P.A. Cundall and O.D.L. Strack. A discrete numerical model for granular assemblies. *Géotechnique*, 29 (1):47–65, 1979.

B. Dai, J. Yang, and X. Luo. A numerical analysis of the shear behavior of granular soil with fines. *Particuology*, 21:160–172, 2015.

P. Dantu. Contribution à l'étude mécanique et géométrique des milieux pulvérulents. In *Proceedings of the 4th International Conference on Soil Mechanics and Foundations Engineering*, 1957.

N. Das. *Modeling Three-Dimensional Shape of Sand Grains Using Discrete Element Method*. PhD thesis, University of South Florida, 2007.

H. Dong and M.J. Blunt. Pore-network extraction from micro-computerized-tomography images. *Physical Review E*, 80(3):036307, 2009.

H. Edelsbrunner and N.R. Shah. Incremental topological flipping works for regular triangulations. *Algorithmica*, 15(3):223–241, 1996.

R. Fell and J.-J. Fry. *Internal Erosion of Dams and Their Foundations: Selected and Reviewed Papers from the Workshop on Internal Erosion and Piping of Dams and Their Foundations, Aussois, France, 25–27 April 2005*. CRC Press, 2007.

Mark Foster, Robin Fell, and Matt Spannagle. The statistics of embankment dam failures and accidents. *Canadian Geotechnical Journal*, 37(5):1000–1024, 2000.

S.A. Galindo-Torres, A. Scheuermann, H.B. Mühlhaus, and D.J. Williams. A micro-mechanical approach for the study of contact erosion. *Acta Geotechnica*, 10(3):357–368, 2015.

F. Gao and L. Han. Implementing the nelder-mead simplex algorithm with adaptive parameters. *Computational Optimization and Applications*, 51(1):259–277, 2012.

S.J. Garner and R.J. Fannin. Understanding internal erosion: a decade of research following a sinkhole event. *The International Journal on Hydropower & Dams*, 17(3):93, 2010.

H.M.D. Harshani, S.A. Galindo-Torres, A. Scheuermann, and H.B. Muhlhaus. Micro-mechanical analysis on the onset of erosion in granular materials. *Philosophical Magazine*, 95(28-30):3146–3166, 2015.

P.-Y. Hicher. Modelling the behavior of soil subjected to internal erosion. In *6th International Conference on Scour and Erosion, ICSE6, Paris*, pages 27–31, 2012.

P.-Y. Hicher. Modelling the impact of particle removal on granular material behaviour. *Géotechnique*, 63 (2):118–128, 2013.

U. Homberg, D. Baum, S. Prohaska, U. Kalbe, and K. Witt. Automatic extraction and analysis of realistic pore structures from μct data for pore space characterization of graded soil. 2012.

Z. Hu, Y. Zhang, and Z. Yang. Suffusion-induced deformation and microstructural change of granular soils: a coupled CFD–DEM study. *Acta Geotechnica*, 14(3):795–814, 2019.

B. Indraratna and F. Vafai. Analytical model for particle migration within base soil-filter system. *Journal of Geotechnical and Geoenvironmental Engineering*, 123(2):100–109, 1997.

V.S. Istomina. Filtration stability of soils. *Gostroizdat, Moscow, Leningrad*, 15, 1957.

M. Jean and B. Cambou. *Micromécanique des matériaux granulaires*. Hermes Science, 2001.

K. Kawano, C. Sullivan, and T. Shire. Using DEM to assess the influence of stress and fabric inhomogeneity and anisotropy on susceptibility to suffusion. In *Proceeding of 8th International Conference on Scour and Erosion, Harris, Whitehouse & Moxon (Eds.)*, pages 85–94, 2016.

K. Kawano, T. Shire, and C. O'Sullivan. Coupled particle-fluid simulations of the initiation of suffusion. *Soils and Foundations*, 58(4):972–985, 2018.

T.C. Kenney and D. Lau. Internal stability of granular filters. *Canadian Geotechnical Journal*, 22(2): 215–225, 1985.

T.C. Kenney, R. Chahal, E. Chiu, G.I. Ofoegbu, G.N. Omange, and C.A. Ume. Controlling constriction sizes of granular filters. *Canadian Geotechnical Journal*, 22(1):32–43, 1985.

A. Kézdi. *Soil physics-selected topics-developments in geotechnical engineering - 25*. Elsevier, 1979.

F.H. Kim, D. Penumadu, J. Gregor, N. Kardjilov, and I. Manke. High-resolution neutron and X-ray imaging of granular materials. *Journal of Geotechnical and Geoenvironmental Engineering*, 139(5): 715–723, 2012.

P.V. Lade, C.D. Liggio, and J.A. Yamamuro. Effects of non-plastic fines on minimum and maximum void ratios of sand. *Geotechnical Testing Journal*, 21:336–347, 1998.

J. Lafleur, J. Mlynarek, and A. Rollin. Filtration of broadly graded cohesionless soils. *Journal of Geotechnical Engineering*, 115(12):1747–1768, 1989.

S. Li, A.R. Russell, and D. M. Wood. Stress-strain behavior of soils having undergone different amounts of internal erosion. *European Working Group on Internal Erosion in Embankment Dams & their Foundations*, page 114, 2017.

N. Lindow, D. Baum, and H.-C. Hege. Voronoi-based extraction and visualization of molecular paths. *IEEE Transactions on Visualization and Computer Graphics*, 17(12):2025–2034, 2011.

M. Locke, B. Indraratna, and G. Adikari. Time-dependent particle transport through granular filters. *Journal of Geotechnical and Geoenvironmental Engineering*, 127(6):521–529, 2001.

F. Lominé, L. Scholtès, L. Sibille, and P. Poullain. Modeling of fluid–solid interaction in granular media with coupled lattice boltzmann/discrete element methods: application to piping erosion. *International Journal for Numerical and Analytical Methods in Geomechanics*, 37(6):577–596, 2013.

S. Luding. Introduction to discrete element methods: basic of contact force models and how to perform the micro-macro transition to continuum theory. *European Journal of Environmental and Civil Engineering*, 12(7-8):785–826, 2008.

D. Marot, P.-L. Regazzoni, and T. Wahl. Energy-based method for providing soil surface erodibility rankings. *Journal of Geotechnical and Geoenvironmental Engineering*, 137(12):1290–1293, 2011.

N.H. Minh and Y.P. Cheng. A DEM investigation of the effect of particle-size distribution on one-dimensional compression. *Géotechnique*, 63(1):44, 2013.

N.H. Minh and Y.P. Cheng. On the contact force distributions of granular mixtures under 1D-compression. *Granular Matter*, 18(2):18, 2016.

N.H. Minh, Y.P. Cheng, and C. Thornton. Strong force networks in granular mixtures. *Granular Matter*, 16(1):69–78, 2014.

R.A. Moffat and R.J. Fannin. A large permeameter for study of internal stability in cohesionless soils. *Geotechnical Testing Journal*, 29(4):273–279, 2006.

J.J. Moreau. Numerical investigation of shear zones in granular materials. In *Workshop on Friction, Arching, Contact Dynamics*, pages 233–247, 1996.

T.G. Murthy, D. Loukidis, J.A.H Carraro, M. Prezzi, and R. Salgado. Undrained monotonic response of clean and silty sands. *Géotechnique*, 57(3):273–288, 2007.

NFP 94-074. Sols: reconnaissances et essais – Essais à l'appareil triaxial de révolution. *AFNOR (Association Français de Normalisation)*, 1994.

Cong Doan Nguyen, Nadia Benahmed, Edward Andò, Luc Sibille, and Pierre Philippe. Experimental investigation of microstructural changes in soils eroded by suffusion using x-ray tomography. *Acta Geotechnica*, 14(3):749–765, 2019.

K.T. Nguyen. *Etude expérimentale du comportement instable d'un sable silteux: application aux digues de protection.* PhD thesis, Aix-Marseille, 2014.

NYSDOT. Geotechnical design manual: Chapter 5 soil and rock classification and logging. 2013.

M. Oda and K. Iwashita. Study on couple stress and shear band development in granular media based on numerical simulation analyses. *International Journal of Engineering Science*, 38(15):1713–1740, 2000.

A. Okabe, B. Boots, K. Sugihara, and S.N. Chiu. *Spatial tessellations: concepts and applications of Voronoi diagrams*, volume 501. John Wiley & Son, 2009.

C. O'Sullivan. *Particulate discrete element modelling: a geomechanics perspective*. CRC Press, 2011.

J.F. Peters, M. Muthuswamy, J. Wibowo, and A. Tordesillas. Characterization of force chains in granular material. *Physical Review E*, 72(4):041307, 2005.

P. Pirnia, F. Duhaime, Y. Ethier, and J. Dubé. ICY: An interface between COMSOL multiphysics and discrete element code YADE for the modelling of porous media. *Computers & Geosciences*, 123:38–46, 2019.

J.-P. Plassiard, N. Belheine, and F.-V. Donzé. A spherical discrete element model: calibration procedure and incremental response. *Granular Matter*, 11(5):293–306, 2009.

F. Radjai. Features of force transmission in granular media. In Kishino, editor, *Powders and Grains*, pages 157–160, 2001.

F. Radjaï and F. Dubois. *Discrete-element modeling of granular materials*. Wiley-Iste, 2011.

F. Radjai and V. Richefeu. Contact dynamics as a nonsmooth discrete element method. *Mechanics of Materials*, 41(6):715–728, 2009.

F. Radjai and D.E. Wolf. Features of static pressure in dense granular media. *Granular Matter*, (1):3–8, 1998.

N. Reboul, E. Vincens, and B. Cambou. A statistical analysis of void size distribution in a simulated narrowly graded packing of spheres. *Granular Matter*, 10(6):457–468, 2008.

N. Reboul, E. Vincens, and B. Cambou. A computational procedure to assess the distribution of constriction sizes for an assembly of spheres. *Computers and Geotechnics*, 37(1-2):195–206, 2010.

K.S. Richards and K.R. Reddy. Critical appraisal of piping phenomena in earth dams. *Bulletin of Engineering Geology and the Environment*, 66(4):381–402, 2007.

M. Robinson, S. Luding, and M. Ramaioli. SPH-DEM simulations of grain dispersion by liquid injection. In *AIP Conference Proceedings*, volume 1542, pages 1122–1125, 2013.

Q. Rousseau, G. Sciarra, R. Gelet, and D. Marot. Constitutive modeling of a suffusive soil with porosity-dependent plasticity. In *European Working Group on Internal Erosion*, pages 168–179. Springer, 2018.

R. Salgado, P. Bandini, and A. Karim. Shear strength and stiffness of silty sand. *Journal of Geotechnical and Geoenvironmental Engineering*, 126(5):451–462, 2000.

C. Salot. *Modélisation du comportement mécanique d'un matériau granulaire composite par la méthode des éléments discrets*. PhD thesis, Université Joseph-Fourier-Grenoble I, 2007.

M. Satake. Fabric tensor in granular materials. In *IUTAM Conference on Deformation and Flow of Granular Materials, 1982*, pages 63–68. AA Balkema, 1982.

L. Scholtès, P.-Y. Hicher, and L. Sibille. Multiscale approaches to describe mechanical responses induced by particle removal in granular materials. *Comptes Rendus Mécanique*, 338(10-11):627–638, 2010.

U. Schuler. Scattering of the composition of soils. An aspect for the stability of granular filters. In *Geofilters*, volume 96, pages 21–34, 1996.

F. Seblany. *Filter criterion for granular soils based on the constriction size distribution*. PhD thesis, Ecole Centrale de Lyon, 2018.

F. Seblany, U. Homberg, E. Vincens, P. Winkler, and K.J. Witt. Merging criteria for defining pores and constrictions in numerical packing of spheres. *Granular Matter*, 20(3):37, 2018.

R. Shafipour and A. Soroush. Fluid coupled-DEM modelling of undrained behavior of granular media. *Computers and Geotechnics*, 35(5):673–685, 2008.

J.L. Sherard and L.P. Dunnigan. Critical filters for impervious soils. *Journal of Geotechnical Engineering*, 115(7):927–947, 1989.

W.C. Sherman. Filter experiments and design criteria. Technical Report 3-360, Army Engineer Waterways Experiment Station Vicksburg Miss, 1953.

T. Shire and C. O'Sullivan. A network model to assess base-filter combinations. *Computers and Geotechnics*, 84:117–128, 2017.

T. Shire and C. O'Sullivan. Micromechanical assessment of an internal stability criterion. *Acta Geotechnica*, 8(1):81–90, 2013.

T. Shire, C. O'Sullivan, and K. Hanley. The influence of finer fraction and size-ratio on the micro-scale properties of dense bimodal materials. *Geomechanics from Micro to Macro (eds K. Soga, K. Kumar, G. Biscontin and M. Kuo)*, 1:231–236, 2014a.

T. Shire, C. O'Sullivan, K.J. Hanley, and R.J. Fannin. Fabric and effective stress distribution in internally unstable soils. *Journal of Geotechnical and Geoenvironmental Engineering*, 140(12):04014072, 2014b.

T. Shire, C. O'Sullivan, and K.J. Hanley. The influence of fines content and size-ratio on the micro-scale properties of dense bimodal materials. *Granular Matter*, 18(3):52, 2016.

L. Sibille. *Modélisations discrètes de la rupture dans les milieux granulaires*. PhD thesis, Institut National Polytechnique de Grenoble-INPG, 2006.

D.B. Silin, G. Jin, and T.W. Patzek. Robust determination of the pore space morphology in sedimentary rocks. In *SPE Annual Technical Conference and Exhibition*. Society of Petroleum Engineers, 2003.

A. Silveira. An analysis of the problem of washing through in protective filters. In *International Conference on Soil Mechanics and Foundation Engineering*, 1965.

J. Sjah. *Couplage SPH-DEM pour l'étude de l'érosion dans les ouvrages hydrauliques*. PhD thesis, Ecole Centrale de Lyon, 2013.

J. Sjah and E. Vincens. Determination of the constriction size distribution of granular filters by filtration tests. *International Journal for Numerical and Analytical Methods in Geomechanics*, 37(10):1231–1246, 2013.

A.W. Skempton and J.M. Brogan. Experiments on piping in sandy gravels. *Géotechnique*, 44(3):449–460, 1994.

L. Staron, F. Radjai, and J.-P. Vilotte. Multi-scale analysis of the stress state in a granular slope in transition to failure. *The European Physical Journal E*, 18(3):311–320, 2005.

D. Sterpi. Effects of the erosion and transport of fine particles due to seepage flow. *International Journal of Geomechanics*, 3(1):111–122, 2003.

A. Sufian, A.R. Russell, A.J. Whittle, and M. Saadatfar. Pore shapes, volume distribution and orientations in monodisperse granular assemblies. *Granular Matter*, 17(6):727–742, 2015.

K. Szarf, G. Combe, and P. Villard. Polygons vs. clumps of discs: A numerical study of the influence of grain shape on the mechanical behaviour of granular materials. *Powder Technology*, 208(2):279–288, 2011.

H. Taha, N.-S. Nguyen, D. Marot, A. Hijazi, and K. Abou-Saleh. Micro-mechanical investigation of the effect of fine content on mechanical behavior of gap graded granular materials using DEM. In *EPJ Web of Conferences*, volume 140, page 15009, 2017.

H. Taha, N.-S. Nguyen, D. Marot, A. Hijazi, and K. Abou-Saleh. Micro-scale investigation of the role of finer grains in the behavior of bidisperse granular materials. *Granular Matter*, 21(2):28, 2019.

S. Thevanayagam and S. Mohan. Intergranular state variables and stress–strain behaviour of silty sands. *Géotechnique*, 50(1):1–23, 2000.

S. Thevanayagam, T. Shenthan, S. Mohan, and J. Liang. Undrained fragility of clean sands, silty sands, and sandy silts. *Journal of Geotechnical and Geoenvironmental Engineering*, 128(10):849–859, 2002.

C. Thornton. Force transmission in granular media. *Kona Powder and Particle Journal*, 15:81–90, 1997.

D.K. Tran, N. Prime, F. Froiio, C. Callari, and E. Vincens. Numerical modelling of backward front propagation in piping erosion by DEM-LBM coupling. *European Journal of Environmental and Civil Engineering*, 21(7-8):960–987, 2017.

E. Vincens, K.J. Witt, and U. Homberg. Approaches to determine the constriction size distribution for understanding filtration phenomena in granular materials. *Acta Geotechnica*, 10(3):291–303, 2015.

H.-J. Vogel and K. Roth. Quantitative morphology and network representation of soil pore structure. *Advances in Water Resources*, 24(3-4):233–242, 2001.

C. Voivret, F. Radjai, J.-Y. Delenne, and M.S. El Youssoufi. Multiscale force networks in highly polydisperse granular media. *Physical Review Letters*, 102(17):178001, 2009.

V. Šmilauer et al. *Yade Documentation 2nd ed.* The Yade Project, 2015. doi: 10.5281/zenodo.34073. http://yade-dem.org/doc/.

C.F. Wan and R. Fell. Assessing the potential of internal instability and suffusion in embankment dams and their foundations. *Journal of Geotechnical and Geoenvironmental Engineering*, 134(3):401–407, 2008.

X. Wang and J. Li. Simulation of triaxial response of granular materials by modified DEM. *Science China Physics, Mechanics & Astronomy*, 57(12):2297–2308, 2014.

Antoine Wautier, Stéphane Bonelli, and François Nicot. Dem investigations of internal erosion: Grain transport in the light of micromechanics. *International Journal for Numerical and Analytical Methods in Geomechanics*, 43(1):339–352, 2019.

J. Wiącek and M. Molenda. Representative elementary volume analysis of polydisperse granular packings using discrete element method. *Particuology*, 27:88–94, 2016.

Ł. Widuliński, J. Kozicki, and J. Tejchman. Numerical simulations of triaxial test with sand using DEM. *Archives of Hydro-Engineering and Environmental Mechanics*, 56(3-4):149–172, 2009.

K. Witt. Reliability study of granular filters. *Filters in geotechnical and hydraulic engineering*, pages 35–42, 1993.

K.J. Witt. Filtrationsverhalten und bemessung von erdstoff-filtern. *Heft: Institut für Bodenmechanik und Felsmechanik der Universität Karlsruhe*, 104, 1986.

D.M. Wood and K. Maeda. Changing grading of soil: effect on critical states. *Acta Geotechnica*, 3:3–14, 2008.

D.M. Wood, K. Maeda, and E. Nukudani. Modelling mechanical consequences of erosion. *Géotechnique*, 60(6):447–457, 2010.

S.L. Yang, R. Sandven, and L. Grande. Instability of sand–silt mixtures. *Soil Dynamics and Earthquake Engineering*, 26(2-4):183–190, 2006.

A. Yerro, A. Rohe, and K. Soga. Modelling internal erosion with the material point method. *Procedia Engineering*, 175:365–372, 2017.

Z.-Y. Yin, J. Zhao, and P.-Y. Hicher. A micromechanics-based model for sand-silt mixtures. *International Journal of Solids and Structures*, 51(6):1350–1363, 2014.

J. Zhao and T. Shan. Coupled CFD–DEM simulation of fluid–particle interaction in geomechanics. *Powder Technology*, 239:248–258, 2013.

UNIVERSITE BRETAGNE SCIENCES LOIRE POUR L'INGENIEUR

UNIVERSITÉ DE NANTES

Titre : Comportement mécanique des sols érodés: étude numérique basée sur la méthode des éléments discrets

Mots clés : sols granulaires . suffusion . méthode des éléments discrets . comportement mécanique . micro-structure . extraction des particules fines . réseau des pores

Résumé : La suffusion peut induire une perte de particules fines au sein de sols granulaires et par conséquent une modification leur comportement mécanique. Cette thèse a pour objectif d'étudier la conséquence de cette perte de particules fines sur les propriétés mécaniques des sols aux échelles macroscopique et microscopique en utilisant la méthode des éléments discrets (MED). Des échantillons granulaires composés de particules sphériques dont la taille suit une distribution granulométrique lacunaire sont modélisés par la MED. A cause d'un coût de calcul élevé, l'écoulement du fluide à travers l'espace poral entre particules solides n'est pas modélisé. Nous proposons plutôt une représentation de l'état interne du sol après la suffusion suivant trois niveaux de complexité croissante. Pour le niveau 1, des échantillons considérés comme érodés sont générés à une densité donnée et avec un pourcentage des fines plus petit que celui de l'échantillon original. Le niveau 2 consiste à retirer une fraction des particules fines de l'échantillon original à un état de contrainte donné. Pour cela, nous proposons une méthode permettant d'identifier une fraction lâche composée des particules qui ne participent pas significativement à supporter la sollicitation. Le niveau 3 a pour objectif de prendre en compte le transport et le blocage des particules fines par des constrictions dans l'espace poral formé par le squelette solide. Le point essentiel à ce niveau réside dans la description du réseau des pores. Cette étude a montré que les particules fines peuvent avoir un effet négligeable, positif ou négatif sur la résistance mécanique selon le pourcentage de fines. Une extraction des particules fines conduit à une diminution de la résistance mécanique des sols érodés. Nous avons montré que la réduction de la résistance mécanique est plus forte si des particules fines sont retirées de façon aléatoire que si seules des particules fines de la fraction lâche sont retirées. Pour la description du réseau des pores, une nouvelle méthode a été proposée pour associer des tétraèdres voisins résultant de la triangulation de Delaunay. Ce réseau des pores sera incorporé dans un modèle pour prendre en compte le transport et le blocage des particules fines au sein de l'espace poral formé par le squelette solide.

Title : Mechanical behavior of eroded soils : numerical study based on the DEM

Keywords : granular soils . suffusion . Discrete Element Method . mechanical behavior . micro-structure . extraction of fine particles . pore network

Abstract : Suffusion can induce a loss of fine particles to granular soils and consequently a modification of their mechanical behavior. In this PhD thesis, we aim to study the effect of the loss of fine particles caused by suffusion on mechanical properties of soils at the macroscopic and microscopic scales by using the Discrete Element Method (DEM). Granular samples composed of spherical particles with a gap-graded particle size distribution (PSD) are simulated by the DEM. Due to a very high computational cost, the fluid flow through the void space between solid particles is not simulated. Instead, we propose a representation of the internal state of soils after suffusion at three different levels with increasing complexity. For the level 1, a sample considered as eroded is generated at a target density and with a fine content lower than that of the original sample. The level 2 consists in removing a fraction of fine particles from the original sample at a given stress state. We proposed thus a method to identify the loose fraction composed of particles which do not carry significantly stresses. The level 3 aims to take into account the transport of fine particles in the pore network of the solid skeleton and the blockage of fine particles by constrictions. The key point in this model is how to describe the pore network. This study showed that fine particles can have a negligible effect, positive or negative effect on the shear strength depending on fine content. A removal of fine particles causes a significant reduction in shear strength to gap-graded soils. It was also showed that a random removal of fine particles leads to a greater reduction in shear strength than a removal of only fine particles in the loose fraction. For the description of the pore network of the solid skeleton, we propose a new method for merging neighboring tetrahedra issued from the Delaunay triangulation. This pore network will be incorporated into a model to take into account the transport and blockage of fine particles within the pore network of the solid skeleton.